Smart Sensors, Measurement and Instrumentation 7

Alex Mason
Subhas Chandra Mukhopadhyay
Krishanthi Padmarani Jayasundera
Nabarun Bhattacharyya *Editors*

Sensing Technology: Current Status and Future Trends I

Springer

Smart Sensors, Measurement and Instrumentation

Volume 7

Series editor

S. C. Mukhopadhyay, Palmerston North, New Zealand

For further volumes:
http://www.springer.com/series/10617

Alex Mason · Subhas Chandra Mukhopadhyay
Krishanthi Padmarani Jayasundera
Nabarun Bhattacharyya
Editors

Sensing Technology: Current Status and Future Trends I

Springer

Editors
Alex Mason
School of Built Environment
Built Environment and Sustainable Technologies Research Institute
Liverpool John Moores University
Liverpool
UK

Subhas Chandra Mukhopadhyay
School of Engineering and Advanced Technology
Massey University (Manawatu Campus)
Palmerston North
New Zealand

Krishanthi Padmarani Jayasundera
Institute of Fundamental Sciences
Massey University (Manawatu Campus)
Palmerston North
New Zealand

Nabarun Bhattacharyya
Centre for Development of Advanced Computing
Kolkata
India

The book editors are "Guest Editors".

ISSN 2194-8402 ISSN 2194-8410 (electronic)
ISBN 978-3-319-02317-5 ISBN 978-3-319-02318-2 (eBook)
DOI 10.1007/978-3-319-02318-2
Springer Cham Heidelberg New York Dordrecht London

Library of Congress Control Number: 2013953628

Printed on acid-free paper

Springer is part of Springer Science+Business Media (www.springer.com)

Preface

The applications of Sensing Technology include medical diagnostics, industrial manufacturing, defense, national security, and prevention of natural disaster. The correct detection of events by high performance sensors, and appropriate analysis of sensor signals can lead to early warning of phenomena, such as "Superstorm Sandy" which hit the eastern coast of the United States in 2012, and help to prevent deaths from these types of catastrophic incident. There is a need for interaction between researchers across technologically advanced and developing countries working on design, fabrication, and development of different sensors.

This book contains a collection of selected works stemming from the 2012 International Conference on Sensing Technology (ICST), which was held in Kolkata, India. This was the sixth time the conference had been held, and over the years it has become an incredibly successful event—in 2012 it attracted over 245 papers and provided a forum for interaction between researchers across technologically advanced and developing countries working on design, fabrication, and development of different sensors.

The conference was jointly organized by the Centre for the Development of Advanced Computing (CDAC), India, and the School of Engineering and Advanced Technology, Massey University, New Zealand. We whole-heartedly thank the members of CDAC for extending their support to the conference, as well as the authors and the Technical Program Committee: without the support of these people the conference would not be possible.

Since ICST provides a platform for a wide range of sensing technologies, this book presents a broad overview of the work currently undertaken by researchers in this field internationally; the second volume of this book, available separately, focuses specifically on sensors in the bio-mimicking area.

Chapter 1 begins with work discussing a smart system for monitoring of a person's movement and vital signs, a comprehensive system that has been developed in response to the world-wide issue of population ageing. It is thought that such systems will prove essential in the future in order to assist healthcare providers in targeting their efforts toward patients in need of care, thus replacing current periodic visit models for healthcare delivery. Chapter 2 continues with the elder-care theme, proposing an alternative method for the monitoring of vital signs, specifically respiratory systems for signs of some prevailing disorder. Chapter 3 rounds off the healthcare theme with the use of sensors for analysis of

gait during walking in order to monitor and develop, through biofeedback, patient walking patterns, which are both safe and offer sufficient clearance.

Chapter 4 discusses the notion of sensor modeling, which can address major challenges about heterogeneity in sensor data communication, data representation and their semantics. This chapter presents a novel seven layer modeling approach which enables the description of sensor models from the physical properties to the end functionality (i.e. definition of sensor services which can interface seamlessly and work corporately with other enterprise applications). Chapter 5 considers the use of modeling, via small signal analysis, to apply the level determination method of pneumatic volume gauging to ventilated storage vessels.

Chapter 6 sees the first in a sequence of chapters which discuss application of electromagnetic-based sensor systems. Such systems are typically useful for measurements of material dielectric properties, and can often offer advantages over competing sensor technologies in terms of reduced complexity and cost. In particular, this Chapter describes a system for the monitoring of water quality. Chapter 7 discusses the application of a resonant cavity sensor to the problem of monitoring water holding capacity in meat. Chapter 8 discuss the use of microwave tomography for analysis of timber, and finally for this topic, Chap. 9 considers the use of microwave frequency technology for the purpose of structural health monitoring, namely the monitoring of metallic structural elements.

Chapters 10–13 focus on sensors suited for the purposes of gas sensing, particularly through the use of nano-structures (Chaps. 10 and 11) and thick film resistors (Chaps. 12 and 13). These chapters discuss the design, construction, and rigorous testing undertaken for a variety of sensor types developed by researchers at a number of Institutions-based in India.

Chapter 14 discusses work of Japanese researchers, who have developed a laser induced breakdown spectroscopy (LIBS) system, and are looking at novel ways to improve its sensitivity for measurement purposes. Chapter 15 considers the development of an image analysis system which is demonstrated as having use in security applications, as well as for monitoring for abnormalities in buildings services systems, thus showing huge potential for future works in a number of applied areas.

Chapter 16, while not dealing directly with development of sensing, discusses important issues in the area of energy harvesting. Energy is typically a significant challenge for researchers considering remote or environmental monitoring applications since batteries have a finite lifetime. Thus, this work supports the work of others (e.g., systems such as those discussed in Chaps. 1–3), ensuring that sensor network systems have a prolonged operational life-span.

The final chapter of the book discusses an area of future potential and need for sensor development, that of radiation contamination in water. Tragic events such as Chernobyl and Fukushima have led to water sources being threatened by high levels of radiological contamination. These impact both on drinking water as well as food sources through the food chain and thus cause a significant interest. The chapter focuses on the most common sources of radiological contamination of water; it reviews the current regulatory approach to the measurement of such

contamination and critically discusses the advantages and limitations of traditional laboratory-based methods of water samples analysis as compared to novel emerging technologies that could be potentially implemented into online monitoring system for continuous verification of water quality and safety.

This book is written for academic and industry professionals working in the field of sensing, instrumentation and related fields, and is positioned to give a snapshot of the current state of the art in sensing technology, particularly from the applied perspective. The book is intended to give broad overview of the latest developments, in addition to discussing the process through which researchers go through in order to develop sensors, or related systems, which will become more widespread in the future.

We would like to express our appreciation to our distinguished authors of the chapters whose expertise and professionalism has certainly contributed significantly to this book.

Alex Mason
Subhas Chandra Mukhopadhyay
Krishanthi Padmarani Jayasundera
Nabarun Bhattacharyya

Contents

Chapter 1
A Novel Smart Sensing Platform for Vital Signs and Motor Activity Monitoring

M. Ribeiro, O. Postolache and P. Girão

Abstract Tele-monitoring associated with vital signs and motor activity represents nowadays an important issue considering the necessity to increase the number of medical services for the aged people living in their houses. The latest developments in the field of mobile devices, wireless communications and Internet access promote these types of solutions. The chapter presents a critical analysis of smart sensing solutions existing in the market and proposes a novel architecture designed for fast prototyping of sensing systems for human motor and cardiac activity monitoring. An extended description of the hardware, firmware, and software associated with proposed smart sensing platform is described in the chapter.

Keywords Cardiac activity monitoring · motor activity monitoring · Ubiquitous systems · Modular sensing platform · Sensors · Hardware redesign · Code reuse · Wireless sensor networks (WSN)

1 Introduction

New reality of global aging demographics and worldwide chronic diseases is forcing healthcare providers to move costs and care away from the hospital and primary care environment, and introduce a modern approach to healthcare through the usage of tele-healthcare that provides information about the patient health status. In this context, the development of reliable monitors for vital signs and motor activity continues to be an important challenge for biomedical research

O. Postolache (✉)
Instituto de Telecomunicações and ISCTE-IUL, Lisbon, Portugal
e-mail: opostolache@lx.it.pt

M. Ribeiro · P. Girão
Instituto de Telecomunicações and DEEC IST-UL, Lisbon, Portugal

A. Mason et al. (eds.), *Sensing Technology: Current Status and Future Trends I*,
Smart Sensors, Measurement and Instrumentation 7, DOI: 10.1007/978-3-319-02318-2_1,

groups taking into account the high diversity of measurements that must be done desirably in a non-invasive and unobtrusive way. It must be also considered the flexibility, transparency, and adaptability of the real time platforms used for fast prototyping of biomedical monitors as part of pervasive healthcare systems.

As part of the measuring channels, the sensors, mostly still analog, must have a digital interface that allows connectivity to any computer, smartphone, tablet or other intelligent electronic device. This property together with the identification and on board data processing, allows sensors to be defined as smart [1, 2]. However, mixing smart sensors data acquisition, embedded processing, and communication, at the firmware level can lead to harder maintenance of the code or even a complete redesign if the communication paradox changes completely, for example, from a wired solution to a wireless and networked one, implying an extended development time. To reduce this time a solution is to get started with a state of the art in the field, reducing the development time of a new biomedical signal monitor. This solution recurs to already tested modules, such as OEM products, good experience being reported by the authors using a BlueSentry OEM module designed to develop an embedded cardio-respiratory measuring system expressed by a smart wheelchair [3] or a motor activity measuring system based on a smart walker [4]. OEM products help to get the work done faster, allowing incrementally building of a new prototype based of modularity of these products. As a promissory solution in the field of OEM open-hardware open-software can be also mentioned the SHIMMER platform [5] that combines individual wireless modules with capability of electrocardiogram (ECG) and acceleration measurement to perform a continuously monitoring of a patient status. Some limitations are related to the embedding processing complexity of the acquired signals and to the multi-point communication capability, which makes this solution less attractive when multiple parameters are measured using measuring modules distributed on different body regions.

Taking into account the needs but also the OEM platforms in the market, this chapter presents an extended hardware and software description of a new smart sensing platform that was briefly presented during its evolution [6, 7], which allows fast prototyping of vital signs and motor activity monitors implemented as wearable or integrated in daily used objects such as beds, wheelchairs, and walkers. Elements related to the modular system firmware, as well as graphical user interface and data management implemented in a host computer, is also presented in the context of cardiorespiratory monitoring through photoplethysmography monitoring and motor activity monitoring using inertial measurement unit.

2 Smart Sensing Platform Architectures

In order to develop an appropriate platform that can be used for fast prototyping of vital signs and motor activity monitors, a study concerning the existing solutions was carried out. The studied platforms are characterized by no less than one microcontroller (MCU) and their firmware includes a Hardware Abstraction Layer

(HAL), which controls the microcontroller's peripherals, and the program code (PROGRAM). Important part of the study concerns the sensor's physical layer, denominated SENSOR PHY, that consists of the sensor itself (or multiple sensors), either digital or analog, and the signal conditioning circuits. The considered architectures may include different types of wired and wireless communications and data storage. In the next paragraphs are presented a set of representative architectures that may be used in the vital sign and motor activity monitor set-ups.

2.1 Fully Embedded Architecture

In this type of architecture, represented in Fig. 1, all the components (microcontroller, interfaces, memory, conditioning circuits, and sensors) are embedded in one single board, except the mechanical structure of some sensors that may have to be in direct contact with the physical quantity being measured. In the figure the dashed line correspond to physical links between the sensor board and the microcontroller board that also includes the power supply. Some sensors, such as accelerometers, temperature sensors or relative humidity sensors may also be placed on board if the platform is also used to measure the board vibration/motion and air quality conditions. For this type of architecture the main board includes the sensor's signal conditioning circuits, the communication and data storage modules, the microcontroller and its firmware that, in turn, includes the main program, the hardware abstraction layer, and other libraries that may be used.

This is a typical situation of commercial end-products or custom boards that serve a very specific purpose and for which, in a near future, is not planned to add new features that require the addition or redesign of the hardware. Hence, in terms of hardware, this architecture provides any or very few modular elements. The only ones that may be considered as such are the mechanical sensors that can be used interchangeably in the same sockets of the main board. For example, if every sensor's output is an analog signal, they can be all sampled the same way by using an analog-to-digital converter (ADC) (and the same channel). Examples of commercially available solutions that use this architecture are the Bionomadix from Biopac System Inc. [8], ergoPlux from PLUX Wireless Biosignal [9], and the gMOBIlab + from G.tec Medical Engineering [10], all of them used for biosignal acquisition. Another example of this architecture is the jNode [11], a wireless sensor network platform that supports distributed inertial kinematic monitoring. This platform has the very specific purpose of movement monitoring. For this platform the sensors, data storage, and communication modules are all included in the same board.

Work related the design and implementation of this kind of architecture has been done by our group [12, 13] .

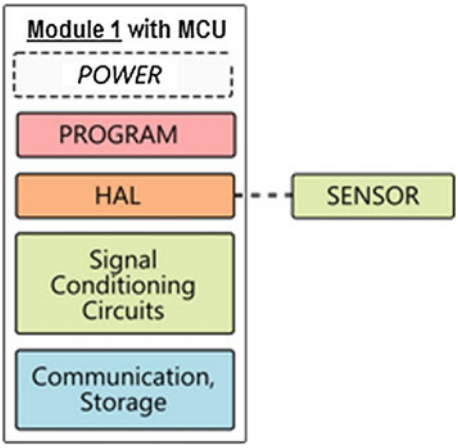

Fig. 1 Architecture #1: fully embedded architecture (HAL—hardware abstraction layer)

2.2 Increasing Modularity

In a different architectures the main board (Module 1 of Fig. 1) includes all the blocks of the fully embedded architecture except the sensors and signal conditioning circuits that are mounted on a separate board (Module 2 of Fig. 2). Additionally, external boards can be used to extend data communication or storage options that are already available in the main board. The connection between boards is generally realized through specific headers or sockets or by the so called expansion connectors. Although with a different designation, the latter may also be a header or socket. However, this differentiation pretends to highlight the differences of their use. While some headers and sockets available on the main board may serve a single and specific purpose, expansion connectors are usually used to expose unused pins of the digital controller, and for that reason offer greater flexibility. As an exception of what is represented in Fig. 2, some boards that use this kind of architecture may also include some sensors on board. These are generally digital sensors (e.g. 1-wire sensors) or sensors that require reduced conditioning circuits. Some examples of such sensors are digital accelerometers and digital temperature sensors.

The architecture presented in Fig. 2 is much more modular than architecture#1 described in the previous paragraph. Not only the sensors but also the communication and storage boards may be added or changed to extend the system capabilities. Some examples of this architecture include the Shimmer [5], MicroLEAP [14] and Eco [15] platforms.

Our research group has also designed and implemented solutions based on this architecture [16, 17].

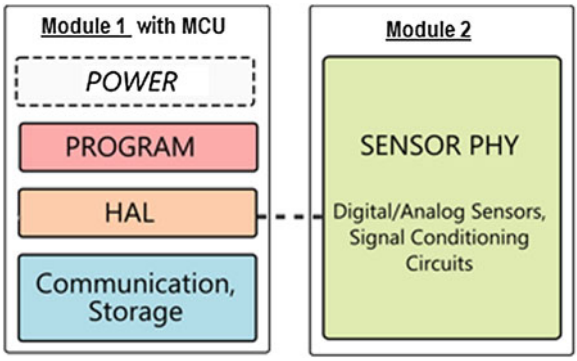

Fig. 2 Architecture #2: increasing modularity and extending functionality

2.3 Fully Modular

A fully modular architecture is characterized by the existence of the main module (Module 1) that includes a microcontroller (MCU), which communicates through the HAL with the sensor module (Module 2) and with a communication and storage module (Module 3) materialized usually by wireless communication bridges (e.g. Wi-Fi, Bluetooth or ZigBee) and microSD card reader. The block diagram of this architecture is presented in Fig. 3.

These types of platforms are used for general purpose prototyping and they do not focus on a specific application. A very popular example is the Arduino platform [18]. Another example is the .NET Gadgeteer compatible boards [19].

A platform based on the above presented architecture was implemented by our group and its functionalities are related to vital signs, motor activity and indoor air quality monitoring. The implemented platform, as part of a smart wheelchair prototype, is also compatible with IEEE1451.4 protocol for smart sensors [20].

2.4 Smart Sensing Platforms: A Critical Analysis and a Novel Solution

Analyzing the above presented architectures it can be mentioned that the hardware is modular in the sense that not all the electrical circuits are included in the main board. Instead, additional boards that can be connected to the main board provide additional circuits and features that can be used for several and distinct applications. However, each one of these boards may use different resources of a single microcontroller and this situation usually requires firmware changes. The firmware (MCU embedded software) is written according to the type of the communication boards and need to be adapted to the type of the sensors used. If changes need to be done either for communication or sensor related code (or both), the whole program needs to be changed, recompiled, and uploaded to the target board. The

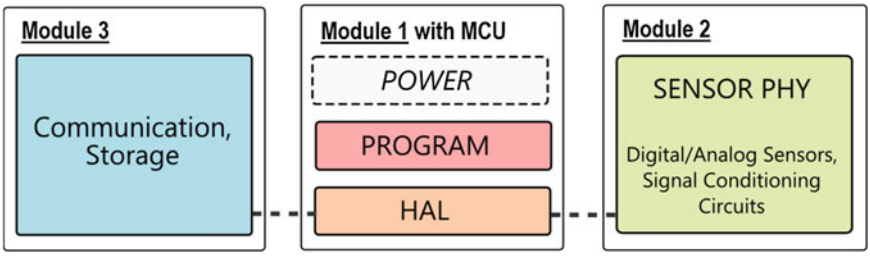

Fig. 3 Architecture #3: fully modular architecture

multiplicity of possible configurations using the same hardware may lead to code maintenance issues especially with the increasing complexity of each part of the overall system.

To overcome this drawback, a novel architecture is proposed in which the communication and sensor modules are completely separated. Thus, we consider one board for communication and another for sensor's related functionalities (signal conditioning circuits and digital processing), each one containing a microcontroller. This architecture requires a communication protocol associated with the communication between the boards. The existence of an MCU in each board makes the digital interface easy to be implemented and also allows distributed processing. Referring to the digital interface, this implies the development of a protocol stack that is used in both boards so both can understand each other, the "plug in play functionality" being assured.

This novel architecture presents the following capabilities:

- Plug-and-play capability: the sensor does not need to know how data is transmitted or stored, and the communication module does not need to know how the acquisition and the processing are done at the sensor board level. Each board has its own role in the system and communicates through a common digital interface that enables plug-and-play operation.
- Interoperability and tool chains: since the digital interface remains compatible (i.e., each board has a compatible protocol stack), each board can use a different microcontroller with different specifications and from different manufacturers. This is very important for developers because they can use their preferred embedded tool chain to develop new sensors and appropriate processing as well as new communication boards. For example, it may be appropriate to use a powerful processor in a communication board (e.g. 32bit ARM processor) but the sensor that one pretends to develop is so simple that a low-cost 8bit microcontroller may be enough. Also, some developers prefer to use PIC (from Microchip), for example, while others prefer to use ATmegas (from Atmel), and with this architecture they can take advantage of boards developed with different microcontrollers (as long as they do not want to change its firmware) and keep the microcontroller of their choice to develop new boards.

- Code readability and maintenance: the functions of the system are physically isolated. This means that the overall system functionality is split in two or more blocks of code (programs) each one running on each own microcontroller. This not only greatly improves the readability of code (each board's program will necessarily be less complex and contain less lines of code than if a single microcontroller was used), but also avoids updating the whole system. Instead, whenever one needs to make firmware changes just the affected board needs to be updated. The basic idea here is to apply the divide and conquer paradigm to hardware in order to further divide the firmware and improve the code maintenance of parts that constitute the whole system.

There are, however, some drawbacks when compared with the previous architectures:

- Latency: the digital interface used for communication between boards increases the time spent on transmitting or storing data. Increasing the rate at which data is transmitted in the digital interface will decrease latency but, in turn, it will also increase power consumption. That is a compromise to take into consideration at the design phase of a new system and which depends on the final application requirements (performance versus power).
- Power consumption: two MCUs will always consume more power than one.

The advantages provided by the novel proposed architecture, that we named Quick (Qk), may easily surpass the drawbacks specially when used for fast prototyping purposes. Also, although less efficient in terms of power consumption, it can still be "low power enough" for many applications if certain optimizations are implemented (e.g. keeping microcontrollers in a very low power state as long as possible and powering off peripherals not being used).

3 Qk Smart Sensing Platform: Hardware

The Quick (Qk) smart sensing platform is characterized by distributed intelligence. Each module has a microcontroller that performs specific tasks, the microcontroller being connected using a specific digital communication interface. The platform comprises a total of 5 physical elements denominated: QkHost, QkGateway, QkNetwork, QkModule and QkDevice.

3.1 Qk Platform: General Description

The novel architecture is based on the fundamental concept of separating communication from sensing: one board (QkModule) performs the data transmission to

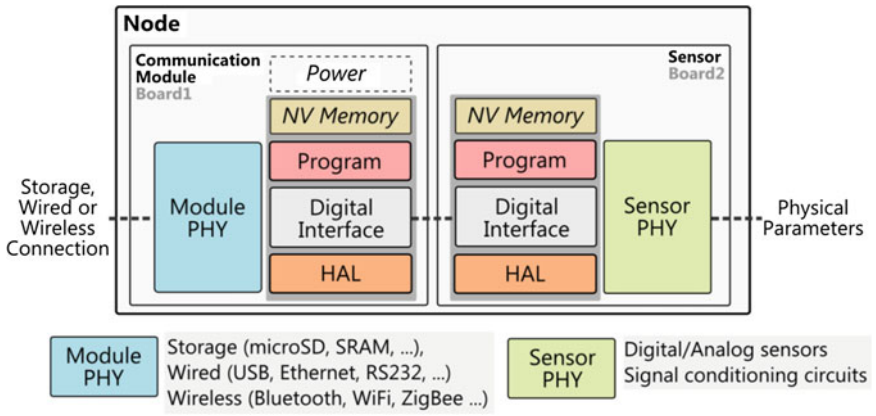

Fig. 4 Block diagram of the novel smart sensing architecture

a host device, while the other one, QkDevice, is related to data acquisition and primary processing. For simplicity, these two boards can be seen as a single element of the platform, called QkNode. The block diagram of the designed and implemented architecture is presented in Fig. 4.

In Fig. 4 can be noticed the boards (board 1 and board 2) that correspond to the above mentioned QkModule and QkDevice, each of them having a microcontroller. The implemented digital interface permits the communication between the two boards in a transparent way. The data processed by the sensor board and received by the communication board is transmitted to the host computer (QkHost) that runs high level software that includes libraries, advanced data processing and graphical user interface (GUI) applications that are able to interact with Qk boards. QkHost may also be a smartphone or other embedded system that needs to access a QkDevice board's data. A wired or wireless connection can be established between a QkHost and a QkModule board. This is depicted in Fig. 5.

In order to extend the communication capabilities between the QkModule and QkHost (smart phone, tablet, PC) including protocols such as IEEE 802.15.4, Zigbee or CAN, and at the same time maintaining the plug-and-play capability, the platform includes two additional types of boards: QkNetwork and QkGateway. Together, these two boards operate as a bridge, translating one protocol to another one. A QkGateway board provides the communication technology that is available in a given QkHost device while a QkNetwork board makes it compatible with the network communication technology being used. A QkNetwork board can interact with all the QkModule boards that use the same technology, and at the same time, it serializes the information coming from the different QkNodes in the network. The network communication topology is represented in Fig. 6.

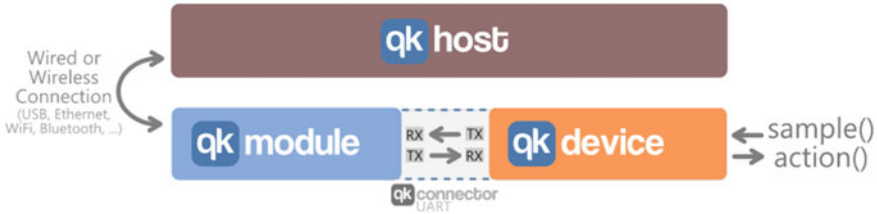

Fig. 5 Point-to-point communication topology

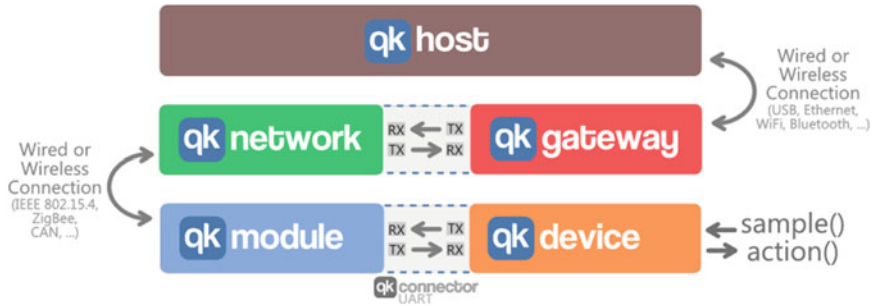

Fig. 6 Qk Network communication topology

3.2 Qk Boards

According to the above presented elements, the QkModule is materialized by a set of boards that perform functionalities such as data storage and wired or wireless data communication (Fig. 7). In the figure are presented different QkModule implementations including the microSD data storage board (Fig. 7a), USB wired communication board (Fig. 7b), wireless communication through Bluetooth board (Fig. 7c) and wireless IEEE802.15.4 or ZigBee network board (Fig. 7d). Several elements concerning the implemented boards are presented next.

microSD QkModule: The module was implemented to offer an alternative when the host device cannot be wired or wirelessly reached. Local data storage may be the best option. SD memory cards are commonly used for data logging purposes because nowadays most computers have slots to read these cards. However, to access its data from a computer, a file system (e.g. FAT) needs to be implemented on the SD card. The designed microSD QkModule implements a FAT16 file system based on FatFs. When a microSD card in inserted in the microSD slot, two CSV files and one text file (.txt) are automatically created:

- DATA.CSV: this file stores data coming from the QkDevice. Data values are comma separated so they can be readily processed by spreadsheet software. By default, the first data column is used for time-stamps but this can be disabled;

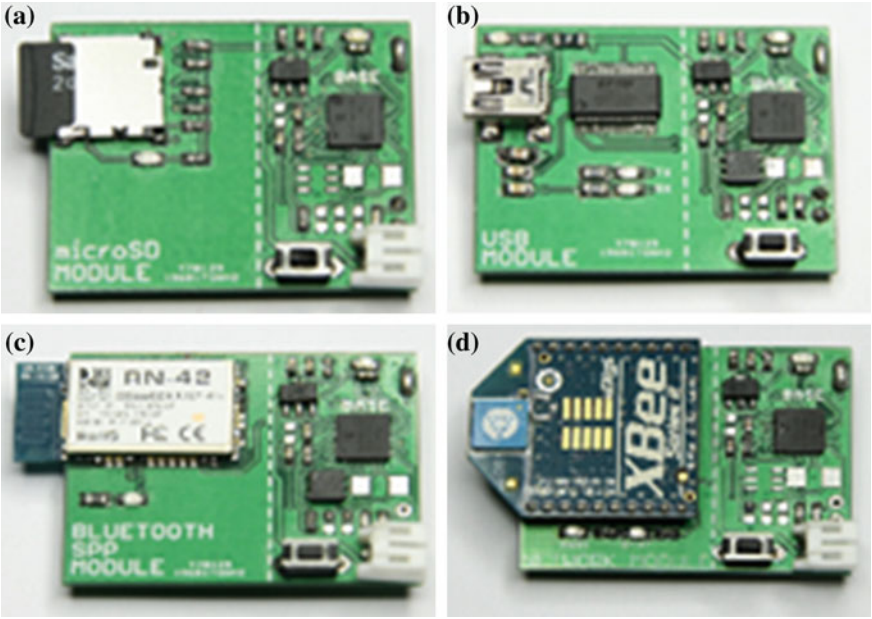

Fig. 7 QkModule: **a** microSD card module **b** SDcard module, **c** Bluetooth module, **d** ZigBee Module

- EVENTS.CSV: Events coming from the QkDevice are logged on this file. Since the events are asynchronous, every event is time-stamped;
- QK.TEXT: Notifications and other important information about the board are printed on this text file. For example, when a QkDevice board is attached/removed from the microSD QkModule board, a new message indicating such action is printed in the file. Furthermore, when the sampling frequency changes, a message indicating such action is also printed. This is particularly important because in the case data is not time-stamped the user can know at which frequency it was sampled. Every message in this file is time-stamped. If these files already exist on the memory card, they will be overwritten.

USB QkModule: Old-fashioned serial ports have been replaced by USB technology. USB clearly brings lots of advantages when compared to old RS-232 technology, namely the plug-and-play capability. However, from an implementation point of view, it also adds much more complexity. USB has many classes, each one serving a very different and specific purpose. One of them is the USB Communications Device Class (CDC) that emulates an RS-232 serial port. This class enables the compatibility of this technology with old equipment that still uses serial ports, such as modems. Also, microcontoller's UART is still commonly used in conjunction with communication standards such as RS-232. In order to use USB technology with CDC there are essentially two approaches that may be followed: embedded USB stack or external integrated circuit. As mentioned, mixing

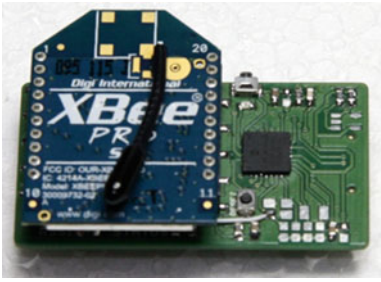

Fig. 8 XBee QkNetwork

communication code with our own application code may result in code maintenance issues. For that reason we choose to use an external integrated circuit that implements a USB-UART bridge. Hence, the FT232R integrated circuit, from FTDI, was chosen. Every data sent out through the microcontroller's UART is transferred to the Virtual COM Port the chip creates on the computer.

Bluetooth QkModule: The Bluetooth module allows wireless point-to-point communication, the Serial Port Profile (SPP) being used. Like the FTDI chip discussed above, this creates a Virtual COM Port in the host device. RN-42, from Roving Networks, was selected due to its reliability, ease of use, and low cost.

XBee IEEE 802.15.4 QkModule: This QkNetwork board developed is based on XBee modules, from Digi, which enable IEEE 802.15.4 communication. Considering that a network was previously created by an XBee QkNetwork board (the coordinator), every QkDevice that is connected to a XBee QkModule board automatically joins the Personal Area Network (PAN). Its 16bit address may be configured remotely or by using the X-CTU software provided by Digi. To integrate XBee IEEE 802.15.4 QkModule in an IEEE 802.15.4 network associated with distributed measurement of vital signs (e.g. body area network) a QkNetwork board (Fig. 8) was designed and implemented. This board is meant to be connected to a QkGateway board and, once connected, it acts as a transparent bridge, i.e., packets received by XBee QkModule boards are immediately sent to the QkGateway board (Fig. 9). It receives data from XBee QkModule boards, and can broadcast or send data to a single board (unicast).

Referring to QkModules, they present a board to board connector (BBC) that includes transmit and receive serial communication lines such as TX and RX (MTX, MRX) for UART or SDI and SDO in the SPI case. The SDI and SDO are multiplexed, SDI SDO meaning that just one of the protocols may be used. Additionally, a set of detection lines, DETM and DETS, are used to detect the board connection status (the lines are pulled-high and when a board is connected the lines are pulled down), thus allowing the module board to detect the sensor board insertion and vice versa. The BBC is also used to reprogram the microcontroller, either via a serial boot loader (if the microcontroller contains one) or directly via an in-circuit programmer (e.g. Microchip ICD3).

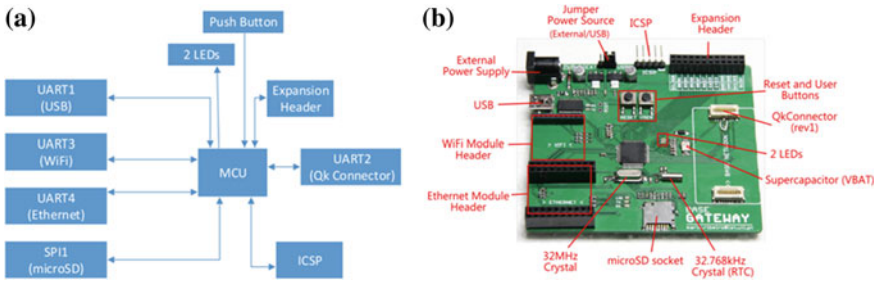

Fig. 9 QkGateway: **a** block diagram, **b** hardware implementation

Referring to the microcontrollers, the criteria used to select each unit were different for the QkModule and the QkDevice. Each module board must contain: at least two UARTs, one to interact with a communication module and another to communicate with the sensor board; one timer, to generate delays; one real-time clock/counter (RTCC), to timestamp data and generate interrupts with long intervals (minutes, hours or even days); one EEPROM, to store configuration parameters; at least one SPI module and an I2C module.

The microcontroller for the sensors board must have: at least one UART, to communicate with the module's board; two timers, one generating periodic interrupts (periodic sampling) and another used for delays; and an EEPROM to store configuration parameters.

Taking not only these hardware requirements into account but also the other considerations described in the above paragraphs, the chosen microcontrollers were PIC24FJ64GB002, for module boards, and PIC24F32KA302, for the sensor development board. These are 16bit microcontrollers from Microchip capable of 16MIPS and both featuring low-power technology. The PIC24FJ64GB002 has 64kB of program memory (FLASH), 8kB of data memory, an RTCC module, 5 V tolerant pins (which allow connecting 5 V powered sensor boards) and 15 pins that can be remapped. This last feature is particularly important due to the low pin count and allows using the same pins to interface communication or storage modules that have different interfacing requirements. For example, while USB, Bluetooth, and Network modules use UART, microSD card needs an SPI interface. In that case, the UART TX pin is remapped with SPI SDO pin and the UART RX pin is remapped with SPI SDI. Then, for example GPIO0 is remapped with SPI SCLK pin and another GPIO0 can be used as the SPI Chip Select (CS) pin.

Time precision is most critical for controlling sampling frequency and data rate transmission, such as the baud rate of the UART. The platform was successfully tested with baud rates up to 128kbps by using the maximum oscillator frequency (32 MHz) produced by the internal 8 MHz oscillator in conjunction with an internal 4xPhased-Locked Loop (PLL).

For analog sensors, the resolution of the ADC may be very important, depending on the requirements of the application. So, instead of 10bit ADC

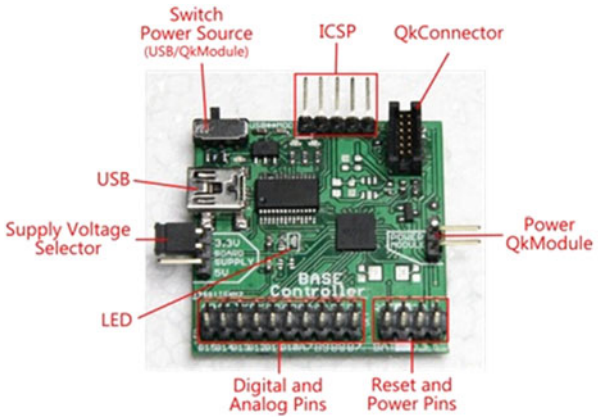

QkConnector

VBAT	GND
+3V3	RST
MTX	-
MRX	-
-	DETM
-	DETD

Fig. 10 QkDevice development board

available on most Microchip's 16bit microcontrollers, it was selected the PIC24F32KA302 which has an ADC with 12bit resolution and also contains an internal 256kB EEPROM. This microcontroller does not have pins that can be remapped but has the required UART and timers. All unused pins are available in the development board as well as reset, GND, 3.3 V, and 5 V pins. The board supports 3.3 V and 5 V supply selected via a jumper. A switch button allows selecting power source: from on board USB connector or from module. The USB port can be used for debugging during development or to program the microcontroller if a boot loader is already present (this platform uses the ds30 loader).

Referring to the QkDevice Development Board (Fig. 10), it was designed and implemented to facilitate and boost the prototyping and development of new sensing boards related to vital signs and motor activity monitoring other than the already implemented expressed by a photoplethysmography and Inertial Measurement Unit (IMU) boards.

In Fig. 10 can be observed the ICSP (In Circuit Serial Programming), that represents the programming header, a set of digital and analog pins associated to the MCU I/O that can be used to connect the sensing channels during the prototype implementation, a USB port, and the Qkconnector used to connect the QkDevice with the QkModule board.

4 Qk Smart Sensing Platform: Firmware

An important component of the platform is its firmware expressed by: QkProgram, QkPeripheral and QkDSP, which are described next.

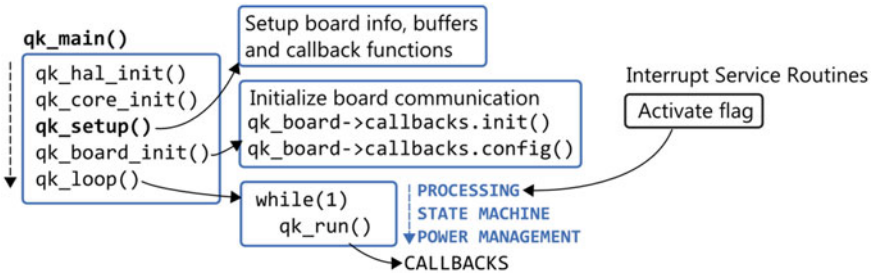

Fig. 11 The main loop of the Qk embedded framework

4.1 QkProgram: The Embedded Framework

QkProgram is a library that provides the core features of the framework which includes a main loop that controls the sampling (in the case of QkDevice boards), handles the communication between boards, and provides functions and data structures that allow a developer to easily build a new prototype by exclusively focusing on the function it adds to the platform.

The developer has only to implement the functions that are strictly dependent on the device to be developed and this is accomplished by using function pointers. When these functions, called callback functions, need to be executed, the main loop of the program invokes them appropriately. The embedded framework also provides data structures that are used to store information about the device, such as, firmware version and configurations, or to store sampled data. When the microcontroller receives a byte through the UART it generates an interrupt. The same happens when a timer expires or when Qk boards are attached/detached. Interrupt code should be as short as possible. This assures that the CPU can return to the main task in a timely manner. Hence, interrupt service routines are only used to signal a given asynchronous event by activating a flag and all the required processing is then performed by the qk_run function, i.e., it polls the flag, runs the processing code and then clears the flag. This is depicted in Fig. 11.

4.2 QkPeripheral: A Portable Peripheral Library

Configuring peripherals registers is always a time consuming task because it requires understanding how a given peripheral works by reading the microcontroller's datasheet and writing low level code to make it work as desired, but is also a critical aspect of any microcontroller based embedded system. Even though many microcontrollers from different manufacturers have peripherals with identical functionality, they are set up quite differently. QkProgram provides a HAL but it only covers the peripherals that are mandatory for the platform's core to work.

Additional peripherals, such as additional timers, ADC, and digital interfaces, which are available on the microcontroller and are not used by QkProgram, can be used in user application. The QkPeripheral library is an abstraction layer to those common peripherals and it allows increasing the portability of code written for devices prototyped with the Qk platform. It provides generic and simple functions that implement the most essential function of a peripheral. The multiplicity of a peripheral varies a lot among microcontrollers, and as such, the library only implements functions for a single instance, i.e., even if the microcontroller provides more than one additional timer, for example, the library includes support for a single one. Currently, the library supports the following peripherals: GPIO, timer, ADC, UART, PWM, SPI and I2C.

4.3 QkDSP: Fixed-Point Digital Signal Processing Algorithms

Biomedical signals are affected by noise and, in many cases, the use of DSP algorithms, such as digital filters, is mandatory for accurate extraction of physiological parameters. Filters are used for noise reduction but also to extract meaningful information from digital signals. Some implementations may be complex and require considerable computational power and memory. Hence, small and low power embedded systems present some challenges due to their lack of processing power and scarce memory. A library that makes digital filters easy to use and implement at the embedded level was implemented and is called QkDSP. This library not only allows the developer to abstract from the implementation details, but also helps to keep the code more organized, since several filters may be implemented by using the same structures and functions. QkDSP provides data structures and functions for the following filters: i) Moving Average (MA), ii) Exponential Moving Average (EMA), iii) Finite Impulse Response (FIR), iv) Infinite Impulse Response (IIR).

All filters except the MA filter, which does not use fractional numbers, are implemented in fixed-point format. The coefficients of EMA and FIR filters use Q15 format representation, which means that the fractional part of the fractional number is represented with 15 bits while the remaining bit is the sign bit. On the other hand, the format representation of the coefficients of IIR filters should be specified by the developer.

5 QkHost: High Level Software

In order to assure the remote control and data communication between the host computer and the smart sensing platform, QkHost high level software was developed using Qt, a C ++ cross-platform graphical framework from Digia.

Several Qk applications such as QkLib, QkRaw and QkViewer were developed and described in the following paragraphs.

5.1 QkLib: A Cross-Platform C++ Shared Library

The QkLib is a shared library that may be used by other Qt applications that pretend to interact with Qk hardware. It not only implements the core functionality but also provides some GUI widgets that can be integrated into other applications. These widgets provide a simple way to establish a serial connection with the platform and search for Qk boards. An implemented widgets example can be seen in Fig. 12.

5.2 QkRaw: Debug and Configuration

Debugging Qk boards during its development phase proved to be a hard task. The QkRaw program, shown on Fig. 13, was implemented to facilitate this task. QkRaw consists of a terminal (QkTerminal) and each printed line corresponds to a single packet sent.

The packet is parsed and some information is presented on the same line, with the following sequence:

<source > < address > < code name > < data bytes>

where the source field is the board that sent the packet and is represented with a letter: G for QkGateway, N for QkNetwork, M for QkModule and D for QkDevice, the address is the source's 16bit address and is always 0x0000 for QkGateway and QkNetwork boards since only one board of this type is allowed in the same serial connection, the code name field displays the name of the packet's code, which greatly helps to visually identify the kind of information that is contained in the packet and, finally, the data bytes field displays the packet's bytes in hexadecimal format, excluding the bytes related to the source's address.

Fig. 13 also shows the following widgets: QkLogger (used to log events), QkExplorer (explores every board used in the same serial connection and allows updating and saving configurations), and QkDebug (prints debug strings sent by Qk boards).

5.3 QkViewer: Real-Time Data Visualization

The QkLib can be used to access sensors data for further processing. However, for many applications, it is only necessary to have a way to visualize the data,

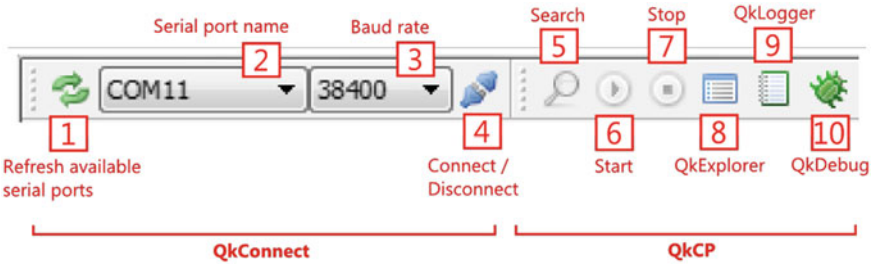

Fig. 12 GUI widgets: QkConnect and QkCP

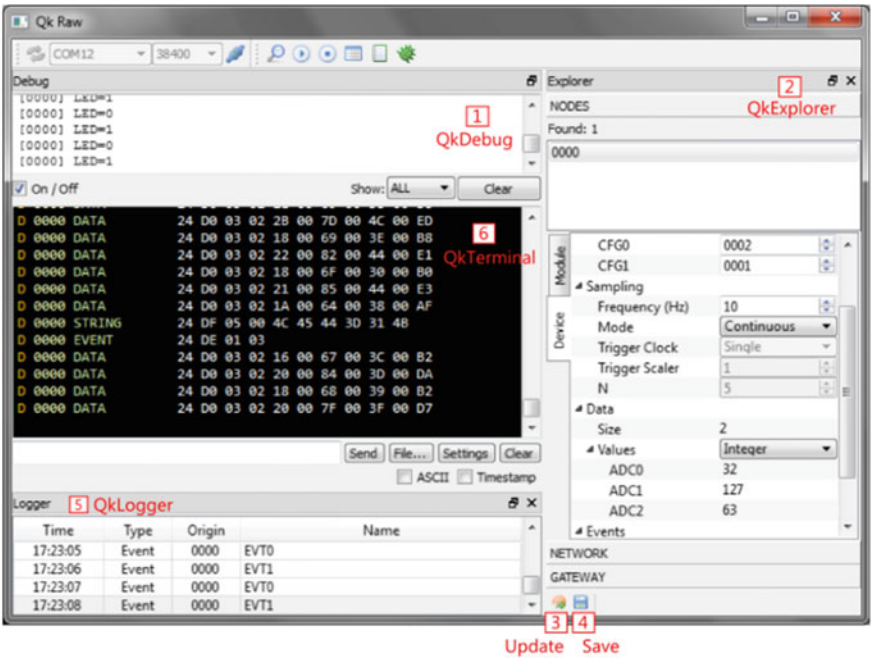

Fig. 13 QkRaw: a GUI for debugging

generally by using charts, plots or other kind of displays. For this reason, the QkViewer, presented in Fig. 14, was developed.

QkViewer allows adding as many plots as needed to the plotting area and each plot has its own waveforms. Each waveform corresponds to a single sensor's output data and the Waveform Manager (1) allows selecting that data from a given node (if multiple nodes are used, otherwise only the address 0x0000 will be available). The plots are interactive and easily configurable. The name of the axes, the title and the legend of the plot can be edited by double-clicking on it. The plot

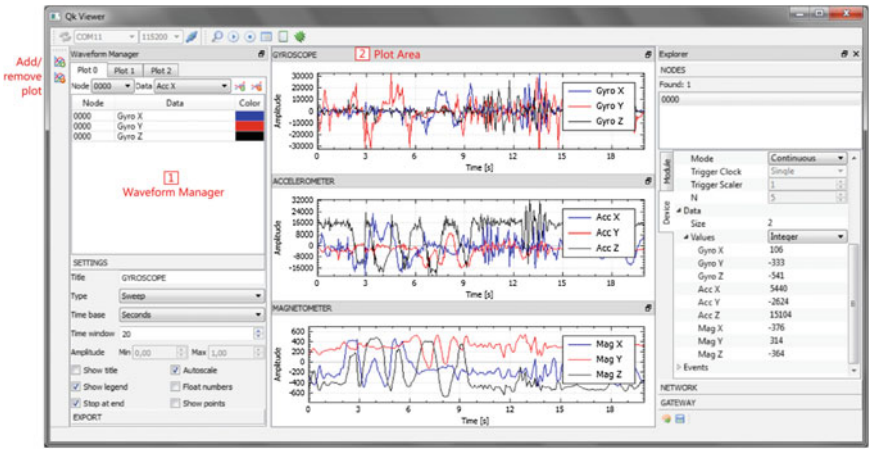

Fig. 14 QkViewer: plotting data (1 node, 3 plots, 9 waveforms)

can also be dragged and vertical/horizontal zooming can be accomplished by clicking on the vertical/horizontal axis and using the mouse's scroll wheel to zoom in or out. The Waveform Manager can be used to set the plot's time window and it enables other features, such as, auto scale, stop plotting when the values reach the end in the time window, and mark sampling points with circles over the plot's line.

6 Qk Smart Sensing Platform Applications

In order to test the smart sensing platform capabilities, two applications were considered: the motor activity and the cardiac activity monitoring of humans. Thus, QkMotion and QkPhotoPlethys, as members of QkDevice board class fully compatible with QkModule, were designed and implemented.

6.1 QkMotion: Motor Activity Monitoring

To perform the motor activity monitoring of subjects during the usual activity as part of an ambient assisted living implementation, including also reliable fall detection component for alarm generation in critical situations, different sensing systems are known in the literature [21, 22]. The main hardware components of these kinds of systems are MEMS inertial sensors, particularly 3D accelerometers. In order to extract additional information related to subjects motion, the latest implementations already commercial available are known as inertial measurement units. Related to motor activity monitoring can be mentioned Xsense [23] that also

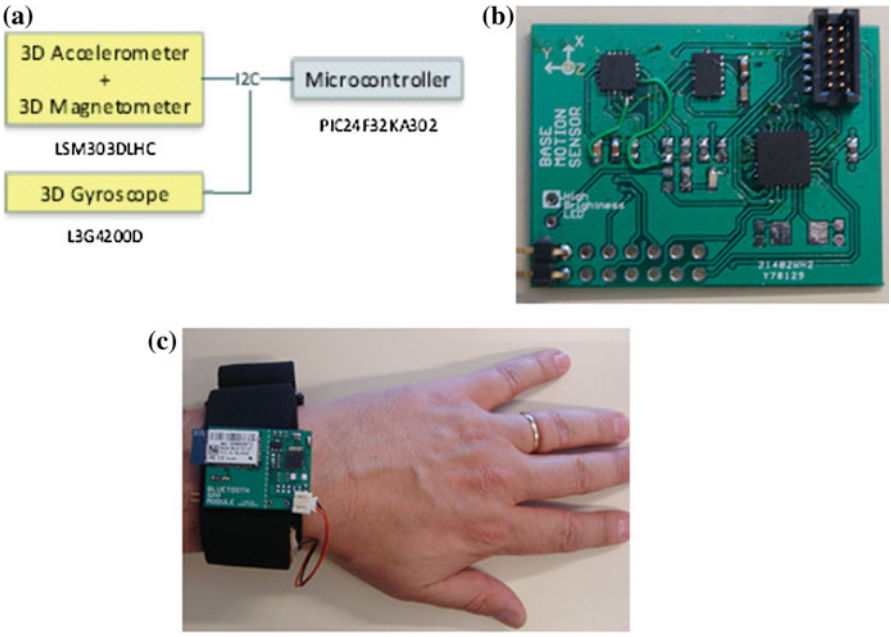

Fig. 15 QkMotion: block diagram and implementation **a** IMU block diagram, **b** Qk motion board implementation, c)Qk motion and Bluetooth QkModule for evaluation of hand motion)

provides an inertial measurement unit, which includes a set of three MEMS sensors expressed by a 3D accelerometer, a 3D gyroscope, and a 3D magnetometer. The sensor data is fused to extract accurate information about orientation and motion tracking. Lord Microstrain provides and accurate IMU (3DM-GX3® -15) [24] that is applied for personnel tracking and inertial aiding of GPS. In this context, and considering the previous work related to motor activity monitoring [12], a particular QkDevice for Qk smart sensing platform—QkMotion device—that materializes an Inertial Measurement Unit was designed and implemented. The QkMotion includes a gyroscope (L3G4200D) and an accelerometer-magnetometer (LSM303DLHC) connected to the QkMotion microcontroller using I2C protocol (Fig. 15).

The 3D acceleration, full magnetic field and 3D angular rate informations are used as input values of a data fusion algorithm associated with the designed and implemented prototype of inertial measurement unit. These algorithms (e.g. Kalman based filters [25, 26]) are usually complex and demand large computational load. S.O. Madgwick proposed an alternative approach, a novel orientation algorithm designed to support a computationally efficient, wearable inertial human motion tracking system for rehabilitation applications which is presented in [27]. The filter calculates the orientation by numerically integrating the estimated orientation rate. It is computed as the rate of change of orientation measured by the gyroscopes. The magnitude of the gyroscope measurement error is removed in the

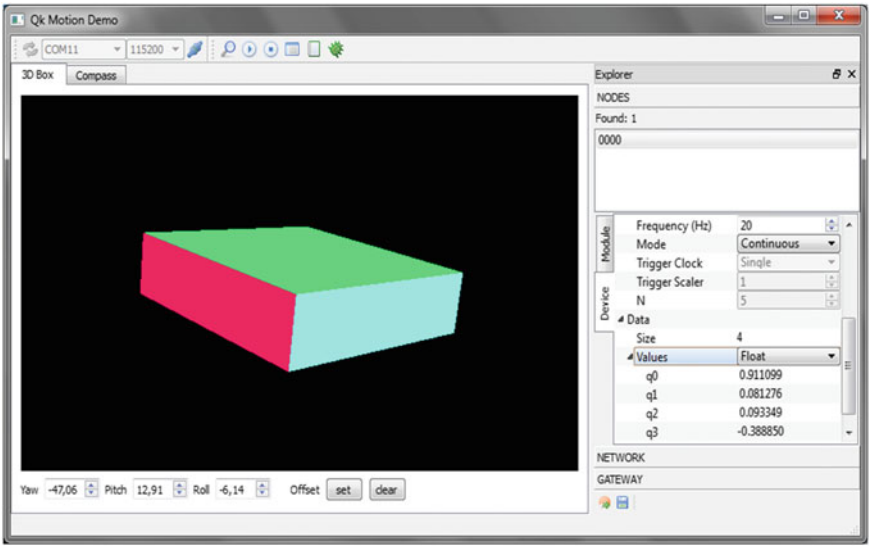

Fig. 16 QkMotion's IMU test GUI

direction of the estimated error, which is computed based on accelerometer and magnetometer measurements.

A Graphical User Interface (GUI) was developed (Fig. 16) to control the platform and to visualize the position of the object whose motion is considered. Data is sent in quaternion format and then converted into Euler angles in the GUI application. An OpenGL 3D box gives visual feedback of those angles by reproducing the same orientation of the physical sensor board that it is attached to the monitored object (e.g. an arm during a physiotherapy session). On the right side of the GUI there is an Explorer widget (dock widget) that allows to identify and monitor all connected sensors as well as to configure them. The evolution of yaw, pitch and roll angles during motor activity assessment tasks are presented using digital displays that appear at the GUI's bottom part.

Considering the 3D magnetometer as part of QkMotion Hardware, a compass functionality can be easily implemented. The GUI used to QkCompass data visualization is presented in Fig. 17.

To assure appropriate graphical representation of the signals associated to the motor activity, a specific GUI, part of QkViewer software, was designed. The evolution of the acceleration, angle rate, and magnetic angular rate during motor activity sequence including walking, running and jumping is presented in Fig. 18.

The sensor board can also generate events, such as free fall or when motion reaches a threshold level in any three dimensional coordinate (X, Y, Z).

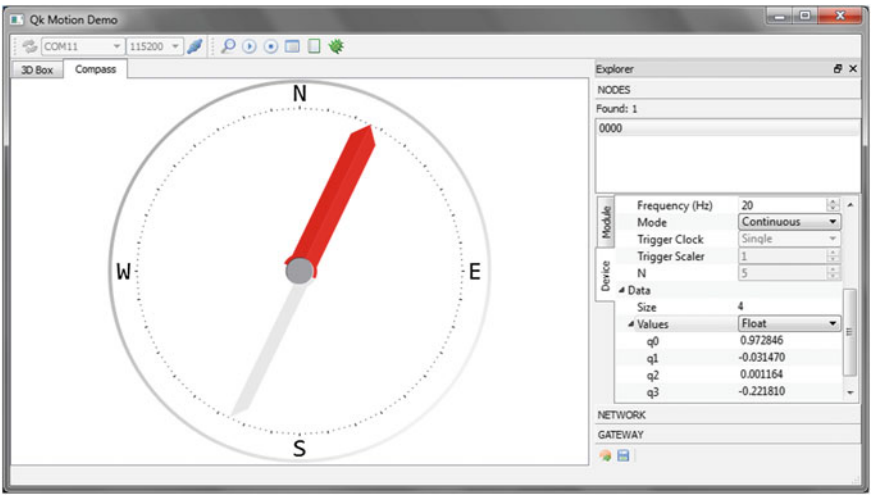

Fig. 17 QkMotion as a compass

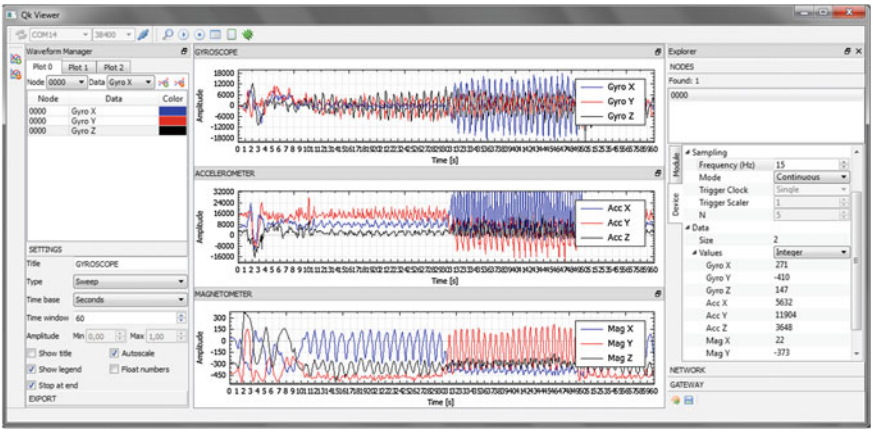

Fig. 18 GUI associated with QkViewer software: acceleration, angle rate and magnetic rate evolution for the motor activity monitoring case

6.2 QkCardio: Cardiac Activity Monitoring

Using the modular system, including the photoplethysmography (PPG) sensor [7], and the QkDevice development board, cardiac and respiratory activities monitoring can be carried out. The analog signals provided by PPG are acquired and processed by the QkDevice microcontroller to calculate physiological parameters such as heart rate, SpO2 and even respiratory rate taking into account the

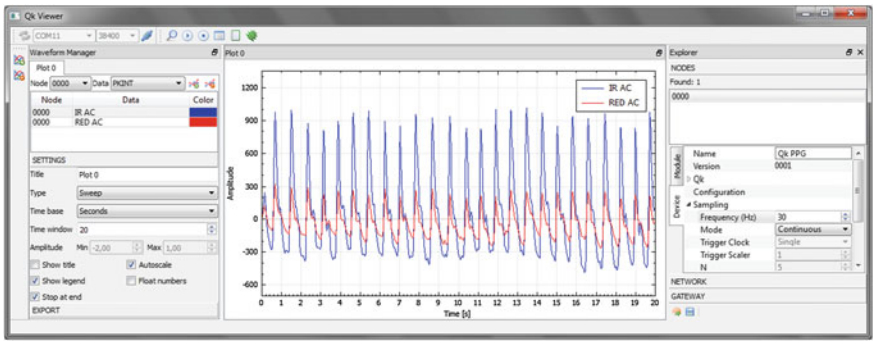

Fig. 19 GUI associated with Qk viewer software: Photoplethysmography monitoring case

capability of the system to be programed according to the digital filtering requirements. Fig. 19 presents the designed and implemented GUI of QkViewer that permits to visualize the PPG signals obtained for infrared (940 nm) and red (660 nm) light excitation beams of the PPG sensor LEDs. The PPG waves output by a broadband light detector are used to extract the SpO2 information using the algorithm described in [7]. The SpO2 values, included in the 92 % to 99 % interval, are validated by a Medlab P-OX100 system.

As it was presented for the motor activity monitoring case, the QkViewer GUI permits to set-up the acquisition parameters (acquisition type: single, continuous, sampling rate, number of channels) and is also able to identify and show automatically the type of the sensor connected to the system.

7 Conclusion

A new smart sensing platform with high degree of modularity, high flexibility and interoperability, and "plug-and-play capability" named Quick (Qk) designed having in mind fast prototyping of vital signs and motor activity wearable monitors was described. This smart sensing platform was designed and implemented after a critical analysis of the existent solution in the field of physiological parameter monitoring. They are mostly proprietary solutions with less flexibility concerning communication, embedding processing and sensing. The usage of such platforms reduces or precludes the possibility of developers to include new wireless communication capabilities according to the requirements of new healthcare systems that value point-to-point Bluetooth to multipoint IEEE802.15.4 wireless communication.

The Qk boards were developed to assure the main functionalities of wearable monitors including sensing, embedded processing and wireless communication. They permit a short time cardio respiratory and motor activity monitor setup, satisfying at the same time the basic system concept for pervasive healthcare.

With the boards (QkModule, QkDevice, QkNetwork and QkGateway) and software tools provided by the platform, even persons without technical knowledge may take advantage of the developed smart sensing boards since they are highly configurable and firmware changes are not required to use them in different communication topologies. Both firmware and software frameworks allow developers to prototype new electronic sensing devices easier and faster as well as developing new graphical user interfaces adapted to the user requirements.

Particular elements regarding the design and implementation of an inertial measurement unit with sensor data fusion and the cardiac assessment through photoplethysmography sensing were considered. Results related to the use of the implemented inertial measurement unit highlight the capability of the system to be used as motor activity monitor to assist in physiotherapy sessions, underlining the flexibility of the implemented platform, which recommends it as an interesting solution in the field of pervasive healthcare and part of future architectures associated with Internet of Things and Machine to Machine implementation for health status assessment, remote rehabilitation and environment quality (e.g. air quality) monitoring.

References

1. IEEE Standard for a Smart Transducer Interface for Sensors and Actuators—Common Functions, Communication Protocols, and Transducer Electronic Data Sheet (TEDS) Formats, IEEE Std 1451.0-2007, pp.1–335, 21 Sept 2007
2. ISO/IEC/IEEE Standard for Information technology—Smart transducer interface for sensors and actuators—Part 4: Mixed-mode communication protocols and Transducer Electronic Data Sheet (TEDS) formats, ISO/IEC/IEEE 21451-4:2010(E), pp.1–448, 20 May 2010
3. O. Postolache, P.M. Girão, R. Madeira, G. Postolache, Microwave FMCW Doppler radar implementation for in-house pervasive health care system", in *Proceedings of IEEE International Workshop on Medical Measurements and Applications*, Ottawa, Canada, vol. 1, pp. 47–52, 2010
4. O. Postolache, P. Girão, J.M. Pereira, G. Postolache, Smart walker for pervasive healthcare, in *Procedings of International Conference on Sensing Technology—ICST*, Palmerston North, New Zeeland, vol. 1, pp. 1–5, December, 2011
5. Shimmer, Wireless Sensing Solutions for werable applications, online at: http://shimmer-research.com/
6. M. Ribeiro, O. Postolache, P.S. Girão, Architectures for modular smart sensor systems, in *Proceedings of International Conference on Sensing Technology—ICST*, Kalkata, India, vol. 1, pp. 1–7, Dec 2012
7. M. Ribeiro, O. Postolache, P.S. Girão, Modular platform architecture for fast prototyping of vital signs and motor activity monitors, in Procedings of IEEE International Instrumentation and Technology Conference.—I2MTC, Minneapolis, United States, vol. 1, pp. 1–6, May 2013
8. Biopac System Inc., Bionomadix–Wireless Physiology Monitoring Devices, online at: http://www.biopac.com/research.asp?CatID=57&Main=BioNomadix D Wireless Physiology
9. PLUX PLUX, Wireless Biosignals S.A., ergoPLUX biosignals acquisition system, online at: http://www.ergo.plux.info/manual/ergoPLUX_manual.pdf

10. gtec-medical engineering, g.MOBIlab + g.tec's portable biosignal acquisition and analysis system, online at http://www.gtec.at/Products/Hardware-and-Accessories/g.MOBIlab-Specs-Features
11. M. Scholl, K. Laerhoven, D. Gordon, M. Scholz, M. Berning, jNode: a sensor network platform that supports distributed inertial kinematic monitoring, in *Ninth International Conference on Networked Sensing (INSS) 2012*, pp. 1–4, June 2012
12. O. Postolache, P. Girão, M. Ribeiro, M. Guerra, J. Pincho, F. Santiago, A. Pena, Enabling telecare assesment with pervasive sensing and Android OS smartphone, in *Proceedings of IEEE International Workshop on Medical Measurements and Applications*, Bari, Italy, vol.1, pp. 1–5, May, 2011
13. O. Postolache, P. Girão, M. Ribeiro, H. Carvalho, A. Catarino and G. Postolache, Treat me well: affective and physiological feedback for wheelchair users, in *Proceedings of IEEE International Symposium on Medical Measurements and Applications*, Budapest, Hungary, May 2012
14. L. Au, W.H. Wu, M. Batalin, D.H. McIntire, W. J. Kaise, MicroLEAP: Energy-aware wireless sensor platform for biomedical sensing applications, in *2007 IEEE Biomedical Circuits and Systems Conference*, pp. 158–162, Nov 2007
15. C. Park, P. Chou,Eco: ultra-wearable and expandable wireless sensor platform, in *BSN 2006 International Workshop on Wearable and Implantable Body Sensor Networks*, pp. 165–169, 2006
16. O. Postolache, P.M. Girão, H. Ijaz, IEEE 1451.4 embedded smart sensors architecture for wheelchair user monitoring, in *Proceedings of IEEE International Workshop on Medical Measurements and, Budapest*, Hungary, vol. 1, pp. 1–5, May 2012
17. O. Postolache, J.C. Freire, P.M. Girão, J.M. Dias Pereira, Smart sensor architecture for vital signs and motor activity monitoring of wheelchair' users, in *Proceedings of International Conference on Sensing Technology—ICST*, Kolkata, India, Vol. 1, pp. 1–6, Dec 2012
18. Arduino, Medical and Health Related Projects with Arduino, online at: http://medicarduino.net/
19. Microsoft, Microsoft.NET Gadgeteer:Choosing hardware, online at: http://www.netmf.com/gadgeteer/get-started.aspx
20. M.R. Ribeiro, O. Postolache, P.M. Girão, Architectures for Modular Smart Sensor Systems, in *Proceedings of International Conference on Sensing Technology—ICST*, Kalkata, India, vol. 1, pp. 1–7, Dec 2012
21. I.C. Gyllensten, A.G. Bonomi, Identifying types of physical activity with a single accelerometer: evaluating laboratory-trained algorithms in daily life. IEEE Tran. Biomed. Eng. **58**(9) 2653–2656 (2011)
22. Q. Li, J.A. Stankovic, M.A. Hanson, A.T. Barth, J. Lach, G. Zhou, Accurate, fast fall detection using gyroscopes and accelerometer-derived posture information, in *Proceedings of Sixth International Workshop on,Wearable and Implantable Body Sensor Networks*, Berkeley, CA,.(2009) pp. 138–143
23. A.G. Cutti, A. Ferrari, P. Garofalo, M. Raggi, A. Cappello, A. Ferrari, Outwalk': a protocol for clinical gait analysis based on inertial & magnetic sensors, Springer Med. Biol. Eng. Comput. **48**(1) 17–25 (2010)
24. Lord Microstrain, Inertial Sensors: 3DM-GX3® -45 online at: http://www.microstrain.com/inertial/3dm-gx3-45
25. F.M. Mirzaei, S.I. Roumeliotis, A Kalman filter-based algorithm for imu-camera calibration: Observability analysis and performance evaluation. IEEE Trans. Robot. **24**(5), 1143–1156 (2008)
26. W. Gao, Y. Yang, X. Cui, S. Zhang, Application of adaptive Kalman filtering algorithm in IMU/GPS integrated navigation system, Geo-spatial Inf. Sci. **10**(1) 22–26
27. S.O.H. Madgwick, A.J.L Harrison, R. Vaidyanathan, Estimation of IMU and MARG orientation using a gradient descent algorithm, in *2011 IEEE International Conference Rehabilitation Robotics (ICORR)*, pp.1–7, June –July 2011

Chapter 2
Real-Time Monitoring of Respiratory Diseases of Distantly Located Elderly Impaired Patients

S. Bagchi and M. Chattopadhyay

Abstract This paper presents a cost effective on-line ventilation monitoring system for impaired elderly persons using optical wireless sensory system. In this work, we have tried to develop this system especially for aged physically disabled people by introducing a cordless optics based sensing system as a secondary transducer which carries many distinctive features like (i) no electrical signal is directly connected with the subject's body, thus providing a shock hazard free module, (ii) any hardware interfacing circuit (for computer compatible signal) not required which again minimizes complex circuitry and finally generates (iii) a noise free computer friendly output. The processor analyses the signal and communicates information to the distantly located physicians through blue tooth technology. Here, we have developed an algorithm which monitors important spirometric values such as Forced Expiratory Volume of air in first one second (FEV1), Forced Vital Capacity (FVC) and Peak Expiratory Flow (PEF) continuously, so that any deviation from the safe limits will allow the system to send a warning sign to the physician's mobile and at the same time it will send numerical and graphical respiratory information of the subject to the web-server. Our study is limited to two common respiratory diseases like chronic obstructive pulmonary disease (COPD) and chronic restrictive pulmonary disease (CRPD). We have studied the respiratory activities of 50 male impaired elderly persons. The sent information through the wireless technology using telemetering platform is in very close agreement with the actual clinical conditions as the performance of the proposed sensory system is verified with a standard calculator. We have extended our studies with time-constant of the respiratory circuit for assessing the common obstructive and restrictive respiratory diseases. In addition, we have focussed by widening our studies towards the common obstructive respiratory diseases, like bronchial asthma and emphysema. Finally, the influence of changes in the respiratory system (air tract and alveoli) due to emphysema and bronchial asthma has been accessed through exhaled air flow-volume patterns.

S. Bagchi (✉) · M. Chattopadhyay
Heritage Institute of Technology, Department of Applied Electronics and Instrumentation Engineering, Kolkata, India
e-mail: sjb.prof@gmail.com

A. Mason et al. (eds.), *Sensing Technology: Current Status and Future Trends I*, Smart Sensors, Measurement and Instrumentation 7, DOI: 10.1007/978-3-319-02318-2_2,

Keywords Wireless optical sensor · FEV1 · FVC · PEF · COPD · CRPD · Shock hazard · Telecommunication network · Data base management system · Telemonitoring platform · Time-constant · Bronchial asthma and emphysema

1 Introduction

Globally, the proportion of older people is growing faster than any other age group. In 2000, one in ten, or about 600 million, people were 60 years or older. By 2025, this figure is expected to reach 1.2 billion people, and in 2050 around 1.9 billion [1, 2]. Modernization and urbanization, as well as shifting values regarding family care for aged people, has contributed to a marked breakdown of community and intergenerational support mechanisms causing an increasing numbers of frail older and impaired community become both dependent and isolated [3–5]. By considering these aspects, we have tried to develop a low cost device with telemetering concept to monitor the real time respiratory disorders. In this regard, various sensing devices and telecommunication based technologies have been proposed. A mobile phone based scheme has been introduced to receive and display the air- flow information during inhalation and exhalation. The obtained signal is transmitted via Bluetooth to the processing and diagnostic unit with wireless protocol between sensors and the electronics board. A MEMS based silicon hot wire anemometer was used for flow measurement [6]. A scheme of virtual reality and telemedicine for comfort and safe health care in their homes using communication technology was placed for old and disabled patients, eradicating costly and potentially hazardous journeys to hospitals [7]. A convenient, accessible spirometric telemonitoring system for assessing lung function was described by Jannett et al. [8]. A patient's spirometric data, useful in assessing lung functions, are measured using a home spirometer and are transmitted over a telephone line to a database maintained by an institutional computer system. The importance of wireless technology was described by Tam Vu Ngoc for distantly located subjects. The technology invaded the medical area with a wide range of capability especially for the old and impaired patients [9]. A wireless breathing support system was assembled by an optical sensor, an accelerometer, a microcontroller, a Bluetooth module and a laptop computer for remote staying physicians. The optical sensor, which is attached to the patient's chest, measures chest circumference and outputs the variations of circumference (referencing the breathing pattern) as serial digital data [10]. Max Skorning and his team conducted a simulation based study to investigate the feasibility of tele-consulatation that included monitoring and transmission of audio and visual information to a remotely located physician [11].

Moreover, different sensing technologies were proposed to measure important spirometric values. An optical fiber sensor, based on the macro-bending loss effect,

was redeveloped for thoracic and abdominal circumference measurements. This non-invasive plethysmographic respiratory system used for health monitoring was reported by Augousti et al. in year 2005 [12]. In the same year, a different proposal given by Lay-Ekuakille et al. has introduced a smart improvement in Pneumotachographic system via breath recognition and opto-isolation. They adopted optically coupled amplifier to allow inspiration recognition to select different patients' (child, young, or old man) breath to enhance the sensitivity of the differential pressure sensor [13]. In year 2010, Lipi Mohanty and Kevin S. C. Kuang invented a breathing rate sensor with plastic optical fiber, demonstrating the ability to quantify the breathing rate and monitor different breathing patterns up to a resolution of 1 breath/second (1 Hz). They applied the principle of coupling loss in designing this sensor to take advantage of the large core size of plastic optical fiber [14]. Wook Jae Yoo et al. in 2010, proposed an optical fiber-based respiration sensor for a noninvasive respiratory monitoring gadget, where they fabricated two types of noninvasive nasal-cavity-attached fiber-optic respiration sensors. One is a silver halide optical-fiber-based respiration sensor that can measure the variations of infrared radiation generated by the respiratory airflow from the nasal cavity. The other is a thermo chromic-pigment-based fiber-optic respiration sensor that can measure the intensity of reflected light which changes due to color variations of the temperature-sensing film [15]. In the same year, a non-contact type optical procedure was reported by Wolfgang Drexler et al. for precise measurement of respiration rate and flow. This method was based on the measurement of external chest wall movement by a laser Doppler vibrometer [16].

In this paper, we present a tele-monitoring platform [17–19] for real-time respiratory signal acquisition, transmission and display. The proposed platform was devised as a tool for remote caring system having:

- interface with measurement instrumentation through Bluetooth;
- local data acquisition and visualization; and
- data transmission to a remote server such as hospitals.

The rest of the paper is organized as follows: we have started with system overview, followed by the schematic layout of the patient unit and operational algorithm. The next section describes the statistical data of the subjects with results and discussions in which the performance assessments have been made with standard reference spirometric values. As COPD deals with different varieties of chronic obstructive pulmonary diseases, a response study has been carried out to distinguish two specific types of COPD viz. emphysema and bronchical asthma. In order to perform such a bio-medical analysis, we are indebted to doctors and operators of various hospitals as mentioned in acknowledgement section. Finally the pros and cons of our designed system are discussed in conclusion.

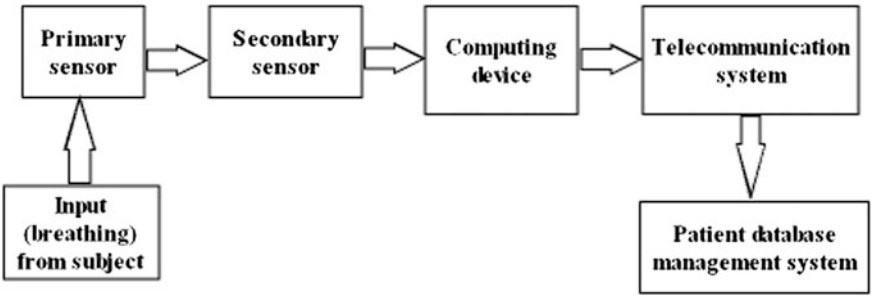

Fig. 1 Block diagram of the proposed device

2 System Overview

The schematic setup of the proposed system is depicted in Fig. 1, which consists of three major sections. The first section is patient unit (PU). Second section is the telecommunication network that bridges the patient's data base management system (third section) with the first section. The third section is powered by advanced tools for the intelligent processing and analysis of the subject's telecommunicated data, which aid the physicians for easy evaluation of the severity and effective recommendations about the treatment.

The patient unit comprises of a primary transducer that transduces the ventilation profile of the subject into analogous linear mechanical displacement, which is further transformed into replicated radio-frequency signal by the cordless optical sensor (secondary transducer).

The computer captures and decodes the information sent by the sensor with the help of an algorithm written in C language. This high level language based program enables the processor to provide numerical and graphical displays of the ventilation status of the subjects.

3 Schematic of Patient Unit

The schematic diagram of the patient unit (PU) is shown in the Fig. 2. In order to have an efficient performance from the PU, we have designed the primary sensor composed of two coaxial cylinders, made-up of plastic. One end of the stationary outer cylinder is open to atmosphere and its tapered end goes to the mouth of the subject. It must be remembered that the nose of the subject is kept clipped off during the experiment. The inner cylinder experiences linear and bidirectional movement according to the inhalation and exhalation patterns of the subject. The optical sensor as secondary transducer senses this movement. It has been reported

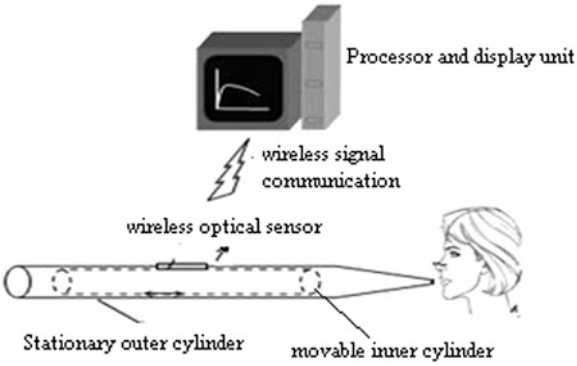

Fig. 2 Schematic set-up of the patient unit

that such cost-effective optical sensors are used extensively for displacement measurement in different applications [20].

The wireless optics based sensor communicates a noise free signal to the computing device. The computer after computation provides a graphical impression suggesting the respiratory disorder like COPD or CRPD, if any. The old and impaired patient is electrically isolated from the computing device thus no fear of electrical shock hazards.

4 Operational Algorithm

The sensing system of the device translates the real time breathing pattern of the subject into computer compatible signal which is captured as well as displayed by the processing device. Then the spirometric values are calculated from this pattern and compared with the safe limits continuously. If the real time spirometric values are beyond the safe limits for a preset time (user defined, here we have set it for 5 min), then the processor will put forward a call to the physician's mobile phone and at the same time the device will transmit the pattern to the web server for quick remedial clinical response to the subject. Fig. 3 depicts the flow chart for the operational algorithm of the projected system.

5 Statistical Data of the Subjects

We studied the respiratory activities 50 male volunteers. As per their age, weight, height and ventilator status, the subjects were divided into two groups (Table 1). Group-I consisted of 25 subjects who were clinically suffering from chronic obstructive pulmonary disease (COPD). Group-II was formed with another 25 patients who were distressed with chronic restrictive pulmonary disease (CRPD).

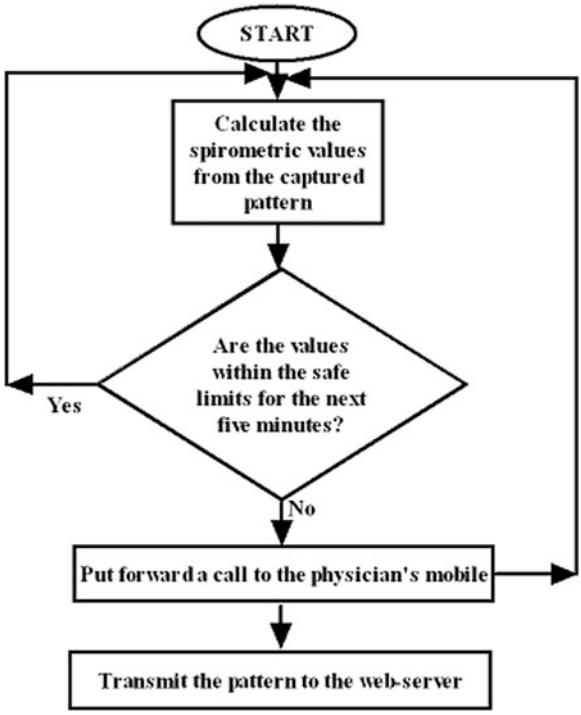

Fig. 3 Flow chart of the operational algorithm of the system-server

Table 1 Statistical data of the subjects

Group	Respiratory status of the subjects	Age group (Years)	Height limits (Cms.)	Weight limits (Kgs.)
I	COPD	60–80, mean ± 3.4	140–185, mean ± 10.8	50–75, mean ± 8.8
II	CRPD	60–85, mean ± 2.8	150–170, mean ± 2.1	50–85, mean ± 5.7

6 Experimental Results with Discussions

6.1 Phase-I

In phase-I, we checked the performance of the patient unit and observed the ventilation disorders of COPD and CRPD abused old and disabled patients both numerically and graphically.

The numerical values which we obtained (Table 2) and the graphical patterns, which we observed in Figs. 4 and 5, were in close agreements with the genuine clinical conditions of the subjects. Fig. 4 depicted the exhaled volume of air–time

Table 2 A summary of experimental results of three important respiratory values and their agreement with the reference values as obtained from the PU and PMU

Groups	Average value of FEV1 (liters)		Average value of FVC (liters)		Average value of (FEV1/FVC) %	PEF (liters/second)	
	Values obtained from PU	Recommended values (range)	Values obtained from PU	Recommended values (range)		Values obtained from PU	Recommended values (range)
Normal	4.3	1.98–5.35	5.4	2.16–6.45	80	6.5	5.28–13.95
COPD	2.5	0.41–2.72	3.1	0.71–4.02	39	1.8	1.02–9.55
CRPD	2.1	0.95–3.01	2.8	1.08–4.13	75	5.0	2.35–10.80

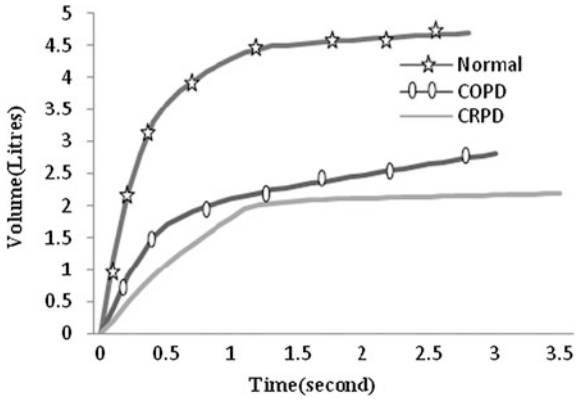

Fig. 4 Volume versus time curves of Normal, COPD and CRPD subjects

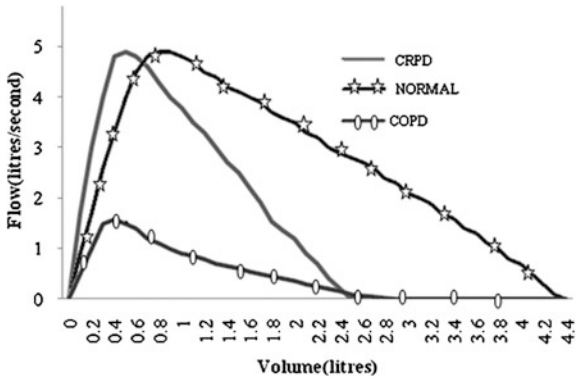

Fig. 5 Exhaled flow-volume curves of normal, COPD and CRPD affected subjects

response of normal, COPD and CRPD patients on a single graph for an easy comparison (using our proposed PU).

The air flow-volume profile was derived from Fig. 4, where airflow in liters/sec. (along vertical-axis) versus volume in liters (along horizontal-axis) was plotted for each of the cases as stated above shown in Fig. 5.

6.2 Phase-II

In phase-II, the patient's data are transmitted through internet to web-server, accessible to the medical center or home-care provider. In emergency situations (as per the algorithm developed by us) the clinician has the ability to connect, through internet in order to receive the most up-to-day data about the patient.

6.3 Phase-III

We checked the working ability of the algorithm designed for system. When the patient's breathing parameters were normal, the PU did not send any alarm notice to the mobile of the physician. When the exhalation values crossed the safe limits, the PU sent warning call to the physician and patients' data to the web-server at the same time after confirming the abnormalities for five minutes in our case or any preset value.

After discussing these three phases, finally we have given a summary of the experimental results of important spirometric values with the reference values in a tabular form as shown in Table 2. The PU evaluates the numerical values of FEV1, FVC and PEF from the spirograms and its derivatives. In Table 2, both the real time spirometric values and the recommended tolerable ranges of the same are put side by side by the PU for meaningful comparison which is very important for the PU to send a false free notification to the physician.

Then the doctor could access the web-server using his laptop or personal computer to assess the patient's respiratory status and put effective recommendations about the treatment. Data collected from phase-I and phase-II were compared and found that they were exact replica of each other and were very close to the clinical ventilation status of the patient.

7 Performance Evaluation of the Sensing System

The measure of accuracy of our proposed sensory system is essential because it is using as a condition monitoring unit for old as well as impaired subjects. In order to ensure the results obtained by our projected device, we have adopted a standard calculator for necessary comparison as discussed in Sect. 7.1.

In Sect. 7.2, we tried to authenticate our investigations through another parameter called as time constant of the breathing mechanics, which is indicative of the status of the respiratory system.

7.1 Using Predicted Values Calculator

We have further verified our experimental data with that from the Pulmonary Function - Reference Normal Predicted Values Calculator [21–23]. Figs. 6 and 7 depict the graphical comparison of these two for the normal FEV1 and FVC values of 10 subjects having similar statistical data. In these graphs, we have demonstrated the performance of our proposed device relative to Pulmonary Function - Reference Normal Predicted Values Calculator.

We have observed a close agreement between these two (Pulmonary Function - Reference Normal Predicted Values and our proposed spirometer as supported by

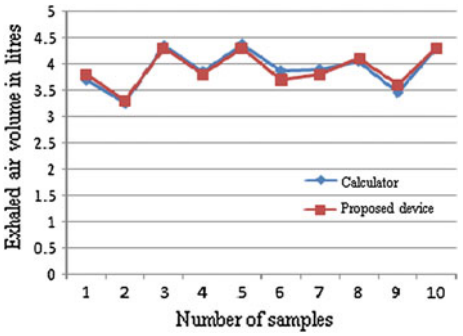

Fig. 6 A comparative graphical display of FEV1 values between the normal reference calculator and proposed spirometer

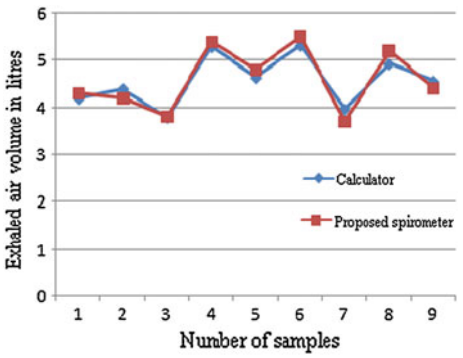

Fig. 7 A comparative graphical display of FVC values between the normal reference calculator and proposed spirometer

Table 3 Results of statistical data analysis

Parameters	Correlation Coefficients
FEV1	+0.96
FVC	+0.97

the Table 3). The effectiveness of the optical sensory scheme along with the computational device has been verified with experimental studies on fifty different human respiratory systems. Though the experimental results are suggestive for qualitative diagnosis, still there is a scope to enhance the performance of the gadget by optimizing the design of the primary sensor. Moreover, the simplicity of the system (we have described in this paper), allows even unskilled technicians/ operators to capture the breathing information in remote parts of our country. The promising attribute of the device is that its cost is much less (US$150) compared to the prices of other such instruments available in the market (US$1500-$2500). The added advantages of our optical sensing scheme are to provide almost maintenance free device with complete electrical isolation between the patient and system which minimizes the electrical shock hazards.

Hence the outcome of our study helps the medical practitioners to make better quantitative assessments of their patients' pulmonary health.

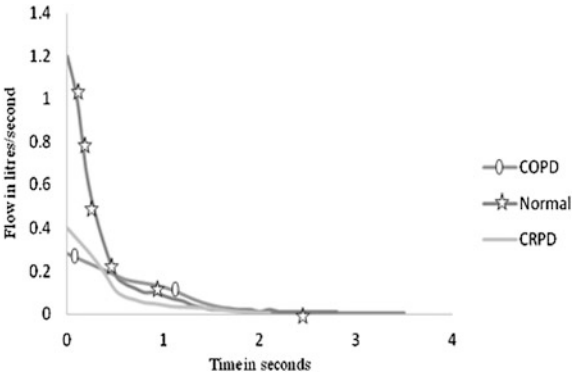

Fig. 8 Speed of responses, constructed from mean data of ten normal, ten COPD and ten CRPD abused subjects

7.2 Using Speed of Response Approach

We have then extended our studies to validate the experimental data using another parameter called as the time constant of the respiratory system, which is indicative of its speed of response. Time constant (τ) is a parameter that decides how rapidly one can inspire and expire. It is the product of lung compliance (C_L) and airway resistance (R_{AW}) and has the dimension of time.

Mathematically, the time constant can be expressed as $\tau = R_{AW}.C_L$ [24].

A larger time-constant implies that the lung takes more time to exchange gas air between alveoli and atmosphere. For a given driving pressure, if air way resistance is high, the lung will take more time to move air into and out of the lung causing a reduction n air flow. Reduced elastic coil i.e. higher compliance, on the other hand, will be the basis higher time constant to the expiratory circuit.

A variation of rate of respiratory flow with time is shown in Fig. 8 for COPD, Normal and CRPD patients by considering the mean data of thirty subjects (ten in each case). In Fig. 8, the speed of response for Normal patients comes down sharply from a maximum value of 1.2 liters/second, while in other two cases the maximum flow rate lies between 0.3 and 0.4 liters/second. The response of COPD abused subjects is slower in comparison to that of CRPD implying that time constants of the respiratory circuit of the obstructive nature is more.

8 Analysis of Specific Chronic Obstructive Pulmonary Diseases

We then moved towards more specific obstructive respiratory diseases to check the performance of our proposed device. In this study, two different abnormal ventilation responses have been observed, one is bronchial asthma and other one is

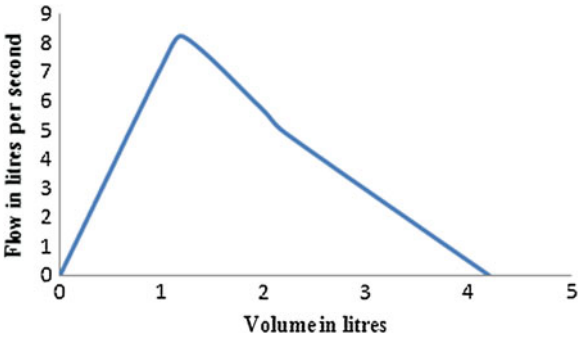

Fig. 9 Exhaled air flow-volume curve of normal subjects

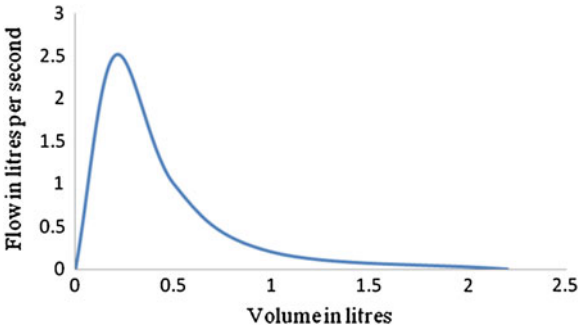

Fig. 10 Exhaled air flow-volume curve in emphysema

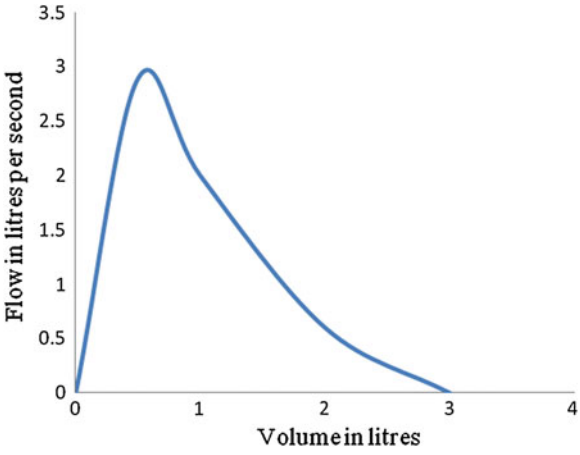

Fig. 11 Exhaled air flow-volume curve in bronchial asthma

emphysema. These responses can be identified from the spirograms and its derivatives.

In this investigation, we are studying the flow-volume profile which is the derivative of the spirogram. Here, air flow in liters/sec. (along vertical-axis) versus volume in litters (along horizontal-axis) is plotted for each of the cases as stated above shown in Figs. 9, 10 and 11.

8.1 Case 1: Spirograms Showing Normal Respiratory Behaviors

We have obtained the spirograms of ten healthy male volunteers (Table 1: for statistical data). The computing device generates the exhaled flow-volume response of a normal subject, using our proposed device in the Fig. 9. We have observed that the curve rapidly mounts to a peak point giving peak expiratory flow (PEF) initiating from origin (0, 0). We have found that the curve then descends almost through a straight line to a value where flow is zero and air volume is Forced Vital Capacity (FVC). We have found that the observations are in satisfactory agreement with the clinical conditions of the subject.

8.2 Case 2: Spirograms Showing Response for Emphysema

We have studied ten male subjects of same age and height groups as normal, who were clinically suffering from obstructive diseases. Emphysema occurs either because of increased narrowing of airways or because of the reduced driving pressure in the emphysematous lung (because of the destruction of lung tissue).Both of these arise due to the reduced elastic recoil of the lung tissue [25–29]. Exhaled air flow -volume characteristics (Fig. 10), as generated by our device, say that the expiratory flow is reduced at all lung volumes. Peak expiratory flow (PEF) is smaller here relative to its normal value and from the PEF the curve has started to descend following a concave pattern. Higher the concavity, severe is the disease.

8.3 Case 3: Spirograms Showing Bronchical Asthma Reaction

Bronchial asthma is a chronic inflammatory disease of the airways of the lungs to swell and narrow causing episodic attack of shortness of breath, coughing, wheezing, and chest tightness. We have studied ten male subjects of same age and height groups as normal, who were clinically suffering from bronchial asthma. In patients with obstructive lung disease, the small airways are partially obstructed by a pathological condition. Fig. 10 represents the flow-volume response of a patient as we have examined by our proposed instrument. Flow limitation in small airways reduces flow rates at low lung volumes more than at high and mid-lung volumes. We have obtained the shape of the exhaled flow-volume response (Fig. 11) outline similar to the normal record (Fig. 9) but in reduced size. Over all shape is small and oval in outline. From the peak expiratory flow level to the volume-axis the curve descends exponentially with higher time constant relative to that of the emphysema.

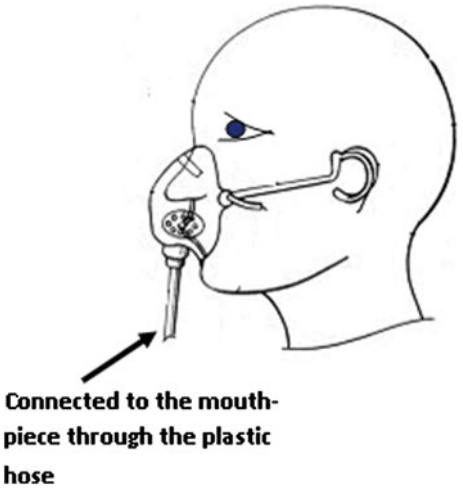

Fig. 12 Arrangement to avoid error due to motion artifact

9 Conclusions

In our present work, the proposed patient monitoring unit (PMU) consists of a data management system and maintains a track of the communicated data of the elderly and disabled patients. The analysis process is done by the distantly located physician.

If the physician is asleep or ignores the alarm signal in emergency cases then the patient will not receive the medical advice in time. In order to avoid such situations, we are now trying to develop an automated decision support mechanism that will send the emergency advises to the patient in no time.

We have observed during our experimental studies that false alarm may be generated due to motion artifact of the elderly impaired subjects. We have overcome this problem by incorporating a mask like mouth-piece connected to the stationary outer cylinder through plastic tube as shown in Fig. 12.

As a concluding remark, we are willing to mention that COPD represents major global causes of death and is estimated to become the third most common reason of death by 2020 [30]. It leads to severe physical disability (breathlessness) causing hospitalization and prolonged medication [31, 32]. In this particular work we have tried to differentiate two severe chronic obstructive pulmonary diseases like emphysema and bronchial asthma. We are now engaged to use the said device to characterize other life threatening respiratory diseases like pulmonary fibrosis, lung cancer etc.

Acknowledgments The authors are willing to acknowledge the doctors of Vision Care Hospital, AMRI Hospital and Mediclue Research and Diagnostic Private Limited, Kolkata for data collection and necessary interpretation.

References

1. J. Wells, *Protecting and Assisting Older People in Emergencies, Humanitarian Practice Network* (Overseas Development Institute, London, 2005)
2. T. Kosastsky, The 2003 heat waves. Euro. Surveill. **10**(7), 148–149 (2003)
3. World Health Organization, World health report 1998, (1998)
4. U. Karsch, Changes in family structure and new roles in family support. In Ageing and health: a global challenge for the 21 century, Proc. WHO symp. 10–13 Nov (1998), (Kobe, Japan)
5. World Health Organization, *Draft Fact Sheet: Older Persons in Emergencies* (World Health Organization, Geneva, 2006).http://www.who.int/hac/crises/international/middle_east/Lebanon_older_persons_7Aug2006.pdf
6. M. Laghrouche, L. Montes, J. Boussey, S. Ameur, Low-cost embedded spirometer based on micro machined polycrystalline thin film. Flow Meas. Instrum. **22**(2), 126–130 (2011)
7. D. Gourlay, K.C Lun, G. Liya, Virtual reality and telemedicine for home health care. Comput. Graph. **24**(5), 695–699 (2000)
8. T.C. Jannett, S. Prashanth, S. Mishra, V. Ved, A. Mangalvedhekar, J. Deshpande, An intelligent telemedicine system for remote spirometric monitoring, system theory. In Proc. Thirty-Fourth Southeast. Symp. 53–56, (2002)
9. Tam Vu Ngoc, Medical Applications of Wireless Networks. http://www.cse.wustl.edu/~jain/cse574-08/ftp/medical/index.html
10. H. Tawa, Y. Yonezawa, H. Maki, H. Ogawa, I. Ninomiya, K. Sada, S. Hamada, W.M. Caldwell, A wireless breathing-training support system for kinesitherapy, engineering in medicine and biology society, EMBC 2009. In Annu. Int. Conf. IEEE 5179–5182 (2009)
11. M. Skorning, S. Bergrath, D. Rörtgen, S.K. Beckers, J. C. Brokmann, B. Gillmann, J. Herding, M. Protogerakis, C. Fitzner, R. Rossaint, Teleconsultation in pre-hospital emergency medical services: real-time telemedical support in a prospective controlled simulation study. Resuscitation (**83**)5, 626–632 (2012)
12. A.T. Augousti, F.-X. Maletras, J. Mason, Improved fibre optic respiratory monitoring using a figure of eight fiber optic coil. Physiol. Meas. **11**(4), 346–360A (2005)
13. A. Lay-Ekuakille, A.V. Scarano, A. Trotta, Instrumentation and measurement technology conference, proc. IEEE **1**, 381–383 (2005)
14. L. Mohanty, K.S.C. Kuang, A breathing rate sensor with plastic optical fiber. Appl. Phys. Lett. **97**, 073703 (2010). http://dx.doi.org/10.1063/1.3480601
15. W.J. Yoo, K.W. Jang, J.K. Seo, J.Y. Heo, J.S. Moon, J.H. Jun, J.-Y. Park, B. Lee, Development of optical fiber-based respiration sensor for noninvasive respiratory monitoring. Opt. Rev. (**18**)1, 132–138 (2011)
16. J. Popp, W. Drexler, V.V. Tuchin, D.L. Matthews, A non-contact optical procedure for precise measurement of respiration rate and flow. Proc. SPIE 7715, 77150G (2010). http://dx.doi.org/10.1117/12.854482
17. E.J. Gómez, M.E. Hernando, A. García, F. Del Pozo, J. Cermeño, R. Corcoy, E. Brugués, A. De Leiva, Telemedicine as a tool for intensive management of diabetes: the DIABTel experience. Comput. Methods Programs Biomed. **69**, 163–177 (2002)
18. R. Bellazzi, S. Montani, A. Riva, M. Stefanelli, Web-based telemedicine systems for home-care: technical issues and experiences. Comput. Methods Programs Biomed. **64**, 175–187 (2001)
19. R. Belazzi, C. Larizza, S. Montani, A. Riva, M. Stefanelli, G. d'Annunzio, R. Lorini, E.J. Gomez, E. Hernando, E. Brugues, J. Cermeno, R. Corcoy, A. de Leiva, C. Cobelli, G. Nucci, S. Del Prato, A. Maran, E. Kilkki, J. Tuominen, A telemedicine support for diabetes management: the T-IDDM project, Computers Methods and Programs in. Biomedicine **69**, 147–161 (2002)
20. T.W. Ng, The optical mouse as a two dimensional displacement sensor. Sens. Actuators, A **107**, 21–25 (2003)

21. D.W. Dockery et al., Distribution of forced vital capacity and forced expiratory, volume in one second in children 6 to 11 years of age. Am. Rev. Respir. Dis. **128**, 405–412 (1983)
22. H. Hedenström, P. Malmberg, K. Agarwal, Reference values for lung function tests in females. Bull. Eur. Physiopathol. Respir. **21**, 551–557 (1985)
23. H. Hedenström, P. Malmberg, H.V. Fridriksson, Reference values for lung function tests in Men: regression equations with smoking variables. Upsala J. Med. Sci. **91**, 299–310 (1986)
24. Harry Bass, The Flow Volume Loop: Normal Standards and Abnormalities in Chronic Obstructive Pulmonary Disease, CHEST, **63**(2),171–176 (1973)
25. D.L. Fry, The physics of air flow in emphysema. Am. Rev. Resp. Dis. **80**, 123–127 (1958)
26. E.A. Gaensler, I. Lindgrcn, Chronic bronchitis as an etiologic factor in obstructive emphysema. Am. Rev. Res. Dis. **80**, 185 (1959)
27. J. Gough, Discussion of the diagnosis of emphysema: the pathological diagnosis of emphysema. Proc. Royal Soc. MWd. **43**, 576 (1932)
28. R.V Christie, Elastic properties of emphysematous lungs and their clinical significance, J. Clin. Invest. **13**, 295 (1934)
29. J.E. Cohn, D.G. Carroll, R.L. Riley, Respiratory acidosis in patients with emphysema. Am. J. Med. **17**, 447 (1954)
30. S. Christopher, M. Stevenson, M.A. Birrell, Moving towards a new generation of animal models for asthma and COPD with improved clinical relevance. Pharmacol. Ther. **130**(2), 93–105 (2011)
31. P.J. Barnes, Chronic obstructive pulmonary disease. NEJM Med. Prog. **343**, 269–280 (2000)
32. T. Welte, D.A. Groneberg, Asthma and COPD experimental and toxicologic pathology, Nervenarzt **57**(2), 35–40 (2006)

Chapter 3
Real-Time Position Sensing for Biofeedback-Based Gait Training

R. van der Straaten and R. Begg

Abstract Fundamental to adaptive gait control is the fine motor task of maintaining adequate foot or toe clearance during the swing phase of the gait cycle to safely clear surface irregularities. Through the development of motion analysis systems it is possible to track the position and orientation of the toe position with respect to the walking surface and calculate toe clearance. The purpose of this chapter is to describe how a sensor-based motion analysis system measures minimum toe clearance (MTC) and how real-time biofeedback can help to achieving a safer walking pattern with sufficient clearance. The vertical displacement of the toe was projected on to a screen in front of the participants, so they could adjust their toe clearance if needed to a target MTC line. The technique has been applied to a group of participants (young and older adults) for their gait training and assessment. All participants performed 40 min treadmill walking protocol, which included 10 min normal walking, 20 min walking with visual biofeedback when the participants were required to maintain their MTC height within the target range, and finally 10 min walking without the biofeedback (i.e., retention condition). Results are presented using examples taken from both young and older adults. Overall the findings indicate that both young and older adults are able to significantly increase their toe clearance with feedback. Further subject-specific analysis of the results showed that older adults mainly exploited the knee and hip joints to increase MTC, while young adults predominantly used their ankle joint motion to achieve higher MTC height. The findings confirm that real-time biofeedback of lower limb kinematics is effective to change gait patterns, and has a great potential in rehabilitation, biomedical and healthcare applications.

Keywords Biofeedback · Gait analysis · Minimum toe clearance · Tripping · Position sensors · Ageing healthcare

R. van der Straaten · R. Begg (✉)
Biomechanics Unit, College of Sport and Exercise Science (CSES) and Institute of Sport Exercise and Active Living (ISEAL), Victoria University, Melbourne, Australia
e-mail: rezaul.begg@vu.edu.au

A. Mason et al. (eds.), *Sensing Technology: Current Status and Future Trends I*, Smart Sensors, Measurement and Instrumentation 7, DOI: 10.1007/978-3-319-02318-2_3,

1 Introduction

Numerous studies in medical and applied health science domains use gait analysis to assess human locomotion. Common goals are evaluation of locomotor function, detection of gait abnormalities, pathologies and ageing effects in order to plan, treat and improve walking ability. It is also used in sports applications to identify posture or movement related problems, improve efficiency and decrease running injuries.

Gait analysis systematically studies human motion for measurement and interpretation of biomechanical features of body movement, such as walking and running and is often augmented by instrumental equipment [1]. Motion analysis systems offer the possibility to calculate the location and orientation of a sensor in space. By placing the sensor on the body of a human, it is possible to follow the sensor in three dimensions and obtain precise movement of the joint or segment with which the sensor is attached to.

To achieve a successful swing with sufficient floor clearance, the effective length of the swing limb needs to be reduced to allow the limb to swing in front of the body without contacting the ground. In normal walking, limb shortening and floor clearance are the result of progressive and coordinated movement between the pelvis and the hip, knee, and ankle joints of both the swing and stance limbs [2]. Due to environmental obstacles, such as stairs, kerbs or surface irregularities like for example broken pavement, continuous adaptation of the joint kinematics is required to safely complete the task [3]. Unintentional foot–ground contact increases the risk of tripping and when an individual cannot recover from this destabilization, a fall will occur. Consequences of a fall are diverse and lead to estimated 20–30 % of mild or severe injuries. The major underlying causes for falls-related hospitalizations are hip fractures, traumatic brain injuries and upper limb injuries [4]. Trip related falls account for about 53 % of all falls in healthy elderly population (65 years and older) and is identified as one of the leading causes of a fall [5]. It is, therefore, important to understand the predictors of a fall and develop techniques to decrease the incidence of tripping related fall.

Minimum toe clearance (MTC) occurs during the mid-swing phase of the gait cycle and is defined as “the minimum vertical distance between the lowest point of the foot and walking surface” [6]. MTC and is directly associated with the mechanism of a trip, because a trip occurs when MTC is reduced to zero [7]. Therefore, MTC has been identified as an important gait parameter in successful negotiation of the environment. The literature is, however, not always consistent between minimum foot clearance (MFC) and minimum toe clearance (MTC). There is some disagreement that the toe may not necessarily be the lowest point during the swing. Some studies, therefore, prefer to use MFC. Other studies assume that the toe represent the lowest point in the mid-swing phase of the gait cycle and use MTC. In this chapter, we assume the toe represents the lowest point in the swing phase and therefore MTC will be used.

Various studies [3, 8, 9] report lower MTC values for older adults compared to younger, although, none of these studies reported a significant difference in MTC height between the two groups. Instead MTC variability was reported to be significantly greater for older adults. By shifting the MTC height to safer bounds and reducing MTC variability, tripping risk can be reduced [8]. Moreover, real-time visual biofeedback of lower limb kinematic gait parameters has been shown to be an effective application to both increase MTC and decrease MTC variability [10]. Other effects of ageing on the gait cycle measures are well understood. For example, older individuals have a significantly reduced walking velocity, compared to younger people [8, 11, 12]. Step length was decreased for older individuals, however, no significant age related differences were reported [11]. Single and double support times increased significantly for the elderly [8, 11] and age effects on joint angles indicate a reduced range of motion of the ankle and knee joint at heel contact [11].

With biofeedback of external information, mostly visual or auditory of internal biological processes and functions that would not otherwise be sensed [13], can enhance an individual's ability to change physiological activity or behaviour [14]. The intention of this chapter is to focus on the measurement of minimum toe clearance by using sensor based motion analysis system and the associated analysis and interpretation of the data for various applications. Finally, we will demonstrate how visual biofeedback of MTC data can help to improve movement function for applications such as fall prevention in older individuals or gait rehabilitation in stroke patients who need to relearn locomotion function.

2 Sensor-Based Motion Analysis and Biofeedback Aided Walking

Human locomotion is a periodic repetitive cyclic movement of the left and right limbs, half a cycle out of phase. To understand this periodic walking sequence better, the full gait cycle needs to be described. Typically in human gait there are two major phases: stance phase and swing phase as illustrated in Fig. 1. Stance phase is defined as the duration during which the foot is in contact with the ground whereas during the swing phase the foot is off the ground. In the stance phase the hip, knee and ankle joints generate an extensor moment to prevent the stance limb collapsing. In the swing phase during which the body moves forward, the foot of the swing limb moves from one stance (Toe Off) to the next stance (Heel Contact). This motor task is accomplished through a precise coordination of the kinematic chain consisting of the pelvis, thigh, shank and foot of both the swing and stance limbs. One gait cycle, also known as a stride, is usually described as the duration from the heel contact to the next heel contact of the same limb e.g., right limb [6, 15, 16].

The swing phase is most important while relating to the tripping and related phenomenon in understanding a trip event. Tripping mainly occurs when the foot

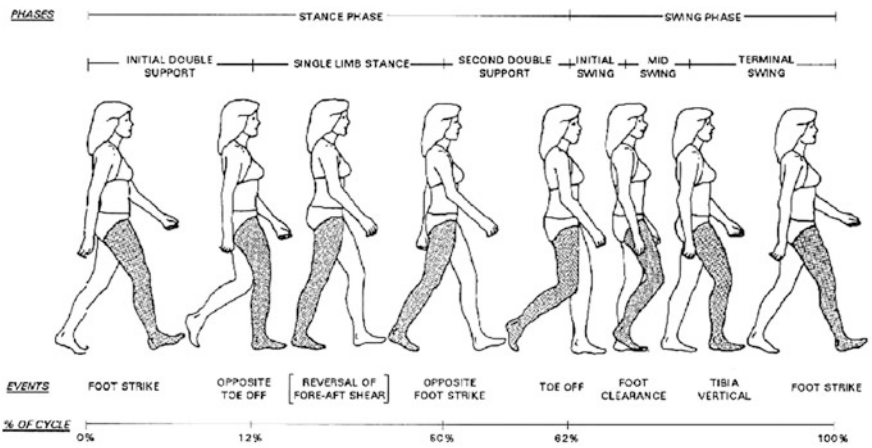

Fig. 1 One complete gait cycle illustrating specific gait events and major stance and swing phases [15]

is off the ground and unintentional contact the ground due to an over ground obstacle. A critical event in the swing phase is MTC, which occurs approximately halfway through the swing phase as illustrated in Fig. 2. During this event, the foot travels with maximum horizontal velocity (about 3 times the body's velocity) and the foot is only within a few centimeters above the ground. Figure 2 describes the full foot trajectory during the swing phase and as can be seen there are two other events, first maximum (Mx1) and second maximum (Mx2) where the toe reaches maximum clearances before and after the MTC, respectively. Mx1 is a local maximum, between toe off and MTC, which arises when the toe is lifted from the ground to make the swing. Mx2 is a local maximum, between MTC and heel strike, which arises at the end of the swing just before the heel is preparing to touch the ground as heel contact [17]. Through 3D motion analysis kinematic parameters describing position-time data at the various human gait events can be recorded that are necessary in order to define MTC in the swing phase.

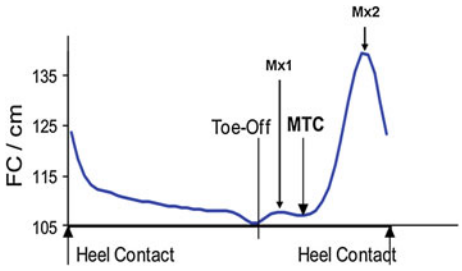

Fig. 2 Vertical displacement/time characteristics of the toe (FC) with key events including local maximum 1 and 2 (Mx1 and Mx2), and Minimum Toe Clearance (MTC) approximately half way through the swing phase

2.1 Sensing Foot Trajectory for Biofeedback Gait Training

For accurate measurement of three-dimensional (3D) motion of the human body, or more specific human walking, optical-sensor measurement systems can be used to determine the location of the sensor in space. With an Optotrak Certus® opto-elctric movement analysis system (Northern Digital Inc., Canada) it is possible to track an active Infra-Red Emitting Diode (IRED). By mounting this IRED on the human body it is possible to track movement in three dimensions (X, Y, Z) using three fixed cameras located on a tower (Fig. 3, right). In this particular configuration, the X-axis represents movement in the anterior-posterior direction, the Y-axis indicates medio-lateral displacement and Z-axis provides vertical displacement of the IRED marker. Two camera units positioned on both side of the treadmill (Fig. 3, left), allow simultaneous time-synchronised sampling of two feet movement. The system is highly accurate and reliable, with an accuracy of 0.1 mm and resolution of 0.01 mm at a distance of 2.5 m. The system has a maximum marker frequency of 4,600 Hz (when one marker is used) with a capture volume extending to 4.2 m width $\times$ 3 m height using cameras located up to approximately 7 m from the participant. The system is compatible with other motion capture software, such as Visual3D (C-Motion Inc.) that offers the opportunity for real-time streaming of visual feedback from the IRED marker position. Real-time biofeedback was, therefore, provided via Visual3D (C-Motion Inc.), by tracking the (vertical) displacement of the toe marker and projected in front of the individual on a screen as the subjects walked on a treadmill (See Fig. 4).

Begg and colleagues [10] used a set up similar to the one illustrated in Fig. 3 (left) to record foot clearance in real-time, and to provide biofeedback of the toe position to the participants. Two walking conditions were completed: baseline and

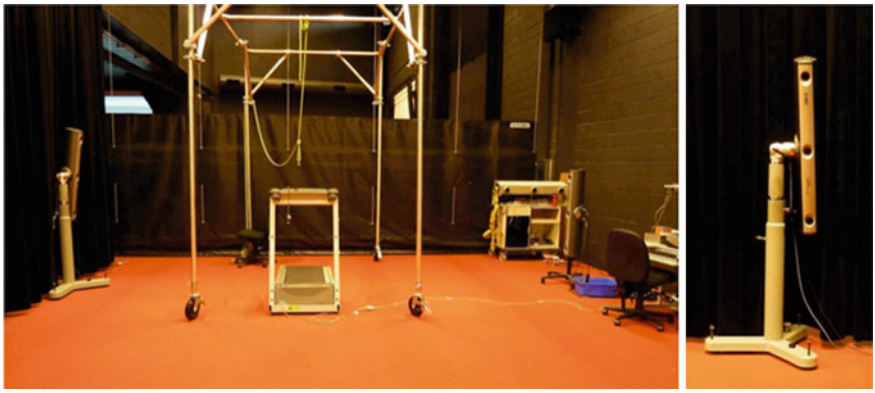

Fig. 3 Experimental set up showing the alignment of the Optotrak system on both sides of the treadmill, including a harness construction that would prevent the participants from falling. One of the Northern Digital's Optotrak camera towers, with three infrared cameras (black dots), to measure the location and orientation of the IRED markers in space

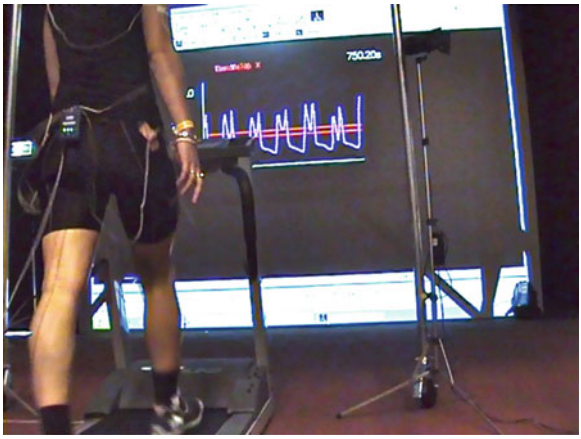

Fig. 4 Example of how the participants walked with the biofeedback. The toe trajectory (vertical displacement) of the right toe is projected in front of the participant, together with the upper and lower boundaries (horizontal lines)

biofeedback. In a continuation of this research a third condition, retention, was added to see how people retain movement patterns learnt during the feedback phase if they were asked to walk as they did during the biofeedback condition, but without the feedback of foot clearance provided. The participants were instrumented with IRED markers, attached to the left and right foot at the 5th metatarsal head (toe), calcaneus (heel), lateral malleolus (ankle), lateral epicondyle of the femur (knee), greater trochanter (hip) and acromion (shoulder). With these additional IRED sensors it was possible to calculate swing limb joint kinematics and Toe Clearance Sensitivity (TCS) described later. The TCS was determined to indicate which of the lower limb joints is more sensitive in altering the MTC height.

The protocol used here was a continuation of Begg et al. [10] and baseline walking data were undertaken first for first 10 min, and from these data MTC mean and standard deviation (SD) were calculated for each participant's preferred dominant foot (as confirmed by the participant). Using the baseline MTC data upper (1.5 × baseline MTC mean) and lower (lower bound+3 × baseline MTC SD) bounds for the virtual biofeedback target bands were calculated. Based on pilot work and previous research [8, 18] the target range of 3 SD was found suitable for making the task sufficient challenging.

Following 5 min rest, participants were asked to walk (*biofeedback condition*) for 20 min, while maintaining their MTC within the virtual horizontal band (lower and upper boundary) projected onto the toe clearance toe trajectory (Fig. 4). Following the biofeedback walking trial, another 5 min rest was given before the participants performed a further 10 min of walking (*retention condition*) where they were instructed to continue walking with the new 'higher MTC' walking pattern as in the biofeedback condition but now no biofeedback was presented.

2.2 Minimum Toe Clearance (MTC) Data Analysis

Gait events were calculated using the standard Visual3D software (C-Motion Inc.) and also Visual3D scripts developed in-house. With the toe and heel kinematics gait events of right toe-off (RTO) and right heel-strike (RHS) were identified by applying the gait event described earlier [19]. The swing phase, between Right Toe Off (RTO) and Right Heel Strike (RHS) was time normalised to 100 % of swing. The events MTC, Mx1 and Mx2 were identified having MTC as the local minimum between RTO and RHS, Mx1 as the local maximum between RTO and MTC, which arises as the participants lift their foot after RTO to make the swing and Mx2 as the local maximum between MTC and RHS, which arises when the foot travels from MTC (mid-swing) to the end of the swing, just before RHS [17] (Fig. 2). Left and right hip, knee, and ankle angles in the sagittal plane were computed using the x–z position of the markers and time normalised to 100 % of the swing phase.

2.3 Toe Clearance Sensitivity (TCS) Analysis

Toe Clearance Sensitivity (TCS) was determined based on the mathematical model developed by Moosabhoy and Gard [2]. They used a two-dimensional model of the swing leg, in which hip flexion, knee flexion and ankle dorsiflexion are defined as positive joint rotation (Fig. 5). In this coordinate system, the origin is established in the plane of the walking surface. Toe clearance is purely defined by the vertical coordinate of the toe marker (y_T).

By calculating the coordinates over the entire swing phase, the sensitivity indicates the relative ability of the joints to affect toe clearance. A positive TCS indicates that the toe clearance increases for a positive rotation of a particular joint. The magnitude indicates how sensitive toe clearance is to minute joint changes, whereas the sign (i.e. positive or negative) of the sensitivity value indicates whether the rotation increases or decreases toe clearance [2]. The TCS was calculated for hip, knee and ankle joints for the three walking conditions (i.e. baseline, biofeedback and retention) in order to determine how visual-biofeedback affected the relative influence of each joint on toe clearance at any time during the swing phase.

2.4 MTC Data for the Baseline, Feedback and Retention Conditions

Previous research [8] showed that MTC is not normally distributed, i.e., skewness and kurtosis deviate from zero. Therefore, a non-parametric test, Mann–Whitney U test, was performed to identify any differences between the two independent groups. In order to identify any differences within a group (i.e., related conditions)

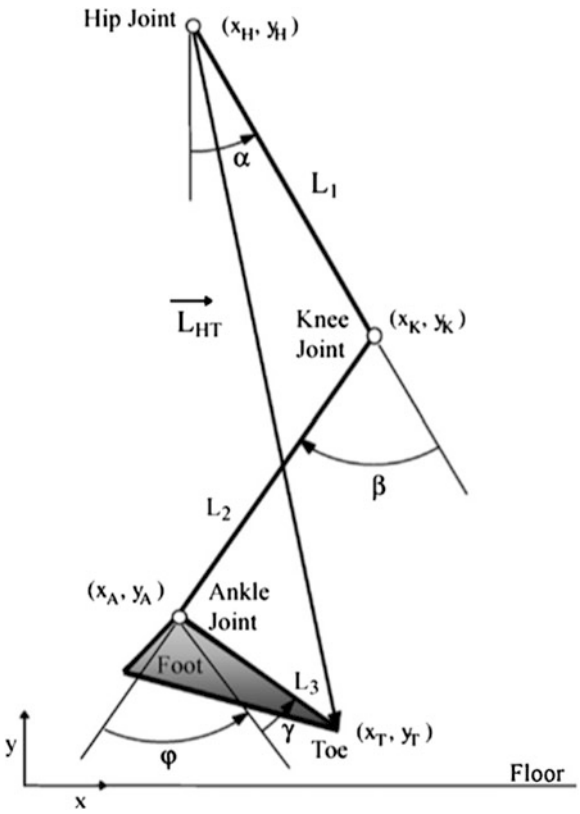

Fig. 5 Definition of the leg model by Moosabhoy and Gard [2]. Defining angle conventions, segment lengths and coordinate systems used for the sensitivity analysis. Hip flexion (α), knee flexion (β), Ankle dorsiflexion (γ), Thigh segment length (L_1), Shank segment length (L_2) and Ankle-toe distance (L_3)

a Wilcoxon signed-rank test was performed. To identify the effectiveness of biofeedback the success rate was determined. The success rate is the percentage of occasions when the participants lifted their toe within the projected targeted range. This percentage was also computed for the number of times below or above the projected range.

The included participants generated approximately 500 gait cycles; however, the actual number of MTC data points depended on the subjects' preferred walking speed. The success rate that provides an estimation about the effectiveness of the three walking conditions, in maintaining the toe's ground clearance within the targeted range in older participants was greater than young adults for biofeedback and retention walking trials.

In baseline and biofeedback walking, older adults showed higher MTC (17.5 ± 6.8 and 33.4 ± 9.9 mm, respectively), compared to the young adults (12.5 ± 3.8 and 27.9 ± 8.1 mm, respectively). These differences were not statistically

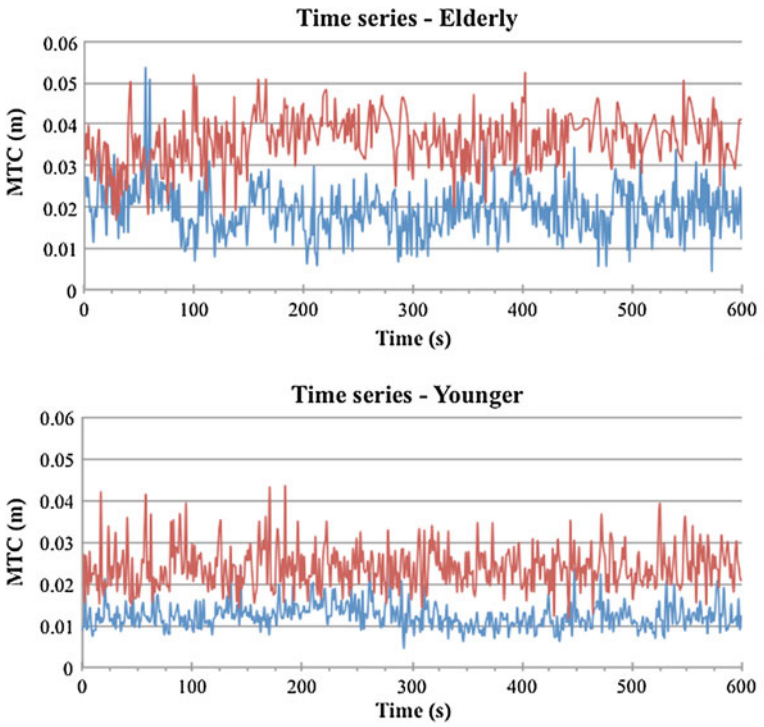

Fig. 6 Individual MTC time-series for a young and an older adult in baseline walking (*blue*) and biofeedback aided walking (*red*) show an increase of mean MTC and MTC variability [10]. The first 10 min data of the 20-minute biofeedback trail are presented

significant, however, an increase of the mean MTC and MTC variability is clearly visible in the time series data (Fig. 6). In retention MTC was significantly ($p < 0.05$) greater for young adults (40.6 ± 11.9 mm) compared to the older adults (32.5 ± 13.7 mm). Both groups increased their MTC significantly ($p < 0.01$) in biofeedback and retention, compared to normal comfortable walking. In addition, young adults showed significant increase in MTC in retention compared to biofeedback walking ($p < 0.01$).

3 Biofeedback and Toe Clearance Strategies

To determine the toe clearance strategy and which of the lower limb joints is most sensitive to an increase of MTC, lower limb kinematics and TCS data were compared for the three walking conditions. Young and elderly adults show similar patterns of increased ankle dorsiflexion, increased knee flexion, and increased hip flexion during biofeedback and retention walking (see sample plots in Fig. 7).

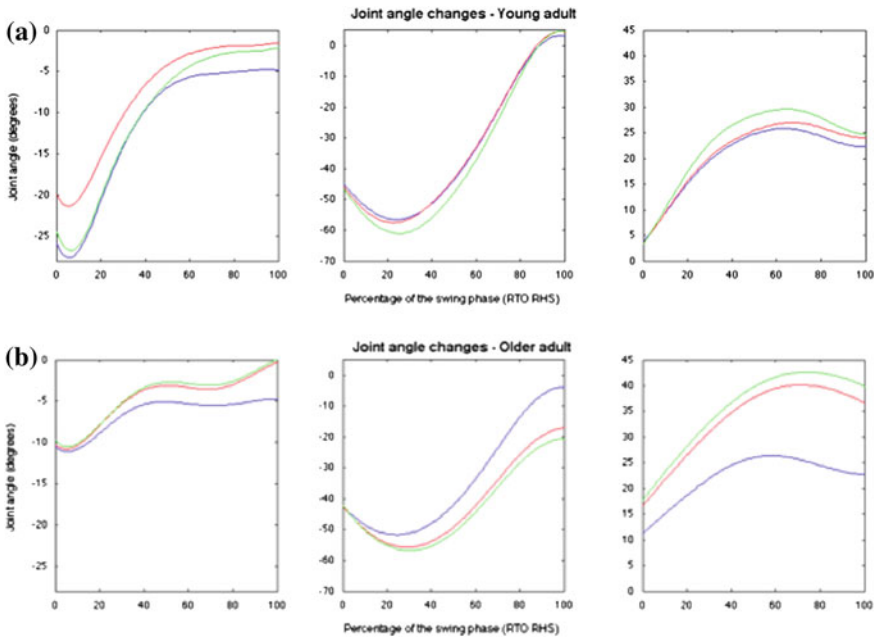

Fig. 7 Minute joint changes of the lower limb during the swing phase for a young adult (**a**) and an older adult (**b**). The left panels represent ankle dorsi/plantarflexion, the middle panels show knee flexion extension and the right ones show hip flexion/extension during baseline (*blue*), biofeedback (*green*) and retention (*red*) walking

However, in biofeedback and retention walking this older subject displayed more plantar flexion when the foot travels from mid-swing to heel strike, similar results were found for the knee joint. Instead to increase MTC the older adults seem to lift their hip (i.e. more hip flexion).

The TCS results, which provide information about the toe clearance sensitivity, indicate that for both young and older adult, at MTC the leg is orientated in such a position that the toe clearance is most sensitive to a (rotational) change in the hip joint, followed by the ankle and knee joints (Fig. 8). The magnitude of the TCS is slightly higher at toe off and heel strike for the younger adult, this indicates the rotational change has a greater positive effect on MTC. The negative sensitivity of the hip corresponds with a negative effect on the toe clearance. Throughout the swing phase this effect changes and at heel strike the hip becomes most sensitive to increase MTC instead of the knee. The ankle supplies a positive effect through the entire swing.

By translating these results to normal human gait the TCS results might make more sense. At toe off knee flexion has the greatest effect on lifting the toe and together with the hip (i.e., hip flexion) the swing leg will be positioned in front of the body. From MTC up to heel strike the leg is preparing for the landing. Therefore the knee extensors will lengthen the leg (negative effect on toe clearance). From MTC any change of hip flexion will lift the toe and provides therefore a positive effect on

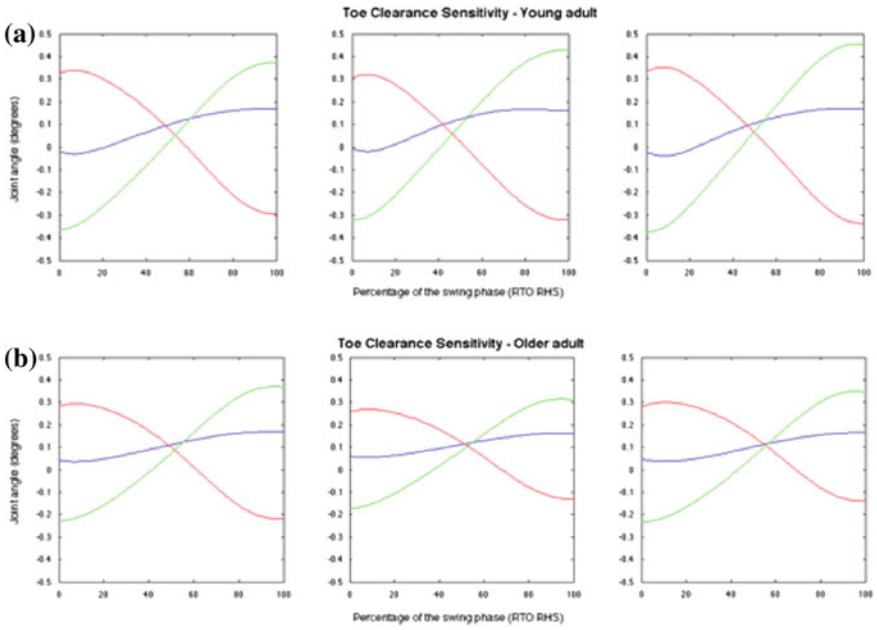

Fig. 8 Toe clearance sensitivity for a young adult (**a**) and an older adult (**b**) for baseline walking (*left*), biofeedback walking (*middle*) and retention walking (*right*). Ankle sensitivity is represented by the *blue line*, knee sensitivity by the *red line* and hip sensitivity by the *green line*

the toe clearance. Any change of the ankle joint (i.e., dorsiflexion) provides a positive effect through the entire swing phase, especially from MTC to heel strike.

Concerning the strategy the older adult uses the knee and hip joints significantly more compared to the younger adults, which seem to involve also the ankle dorsiflexors to increase MTC (Fig. 7). The strategy used by this older adult is likely to compensate for the reduced range of motion at the ankle joint, whereas the young adult controlled a higher MTC using greater proportion of ankle dorsiflexion. It is possible that older adults preferred primarily to use the knee and hip to control MTC due to potential weakness of their ankle dorsiflexors e.g., Tibialis Anterior, as weak ankle dorsiflexors in older adults were reported in the past [20].

4 Biofeedback Applications

Since its origin biofeedback was used to train muscle activity for static positions or movements independently to function, however, this did not correlate to motor function improvements [21]. Nowadays biofeedback is commonly used in task oriented repetitive training and therapies for functional dynamic movement, to optimize motor function improvement. Functional task orientated training inspires the patients to negotiate the environment to solve any movement deficit. Moreover

daily life situations demand for continuous adaptation to the environment. Therefore targeted task-orientated learning must be linked to a functional context [21].

For healthy human, locomotion is an automated task that requires only little higher mental function. In contrast neurological patients frequently suffer from balance and mobility impairments or decreased muscle strength, motor coordination and sensory orientation [22]. Rehabilitation programs for neurological patients, such as stroke and Parkinson's often focus on relearning and restoring damaged motor skills and functions or in less severe situations on the improvement of the progressive reduction in speed and amplitude of movements [22, 23].

For example, by combining force-platform with a visual biofeedback system subjects are able recognize their centre of pressure in real time. By using this type of biofeedback it is possible for subjects to adopt a strategy to keep their postural control steady. Clinical relevance for an asymmetric weight distribution might be

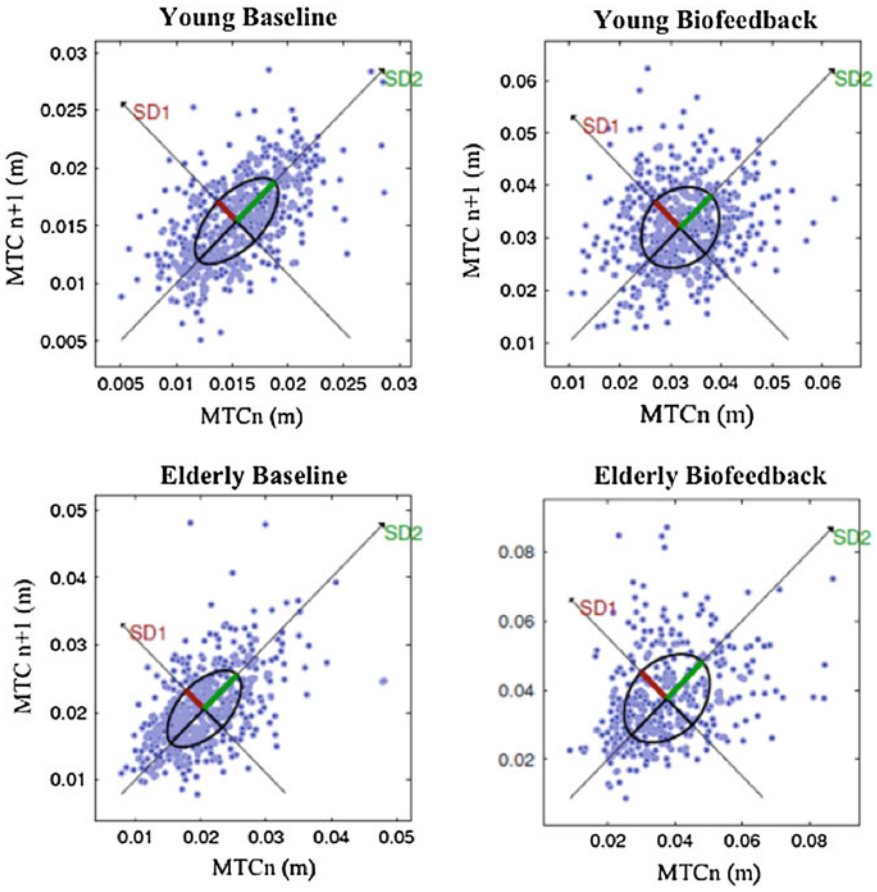

Fig. 9 Representative Poincaré plots in baseline and biofeedback walking for one typical young and older adult [10]

found in stride-to-stride gait variability and deficits in inter-limb coordination during gait. This might play a critical role in the development of gait disturbances and freezing of gait in Parkinson's patients [24]. Altering the mechanics of locomotion using real-time biofeedback has been used successfully in a number of gait conditions. Training using inertial sensors and visual biofeedback cues has been used to improve walking speed and step length in children with cerebral palsy [25]. Treadmill gait training with the use of biofeedback was found to be effective for relearning locomotion functions in post stroke hemiplegic patients [26], and to reduce lower extremity loading in runners [20].

In the study of Begg et al. [10] and the results presented in this chapter the purpose of the provided biofeedback was to determine and change the toe clearance strategy to increase MTC. In Begg et al. [10], the Poincaré non-linear analysis (Figs. 9 and 10) confirmed the SD1 (short-term variability) was higher in baseline walking for the older group, reflecting a greater stride-to-stride adjustment of toe trajectory, but the SD1 index did not differ for the two groups during biofeedback walking. The SD2 indices, which reflect long-term variability, were higher for the older adults both in the baseline and biofeedback conditions.

The SD1/SD2 ratio confirms that the younger adults were more stable in maintaining MTC within the boundaries without much deviation from an established locomotor pattern. Furthermore, both groups increased their MTC during the biofeedback walking condition and in the follow-up retention walking. In biofeedback walking young and older adults increased MTC around 30 mm, but in retention only the young adults increased MTC by a further 41 mm while older adults kept their MTC to about their biofeedback MTC level.

More evidence for the older adults' performance was shown with their greater success rate in maintaining MTC within the target. During biofeedback walking the lower bound was set to 150 % above the participants' average MTC

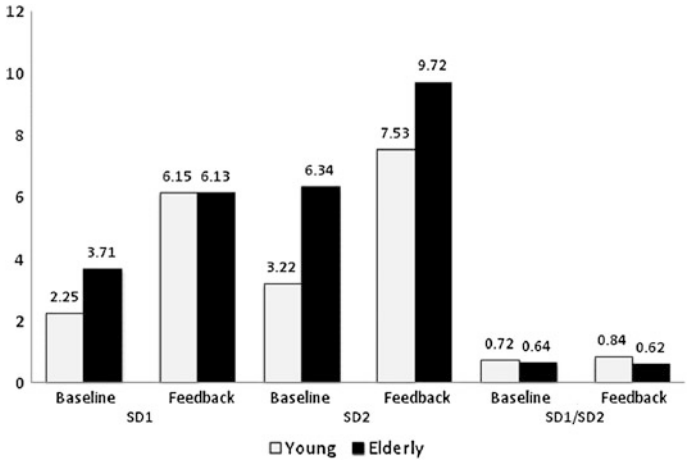

Fig. 10 Mean of SD1, SD2, and SD1/SD2 Poincaré indices for MTC in baseline (10 min) and biofeedback treadmill walking (20 min) for 10 young and 10 older participants [10]

determined from baseline walking condition. The upper bound was set to 3 times baseline SD above the lower bound. Older adults had greater success rate than young adults in targeting their MTC within the target band during both biofeedback (51 and 40 %, respectively) and retention (37 and 11 %, respectively) walking. This suggests that older adults not only adapted better to the biofeedback walking, but also retained the new walking pattern better than the young group.

These findings presented here confirm that concurrent visual biofeedback of lower limb kinematic gait parameters is effective in changing toe trajectory. Older adults seem to apply a strategy in which hip and knee joints were exploited in order to increase the MTC height, while young adults used their ankle as well. To fully understand of the long terms effects of biofeedback on older adults' gait control, further work is required. However, the preliminary results presented in this chapter suggest considerable potential for biofeedback-based gait training and rehabilitation.

Acknowledgments The work was supported in part by the Australian Government's *Collaborative Research Networks* (CRN) program.

References

1. M.W. Whittle *Gait Analysis: An Introduction*, 3rd edn. (Butterworth Heinemann Ltd, Oxford, 2001)
2. M.A. Moosabhoy, S.A. Gard, Methodology for determining the sensitivity of swing leg toe clearance and leg length to swing leg joint angles during gait. Gait. Posture **24**, 493–501 (2006)
3. P.M. Mills, R.S. Barrett, S. Morrison, Toe clearance variability during walking in young and elderly men. Gait. Posture **28**, 101–107 (2008)
4. World Health Organisation, *WHO Global Report on Falls Prevention in Older Age*. (Geneva, 2007)
5. R.J. Best, R.K. Begg, Overview of movement analysis and gait features, in *Computational Intelligence for Movement Sciences: Neural Networks and Other Emerging Techniques*, 1st edn. (IGI Publishing, Atlanta, GA, USA, 2006), pp. 1–69
6. D.A. Winter, *The Biomechanics and Motor Control of Human Gait: Normal, Elderly and Pahtological* (University of Waterloo Pres, Waterloo, 1991)
7. R.S. Barrett, P.M. Mills, R.K. Begg, A systematic review of the effect of ageing and falls history on minimum foot clearance characteristics during level walking. Gait. Posture **32**, 429–435 (2010)
8. R. Begg, R. Best, L. Dell'Oro, S. Taylor, Minimum foot clearance during walking: strategies for the minimisation of trip-related falls. Gait. Posture **25**, 191–198 (2007)
9. W.A. Sparrow, R.K. Begg, S. Parker, Variability in the foot-ground clearance and step timing of young and older men during single-task and dual-task treadmill walking. Gait. Posture **28**, 563–567 (2008)
10. R.K. Begg, O. Tirosh, R. van der Straaten, W.A. Sparrow, Real-time biofeedback of gait parameters using infrared position sensors. Presented at the international conference of sensing technology (ICST, 2012)
11. R.K. Begg, W.A. Sparrow, Ageing effects on knee and ankle joint angles at key events and phases of the gait cycle. *J. Med. Eng. Technol.* **30**, 382–9 (2006)

12. D.A. Winter, A.E. Patla, J.S. Frank, S.E. Walt, Biomechanical walking pattern changes in the fit and healthy elderly. Phys. Ther. **70**, 340–347 (1990)
13. J.V. Basmajian, Biofeedback in rehabilitation: a review of principles and practices. Arch. Phys. Med. Rehabil. **62**, 469–475 (1981)
14. V.G. Femery, P.G. Moretto, J.M. Hespel, A. Thevenon, G. Lensel, A real-time plantar pressure feedback device for foot unloading. Arch. Phys. Med. Rehabil. **85**, 1724–1728 (2004)
15. J. Rose, J.G. Gamble, *Human Walking* (Williams and Wilkins, Baltimore, 1994)
16. D.A. Winter, Foot trajectory in human gait- A precise and multifactorial motor control task. Phys. Ther. **72**, 45–53 (1992)
17. H. Nagano, R.K. Begg, W.A. Sparrow, S. Taylor, Ageing and limb dominance effects on foot-ground clearance during treadmill and overground walking. Clin. Biomech. **26**, 962–968 (2011)
18. A.H. Khandoker, M. Palaniswami, R.K. Begg, A comparative study on approximate entropy measure and poincare plot indexes of minimum foot clearance variability in the elderly during walking. J Neuroeng Rehabil **5**, 4 (2008)
19. J.A. Zeni Jr, J.G. Richards, J.S. Higginson, Two simple methods for determining gait events during treadmill and overground walking using kinematic data. Gait. Posture **27**, 710–714 (2008)
20. M.J. Spink, M.R. Fotoohabadi, H.B. Menz, Foot and ankle strength assessment using hand-held dynamometry: Reliability and age-related differences. Gerontology **56**, 525–532 (2010)
21. H. Huang, S.L. Wolf, J. He, Recent developments in biofeedback for neuromotor rehabilitation. J. Neuroeng.Rehabil. **3**, 11 (2006)
22. P. Langhorne, J. Bernhardt, G. Kwakkel, Stroke rehabilitation. Lancet **377**, 1693–1702 (2011)
23. G. Frazzitta, R. Maestri, D. Uccellini, G. Bertotti, P. Abelli, Rehabilitation treatment of gait in patients with parkinson's disease with freezing: A comparison between two physical therapy protocols using visual and auditory cues with or without treadmill training. Mov. Disord Official J. Mov. Disord. Soc. **24**, 1139–1143 (2009)
24. H. van der Kooij, E.H. van Asseldonk, J. Geelen, J.P. van Vugt, B.R. Bloem, Detecting asymmetries in balance control with system identification: first experimental results from Parkinson patients. J. Neural Trans **114**, 1333–1337 (2007)
25. R. Baker, J.L. McGinley, M.H. Schwartz, S. Beynon, A. Rozumalski, H.K. Graham, O. Tirosh, The gait profile score and movement analysis profile. Gait. Posture **30**, 265–269 (2009)
26. E. Rutz, R. Baker, O. Tirosh, J. Romkes, C. Haase, R. Brunner, Tibialis anterior tendon shortening in combination with Achilles tendon lengthening in spastic equinus in cerebral palsy. Gait. Posture **33**, 152–157 (2011)

Chapter 4
A Comprehensive Seven Layer Sensor Model: Cyber-Physical System

R. Dasgupta, D. Chattopadhyay, A. Pal and T. Chakravarty

Abstract Sensors and sensor devices with diverse capabilities and complexities are major physical elements in a cyber-physical system. Sensor model is a software model of a sensing system. Various sensor modelling techniques are available but there is a conspicuous absence of a method to create a formal and comprehensive description of a physical sensor. It can address major challenges about heterogeneity in sensor data communication, data representation and their semantics. A novel seven layer sensor modelling approach enables to describe a sensor right from its physical properties to end functionality where it defines the sensor services which can interface seamlessly and work corporately with other enterprise applications.

Keywords Sensor · Sensor devices · Sensor model · Service-oriented architecture · Service-oriented device architecture · Heterogeneity · Diverse capabilities · Seven-layer sensor model · Interoperable data services · Operating environment description · Failure prognosis · Smart meter data model

1 Introduction

A cyber-physical system (CPS) is a system which is a network of interacting elements with physical input and output rather than a standalone device [1]. It has a tight coordination between its computational and physical elements. Advancement of science and engineering has improved the coupling between them thereby dramatically increase the functionality, reliability, adaptability, autonomy, safety, and usability of a cyber-physical system. Common applications of CPS typically

R. Dasgupta (✉) · D. Chattopadhyay · A. Pal · T. Chakravarty
TCS Research, Kolkatta, India
e-mail: ranjan.dasgupts@tcs.com

A. Mason et al. (eds.), *Sensing Technology: Current Status and Future Trends I*, Smart Sensors, Measurement and Instrumentation 7, DOI: 10.1007/978-3-319-02318-2_4,

fall under sensor-based systems and autonomous systems e.g. wireless-sensor area network for environmental monitoring, body-area network for healthcare monitoring, autonomous automotive system, process control system, distributed and cloud robotics system, automatic pilot avionics system. Nowadays mobile cyber-physical system (MCPS) in which the physical element in question has inherent mobility is becoming a prominent subcategory of CPS. The rise in popularity of smartphones has increased interest in the area of MCPS. Tasks that require more resources than that of locally available, one common mechanism is to implement smartphone-based MCPS nodes that utilizes the network connectivity to link the mobile system with either a server or a cloud environment, which enables complex processing applications such as track and analyze CO_2 emissions, measure carbon footprint, detect traffic accidents and provide situational awareness services and monitor cardiac patients, which might have been otherwise impossible under local resource constraints. In a nutshell both CPS and MCPS is an integration of computation and physical processes [2].

Interacting physical devices e.g. sensors, sensor devices, actuators, which are key physical elements of a CPS or MCPS, are heterogeneous in nature and have varying degree of complexities and capabilities [3, 4]. They enormously vary from simple to complex and are very much diverse in their characteristics [5]. Current sensor systems are non-standard. Ad-hoc integration of these physical devices in order to carry out pervasive computing always results in a system that lacks of openness, scalability, flexibility, reliability, portability and interoperability. Heterogeneity lies inside plethora of wired and wireless communication protocols to collect sensor data, its proprietary representation and extract its meaning is always a severe issue. Major business challenges that crop up around lack of interoperability among heterogeneous sensors are (1) sensor data communication, (2) sensor data collection (3) sensor data representation (4) sensor data semantics (5) sensor operating environment.

Sensor model is a software model of a sensing system [6]. It should be a comprehensive description of a physical sensor which can provide software services known as sensor services. Application and services are sensor data's destination. Therefore deal with various types of sensor data representation across all types of sensor devices and their diverse data semantics is always a challenge for sensor data services. It also figures out the importance of interoperable sensor services that should play a major role in order to cope up with such challenges. To realize a cyber-physical system we need sensor model beforehand. Various sensor modeling techniques are available [7, 8], but there is a conspicuous absence of a method to create a comprehensive model that can address all aforesaid challenges and establish the correctness and validity of CPS functionality. Several sensor description methods are being used to create a software sensor model but every approach has its own advantage and limitation. We have envisaged that all available sensor data modeling techniques have to overcome a whole lot of challenges to provide a generic sensor service.

Obviously creating any sensor services and makes them co-existent and interoperable with other information and communication technology (ICT) application

is a serious business intelligence (BI) problem. A quite a bit of work has been done and standard has evolved but to address challenges only about sensor communication interoperability. A very little work has been done on syntax and semantic interoperability of sensor data. The evolution of service oriented architecture (SOA) anticipates that it will enable easy and scalable integration of devices [9]. However it assumes that the interoperable sensor services [10] are already available. But the assumption remains questionable. This is due to the fact that the method to describe the conversion of hardware pieces into software entities and thereby creating an interoperable software service out of a software description is still a big challenge. Physical sensor means sensor and sensor nodes collectively until otherwise specified. Other than providing a mere interfacing service to access and control sensor devices, sensor services should also provide interoperability with other software services inside SOA framework. Several approaches started focusing towards it but none of them can be used to create a sensor service that cannot only interact with physical sensors but also can co-exist with other SOA based ICT services in an interoperable manner. All available sensor description methods specify their own way how sensors and sensor data are discovered and accessed on the web. They either specify web services or generate device service bundles to provide interoperability between repositories of heterogeneous sensor data and applications that use them. Nonexistence of any sensor modeling framework that can annotate sensor data semantics and transcode all variants of sensor specifications into a uniform format is a key issue.

2 Types of Sensors

Physical sensors can broadly be categorized into two types (1) static or fixed sensors and (2) mobile sensors.

2.1 Static Sensor

Static sensors are sensors that are usually installed in fixed places in indoors and outdoors. They are the physical sensors used for static sensing and must be available for a long time. However the current trend is to reduce their cost, improve packaging, and energy consumption and connectivity through various industry standard wireless sensor network topologies. Static sensors can be further categorized according to their type of sensing.

2.2 Environmental Sensing

Various types of environmental parameters usually sensed are (1) temperature, (2) humidity, (3) pressure, (4) pollution, (5) radiation, (6) air-flow, (7) soil, (8) light, (9) wind.

2.2.1 Human Activity Sensing

Different types of human activity can be sensed using (1) motion detection, (2) acoustic noise, (3) surveillance camera, (4) energy/water/gas consumption, (5) healthcare (ECG, BP, Oximeter, Body Fat Analyzer, Blood Glucose, Pedometer etc.), (6) biometric sensors (fingerprint, retina scan etc.), (7) brain activity sensors (EEG, EMG etc.).

2.2.2 Infrastructural Sensing

Infrastructural sensing parameters are (1) water pressure, (2) flood/water leakage, (3) water contamination, (4) contact sensing/pressure sensing, (5) smoke/fire, (6) electricity Grid sensors (phasors, power factor etc.), (7) corrosion, (8) vibration.

2.3 Mobile Sensor

Mobile sensors are categorized into two types (1) vehicular sensing and (2) mobile phone based sensing.

2.3.1 Vehicular Sensing

Vehicular sensing focuses on sensing various parameters of a moving vehicle like (1) location, (2) speed and acceleration, (3) vehicular on-board diagnostics or OBD, (4) path planning and control of UAV, (5) swarm movement of mobile robot.

2.3.2 Mobile Phone Based Sensing

Participatory sensing using mobile phone is becoming an important feature as sensor-enabled phones are located everywhere and there is no need for deploying and maintaining them. They act as perfect ubiquitous source of information. Any

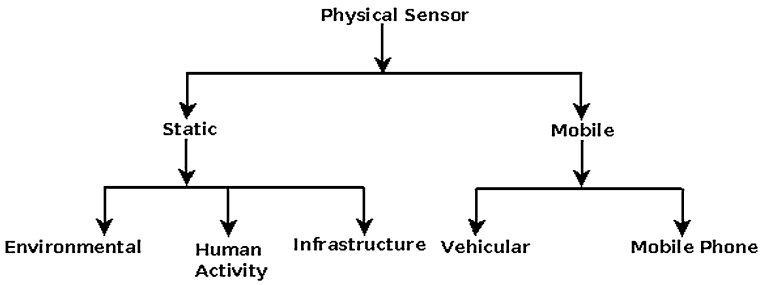

Fig. 1 Taxonomy of physical sensor devices

basic or feature phone today has microphone and camera as two basic sensors. Additionally, smart phones have GPS receiver, accelerometer, gyro meter and magnetometer (digital compass) as sensors. In future the following sensors may find their position and importance in mobile phones.

- Ultrasound sensors—improvement of microphone and speaker frequency response enable to start supporting ultrasound sensors.
- Altimeter sensors—will be used in creating a 3D localization.
- Healthcare sensors—heart monitors, perspiration monitors, portable X-Ray, USG etc.
- Sensors to monitor mood and excitement level.
- Sensors to identify user through activity analytics—it can be an alternative to biometric identification.

Taxonomy of physical sensors is shown in Fig. 1 whereas an exhaustive sensor list can be found here [11].

3 Overview of Sensor Services

The sensor standards define a web service interface which allows outside elements to read sensor information and access dataset. A sensor service can receive multiple inputs and provides a single output after processing them. They can be categorized into three classes [11].

3.1 Physical Sensor Service

A physical sensor service is directly bound to a hardware sensor. It is the most fundamental type of sensor service. It is used to receive input from hardware sensor and process them to produce real world output.

3.2 Basic Virtual Sensor Service

A basic virtual sensor service is composed of a set of physical sensor services which detect the same type of phenomenon. Unlike the physical sensor service which represents a hardware sensor, a virtual sensor service is a purely software sensor. A basic virtual sensor service accepts multiple inputs from its member physical sensor services, processes and aggregates them to produce a single output. All inputs to a basic virtual sensor service are of same type in terms of units of measurement.

3.3 Derived Virtual Sensor Service

A derived virtual sensor service is composed of a set of basic virtual sensor services, each of which detects a different type of phenomenon. As the name indicates, the output of this type of virtual sensor service is derived from multiple inputs. Hence, the type and measurement unit of output is totally different from that of any of its member sensor services.

4 Overview of Mostly Used Sensor Models

Mostly used sensor models to specify a physical sensor are primarily limited in their scope of sensor descriptions. They use different perspective to fully examine, analyze and describe physical sensors. We provide a brief overview of existing models.

4.1 SWE and SensorML

Open geospatial consortium (OGC) defined sensor web enablement (SWE) framework to address specific interoperability challenges [12]. OGC has come up with standards like Sensor Model Language (SensorML), Observation and Measurement (O&M) schema and Transducer Modeling Language (TML). SensorML specifies models and XML encoding that provide a framework for definition of the geometric, dynamic, and observational characteristics of sensors and sensor systems. Different sensor types can all be supported through the definition of atomic process models and process chains. TML is aimed to standardize an option for streaming multiplexed data from a sensor system and for describing the system as well as data encoding.

SWE common data model defines low level data models for exchanging sensor related data between nodes of the SWE framework. These models allow applications and/or servers to structure, encode and transmit sensor datasets in a self-describing way. It is a data processing model. It is nothing more than data and process representation. Each sensor in the real world is depicted in SensorML by a process model, whereas the connections between the sensors are shown by a process chain. It just specifies the connections between process models without specifying the sequence in which these processes will be executed. A device modeled as a process consists of inputs, data processing methods and outputs. A collection of such processes are linked by process chain models CPS [4]. It is useful for sensor data interpretation and preprocessing to bridge the gap between low-level and hard-to-use data with higher abstractions. It assumes that there should be other standards that convert the signal and parse the protocol.

4.2 Device Kit

Device Kit is another modeling technology that facilitates application interface with physical sensors using java bundle on an open services gateway initiative (OSGI) framework [13]. The XML-based device kit markup language (DKML) models a sensor across application agent, device, transport, and connection layers (discussed later). A generic abstract model helps programmers to develop application for sensor devices without knowing its hardware specific information. It follows concept of service oriented device architecture (SODA) and is a core component of IBM data capture and delivery toolkit (DCDT) for web sphere premises server [14]. It provides a common interface for the application code to interact with sensors and actuators.

The device kit environment consists of following components mainly (1) an application, (2) a run time and (3) a hardware device. The run time is divided into (1) device layer, (2) transport layer, and (3) connection layer. A software stack of device kit is depicted in Fig. 2.

4.2.1 Connection Layer

Connection layer supports reading and writing of byte streams to sensor device. It does not understand the semantic (meaning) of bytes but supports the delivery of output bytes and receiving of input bytes.

4.2.2 Transport Layer

Transport layer supports sending and receiving of messages. It interprets the format of a message; but does not understand its meaning. When a sensor device

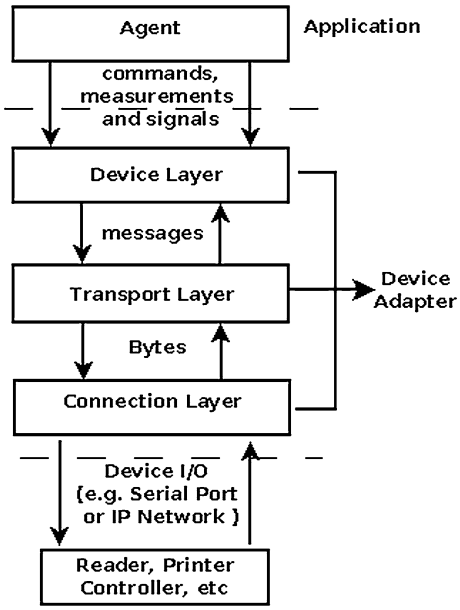

Fig. 2 Device kit adapter

requests to send a message, the transport layer formats the message into correct bytes and writes to the connection. Similarly it also reads input bytes from the connection and parses them into received messages. Subsequently sensor devices are notified.

4.2.3 Device Layer

Device layer provides application an interface to the sensor device. It shields the application from its low level hardware details. It understands the format of messages and any parameters within a message. When an application executes a command, the command requests transport layer to send the message. Similarly signal listeners are notified if any message received from the transport layer.

4.2.4 Application Agent Layer

Application agent layer works as an adapter and profile layer provides the application a common interface profiles (GPIO profile, control profile) against a set of common functionality of sensor devices. This layer uses a publish/subscribe SOA interface. The adapter and profile shields the application from the fact of knowing which of the common hardware device is being used.

4.3 Device Description Language

Device Description Language (DDL) is developed by University of Florida to support automatic device integration [15]. It enables a uniform schema to describe sensors and devices. In DDL a device is depicted as an encapsulation of three things:

- a set of properties catering information on vendor, capabilities and operating conditions;
- internal mechanism is device specific operation;
- interface that bridges between external world and internal mechanism.

DDL classifies devices into three categories (1) sensors, (2) actuator and (3) complex device. Each DDL descriptor file describes a single type of device in XML format. It contains:

4.3.1 Information for Service Registration and Discovery

It provides e.g. device name, model, function description, etc.

4.3.2 Description of Device Operations

- Each operation is a collection of input-processing-output function chain.
- Low-level communication between a device and its service are represented as 'Signals'.
- High-level semantics of signals are 'Readings'.

Figure 3 depicts the device model using DDL [16].

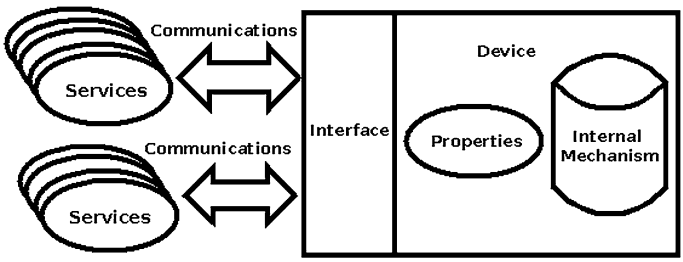

Fig. 3 Device model in DDL

4.4 IEEE 1451 Smart Transducer Interface

IEEE 1451 [10] is a set of smart transducer interface standards developed by the Institute of Electrical and Electronics Engineers (IEEE).The goal of the IEEE 1451 family of standards is to allow the access of transducer data through a common set of interfaces irrespective of their connectivity with the systems or networks via a wired or wireless means. It provides the common interface and enabling technology for the connectivity of transducers to control devices and data acquisition systems. The key definition of data formats and communication protocols of transducer electronic data sheet (TEDS) is specified in IEEE 1451.2. Transducers with signal conditioning and conversion modules can be combined into a single entity called a smart transducer interface module (STIM). Likewise, the application algorithm and network communication modules can be grouped into a building block called a network capable application processor (NCAP). With this functional partitioning, transducer to network interoperability can be achieved in these manners:

- STIMs from different sensor manufacturers can be "plug-n-play" with NCAPs from a particular sensor network supplier.
- STIMs from a sensor manufacturer can plug-n-play with NCAPs supplied by different sensor or field network vendors.
- STIMs from different manufacturers can be interoperable with NCAPs from different field network suppliers.

IEEE 1451.1 developed a smart transducer object model in a frame of network-capable application processors (NCAPs) to support multiple control networks. IEEE 1451.3 extends the parallel point-to-point configuration to distributed multi-drop systems. IEEE 1451.4 is an emerging standard for adding plug-n-play capabilities to analog transducers via a mixed-mode interface of analog and digital operating modes. IEEE 1451.5 defined the wireless communication and TEDS formats and specified sensor-to-NCAP connection for IEEE 802.11 family, IEEE 802.15 family or ultra-wideband (UWB) connections. IEEE 1451.6 proposed the TEDS using the high-speed control area network (CAN) interface for measuring devices and closed-loop controllers. Figure 4 shows the general framework of smart transducer interface of IEEE 1451 family and describes different parts of the IEEE 1451 standard [17].

IEEE 1451 also describes service-oriented sensor data interoperability architecture. It achieves data interoperability between IEEE 1451 smart transducers and OGC-SWE web services through the smart transducer web services (STWS).

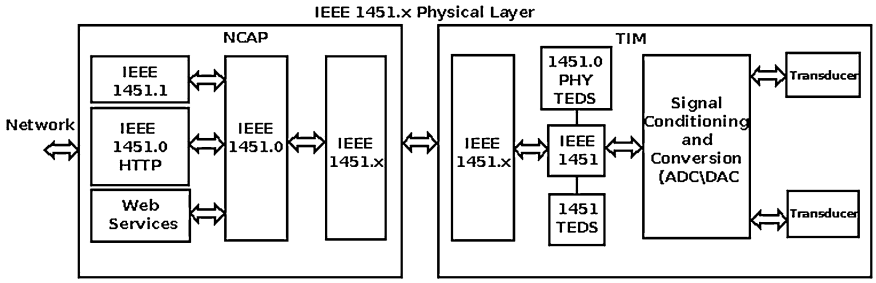

Fig. 4 IEEE 1451 standard

4.5 ECHONET

ECHONET is the acronym for energy conservation and homecare network. It is proposed as set of ISO IEC standards, spearheaded by Japanese device manufacturers. ECHONET describes a communication protocol for a reliable, low-cost home network and provides an option to attach ECHONET adapter to legacy devices [18]. This standard specifies an open system architecture that enables the integration of a variety of home appliances and sensors from multiple vendors. ECHONET provides a device specification that explicitly defines their properties and access methods so that vendors conform to a uniform interface. The ECHONET device object specification lists several classes, each one representing a device or sensor used in the home network. Each class's properties and methods are explained in plain text, with their types and value ranges explicitly specified in a way similar to a java API document. An ECHONET software stack is depicted in Fig. 5.

The ECHONET communication middleware specifications were designed primarily to enable the concealment of lower-layer transmission medium (e.g. Ethernet, Bluetooth, Wi-Fi, Zigbee) differences from application layer perspective. The ECHONET adapter adds ECHONET node functionality to a device that can't function as an ECHONET node by itself.

The common shortcoming of the above described standards is that these standards ignore the importance of operating environment (for the sensors) and the description of interoperable sensor services to provide interoperability in terms of data semantics. There is a scope for a new comprehensive sensor description model and interoperable sensor services that can co-operate with other enterprise applications inside a SOA framework.

A method to overcome the shortcoming by proposing a comprehensive seven layer sensor description model is presented in the following section. A seven-layer sensor modeling approach enables user to create a comprehensive description of a soft sensor by defining specification from physical description to its end functionality (a complete scope of any sensor description) where end functionality means sensor as a software service.

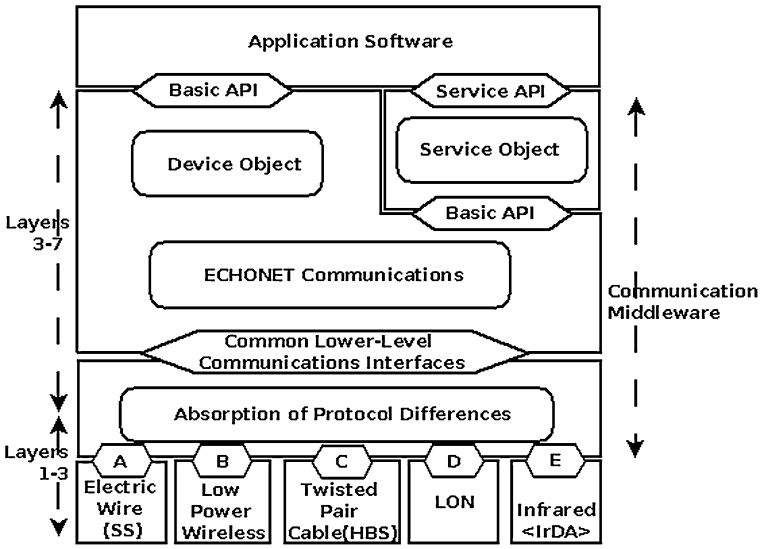

Fig. 5 ECHONET standard

5 Seven Layer Sensor Description

The proposed seven layer cyber-physical sensor model provides an elaborate and comprehensive specification of a physical (or soft) sensor. It is an approach that enables one to describe a sensor from its physical properties (interacting with immediate environment) to end functionality where it defines sensor services to talk with end applications. SOA framework considers a physical sensor as a sensor service and, is interested in its interoperability with other software services. Middleware is interested in sensor semantics such as measurements, command and sensor data formats whereas physical, signal or protocol information is extremely important for the low-level device software. Hence, the usefulness of the seven-layer sensor architectural description is the availability of required information across all layers. Figure 6 depicts the proposed seven-layer sensor data model followed by description of each layer [19].

5.1 Operating Environment Description (Layer 1)

The bottom most layer that describes operating environment of a physical sensor or sensor devices. It specifies how environmental parameters like noise, sensor location, and atmospheric refraction influence a device's physical characteristics such as sensitivity, error rate, SNR, SINAD etc. It provides an explicit specification

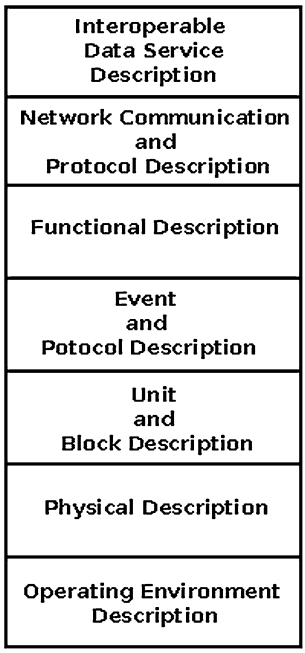

Fig. 6 Proposed sensor model seven-layer stack

of an operating environment which immediately surrounds the physical sensors and describes how it influences sensor response against any physical event or excitation.

5.2 Physical Description (Layer 2)

Physical description explains a device's physical characteristics, such as mechanical and electro-mechanical properties, form factor, sensitivity. These external properties don't describe internal mechanisms or functions, and are usually of little interest to high-level application, but in many cases, parameter such as temperature, humidity range greatly affects typical performance characteristics that can prove critical to real-world deployment. It is similar to a DDL specification of a physical sensor description.

5.3 Units and Block Description (Layer 3)

Units and block description depicts device's physical presence. Despite of the fact that it is of little relevance to sensor services, sensor specification makes the choice

to include pins, ports and block descriptions for the purpose of completeness and comprehensiveness.

5.4 Event and Protocol Description (Layer 4)

Signal events and protocols are the raw readings from a device interface. They can be an analog-to-digital converted value from an analog output or a string from a digital port. Without defining the conversion or parsing method, these data carry no meanings. It acts as a boundary where physical world ends and digital world starts. Standards such as Device Kit and IEEE 1451 choose this layer as the lower boundary of their scope known as transducer interface module.

5.5 Functional Description (Layer 5)

Measurements and data-processing collectively known as functional description is the semantics of signal events and protocols e.g. when a 3-axis accelerometer sends out signals in X, Y & Z directions, they are immediately converted to measurement i.e. role, pitch & yaw. These data are usually directly relevant to application's interest, so this layer becomes the most important one in the description scope and is included by all sensor standards.

5.6 Network Configuration and Protocol Description (Layer 6)

Networking protocol and configuration is the last layer in seven-layer stack before the data is sent to middleware. Description will be similar to standards such as Device Kit and IEEE 1451.

5.7 Interoperable Data Services Description (Layer 7)

It provides a common service oriented interface to sensor devices, manages communication protocol and data format mapping and data semantic interoperability by providing a SOA framework. Exposing device interfaces as SOA services over a network along with other enterprise services transforms SOA to service oriented device architecture (SODA) framework [20]. It is seen (from the above discussions) that two key features of the proposed seven layer model are (1) interoperable data services and (2) integration of operating environment to the physical description of sensors. They are elaborated in the following sections.

6 Detail Description of Interoperable Data Services

Each type of sensor device in the real world can be described as a class with attributes and member functions associated with access rules specified. Dependency relationships among primitive sensor features are shown by association and composition. It is always derived from a domain specific knowledge representation to which the particular sensor belongs using ontology (a knowledge representation) e.g. smart meter as an energy sensor belong to the domain of electrical power and energy. The interoperable data services description layer allows all types of standard specification and proprietary user specification. It uses a sensor description development framework to convert all variants of sensor specification into a device object specification and it generates portable sensor services which can be used with any SOA system. It provides a common service oriented interface to sensor devices, manages communication protocol, data format mapping and annotate data with sensor semantics. It creates SODA framework [21] on exposing device interfaces as SOA services over a network. It is an extension to SOA framework to incorporate devices in distributed enterprise systems and when modeled as a service, device access and control can be made available to a wide range of enterprise applications. Interoperable data services not only overcome interoperability issue in device integration but its added functionality enables SODA framework [22] to provide service oriented sensor platform as a service (SOSPaaS). Smart sensor web services (SSWS) is proposed to ease this integration effort. It is based on SOA and is a unified web service for smart transducers. SSWS is a suitable solution for achieving seamless integration of smart transducers with the OGC-SWE and sensor alert applications. SSWS is an amalgamation of different enabling technologies (sensor technologies, semantic web and semantic web services technologies) and provides WSDL-based interoperability by exposing sensor functionality as a service.

7 Application of Operating Environment

None of the existing sensor description standards talk about the effect of operating environment. In our proposed seven layers stack a separate layer has been designated to take into account the effect of operating environment and thus resulting in a comprehensive sensor description model. Following use case explains the application scenario where the introduction of operating environment layer can play vital role.

Let us assume an application where it is required to measure vehicle vertical vibrations and extract useful features for the purpose of future performance prediction. Let us consider a generic model of the sensor-accelerometer for measuring vehicle vibration. Performance prediction or “prognosis” requires an accurate model of the vehicle as well as the excitation like the “rough” road. For such

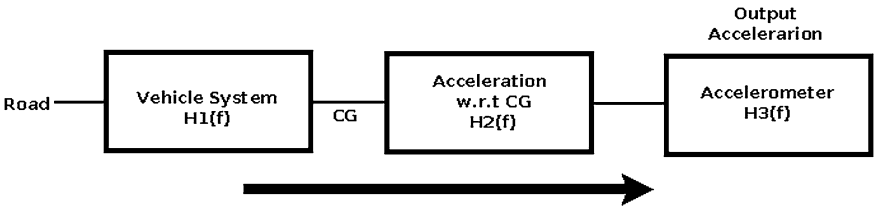

Fig. 7 Disjoint accelerometer

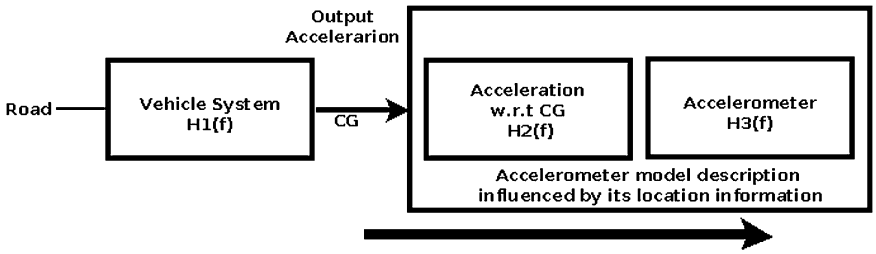

Fig. 8 Vehicle accelerometer

modeling purpose, we consider using half-car model of the vehicle; thereby computing the vertical accelerations of the vehicle chassis as measured at the center of gravity of the vibration. Consider also that the accelerometer is placed laterally with respect to center of gravity (CG). Additionally, we may also consider a place for the sensor which has some kind of absorber in its docking station. Such scenarios require a translation of forces from CG to the sensor. This situation is illustrated in Fig. 7.

Consider the case where we have measured a time-series acceleration output for a given system and we assume that the road excitation is a random function. For a typical model based parametric analysis of the system, we are forced to treat $H_1(f)$ and $H_2(f)$ together and we treat the sensor accelerometer as a standalone device. However the unified representation of the vehicle vibration at an offset point may result in errors of interpretation and therefore future prediction of the vehicle performance. A more elegant solution is to integrate $H_2(f)$ (as operating environment) with $H_3(f)$ as an integrated layer for sensor definition as shown in Fig. 8. However, if we integrate the environment layer with the general accelerometer device, the application of the integrated accelerometer as a sensor now gets limited to the environment for which the definition is created. Hence the nomenclature should also change e.g. we can name it as vehicle-accelerometer. When the operating environment description as given by $H_2(f)$ gets integrated to the physical description of the accelerometer, it becomes computationally simpler and more accurate to determine the sensitivity of core vehicle parameters like suspension.

8 Utilization of Seven Layer Sensor Model

8.1 Failure Prognosis (Electromechanical System)

The utilization of the above described seven layer sensor model (with embedded operating environment layer and interoperable data services) is visualized for 'Failure Prognosis' use case of electromechanical systems like a vehicle. Such methodology is a very useful tool enabling condition based (predictive) maintenance of complex systems and has great business value in lowering the inventory cost, improving future products and enhancing user experience.

The proposed model driven engineering (MDE) framework (as shown in Fig. 9) inside a SODA system uses model driven architecture (MDA) approach to model complex sensory cyber physical systems. It considers a MDA for ground vehicle prognosis or future performance prediction of key components like suspension, shock absorber etc. In this case, we create system models of the vehicle under consideration and simulate its performance over varying road conditions and irregularities. Let us begin with a simplistic model like a half-car model; evaluating the performance, improve analytic and extend the same to more complex but realistic models. A key feature in a model driven architecture for CPS is the sensor which measures and reports back the relevant physical parameters. We typically tend to model the sensor as a calibrated transducer which measures a physical parameter e.g. the vertical vibration of a moving vehicle and report back a calibrated digital data equivalent to the measured value. However, the sensor's performance (3-axis accelerometer for this case) is critically dependent on the position of its placement inside the vehicle as well as its orientation. Generally we account for the probable variations by either an approximate analysis or a rigorous method of analyzing the forces (through first principles) after considering the excitation, the nature of transmission of forces through the system right up to the point of sensor's actual placement. This described philosophy of mathematical modeling is ideal when we are aware of exact system parameters like suspension stiffness, damping factor, absorption ratio for the seats, present mass, coupling ratio between front & rear axle etc. However, very rarely, we will get to know the exact parameter values including the extent of relationship between these parameters for a real vehicle of a given make. For such mitigation, we need to experiment on real vehicles (with embedded sensors) and collect enough relevant data for model validation. The experimental data set along with model parameters are used to minimize uncertainty in performance analysis for different excitations and varying load conditions. This is an iterative process where each separate operating environment (for the sensor) needs a separate and rigorous computation.

But our seven layer sensor description technique reduces these computational overheads while retaining the accuracy on introducing operating environment effects in the sensor model itself as shown in sensor models and operating environment description block in Fig. 3. On the other hand interoperable data services assist uncertainty and sensitivity analysis during simulation in order to predict its

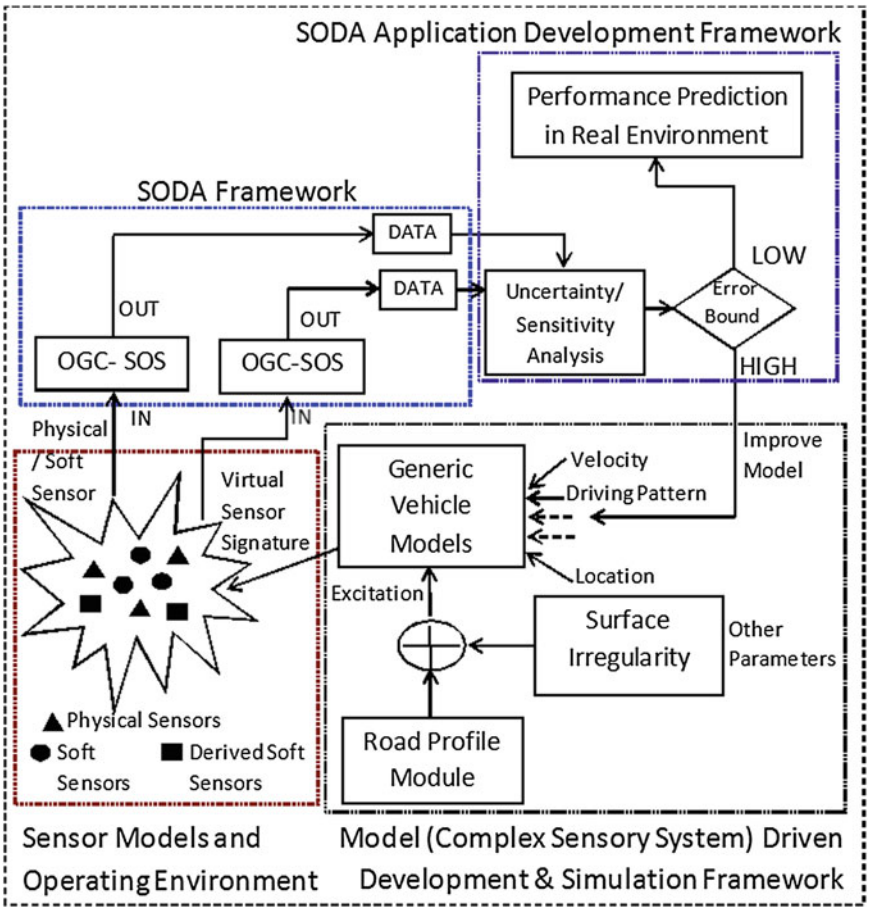

Fig. 9 Failure prognosis of vehicle

future performance more accurately in real-environment. This is illustrated (as per Fig. 5) in model (complex sensory system) driven development and simulation block and SODA [23] application development block along with their interdependencies.

8.2 Smart Meter as Energy Sensor

Comprehensive sensor description primarily specifies two important roles to model smart meter as an energy sensor. They are

- Role of energy sensor independent interface

"End devices may be all different, interoperability can be also achieved at higher levels of the system". It is a typical argument of a meter manufacturer who is promoting its manufacturer-specific solution. Certainly the business model of a system integration industry depends on it. Once a utility buys in it is locked to this meter manufacturer; i.e. meters from other manufacturers can only be integrated into the system with substantial integration costs. This also decreases the number of potential suppliers therefore reduces competition. The purpose of achieving interoperability on device communication level is to simply avoid the high costs of system integration and to keep competition open thereby communication media independent interface between meter and data collector became most important-addressed by layer 4–6 in our seven layer stack.

- Role of interoperable energy data service

The energy sensor data model describes what data have to be present and exchanged to support various use cases. They are either identical or very much similar on each market. Modeling the same use case in different ways does not add value but hinders interoperability. The key to achieve interoperability at device service level is to use a single uniform energy data model having extension mechanisms to support new requirements addressed.

9 Methodology for Comparing Sensor Modeling Techniques

This section proposes that the applicability and usefulness of any sensor description method can be evaluated mainly against following two metrics [24]

- Coverage of sensor description
- Sensor modeling language, tools and support availability

9.1 Coverage of Sensor Description

In order to derive the coverage score (CS) of the *i*th sensor description method we have introduced the following mathematical expression:

$$CS_{ij} = \sum_{i=1}^{N} B_i * W_i / \sum_{i=1}^{N} W_i \tag{1}$$

where C_{ij} = ith feature of jth sensor description, N = No of features, B_i = A Yes (1)/No (0) value of the ith feature and W_i = weight of ith feature.

9.2 Sensor Modeling Language, Tools and Support Availability

Similarly in order to derive the score of availability of software tools (AS) of the ith sensor description method, we have introduced the following mathematical expression:

$$AS_{ij} = \left[\sum_{i=1}^{N} Oi * W_{oi} + P_i\right] / \sum_{k=1}^{M} W_k \tag{2}$$

AS_{ij} = ith feature of jth sensor description on language, tool and software support; N = Total no of features representing format, software support, tools and usage interface; O_i = A Yes (1)/No (0) value of the ith feature evaluated on open source availability of the modeling technique being considered; W_{oi} = weight of ith open source feature; P_i = A Yes (1)/No (0) value of the ith feature evaluated on non-free software license for the modeling technique being considered; W_k = weight of kth type of license in 1–5 range representing; M = Total no of license types being considered.

An empirical analysis is carried out separately in the next section with respect to language, tool and software support availability among all sensor description methods being considered. But it is required to know that the calculated normalized AS_{ij} value of all methods will be use case invariant. Finally we add up C_{ij} and A_{ij} to arrive at the final score and a conclusion is drawn on the best suitable sensor description methods (Table 1).

Table 1 Weight assignment according to the type of software license

Description	W_1	W_2	W_3	W_4	W_5	W_6
Non-free software license	1					
Commercial royalty-free (pay licensed closed-source)		1				
Commercial royalty-free (pay licensed viewable-source)			2			
Commercial royalty-free (free licensed closed-source)				3		
Free-software licenses (free software foundation approved)					3	
Free-software licenses (open source initiative approved)						3
Free-software licenses (GPL 2-incompatible)					4	
Free-software licenses (GPL 2-compatible)						5

10 Comparison of Sensor Modeling Techniques

A technical analysis of existing sensor description methods and their pros and cons are presented in this section considering use case of smart meter as energy sensor.

10.1 Coverage of Sensor Description

All sensor description metods explained in Sects. 3 and 5" used to describe a physical sensor or to create its soft model are primarily limited to their scope of usage.

SensorML provides a generic sensor model for measurement and its post measurement transformation. It shields complexity of any physical sensors by defining a uniform process interface. Its description is mostly useful for sensor data interpretation and preprocessing to bridge the gap between low-level, hard-to-use data and higher abstractions. The process model gives a data driven approach.

Device Kit models a physical sensor which completely abstracts any hardware-specific information. It only models a device by creating device, transport and connection layer descriptions.

DDL only focuses on sensor physical description and its interfacing. It assumes sensor devices without any networking capabilities and is mostly connected to applications via sensor nodes. It adopts a layered approach to divide sensor's functionality.

IEEE 1451 adopts a modular approach that demarcates where physical world ends and digital world starts. It chooses it as the lower boundary of its scope. It provides its description from signal level information up to network configuration and its associated protocol.

ECHONET treats sensor device as an atomic object and provides a sensor description that explicitly defines its properties and access methods. Its scope of description is limited to measurement and command semantics.

Henceforth it becomes obvious that:

- None of above methods provides an explicit specification of an operating environment which immediately surrounds the physical sensors and thereby influences its response to a given physical event or excitation.
- Plug-n-play capability lays foundation for internet of things (IOT) paradigm for connecting transducers to internet. None of above methods other than IEEE 1451 provides technique to establish a transducer independent interface between sensing unit and processing unit.
- Application and services are the sensor data's destination. It always imposes a challenge how to ensure uniformity in data representation and its semantics. Although there is no shortage of protocols standardizing it but in reality inter-operable data services are usually ignored. Creating device profiles, sensor

Table 2 A comparison of sensor description based on seven-layer sensor model

Description	IEEE 1451	DDL	Device kit	SensorML	Echonet	Weight
Operating environment layer	N	Y	N	N	N	1
Physical layer	N	Y	N	N	N	1
Units and block layer	N	Y	N	N	N	1
Event and protocol layer	Y	Y	Y	N	N	4
Functional layer	Y	Y	Y	Y	Y	3
Network configuration and protocol layer	Y	N	Y	N	N	4
Interoperable data services layer	N	N	N	N	N	5
Normalized CS value	0.52	0.43	0.52	0.14	0.14	

device services and provide a cooperating interoperable service component in a SOA framework is another important gap among most of the approaches

Table 2 shows a comparative study among five mostly used sensor modeling standard with respect to their limited scope of definition.

10.2 Sensor Modeling Languages and Available Tools

A standard is an explicit set of specification, yet each sensor description methods are using a diverse set of language construct to create a software specification of a physical sensor.

ECHONET represents sensor properties and interfaces in plain English whereas IEEE 1451 uses interface definition language (IDL). On the other hand SensorML, Device Kit and DDL provide XML schemas together with verbal descriptions explaining their syntax. In addition some of the method also provide open source language processor, datasheet compiler as supporting tools to create sensor services.

Table 3 shows different sensor modeling languages, sensor modeling tools and various software supported by different sensor description standard. Each cell item in the table is assigned with a weight (given in parenthesis) according to the license type it has and a use case invariant normalized score has been calculated using (2) as stated in previous section.

It is evident from Table 1 that IEEE 1451 and Device Kit are emerging as two top contenders as per the use case we have discussed in terms of coverage score as a principal metric of comparison. However empirical analysis of other metric appears in Table 2 signifies that SensorML is ahead of IEEE 1451 method. A final score has been calculated for the given use case adding the normalized scores and a score comparison chart has been drawn (Fig. 10) for all available sensor modeling techniques discussed so far. The technique can be applied also in the same way to other use cases. Therefore it becomes obvious that every approach has its

Table 3 A comparison on language tool and software support

Features	IEEE 1451	DDL	Device Kit	SensorML	Echonet
Format	IDL/XML (5)	XML (5)	XML (5)	XML (5)	Class in plain text (1)
Software support	Open 1451 (4)	ATLAS bundle creator (1)	DKML parser and eclipse plug-in (4)	52North swe stack (5)	NA
Tools	TEDS reader/ writer (4)	DDL language processor (5)	Device kit wizard/ service activation toolkit (SAT) (1)	SensorML webtool (5)	NA
Usage interface	Webservice e.g. STWS (4)	OSGi bundle webservice (1)	OSGi bundle pub sub service (1)	SWE webservices (5)	Java object (1)
Normalized score	0.73	0.55	0.5	0.91	0.1

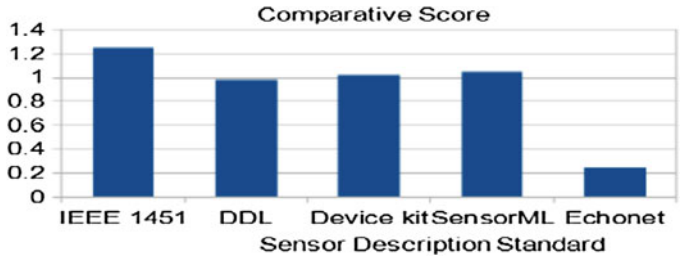

Fig. 10 Score comparison chart—various sensor modeling techniques

own limitation and there is a conspicuous absence of a method to create a comprehensive software description of a physical sensor. Thus our empirical analysis of mostly used sensor description standard in CPS modeling establishes a need of a more comprehensive method.

11 Conclusions

A new multilayer comprehensive sensor model has proposed to describe physical sensors with major focus on interoperable data services and its operating environment. Creation of interoperable data services provides interoperability between repositories of heterogeneous sensor data and applications using them. It is found that all seven layers may not be relevant all the time for describing a particular

sensor. There may be overlap among descriptions across each layer. However the proposed seven layers completely describes all properties and functionalities of a physical sensor in its soft model. Also an evaluation methodology is proposed to mathematically score the sensor description models for a given use case so that merits and demerits can be subjectively evaluated that will help the application developer on prior decision making for selection of a particular model to proceed.

References

1. E. Council, Directive 2000/60/EC of the European Parliament and of the Council of 23 October 2000 establishing a framework for Community action in the field of water policy, OJ L, vol. 327, pp. 1–73, Dec. 2000
2. R. Cartwright, K. Kelly, F. Koushanfar, W. Taha, Model-Centric Cyber-Physical Computing, Department of Computer Science and Department of Electrical and Computer Engineering Rice University, Houston, TX 77025
3. C. Chen, S. Helal, Sifting through the jungle of sensor standards. *IEEE Pervasive Comput.* **7**(4), 84–28 (2008)
4. K. Kazemi, Integration of Component-Based Frameworks with Sensor Modeling Languages for the Sensor Web, Thesis submitted to the Faculty of Graduate and Postdoctoral Studies in partial fulfillment of the requirements for the Degree of Master of Applied Science in the Program of Electrical and Computer Engineering, Oshawa, Canada, August 2010
5. D. Zhang, M. Zhu, H. Cheng, Y. Koh, M. Mokhtari, Handling Heterogeneous Device Interaction in Smart Spaces. Ubiquitous Intelligence and Computing (Springer, Berlin, 2006), pp. 250–259
6. P. Derler, E A. Lee, A. L. Sangiovanni-Vincentelli, Addressing Modeling Challenges in Cyber-Physical Systems, Electrical Engineering and Computer Sciences University of California at Berkeley, UCB/EECS-2011-17, March 4, 2011
7. P. Hu, R. Robinson, J. Indulska, Sensor Standards: Overview and Experiences, The University of Queensland and NICTA, ISSNIP-International Conference on Intelligent Sensors, Sensor Networks and Information Processing, pp. 485–490, 3–7 Dec 2007
8. K. Lee, B. Reichardt, E. Mark, Open standards for homeland security sensor networks. IEEE Instrum. Meas. Mag. **8**(5), 14–21 (2005)
9. M.I. Mabrouk, *SOA Fundamentals in a Nutshell*. IBM developer Works (2008)
10. E.Y. Song, K.B. Lee, Service-oriented Sensor Data Interoperability for IEEE 1451 Smart Transducers, in I2MTC 2009-International Instrumentation and Measurement Technology Conference Singapore, 5–7 May 2009
11. D. Chattopadhyay, R. Dasgupta, A survey of available sensor data modeling techniques, in NCCCS 2012 : National Conference on Computing and Communication Systems, Dr. B.C Roy Engineering College, Durgapur, West Bengal, India, November 21–22, 2012
12. M. Botts, OpenGIS® Sensor Model Language (SensorML) Implementation Specification, Open Geospatial Consortium Inc and University of Alabama in Huntsville, 17 July 2007
13. D. Maples, P. Kriends, The open services gateway initiative: an introductory overview. IEEE Commun. Mag. **39**(12), 110–114 (2001)
14. A. Eisma, IBM Data Capture in IBM WebSphere Premises Server, OSGi Alliance Community Event, Berlin, Germany, June 10–11, 2008
15. C. Chen, H.-I. Yang, R. Bose, *Device Description Language Specification-Version 1.2* (Mobile and Pervasive Computing Laboratory, University of Florida)

16. J. King, R. Bose, H.-I. Yang, S. Pickles, A. Helal, Atlas: A service-oriented sensor platform: hardware and middleware to enable programmable pervasive spaces, in SenseApp 2006, Annual IEEE Conference on Local Computer Networks, pp. 630–638 (2006)
17. E.Y. Song, K. Lee, Understanding IEEE 1451-Networked smart transducer interface standard. IEEE Instrum. Meas. Mag. **11**(2), 11–17 (2008)
18. ECHONET Specifications [Online]. Available: http://www.echonet.gr.jp/english/spec/index.htm
19. D. Chattopadhyay, R. Dasgupta, A novel comprehensive sensor model for cyber physical system—interoperability for heterogeneous sensor, in *6th International Conference on Sensing Technology*, ICST, Kolkata, December 18–21, 2012
20. C. Chen, A. (Sumi) Helal, Device Integration In SODA using Device Description Language, SAINT 2009.[Online].Available: http://www.icta.ufl.edu/dundee/DundeeFloridaExchange/ppt-chao.pdf
21. Archived Eclipse Projects.[Online].Available: http://www.eclipse.org/ohf/components/soda
22. Introducing Devices Profile for Web Services, Microsoft Corporation, 2007
23. S. de Deugd, R. Carroll, K.E. Kelly, B. Millett, J. Ricker, SODA: service-oriented device architecture, IEEE Pervasive Comput. (2006)
24. D. Chattopadhyay, R. Dasgupta, A. Pal, Sensor data modeling for smart meters—a methodology to compare different systems, in *IEEE International Workshop on Cyber-Physical System and Its Computing and Networking Design, ICNC*, San Diego USA, January 28–31, 2013

Chapter 5
Small-Signal Analysis of the Nonlinear Acoustic Behavior of Vented Vessels

R. Brunnader and G. Holler

Abstract Pneumatic volume gauging offers many advantages in comparison to traditional fill-level measurement principles (e.g. tank shape, orientation of the tank and non-uniform surface structure of the fill material do not influence the result). Unfortunately, classical pneumatic volume gauging approaches work well for sealed tanks, but not for vented tanks. This major drawback of pneumatic methods is considered in recent work by using an electroacoustic model to describe the tank system. The electroacoustic model approach takes lumped elements to model the acoustic behaviour of the system. These lumped elements may be assumed independent from pressure and frequency yielding a linearized system model, or can be modelled as pressure- or frequency-dependent properties to better represent the nonlinear behaviour of the vented tank system as indicated by practical measurements. To assess both the applicability of linearized system approaches as well as the origin of the nonlinearity of real systems, a small-signal analysis of a sample tank system was carried out. Results of this analysis are shown in this article, accompanied by theoretical considerations that indicate the flow resistance of the ventilation as a possible cause of the nonlinear behaviour.

Keywords Acoustic measurement · Fill-level-measurement · Nonlinear behavior · Small-signal analysis · Gas flow resistance

1 Introduction

The vast majority of industrial production processes requires storage tanks for liquid and/or powdered materials in which raw materials or the actual product is stored. Monitoring the effective amount of material inside those tanks is an

R. Brunnader (✉) · G. Holler
Institute of Electrical Measurement and Measurement Signal Processing,
Graz University of Technology, Graz, Austria
e-mail: rudolf.brunnader@tugraz.at

A. Mason et al. (eds.), *Sensing Technology: Current Status and Future Trends I*,
Smart Sensors, Measurement and Instrumentation 7, DOI: 10.1007/978-3-319-02318-2_5,

essential key for the automation of the process and must be performed over a wide measurement range with sufficient accuracy. Besides the well-known measurement principles using the filling height [1], also principles based on the free volume inside the vessel can be used. One of these volume-based principles is pneumatic volume gauging. It uses the information received from the system during a periodic pressure excitation of the gaseous part of the vessel. Previous publications show the usability of the pneumatic volume gauging for fill-level applications for closed vessels [2–5]. Unfortunately, many storage tanks are ventilated. Therefore, the measurement principle must be extended to be applicable to non-sealed (vented) vessels. Evaluation measurements to assess the possibility of applying the pneumatic method to vented vessels were done in [6, 7]. The approach in these investigations uses a generalized model that considers the effect of small ventilation holes. The obtained results are promising, but also show limitations (splitting of the free gaseous volume, resonance effects) [8]. Beside these limitations also a nonlinear behavior of the system was observed [9]. This nonlinear behavior will be depicted in the following sections.

2 Electroacoustic Equivalent Circuit

To apply the pneumatic volume gauging for a vented vessel system the vented vessel is modeled by an electroacoustic equivalent circuit. For the electroacoustic equivalent circuit two analogies are postulated, namely the pU-analogy and the pI-analogy, depending on the linked physical variables [10]. For this work the pI-analogy is used to describe the acoustic elements.

2.1 Electroacoustic Elements

In the pI-analogy the pressure p is related to the flux dimension and the volume velocity q is related to the potential dimension. Therefore, the electroacoustic elements are related to the physical behavior as follows [10, 11].

2.1.1 Inductance

In the pI-analogy the inductance represents the reciprocal of the acoustic stiffness s_a of a cavity.

$$L \propto \frac{1}{s_a} \tag{1}$$

For a small dimension of the cavity (compared to the acoustic wavelength) and minor pressure variations ($\Delta p \ll p_0$), the acoustic stiffness can be calculated from the linearized Poisson equation, resulting in:

$$s_a = \frac{\kappa \cdot p_0}{V_0} \tag{2}$$

Thus, the acoustic stiffness is inversely proportional to the cavity volume V_0. With the knowledge of the value of the polytropic exponent κ and the static pressure p_0 the free volume of the cavity can be calculated from the acoustic stiffness and the inductance, respectively.

2.1.2 Capacitance

The capacitance represents the acoustic mass m_a in the pI-analogy:

$$C \propto m_a \tag{3}$$

The acoustic mass is defined as:

$$m_a = \frac{m_{hole}}{A_{hole}^2} \tag{4}$$

with m_{hole} representing the gas mass enclosed in a tube and A_{hole} representing the cross-sectional area of the tube. This relationship is valid for a small dimension of the tube (cross-section and length) compared to the acoustic wavelength.

2.1.3 Resistance

The acoustic resistance represents the losses of the system (e.g. pressure drop inside a capillary tube due to the flow velocity) and the acoustic radiation, respectively. In the pI-analogy the shown resistances are inversely proportional to the acoustic resistances, and therefore represent acoustic conductances:

$$R \propto \frac{1}{R_a} \tag{5}$$

Three effects must be considered regarding the acoustic resistances. First, the acoustic resistance resulting from the acoustic radiation must be considered only if the wavelength is short compared to the dimension of the acoustic element. Second, resulting from the air mass, each acoustic resistance has an acoustical mass in addition to the effective resistance. Consequently, every tube acts as combination of acoustic resistance and acoustic mass. Depending on the dimensions of the acoustic element it acts more than an acoustic resistance or an acoustic mass. E.g. in case of a long, small tube (like a capillary tube), the value of the acoustic resistance is much higher than the value of the acoustic mass.

But generally, every tube must be assumed as an acoustic resistance and an acoustic mass. Third, the acoustic resistance is constant for a linear flow condition inside the acoustic element (tube) only. Unfortunately, at higher flow velocities a linear model is not valid. Section 2.2 focuses on this issue from a theoretical point of view.

2.2 Theoretical Considerations Regarding the Nonlinear Behavior

As mentioned above, the acoustic behavior of a system can described with lumped elements. This description is only valid for systems with geometric dimensions that are small compared to the wavelength of the excitation signal. For the pneumatic volume gauging method this condition holds for almost every vessel, since the excitation signal wavelength varies between 114.3 and 9.5 m (equates to 3 and 36 Hz). With this constraint the acoustic stiffness and the acoustic mass can be assumed constant. Also the acoustic resistance based on the acoustic radiation can be neglected due to the low frequencies used. Therefore, the nonlinear behavior of the system should originate from the acoustic resistance related to the pressure drop caused by the gas flow that is driven by pressure variations induced to the system.

Figure 1 shows the so-called Moody diagram that plots the friction factor λ in relationship to the Reynolds number of the flow. The Reynolds number (Re) is a parameter that provides a measure for the characterization of the flow regime: Typically, the transition between laminar and turbulent flow starts at a Reynolds number of approx. 2,300. The transition region typically passes to Reynolds numbers up to approx. 10,000, above these values only turbulent flow is observed. In all regions, the pressure drop can be written as [12]:

$$\Delta p = \frac{\rho \cdot v^2}{2} \cdot \left(\lambda \cdot \frac{l}{d} + \sum \zeta_i \right) \tag{6}$$

With ρ denoting the flow medium density, v the mean flow velocity, λ the friction factor, l the length of the tube, d the diameter of the tube, and ζ the pressure loss coefficient. ζ can be neglected since this parameter describes losses by reason of valves, tube diameter changes or sharp bends, which are not applicable for our setup. With this simplification (6) reduces to:

$$\Delta p = \frac{\rho \cdot l}{2 \cdot d} \cdot \lambda \cdot v^2 \tag{7}$$

The pressure drop depends on the flowing medium, the geometry of the tube, the friction factor and the square mean flow velocity, respectively. At low Reynolds numbers (left side of Fig. 1) the Hagen-Poiseuille equation is valid. For higher Reynolds numbers, approximation formulae by Colebrook (including the

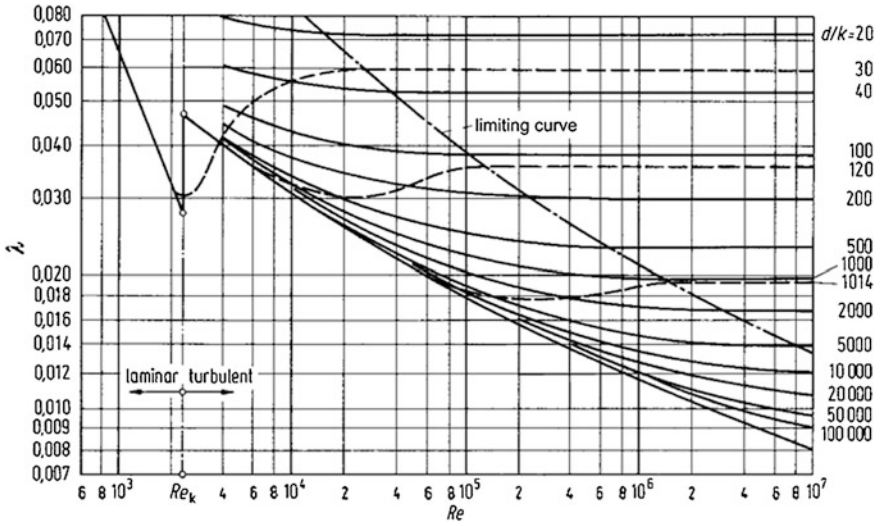

Fig. 1 Moody diagram showing the changes of the friction factor with respect to the reynolds number; the *dashed line* represents approximation by Nikuradse, while *solid lines* depict formula by Hagen-Poiseuille (*laminar region*) and Colebrook (*tubulent region*) [12]

transition region) and Nikuradse (constant friction factor in turbulent region) are applied [12].

2.2.1 Laminar Flow Region

For a laminar gas flow inside a tube the acoustic resistance can be calculated using the Hagen-Poiseuille approximation:

$$R_a = \frac{8 \cdot \eta \cdot l}{\pi \cdot r^4} \tag{8}$$

where η represents the dynamic viscosity, and l and r denote the length and radius of the tube, respectively. Hence, that the acoustic resistance is constant for laminar gas flow inside the tube. In this case the acoustic resistance can be modeled as a lumped element with a constant (frequency and pressure independent) value. Therefore, it is a linear element.

2.2.2 Transition region

Although in this region the behavior of the flow is ambiguous, the Moody diagram (Fig. 1) indicates an increase of the friction factor. Assuming a linear increase of the friction factor in the transition region, the pressure drop can be written as:

$$\Delta p \propto \frac{\rho \cdot l}{2 \cdot d} \cdot \mathrm{Re} \cdot v^2 \tag{9}$$

Considering the definition of the Reynolds number this yields:

$$\Delta p \propto \frac{\rho^2 \cdot l}{2 \cdot \eta} \cdot v^3 \tag{10}$$

With relation to the electroacoustic model for the vessel system, one has to take into account the definition of the acoustic impedance:

$$\underline{Z}_a = \frac{\underline{p}}{\underline{q}} \tag{11}$$

With:

$$\underline{q} = \underline{v} \cdot A \tag{12}$$

where q denotes the volume velocity and A the tube cross-sectional area. This reveals the quadratic relationship between acoustic resistance and volume velocity of the flow:

$$R_a \propto \frac{\rho^2 \cdot l}{2 \cdot \eta \cdot \pi^2 \cdot r^4} \cdot q^2 \tag{13}$$

This results in a nonlinear behavior of the tank system in this region.

2.2.3 Turbulent Flow Region

In the turbulent flow region the friction factor λ becomes constant for higher Reynolds numbers (depending on the surface roughness). In this region the pressure drop can be written as

$$\Delta p = \frac{\rho \cdot l}{2 \cdot d} \cdot \lambda_{const} \cdot v^2 \tag{14}$$

Therefore the acoustic resistance will be

$$R_a \propto \frac{\rho^2 \cdot l \cdot \lambda_{const}}{4 \cdot \pi \cdot r^3} \cdot q \tag{15}$$

As for the transition region, the non-constant acoustic resistance results in a nonlinear behavior. Hence, the varying acoustic resistance will cause nonlinear effects if the volume velocity exceeds a certain value with respect to the geometric dimensions (described by the Reynolds number).

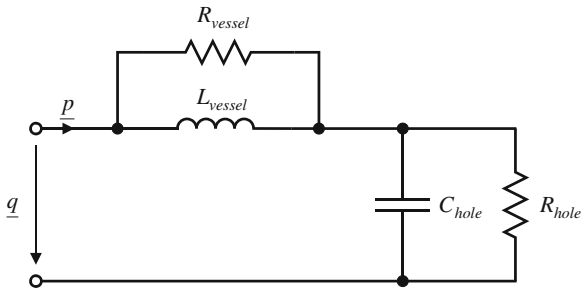

Fig. 2 Equivalent circuit model of a damped Helmholtz resonator (pI-analogy) [10]

2.3 Electroacoustic Model of the Vented Vessel System

With the electroacoustic elements defined in Sect. 2.1 and the considerations in Sect. 2.2 the vented vessel system can be modeled. Figure 2 depicts the electroacoustic equivalent circuit of the vented vessel system. Herein the inductance L_{vessel} represents the free gaseous volume of the vessel and the capacitance C_{hole} represents the ventilation of the vessel, respectively. The corresponding losses are represented by the resistances R_{vessel} and R_{hole}. Considering the low excitation frequency and the dimension of the vented vessel system, the acoustic resistance of the acoustic radiation is negligible. Therefore, the acoustic resistance is only related to the friction losses of the gas flow.

The topology of the obtained network equates to a damped Helmholtz resonator [10]. Therefore, on one hand the measured complex acoustic admittance of the vented vessel system should change with signal frequency. On the other hand, all electroacoustic elements of the model are constant. Hence, the modeled system should have a linear behavior. Practical measurements were done with different ventilated vessel systems [8, 13] showing that this expected behavior is valid for particular constraints. Beside the constraints that the free gaseous volume must not be distributed and the measurement frequency range must be free of resonances, respectively, also the amplitude of the pressure variation must be fixed to a constant value to avoid measurement errors. This necessity of the pressure variation regulation indicates a nonlinear behavior. To investigate this issue several measurement results are presented below.

3 Measurements

As depicted in Sect. 2.2, a nonlinear behavior can be caused by the acoustic resistances, if the gas flow is not in the laminar state. Since the pressure difference between the inside and the outside of the vented vessel system determine the gas flow condition, this pressure difference constitutes the overall behavior of the vented vessel system. Also, the artificially introduced pressure variations can be considered as periodic pressure differences. Therefore, the amplitude of the pressure variations influences the state and behavior of the vented vessel system.

To avoid this effect the pressure variation amplitude can be fixed to a constant value to ensure that the system behavior for particular measurements does not change significantly (this approach was taken during measurements published earlier, e.g. in [8]). The underlying article investigates the influence of the pressure variations on the overall system behavior by employing a small-signal analysis for a set of different operating conditions.

3.1 Measurement Setup

To investigate the influence of the artificially induced pressure variation amplitude Δp to the measured acoustic admittance, the measurement setup from [6–9, 13] was modified slightly.

The aim of the modification is to render possible conducting a small-signal analysis at different gas flow conditions on the vented vessel system. Therefore, via a pressure regulation vale a constant over pressure is generated in the vented vessel system. This over pressure p_{offset} causes a constant gas flow in the vessel and in the ventilation hole, respectively. To obtain different gas flow velocities (flow conditions) the offset pressure is adjusted to predefined values. An additional sensor is applied to the vented vessel to monitor the value of the offset pressure. Figure 3 shows the schematic block diagram of the modified measurement setup. The measurement setup consists of the following main parts:

- An electrodynamic loudspeaker (EDL) inducing the pressure variation (Δp),
- Sensors for detecting the caused volume variation, pressure variation (pressure variation amplitude), offset pressure and the atmospheric pressure,
- Sensor signal preamplifiers, an amplifier for the EDL, A/D and D/A-converters, and
- A computer calculating the acoustic admittance from these values.

With this setup a series of measurements is done. First, the nonlinearity is shown in the time and frequency domain: The time series of the measured pressure variation Δp in relation to the time series of the measured volume velocity q is plotted to show the non-linear behavior in the time domain. To depict the nonlinear behavior in the frequency domain, absolute value and phase angle of the acoustic admittance are plotted as a function of excitation frequency for different pressure variation amplitudes Δp.

Finally, results of the small-signal analysis are shown. Therefore the vented vessel is excited with defined small pressure variation amplitudes at predefined offset pressure values. The resulting acoustic admittance values are plotted in the time domain. All measurements are carried out using sinusoidal pressure variation signals with predefined frequencies (stepped sine excitation).

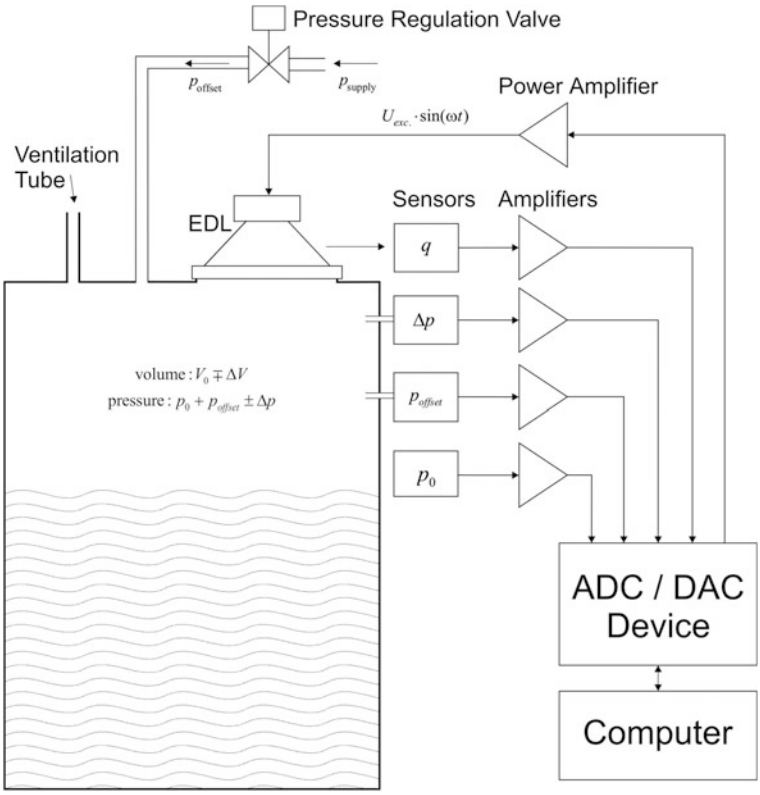

Fig. 3 Block diagram of the measurement setup

3.2 Measurement Results

To depict the influence of the pressure variation amplitude to the vented vessel system, measurements in the time and frequency domain are shown first. These measurements contain results of the vented vessel system at varying pressure variation amplitudes Δp, using the measurement setup as shown in Fig. 3 without applying an offset pressure to the vented vessel system.

3.2.1 p-q-Diagram

To show the nonlinear behavior of the vented vessel system, a p-q-diagram is used. In this diagram the corresponding pairs of pressure variation amplitude values and volume velocity values are plotted. It can be seen from the equivalent circuit model (Fig. 2) that these signals represent the flux dimension and the potential dimension, respectively. Hence, the pressure variation amplitude and the volume velocity correlate and can be used to describe the behavior of the electroacoustic

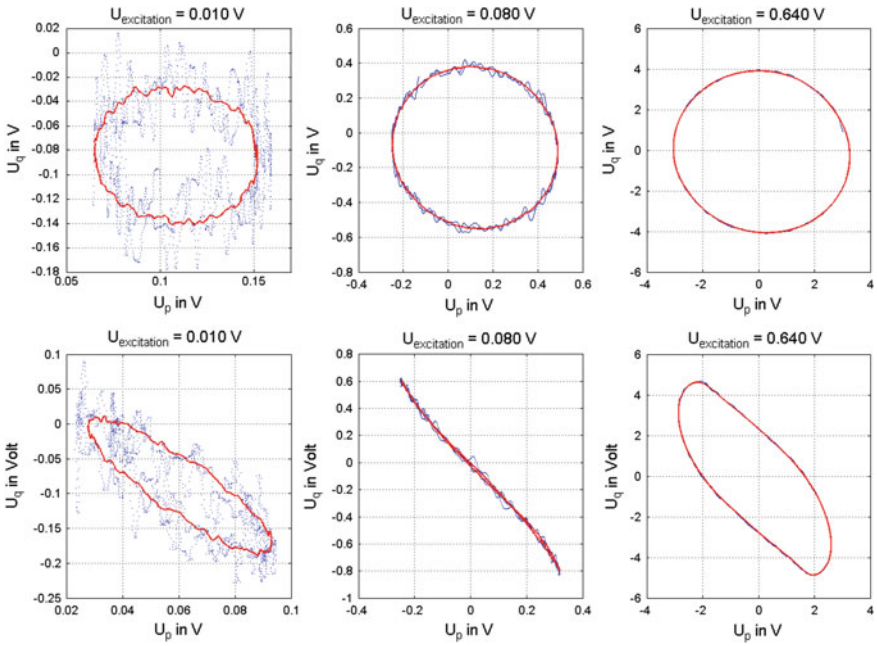

Fig. 4 p-q-diagrams relating the voltage of the differential pressure (Δp) sensor to the volume velocity (q) sensor signal for different excitation levels. *Upper row* closed vessel; *Lower row* ventilated vessel

model. Since any excitation can be assumed as a linear combination of basic excitations, the p-q-diagram of a linear system looks similar for all excitation levels. In contrast, the appearance of the diagrams typically varies for a nonlinear system (e.g. as a function of the amplitude). Consequently, it should be easy to detect if there is a nonlinear behavior of the system under investigation.

Two cases are investigated:

- For the first configuration the vessel is closed (all ventilation holes are sealed).
- The second configuration deals with a ventilated vessel.

In both cases the electrodynamic loudspeaker (EDL) is excited with a sinusoidal signal at a defined frequency using a set of different excitation amplitudes. This results in a set of measurements with varying pressure variation amplitudes for the defined excitation frequency. The excitation frequency is chosen well below the theoretical resonance frequency of the vented vessel system to maximize the influence of the ventilation hole. In Fig. 4 the time series of the measured signals are plotted, depicting the measurement results for the ventilated and the closed vessel setup. For the diagram the voltage from the differential pressure sensor and the volume velocity sensor are used directly without scaling. The blue crosses represent measurement values acquired during two periods of the

excitation signal. The red line is the result of averaging the measurement values over 100 periods. For each setup the measurements were done for three different excitation levels.

The first row of diagrams in Fig. 4 shows the closed vessel setup. In this case, C_{hole} and R_{hole} are shortened in the equivalent circuit. Only L_{vessel} and R_{vessel} remain. Hence, the acoustic system should behave like a lossy inductance. In the p-q-diagram this behavior should be depicted by an ellipse. Assuming a linear system, amplitude variations of the excitation signal should not change the shape. This is apparently true for the first row of diagrams. Despite the higher noise level at low frequencies, the plots show similar behavior for the different excitation levels. Hence, the system seems to be linear.

For the vented vessel setup the equivalent circuit contains all elements shown in Fig. 2. Since the equivalent circuit is still a linear model, the p-q-diagram should maintain its elliptical shape and should not change for different amplitudes. However, from the measured

p-q-diagrams for the vented case (shown in the second row of Fig. 4) it can be seen that there is a major change in the shape.

Two effects can be observed:

- First, the shape of the major axis changes from a straight line to a sigmoid function.
- Second, the ratio between major axis and minor axis changes.

Both effects can be related to the nonlinearity of the system:

The shape change (sigmoid function) indicates the creation of higher harmonics due to the nonlinearity of the vented vessel system. As described in Sect. 2.2, this nonlinear behavior could be caused by the acoustic resistances. Since the shape change is observed only for the vented vessel system, the nonlinearity can be attributed to the acoustic resistance of the ventilation hole. Given that this effect appears at higher excitation amplitudes, which induce higher pressure differences on the ventilation holes, it can be related to a change from laminar to turbulent gas flow in the ventilation hole.

The change in axis ratio corresponds to a change in the phase shift between the two signals. This change can be interpreted as a change of the linearized transfer function (pressure variation related to the excitation signal) in the chosen operating point. Given that the change is mainly related to the acoustic resistances (i.e. losses), the excitation amplitude primarily affects the damping of the system. This corresponds to the fact that a higher gas flow causes a disproportionately higher pressure drop inside the ventilation hole, which results in a higher acoustic resistance. Whereas the first effect cannot be detected by the fundamental harmonic analysis in the frequency domain, the second effect should be observable with this analysis as well.

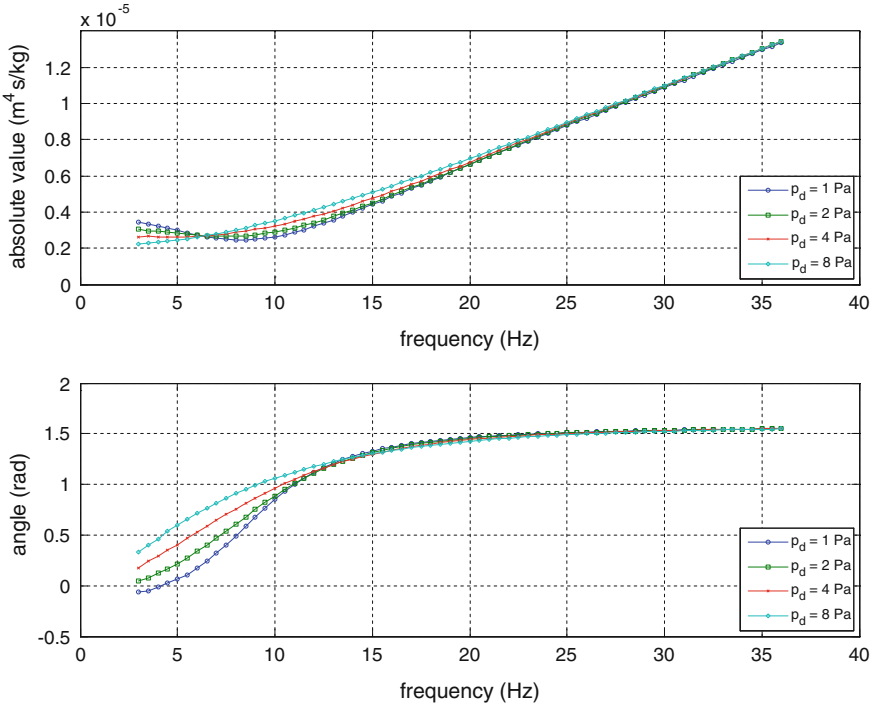

Fig 5 Absolute value and phase angle of the acoustic admittance for a vented vessel at different pressure variation amplitudes Δp

3.2.2 Analysis of the Fundamental Harmonic at Different Pressure Amplitudes

As mentioned above, the fundamental harmonic of each measurement frequency should also indicate the nonlinearity of the vented vessel system. To demonstrate this, Fig. 5 shows the acoustic admittance in the frequency domain (absolute value and phase angle) for a series of measurements. The values are calculated from the fundamental harmonic of the measured signals (i.e. the higher harmonics due to the nonlinear behavior are not considered). For all depicted measurements the same setup of the vented vessel (i.e. constant fill level and ventilation configuration) was used, only the amplitude of the pressure variations Δp was altered. Figure 5 demonstrates that the frequency response of the acoustic admittance strongly depends on the chosen pressure variation amplitude: Low pressure variations yield a clear resonance minimum, whereas higher pressure variation amplitudes result in stronger damped frequency responses (without well-defined minima). Hence, the analysis of the fundamental harmonic indicates that the basic principles defining a linear system (homogeneity and additivity) are not valid. Therefore, the nonlinearity of the system should be considered when applying a fundamental harmonic analysis. In practice, two approaches can be derived from this behavior: The amplitude dependency has to

be considered in the system model, or the system has to be analyzed using a predefined pressure variation amplitude that is not changed in between two measurements, as carried out in prior measurements.

3.2.3 Small-Signal Analysis

As depicted in Fig. 5, the vented vessel system behavior changes with altered pressure variation amplitude Δp. This behavior can be caused by the changing gas flow conditions inside the ventilation hole (compare Sect. 2.2). To investigate this effect, a small-signal analysis is applied to the vented vessel system.

The small-signal analysis is a widely-used method to analyze the behavior of systems for different operating states. In small-signal analysis the system is excited with a low-amplitude signal in addition to a constant offset signal that defines the actual "operating point" of the system [14, 15]. As a result, the dynamic small-signal behavior of the system is obtained for this operating point. Mathematically the small-signal analysis exploits the fact that higher order derivatives from the Taylor-Series can be neglected for small signals (i.e. close to the expansion point of the series) [16, 17]. For the vented vessel system, the operating point is defined by the gas flow condition inside the vessel and the ventilation hole, respectively. For the small signal, a harmonic sinusoidal pressure variation is applied (1 Pa peak amplitude) for all measurements. To change the gas flow condition inside the ventilation hole, the static pressure inside the vented vessel is altered. As explained in Sect. 3.1 this is done using a pressure regulation valve. As a result of the introduced offset pressure a constant gas flow arises through the ventilation hole. In a linear system this constant gas flow can be seen as an offset value and wouldn't cause any change in the behavior of the system. If there is a dependency between system behavior and gas flow condition, as indicated by the measurement results shown in Fig. 5, the system behavior should be changed depending on the amplitude of the constant gas flow.

Figure 6 depicts the results of the small-signal analysis of the vented vessel system. Similar to the results from the fundamental harmonic analysis, the system behavior of the vented vessel changes depending on the offset pressure p_{offset}. Obviously, the damping of the system is influenced by the offset pressure. Therefore the small-signal analysis confirms that the acoustic resistances of the vented vessel system change with the pressure difference between the inside and the outside of the vessel. As observed in the p-q-diagrams, the closed vessel does not change the behavior. This implies, that the nonlinear behavior is related to the acoustic resistance of the ventilation hole R_{hole}. Possibly, it can be explained by the comparatively large cross section area inside the vessel. This large cross section area yields to a low gas flow velocity inside the vessel for all measurement conditions. Therefore, the acoustic resistance R_{vessel} is not changed significantly (compare Sect. 2.2). In contrast, the small diameter of the ventilation hole leads to higher flow velocities and non-laminar flow conditions even for comparably low offset pressure values. Hence, the value of the acoustic resistance of the ventilation hole R_{hole} is a function of the

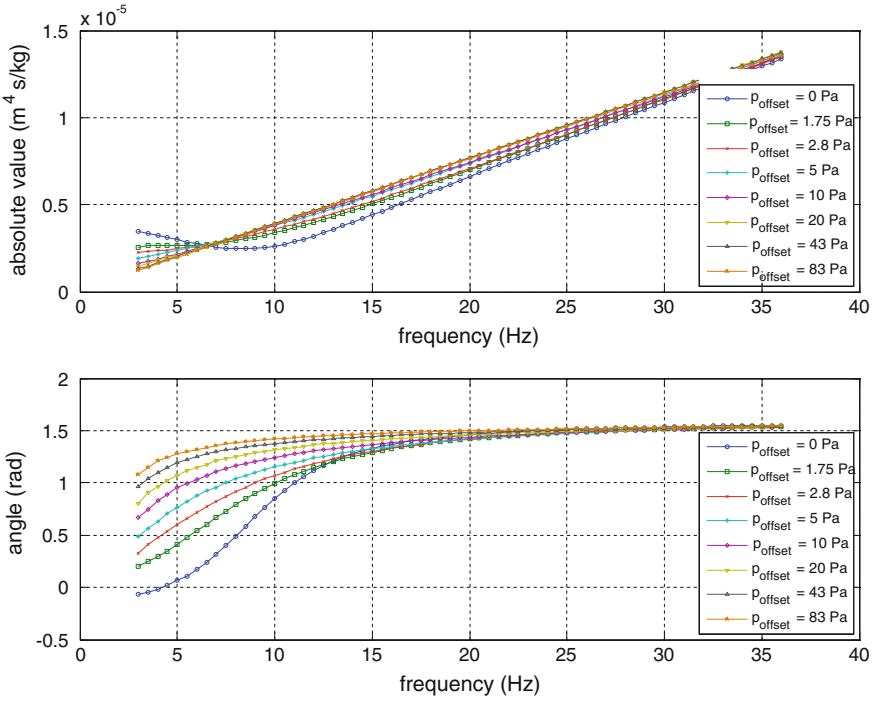

Fig. 6 Absolute value and phase angle of the acoustic admittance for a vented vessel at several offset pressure amplitudes p_{offset}. The pressure variation Δp has an amplitude of 1 Pa

offset pressure. This argumentation is in accordance with the results of the fundamental harmonic analysis, because the pressure variation can also be considered as a periodic offset pressure. Consequently, the acoustic resistance R_{hole} must be considered as a nonlinear element in the case that there appears a turbulent flow condition inside the ventilation hole. As observable in Fig. 6 this nonlinear behavior appears already for small values of the offset pressure, which implies that turbulent gas flow is encountered in the ventilation hole in most cases.

4 Conclusions

The article addresses the nonlinear behavior of pneumatic gauging methods that was observed in previous work related to pneumatic gauging of vented vessel systems. It shows the nonlinear acoustic behavior of a vented vessel system in case of higher pressure variation amplitudes. By theoretical considerations it is shown that the nonlinear acoustic behavior can be related to the acoustic resistance of the ventilation hole. Measurements confirm the theoretical considerations and depict the nonlinear behavior.

As a result of these investigations, strategies for treating nonlinear system behavior in practical measurements will be developed and the selection of an optimum excitation level will be assessed. This optimum excitation level should maximize the signal to noise ratio of the measured signals under consideration of the nonlinear behavior at higher excitation levels. Hence, this will minimize the measurement uncertainty of the pneumatic volume gauging method for the linear model approach.

References

1. G. Vass, The principle of level measurement, Sensors Magazine, no. 17 (2000)
2. http://www.sensorsmag.com/sensors/article/ArticleDetail.jsp?id=328310
3. K. Watanabe, Y. Takebayashi, Volume measurement of liquid in a deformed tank—application to the fuel meter of automobiles. SAE Trans. 871964, October 1987
4. K. Watanabe, Y. Takebayashi, D.M. Himmelblau, Volume measurement of deformed materials in tanks. ISA Trans. **27**(4), 9–19 (1988)
5. H. Kobayashi, K. Watanabe, E. Kawa, Y.S. Chen, and H. Ishizuka, Gauging fuel in deformed tanks by pneumatic methods—application to automobile Fuel Gauges. SAE Trans. 900467, February 1990
6. G. Holler, R. Brunnader, B. Schweighofer, H. Wegleiter, Experimental assessment of a pneumatic level-sensing method for closed tanks applied to water and wooden pellets. Sens. Transducers J. **9**(12/10), 151–160 (2010)
7. R. Brunnader, G. Holler,G. Brasseur, Model verification and parameter evaluation for a pneumatic gauging method for vented tanks. in *Instrumentation and Measurement Technology Conference (I2MTC)*, Hangzhou, pp. 1–6 (2011)
8. R. Brunnader, G. Holler, Experimental validation of a leakage and fill-level estimation method for vented tanks, in *5th International Conference on Sensing Technology*, Palmerston North, New Zealand (2011)
9. R. Brunnader, G. Holler, Applicability evaluation of the pneumatic gauging method for automotive fuel tanks, in *Proceedings IEEE International Instrumentation and Measurement Technology Conference* (I2MTC 2012), Graz, Austria, pp. 833–838 (2012)
10. R. Brunnader, G. Holler, Nonlinear acoustic behavior of vented vessels in reference to pneumatic volume gauging, in *Sixth International Conference on Sensing Technology (ICST)*, Kolkata, India, pp. 527–532 (2012)
11. R. Lerch, G.M. Sessler, D. Wolf, *Elektromechanische Analogien* (in Technische Akustik, Springer Verlag, Berlin, 2009)
12. L.E. Kinsler, A.R. Frey, *Fundamentals of Acoustics*, 2nd edn. (Wiley, New York, 1962)
13. K.-H. Grote, J. Feldhusen, Dubbel-Taschenbuch für den Maschinenbau, 22nd end. Springer, Berlin
14. R. Brunnader, G. Holler, Experimental validation of a leakage and fill-level estimation method for vented tanks, in *Proceedings 5th International Conference on Sensing Technology*, Palmerston North, New Zealand, pp. 395–398 (2011)
15. P. Horowitz, W. Hill, *The Art of Electronics*, 2nd edn. (Cambridge University Press, USA, 1989)
16. U. Tietze, C. Schenk, *Halbleiter-Schaltungstechnik*, 11th edn. (Springer, Berlin, 1999)
17. E. Kreyszig, *Advanced Engineering Mathematics*, 4th edn. (John Wiley & Sons, USA, 1979)
18. A. Gelb, Wallace E. Vander Velde, *Multiple-input describing functions and nonlinear system design*. McGraw-Hill, USA, (1968)

Chapter 6
Flexible Electromagnetic Wave Sensors for Real-Time Assessment of Water Contaminants

O. Korostynska, A. Mason and A. I. Al-Shamma'a

Abstract The implementation of The European Water Framework Directive has triggered the need for new methods and systems which enable the monitoring of chemical and biological pollutants in real time. A paradigm shift in water purification is proposed by rethinking the distribution strategy at point-of-use and developing decentralized purification methodology based on region specific contaminants. To achieve this, specific metering, intelligent monitoring and control techniques are needed that would form part of intelligent building systems monitoring and feedback methods to enable improved operation and feedback at the design and construction process. The aim of this book chapter is to report on the development of a novel proof-of-concept type sensor for real-time monitoring of water composition. In particular, the change in the electromagnetic wave signal in microwave frequency range is used as an indicator of water purity. The sensing element was designed on a flexible substrate to provide for a long-term usage since this configuration is less prone to failure due to mechanical damage. This allows for a broad range of applications where a sensor could be mounted on any curved surface or even just placed bended in a tube or water pipe. Silver metal patterns in various configurations printed on this substrate acted as a sensor head. The developed system confirmed the viability of using microwaves for real-time water contaminants monitoring as the corresponding spectra for air, deionized and tap water were unique and clearly depicted a shift in the resonant frequencies of the sensor when it was placed in contact with water samples.

Keywords Water monitoring · Real-time analysis · Microwave sensor · Flexible substrate · Silver interdigitated pattern

O. Korostynska · A. Mason (✉) · A. I. Al-Shamma'a
Built Environment and Sustainable Technologies (BEST) Research Institute,
Liverpool John Moores University, Byrom Street, Liverpool L33AF, UK
e-mail: A.Mason1@ljmu.ac.uk

A. Mason et al. (eds.), *Sensing Technology: Current Status and Future Trends I*,
Smart Sensors, Measurement and Instrumentation 7, DOI: 10.1007/978-3-319-02318-2_6,

1 Introduction

Domestic user of drinking water in the UK, across the Europe and increasingly all over the world perceive that the water from the tap is safe and meets both health quality standards [1] and aesthetic requirements such as color, turbidity, taste and odor. It is expected as an unspoken rule that the water supply companies do all the necessary steps to clean the wastewater from all known chemicals and contaminants, which could harm humans and animals. However, with the continuous industrial developments, depleting natural water resources, increasing population and corresponding increased demand on domestic and industrial water consumption, it is becoming more and more challenging for the water supply industry to maintain the safety of water [2]. This includes the untreated and treated wastewater from sewerage systems, agricultural sources such as fertilizers and animal waste [3].

Processing wastewater is a highly regulated process, but it also continuously changes to anticipate the emerging and possible unknown water contaminants. In daily use there are up to 70,000 known [4] and emerging [5, 6] chemicals that might be present in various water resources, including for drinking water production [7].

Water distribution systems are vulnerable to intentional and inadvertent contamination. The implementation of The European Water Framework Directive has triggered the need for new methods and systems which enable the monitoring of chemical and biological pollutants in real time. The Environment Agency in England and Wales is responsible for applying the European communities' regulations by maintaining or improving the quality of fresh, marine, surface and underground water.

Water quality standards for different types of water sources (lakes, rivers or oceans) vary due to different intended human use and their ecosystems or environmental conditions. Thus, monitoring of their contents must also vary dependent on the situation.

Wastewater also carries such micropollutants as pharmaceuticals and hormonally active substances [8]. So far, there is little scientific evidence as to the detrimental effects of these compounds on aquatic organisms and the quality of water for drinking [9]. However, as these compounds are considered to be harmful, approaches for the removal of micropollutants from wastewater have been developed either at the source or using new end-of-pipe technology [10]. The chemical and pharmaceutical industry is becoming progressively more aware of environmental problems and has an increased interest in novel real-time water pollutants monitoring systems. Notably, most of pharmaceuticals compounds are not routinely monitored in drinking, surface or wastewater, although a large numbers of compounds were detected when such tests were conducted [10].

There are numerous occasions all over the world when industrial activity results in unpredicted water pollution events with irreversible harmful consequences that affect both the nature and habitat. For example, the operation of Harbin Pharmaceutical Group, a major pharmaceutical company in northeast China's

Heilongjiang Province that specializes in antibiotics, has caused a recent pollution scandal, where waste gases and water that exceeded legal pollution limits were released into the environment by Harbin [11].

Another group of human waste contaminants consists of pesticides, which are usually washed with surface water from agricultural regions [12]. There are also various toxic compounds generated by microorganisms (e.g. microcystins) or multicellular organisms existing in the water. In all developed countries there is defined legislation and regulatory authorities enforcing maximal residual levels of the various contaminants. Microcystins that result from the blooming of toxigenic cyanobacteria [13] can cause severe poisoning episodes in animals and humans when present in drinking water in sufficiently high concentration.

Water quality assessments are based on the analysis of the physical, chemical and bacteriological parameters and require customized apparatus and trained staff. Environmental water monitoring includes measurements of physical characteristics (e.g. pH, temperature, conductivity), chemical parameters (e.g. oxygen, alkalinity, nitrogen and phosphorus compounds), and abundance of certain biological taxa. Monitoring could also include assays of biological activity such as alkaline phosphatase, tests for toxins and direct measurements of pollutants such as heavy metals or hydrocarbons [12]. The presence of nutrients and heavy metals in water is a serious threat to human health.

It is firmly established that the main way that nitrate gets into groundwater is from cattle urine patches. The amount of nitrogen in a cow urine patch is many times that required for pasture growth, and the excess moves down through the soil. Acid rain additionally contributes to the pollution of the water sources, as schematically illustrated in Fig. 1.

Traditional methods of water quality control are lab based and include standard UV–Vis measurements, ion-sensitive electrodes and amperometric sensors. On the other hand, a range of modern real-time monitoring approaches exists, for example fiber-optic sensors, lab-on-chip sensors and biosensors.

Generally speaking, no single system available today can fully address the needs of the customers, i.e. industries and regulatory authorities, in its ability to determine on-spot, in real time, the composition of water to the desired sensitivity level, bearing in mind the desire for system portability and cost-effectiveness.

Therefore, novel real-time monitoring techniques are necessary and they must detect the excess of pollutants established by the official water quality regulations. This requires very sensitive measuring techniques as standards are often close to the current technological limits of detection, e.g. the EU pesticide standard of 0.1 μg/L [1]. One such technique potentially capable to meet the demand for safe water is the used of the electromagnetic wave sensor.

To assure the safety of water and to assist in preventing spreading of contamination, specific sensors need to be present at major points of water use and redistribution to assist in smart water source management, as suggest in Fig. 2.

Thus, continuous real-time water pollutants monitoring system is required at every vital step of water distribution and consumption. It is both economically and strategically more efficient to prevent contaminated water to enter into the water

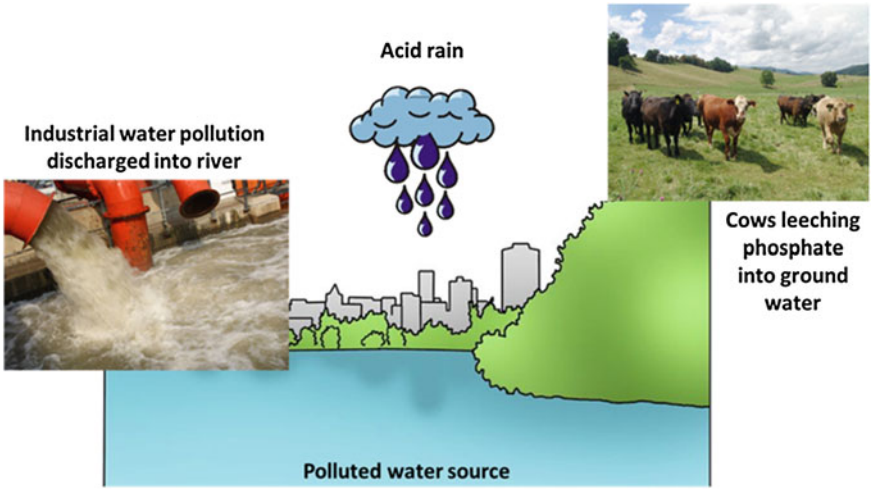

Fig. 1 Sources of water pollution that need continuous quality monitoring

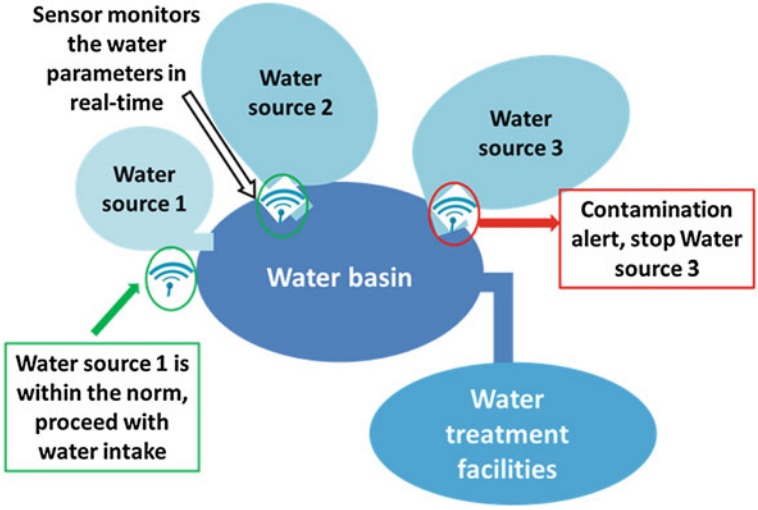

Fig. 2 Concept of water source management based on real-time measurements of water parameters

basin in the first place, rather than to collect all types of water and then treat it in water treatment facilities. Water generated from domestic activities such as laundry, dishwashing, and bathing, also called grey water, can be recycled on-site for uses such as landscape irrigation and constructed wetlands. Most grey water is relatively easy to treat and recycle because of lower levels of contaminants. If collected using a separate plumbing system after a number of filtration stages, domestic grey water

can be recycled directly within the home, garden or company and used either immediately for washing or flushing toilets, or processed and stored for later use.

This approach of source water management is viable at both domestic consumption level, where mini-treatment facilities can be installed locally, and at industrial scale. To achieve this, specific metering, intelligent monitoring and control techniques are needed that would form part of intelligent building systems monitoring and feedback methods to enable improved operation and feedback at the design, construction and maintenance stages.

Based on the review of the current methods of water quality monitoring, one may firmly conclude that most methods are lab based and as such are inadequate for a task of real-time monitoring. Those that can operate on-site normally require specific chemicals which in turn add to the problem of water pollution. Accordingly, the researchers at Liverpool John Moores University have developed a novel concept for in situ monitoring of water contamination in domestic and industrial settings that is based on real-time microwave sensing technique [12, 14–16]. The principle of sensing using microwaves is based on the fact that an object under test interacts with the electromagnetic waves in a unique manner, which can be specifically correlated with the composition of the tested water.

It should be acknowledged that the attempts to use the electromagnetic sensing as a method for the detection of nitrates and contamination in natural water sources have been recently reported [17], where sensors based on the combination of planar meander and interdigitated electromagnetic structure were used. The meander sensors part consisted of two coils. The exciting coil was driven by high-frequency sinusoidal current to create a high-frequency magnetic field. To increase the magnetic field strength, the number of meander turns was increased by introducing several spiral rectangular turns toward the inner section. When this sensor was placed near a material, an electromagnetic field was induced on it, which modified the created field, and the sensing coil, placed above the exciting coil, was used to pick up the resultant field. The operating principle behind the interdigitated sensor is as follows [17]. The positive electrodes are driven by an AC electric potential (same source as the meander) to create an AC electric field between the positive and negative electrodes. These fields pass through material under test; thus, material dielectric properties as well as the electrode and material property affect the capacitance and the conductance between the two electrodes. The meander type of coil was connected in series with the interdigitated coil, and an AC voltage was applied across the combination of the coils. The sensor response was determined by measuring the total impedance of the sensor at different frequencies between 10 kHz and 100 MHz [17].

Notably, this chapter reports on the development of the microwave sensor operating at GHz frequency range with Ag pattern printed on flexible substrate. This sensor is conformable to planar and non-planar surfaces, simple and cost-effective to manufacture using modern printed-circuit technology, mechanically robust when mounted on rigid surfaces, and when the particular patch shape and mode are selected they are very versatile in terms of resonant frequency, polarization and impedance.

2 Current Methods of Water Quality Monitoring

There is an acute need in on-line monitors that are able to detect the excess of pollutants established by the official water quality regulations. Currently water quality assessments are based on the analysis of the physical, chemical and bacteriological parameters and require customized apparatus and trained staff. Typical parameters and techniques used in these monitors are listed in Table 1.

Physical, chemical, biological and radioactive parameters vary widely in all types of water and some high concentrations may be difficult to reduce during the treatment process. In conventional end-of-pipe systems a large part of the pollutants will always be lost to the environment due to leaking, primarily during rain. In the long term, source separation offers the more sustainable solution to the entire wastewater problem, including organic micropollutants. Urine source separation is an elegant solution to the problems of nutrients and pharmaceuticals alike and losses of untreated pollutants to the environment can be minimized [9]. With the continuous industrial developments, depleting natural water resources, increasing population and corresponding increased demand on domestic and industrial water consumption, it is getting more and more challenging for the water supply industry to maintain the safety of water.

Traditional methods of water quality control are lab based and include standard UV–Vis measurements, mass spectrometry, ion-sensitive electrodes and amperometric sensors. In particular, liquid chromatography tandem mass spectrometry has become a key technique for environmental analysis, allowing the detection of a wide range of polar and non-volatile compounds [10]. On the other hand, a range of modern real-time monitoring approaches exists, for example fiber-optic sensors, MEMs, lab-on-chip sensors and biosensors.

Most of the reported wastewater UV–Vis spectrometric applications are based on visual observation and direct comparison of the UV–Vis spectra. For example, the main method for phosphorus detection is using a photo sensor which measures the wavelength of a distinct color (e.g. blue or yellow) that results from a chemical reaction between phosphorus and special reagent [18]. Sensors based on colorimetric UV spectral measurements are widely used in commercially available systems [19], but they all suffer from a number of limitations. In particular, sample handling is problematic, and the acquisition of a reference spectra and calibration process are necessary for samples of different origin.

Fiber optic sensors are used in combination with the UV–Vis methods of water contaminants detection. Normally an optic fiber is suitably doped with a rare earth metal or activated with a transition metal to produce luminescence when exposed to an excitation light source. Fiber optic systems are particularly suitable for harsh and difficult to reach places.

Amperometric, potentiometric and conductometric sensing approaches are widely used in the measurement of pollution in water [20]. These sensors change their properties as a result of interaction with the component being measured. The species of interest are either oxidized or reduced at the working electrode causing a

Table 1 Measured water parameters and associated sensing methods

Parameter being measured	Sensing technology
Aluminum	Colorimetry; atomic absorption spectrometry
Antimony	Atomic absorption spectrometry
Ammonia	Colorimetric (manual; nessler's reagent; automated; berthelot reaction); ion selective electrode
Chlorine	Colorimetric; membrane electrode; polarographic membrane; 3-electrode voltametric method
Conductance	Conductivity cell; annular ring electrode; nickel electrode; titanium or noble metal electrode
Dissolved oxygen	Membrane electrode; 3-electrode voltametric method; optical sensor
Ions (Cl^-, NO_3^-, NH_4^+)	Ion-selective electrodes
Oxidation–Reduction Potential (ORP)	Potentiometric; platinum or noble metal electrode
pH	Titration with sodium hydroxide; proton selective glass bulb electrode, proton selective metal oxide; ion sensitive field effect transistor (ISFET)
Phosphates	Manual or automated colorimetry
Temperature	Thermistor
Total Organic Carbon (TOC)	UV-persulfate digestion with near infrared detection or membrane conductometric detection of CO_2
Turbidity	Optical sensor; nephelometric (light scattering) method

transfer of electrons, thus generating a measureable signal. This change can be recorded as a change in the output signal, i.e. output voltage, current, change in conductivity, capacitance or dielectric constant—whatever parameter gives the most pronounced sensor response [21]. Potentiometric detection is attractive since it possesses numerous advantages when considering the development of real-time sensing technologies, as the recording instrumentation is cost-effective and highly portable. For example, a portable amperometric three-electrode immunosensor for screening of polycyclic aromatic hydrocarbons (PAHs) in water was recently reported [20]. In particular, amperometric detection is based on the measurement of current when a potential is applied to the working and reference electrodes of the system.

The presence of microorganisms in water is generally assessed with five indicators, such as total coliform, fecal coliform, fecal streptococcus, enterococcus, and Escherichia coli. To protect public health, microbiological standards have to be met at each individual treatment works and service reservoir. Notably, the presence of various microorganisms in water, including *salmonella, campylobacter, listeria, Bacillus cereus* and *Escherichia coli O157:h7* is a natural and unavoidable occurrence, but the level of these bacteria should be strictly monitored in real time. Infectious doses of these pathogens (as low as $\sim$10 bacterial cells) increase the vulnerability of the elderly, infants, and people with immunological deficiencies or organ transplants [22]. In recent years, there has been greater recognition of the importance of biosecurity in relation to protection of the environment [23].

Modern lab-on-chip and electrochemical sensing based monitoring systems are complex and combine amperometric/conductimetric sensor, microelectrodes and MEMs arrays, often along with microfluidics facilities. They are promising, but still are very expensive and not widely commercially available.

Thus, significant advances have been made in recent years in technologies to monitor wastewater quality for source water protection, treatment operations, and distribution system management, in the event of accidental (or deliberate) contamination [24]. Generally speaking, however, no single system available today can fully address the needs of the customers, i.e. industries and regulatory authorities, in its ability to determine on-spot, in real time, the composition of water to the desired sensitivity level, bearing in mind the wish for system portability and cost-effectiveness. This could be partially due to the fact that there is no common chemical feature characterizing all water pollutants, except their solubility to a certain level in water [10].

Therefore, novel real-time monitoring techniques are necessary and they must detect the excess of pollutants established by the official water quality regulations [25]. One such technique potentially capable to meet the demand for safe water, is being developed by the authors and uses the electromagnetic wave sensors in microwave region.

3 Electromagnetic Waves Sensing at Microwave Frequencies

Dielectric properties of materials are observed in their interaction with electromagnetic field. At microwaves the material under investigation is usually placed inside a transmission line, such as coaxial or rectangular waveguide, or resonant cavity and its influence onto wave propagation conditions is used to estimate specimen's properties.

Electromagnetic waves sensing in microwave range is a versatile technology which has been successfully used as a sensing method for various industrial applications including solutions concentrations [26] and fluid level measurements [27], material moisture content [28, 29] and wastewater quality control [7], for continuous process monitoring for biogas plants [30] and in the healthcare industry, for example for real-time monitoring of glucose in diabetic patients [16, 31] and for non-invasive monitoring of bodily fluids [32].

Microwave analysis (or microwave spectroscopy) can be applied to suit a broad range of requirements [33, 34] and has a number of advantages over competing technologies for water quality sensing applications, including: (1) true real-time sensing, since an analyte material flows past or through the sensor and an instantaneous measurement is acquired without the need for significant pre-processing; and (2) direct sample measurement—a feature currently unavailable in many competing technologies [2].

The multi-parameter nature of broadband microwave analysis can provide unique signal spectrum signatures. In this work, captured microwave signals are presented in the form of scattering parameters (commonly referred to as S-parameters), with measurement of the reflected (S_{11}) and transmitted (S_{21}) microwave signal being possible. These signals vary depending upon properties of the analyte presented to the sensing structure, such as conductivity and permittivity [35]. The microwave planar printed antennas for various sensing applications are increasingly used due to their versatility, flat profile and low weight. Their design can be tailored to suit particular application, coupled with reliability and cost-efficiency, since they are easily manufactured using common methods for printed circuit board production.

To clarify the principle behind suggested electromagnetic wave sensing, it is worth mentioning that microwave sensors in the form of planar patch patterns operate based upon the fact that an object under test, i.e. water sample, when placed into a vicinity or in direct contact with microwave sensor, interacts with the electromagnetic waves in a unique manner, which can be specifically correlated with the properties of this material. Due to this interaction, the permittivity of the material changes and it manifests itself as a frequency change, attenuation, reflection of the signal or a phase shift. By considering how reflected (S_{11}) microwave signals vary at discrete frequency intervals, the change in the signal can be linked to the composition of the tested water sample.

4 Experimental Procedure

4.1 Interdigitated Pattern Structure

Ag pattern with interdigitated electrodes (IDE) shown in Fig. 3 operating at microwave frequencies was chosen for its versatile design that combines ease of manufacturing with desired functionality. A distinct feature of IDE type sensors is their superior sensitivity to change close to the sensor surface, with this sensitivity decaying rapidly with distance away from the surface. This is advantageous as it reduces significantly the chance of undesirable factors influencing sensor response. Thin flexible substrate provides not only for structural benefits for a wide range of applications, but also plays a pivotal role in controlling the strength of a microwave signal fed into the sensor. Thicker substrates are known to be prone to the following effect: as the height increases, surface waves are introduced which usually is not desirable because they extract power from the total available for direct radiation. The surface waves travel within the substrate and they are scattered at bends and surface discontinuities and degrade the metal pattern and polarization characteristics [36].

Silver was used as a metal material for both bottom layer, which acted as a ground plane, and top IDE pattern to maintain chemical neutrality when the device is placed in contact with water.

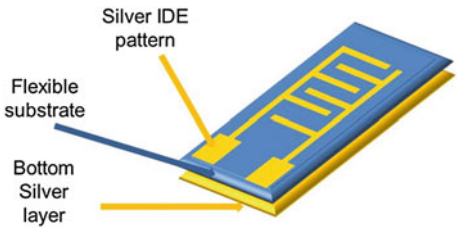

Fig. 3 Ag pattern with interdigitated electrodes

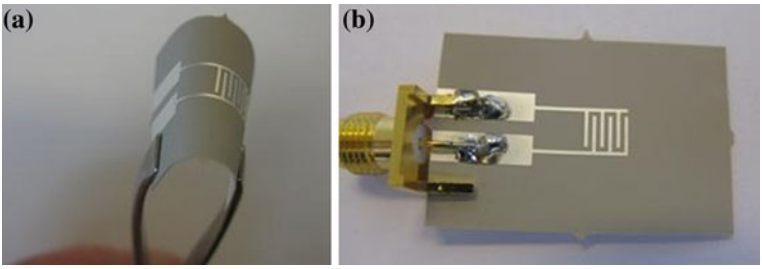

Fig. 4 Images of the microwave sensor: **a** sensor bended to illustrate the flexibility of the substrate; **b** sensor with attached SMA connector [37]

Figure 4a illustrates the manufactured prototype microwave sensor, which is bended to illustrate the flexibility of the substrate. Notably, the sensor dimensions were dictated by a compromise between, on one side, customer requirements for portability and convenience when using the developed water pollution monitoring system, and achieving clearly measurable sensor response with high signal-to-noise ratio to eliminate the need in further signal conditioning and modification.

4.2 Measurement Setup

The microwave IDE sensor was connected via a single SMA connector to allow measurements to be taken using *A Rohde and Schwarz ZVA24 vector network analyzer (VNA)* via a coaxial cable. SMA is a very common, popular and easily available connector, which is used to excite a microstrip line or a microstrip antenna. It is mainly 50 ohm probe with a central conductor extended to connect the microstrip element. Depending on the size of the antenna or substrate, the connector dimensions may be different [38]. Molex–73251–1150 RF/Coaxial SMA Jack STR 50 ohm edge mount connector was used in this work. This SMA type was chosen as it is designed to excite a printed IDE sensor horizontally to maximize the available signal.

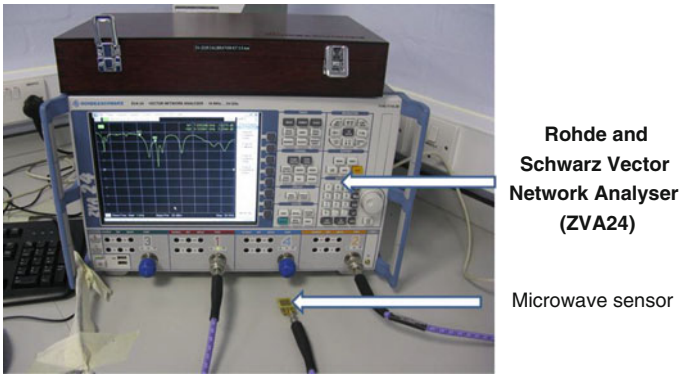

Fig. 5 Measurement setup showing Rohde and Schwarz ZVA24 and a microwave sensor connected via coaxial cable [2]

A Rohde and Schwarz ZVA24 shown in Fig. 5 was used for the purposes of data acquisition from the sensor, with this unit being appropriately calibrated according to manufacturer specifications. The data (60,000 points for each measurement) was captured in the frequency range of 1–20 GHz for the reflected (S_{11}) signals.

5 Results and Discussion

Figure 6 illustrates S_{11} signals distribution taken off the developed flexible microwave sensor in 1–15 GHz frequency range when in contact with air, deionized water and tap water samples. One may note the significant number of

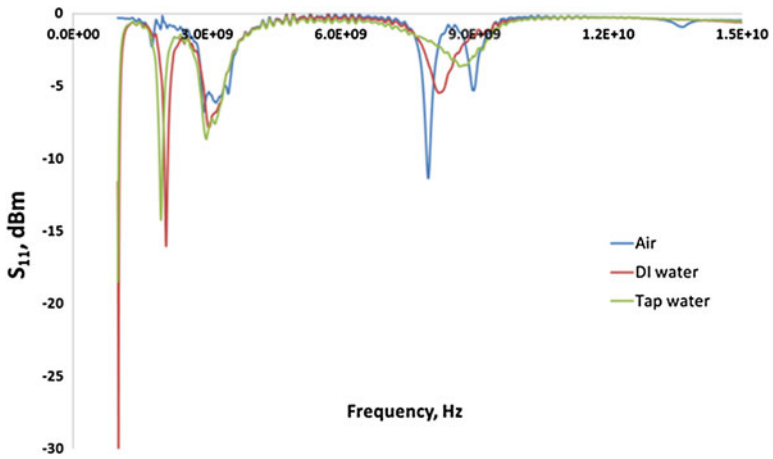

Fig. 6 S_{11} signal distribution of microwave sensor in 1–15 GHz frequency range when in contact with air, deionized water and tap water samples

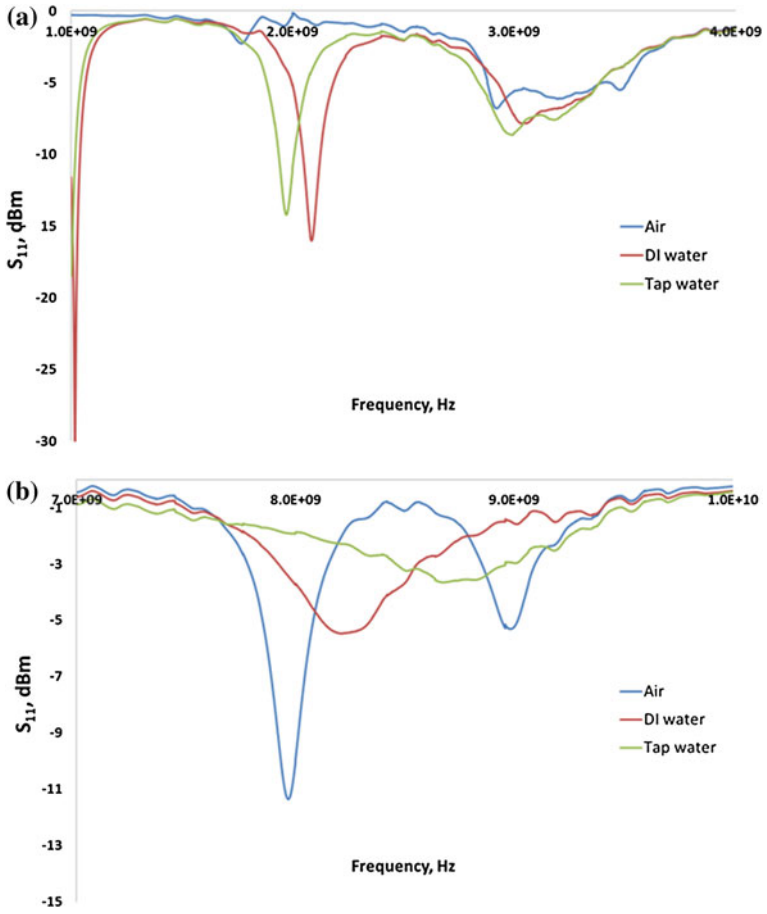

Fig. 7 S_{11} signal distribution of microwave sensor in **a** 1–4 GHz and **b** 7–10 GHz frequency ranges when in contact with air, deionized water and tap water samples

resonant peaks available with the IDE sensor, which indicates that the various sensing elements (or digits) each influence the obtained spectrum. It is believed that this will give significant advantages in terms of identifying the defect type present with greater sensitivity, selectivity and high resolution. Figure 7a, b provide more detailed view of these spectra, focusing on the 1–4 GHz and 7–10 GHz ranges respectively, as there is a distinctive shift in the resonant frequencies of the spectra, corresponding to the sample properties under test. Thus, Fig. 7a shows no peak for the sensor response when not in contact with water at around 2 GHz, whereas once the deionized water was placed onto the sensing pattern, a well-pronounced peak occurred at 2.11 GHz and it has shifted to 1.93 GHz when the water sample was taken from the tap. Similarly, Fig. 7b examines higher frequencies and confirms that the change in the resonant peaks have occurred for all

the samples and, having maintained all other experimental parameters constant, the only explanation to these shifts is that they are connected with the properties of the water, namely its composition.

Three spectra are plotted on common graph to illustrate that each sample has a unique response to the microwave signal resulting in resonant peaks occurring at different frequencies and this particular feature make the developed sensor an attractive option for real-time monitoring of water purity.

Real-time monitoring of wastewater quality remains an unresolved problem to the wastewater treatment industry [39]. Advanced autonomous platforms capable of performing complex analytical measurements at remote locations still require individual power, wireless communication, processor and electronic transducer units, along with regular maintenance visits. Therefore, there is a need to develop an automated cost-effective method of quality monitoring. However, it is believed that the microwave IDE sensor presented in this paper would act as a prototype system capable of achieving this challenging task.

While this work presents a proof of concept work, the eventual aim is to encapsulate this in a small hand-held or desktop diagnostic tool for rapid in situ analysis. Notably, the authors are working on the microfluidic cell with build-in microwave sensor for enhanced sensitivity to allow the detection of even the lowest levels of water pollutants. The work is under pending patents (GB1219016.1 and GB1219929.4).

6 Data Processing and Water Source Management

Advancing from the current laboratory based water composition analysis techniques to online methods could provide the basis for improved and sustainable water usage schemes, better water quality and enhanced water resource efficiency and management. Microwaves based sensing technologies show great promise, and offer the opportunity for affordable sensors which could be applied at point-of-use for continuous or on-demand water analysis to give real-time indication of the impeding problem.

Smart on-spot sensor data processing and energy management can allow continuous transfer of water pollution information into a centralized management center. Notably, the data transfer can be programmed in a way that only changes in the expected water composition are reported, as otherwise the amount of data could be huge and unmanageable. Individual sensors in a sensor network system can be replaced to address the needs of a dynamic situation, as one may never fully predict what kind of water contaminants would be occurring in any region either due to natural caused or as a result of human activities. When one of the sensors at any location records the presence or elevated levels of pollutants, the alert signal can be sent to either stop the usage of the water from that source or to take other necessary action, thus allowing smart preventive monitoring of water resources.

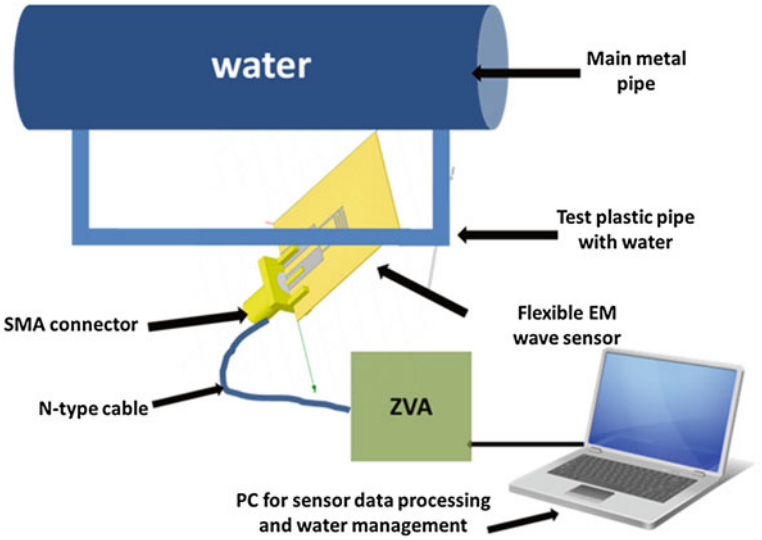

Fig. 8 Flexible microwave sensor built into main water supply system for continuous real-time water quality control and source management

Monitoring and management of water supply sources must be done at key process points, such as wastewater treatment plants, water basins and rivers, processed water transport, distribution and point-of-use locations. This will allow instant alert and timely response to a situation when water pollution of higher than officially permissible level is recorded. Pollution events can be mapped over time to see if they can be predicted and dealt with in preventive manner (Fig. 8).

Additionally, to preserve valuable water resources, a paradigm shift in water purification can be proposed by rethinking the distribution strategy at point-of-use and developing decentralized purification methodology based on region specific contaminants. Specifically, for sustainable building and industry operation, water self-circulation is envisaged, where depending on the level/type of water contaminants, the smart system will decide on where to direct the water: for re-use at application with lower water purity requirements, such as for toilets, or to local cleaning systems that can treat the water on spot.

7 Conclusion

There exists a clear need for better on-line monitoring of water systems given that existing laboratory-based methods are too slow to develop operational response and do not provide required level of public health protection. Novel real-time method of water pollutants monitoring is reported. It is based on a microwave

sensor system with planar printed patterns to which a GHz signal is fed via SMA connector and reflected spectra S_{11} are analyzed. Microwave signal experience a change depending on a type of water contaminant brought in contact with the sensor. Further work is underway to record the response of the sensor to various water contaminants and thus building a reference database. Subsequently, from the database of previously measured test samples, one can determine in real-time what type of water pollutant is present. Other printed sensor patterns and material are being explored to achieve the highest sensitivity and selectivity of the sensor response. Moreover, a combination of different sensors into a single system could be an option when a complex mixture of different water pollutants needs to be precisely determined.

This research was driven by the industrial need for novel real-time monitoring method of water purity that would be able to meet strict regulatory demands and yet be versatile, sensitive and cost-efficient. The proof-of-concept type sensor was developed to verify the applicability of the microwave sensor with silver inter-digitated electrodes to this task. It is believed that the sensor's flexible structure would provide for a long-term usage since this configuration is less prone to failure due to mechanical damage. The sensor response was tested using VNA in 1–20 GHz frequency range. It was clearly seen that the resonant peaks have shifted once the deionized and tap water samples were placed in contact with Ag pattern. Notably, the sensor's response returned to its original position, namely air spectrum, after each water sample measurements, confirming that the developed microwave sensor is reliable, re-usable and thus sustainable solution for water monitoring.

Acknowledgments This work is financially supported by the European Community's Seventh Framework Programme through the FP7-PEOPLE-2010-IEF Marie-Curie Action project 275201, Water-Spotcheck.

References

1. E. Council, Directive 2000/60/EC of the European parliament and of the council of 23 october 2000 establishing a framework for community action in the field of water policy. OJ L **327**, 1–73 (2000)
2. O. Korostynska, A. Mason, A.I. Al-Shamma'a, Monitoring pollutants in wastewater: traditional lab based versus modern real-time approaches, in *Smart Sensors for Real-Time Water Quality Monitoring*, eds. by S.C. Mukhopadhyay A. Mason (Springer, Berlin, 2013), pp. 1–24
3. C. Slater, J. Cleary, C.M. McGraw, W.S. Yerazunis, K.T. Lau, D. Diamond, Autonomous field-deployable device for the measurement of phosphate in natural water, 2007, p. 67550L
4. R.P. Schwarzenbach, B.I. Escher, K. Fenner, T.B. Hofstetter, C.A. Johnson, U. von Gunten, B. Wehrli, The challenge of micropollutants in aquatic systems. Science **313**, 1072–1077 (2006)
5. M. Stuart, D. Lapworth, E. Crane, A. Hart, Review of risk from potential emerging contaminants in UK groundwater. Sci. Total Environ. **416**, 1–21 (2012)

6. S. Rodriguez-Mozaz, M.J. Lopez de Alda, D. Barceló, Advantages and limitations of on-line solid phase extraction coupled to liquid chromatography–mass spectrometry technologies versus biosensors for monitoring of emerging contaminants in water. J. Chromatogr. A **1152**, 97–115 (2007)
7. A. Mason, O. Korostynska, A.I. Al-Shamma'a, Microwave sensors for real-time nutrients detection in water, in *Smart Sensors for Real-Time Water Quality Monitoring*, eds. S.C. Mukhopadhyay A. Mason, (Springer, Berlin, 2013), pp. 197–216
8. T. Heberer, Occurrence, fate, and removal of pharmaceutical residues in the aquatic environment: a review of recent research data. Toxicol. Lett. **131**, 5–17 (2002)
9. T.A. Larsen, J. Lienert, A. Joss, H. Siegrist, How to avoid pharmaceuticals in the aquatic environment. J. Biotechnol. **113**, 295–304 (2004)
10. R. Rosen, Mass spectrometry for monitoring micropollutants in water. Curr. Opin. Biotechnol. **18**, 246–251 (2007)
11. H. Jia, *Pharma pollution is out of control in China* (Chem. World News, June, 2011)
12. O. Korostynska, A. Mason, A.I. Al-Shamma'a, Monitoring of nitrates and phosphates in wastewater: current technologies and further challenges. Int. J. Smart Sens. Intell. Syst. **5**, 149–176 (2012)
13. A. Srivastava, G–.G. Choi, C.-Y. Ahn, H.-M. Oh, A.K. Ravi, R.K. Asthana, Dynamics of microcystin production and quantification of potentially toxigenic microcystis sp. using real-time PCR. Water Res. **46**, 817–827 (2012)
14. R.T. Blakey, A. Mason, A. Al-Shamma'a, C.E. Rolph, G. Bond, Dielectric characterisation of lipid droplet suspensions using the small perturbation technique, in *Advancement in Sensing Technology*, vol. 1, eds. S.C. Mukhopadhyay, K.P. Jayasundera, A. Fuchs, (Springer, Berlin, 2013), pp. 81–91
15. N. Al-Dasoqi, A. Mason, R. Alkhaddar, A. Shaw, A. Al-Shamma'a, Real-time non-destructive microwave sensor for nutrient monitoring in wastewater treatment, in *16th Conference in the Biennial Sensors and Their Applications, September 12, 2011–September 14, 2011*, Cork, Ireland, 2011
16. A. Mason, S. Wylie, A. Thomas, H. Keele, A. Shaw, A. Al-Shamma'a, HEPA filter material load detection using a microwave cavity sensor. Int. J. Smart Sens. Intell. Syst. **3**, 16 (2010)
17. M.A.M. Yunus, S.C. Mukhopadhyay, Novel planar electromagnetic sensors for detection of nitrates and contamination in natural water sources. Sens. J. IEEE **11**, 1440–1447 (2011)
18. N. Al-Dasoqi, A. Mason, R. Alkhaddar, A. Al-Shamma'a, Use of sensors in wastewater quality monitoring—a review of available technologies, in *World Environmental and Water Resources Congress 2011: Bearing Knowledge for Sustainability* 2011, p. 354
19. E. Sten O, The phosphate sensor. Biosens. Bioelectron. **13**, 981–994 (1998)
20. A. Ahmad, A. Paschero, E. Moore, Amperometric immunosensors for screening of polycyclic aromatic hydrocarbons in water, in *16th Conference in the Biennial Sensors and Their Applications, 12–14 Sept 2011*, Cork, Ireland, 2011
21. K. Arshak, O. Korostynska, in *Advanced Materials and Techniques for Radiation Dosimetry* (Artech House, Boston, 2006)
22. W.R.L. Van der Star, W.R. Abma, D. Blommers, J.-W. Mulder, T. Tokutomi, M. Strous, C. Picioreanu, M.C.M. van Loosdrecht, Startup of reactors for anoxic ammonium oxidation: experiences from the first full-scale anammox reactor in rotterdam. Water Res. **41**, 4149–4163 (2007)
23. V. Velusamy, K. Arshak, O. Korostynska, K. Oliwa, C. Adley, An overview of foodborne pathogen detection: in the perspective of biosensors. Biotechnol. Adv. **28**, 232–254 (2010)
24. M.V. Storey, B. van der Gaag, B.P. Burns, Advances in on-line drinking water quality monitoring and early warning systems. Water Res. **45**, 741–747 (2011)
25. O. Korostynska, K. Arshak, V. Velusamy, A. Arshak, A. Vaseashta, in *Recent Advances in Point-of-Access Water Quality Monitoring: Technological Innovations in Sensing and Detection of Chemical, Biological, Radiological, Nuclear Threats and Ecological Terrorism*, ed. by A. Vaseashta, E. Braman, P. Susmann (Springer, The Netherlands, 2012), pp. 261–268

26. B. Kapilevich, B. Litvak, Microwave sensor for accurate measurements of water solution concentrations, in *APMC Asia-Pacific Microwave Conference*, 2007, pp. 1–4
27. J. D. Boon, J. M. Brubaker, Acoustic-microwave water level sensor comparisons in an estuarine environment, in *OCEANS*, 2008, pp. 1–5
28. B. Jackson T. Jayanthy, A novel method for water impurity concentration using microstrip resonator sensor, in *Recent Advances in Space Technology Services and Climate Change (RSTSCC)*, 2010, pp. 376–379
29. C. Bernou, D. Rebière, J. Pistré, Microwave sensors: a new sensing principle. Application to humidity detection. Sens. Actuators B Chem. **68**, 88–93 (2000)
30. T. Nacke, A. Barthel, C. Pflieger, U. Pliquett, D. Beckmann, A. Goller, Continuous process monitoring for biogas plants using microwave sensors, in *Electronics Conference (BEC), 2010 12th Biennial Baltic*, 2010, pp. 239–242
31. O. Korostynska, A. Arshak, P. Creedon, K. Arshak, L. Wendling, A.I. Al-Shamma'a, S. O'Keeffe, Glucose monitoring using electromagnetic waves and microsensor with interdigitated electrodes, in *IEEE Sensors Applications Symposium, SAS*, 2009, pp. 34–37
32. A. Al-Shamma'a, A. Mason, A. Shaw, Patent: Non-Invasive Monitoring Device, US2012150000 (A1), WO2010131029 (A1), EP2429397 (A1), 2012
33. J. Choi, J. Cho, Y. Lee, J. Yim, B. Kang, K. Oh, W. Jung, H. Kim, C. Cheon, H. Lee, Microwave detection of metastasized breast cancer cells in the lymph node; potential application for sentinel lymphadenectomy. Breast Cancer Res. Treat. **86**, 107–115 (2004)
34. E. Nyfors, P. Vainikainen, Industrial microwave sensors, in *Microwave Symposium Digest, 1991, IEEE MTT-S International,* vol 3, 1991, pp. 1009–1012
35. D. Kajfez, Temperature characterization of dielectric-resonator materials. J. Eur. Ceram. Soc. **21**, 2663–2667 (2001)
36. C.A. Balanis, in *Antenna Theory: Analysis and Design*, 3rd edn. (Wiley, United States, 2005)
37. O. Korostynska, A. Mason, A. I. Al-Shamma'a, *Proof-of-Concept Microwave Sensor on Flexible Substrate for Real-Time Water Composition Analysis*, in Proc. ICST 6th International Conference on Sensing Technology, Special focus on Sensors for Agriculture and Environmental Monitoring, pp. 547–550, 2012
38. D. Guha, Y.M.M. Antar, *Microstrip and Printed Antennas: New Trends, Techniques and Applications* (Wiley, UK, 2010)
39. W. Bourgeois, J.E. Burgess, R.M. Stuetz, On-line monitoring of wastewater quality: a review. J. Chem. Technol. Biotechnol. **76**, 337–348 (2001)

Chapter 7
Assessing Water-Holding Capacity (WHC) of Meat Using Microwave Spectroscopy

B. M. Abdullah, J. D. Cullen, O. Korostynska, A. Mason and A. I. Al-Shamma'a

Abstract Water-holding capacity (WHC) is the ability of muscle to retain naturally occurring moisture in meat. WHC is a growing problem in the meat industry affecting yield and quality of the meat. Numerous methods have been applied to determine WHC such as the bag drip method and filter paper compression. However, such methods of measuring WHC/drip loss are time-consuming. This chapter reviews some of the current methods used for determination of WHC. The chapter will also present a novel method to measure drip loss and hence determine WHC using a microwave cavity. The cavity is first modeled using Ansys High Frequency Structure Simulator (HFSS) which is a 3D full wave EM field simulation package that can be used to design microwave structures. The cavity is then constructed, tested and evaluated in LJMU laboratories. Results obtained using different types of meat such as; pork, chicken, beef and lamb are presented and discussed. Attained results indicate that determination of WHC using microwave spectroscopy is a promising alternative to the exciting methods.

Keywords Water-holding capacity (WHC) · Drip loss · Microwave cavity · HFSS · EZ-Dripless · Meat quality · EM sensing

1 Introduction

Often when packaged meat is bought, there is a red solution in the packaging which might be assumed to be blood by many consumers. In fact, it is a result of leakage of water from the joint by drip loss and the solution consists of soluble proteins in water from the breakdown of the meat. Meat products contain a

B. M. Abdullah · J. D. Cullen · O. Korostynska · A. Mason (✉) · A. I. Al-Shamma'a
Built Environment and Sustainable Technologies (BEST) Research Institute, Liverpool John Moores University, Byrom Street, Liverpool L3 3AF, UK
e-mail: A.Mason1@ljmu.ac.uk

A. Mason et al. (eds.), *Sensing Technology: Current Status and Future Trends I*, Smart Sensors, Measurement and Instrumentation 7, DOI: 10.1007/978-3-319-02318-2_7,

Table 1 Dominant constituents of meat products

Meat	Cut	Moisture	Protein	Fat	Ash
Pork	Boston butt	74.9	19.5	4.7	1.1
	Loin	75.3	21.1	2.4	1.2
	Cutlets/chops	54.5	15.5	29.4	0.8
	Ham	75.0	20.2	3.6	1.1
	Side cuts	60.3	17.8	21.1	0.85
Beef	Shank	76.4	21.8	0.7	1.2
	Sirloin steak	76.4	21.8	0.7	1.2
Chicken	Hind leg	73.3	20.0	5.5	1.2
	Breast	74.4	23.3	1.2	1.1

significant amount of water, most products containing in the region of 75 % by weight; this is highlighted in Table 1 which shows a number of meat products and cuts with their associated primary constituents. WHC refers to the ability of meat to retain its water during cutting, heating, grinding and pressing. Our current knowledge on water-holding capacity of meat was based on the fundamental researches by Hamm in 1960 and Offer and Trinick in 1983 [1, 2]. Although it has been over 50 years since this initial work on WHC, water-holding in meat is still rather poorly understood. A hypothesis by the this early research for this phenomenon is that gains or losses of water in meat are due simply to swelling or shrinking of the myofibrils caused by expansion or shrinking of the filament lattice.

WHC is sometimes measured indirectly through a reciprocal property, drip loss, which is the amount of exudates or moisture on the cut loin surface. Some animals retain water after death better than others and this WHC appears to be the key to drip loss. Although the factors governing WHC are unclear, a number of aspects are thought to be influential, including genetic predisposition and the meat handling protocols. The handling and processing of meat can have major effect on WHC such as; size and orientation of cuts; pressure; temperature control and storage. Due to the significant water content in meat, it is one of the most important traits of meat, impacting upon yields, quality, safety and profitability.

1.1 Water-Holding in Meat

Muscle is a highly organized tissue, composed of individual cells known as fibers, which are structured by connective tissue. The structure of a muscle is demonstrated in Fig. 1. Each muscle fiber consists of a high number of single strands or organelles called myofibrils and these are comprised of myofilaments which are based on thin and thick filaments, predominantly made up of actin (thin) and myosin (thick) [3, 4].

The majority (85 %) of water in meat is held within the myofibrils; between the myofibrils themselves; between the myofibrils and the endomysia; between the

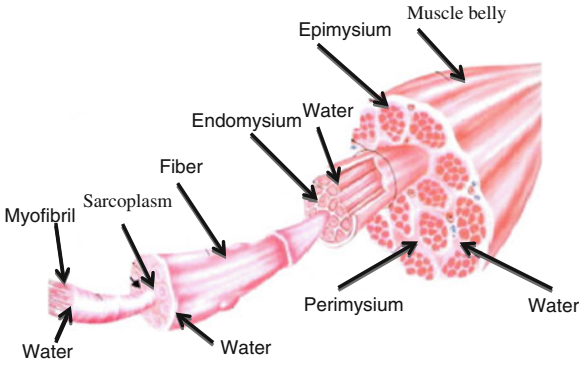

Fig. 1 Muscle components and the locations of muscle water compartments: the intra-myofibrillar component and the extra-myofibrillar component [3, 4]

muscle fibers and perimysia and between the muscle fiber bundles [5]. Myofibrils constitute approximately 80 % of the volume of the muscle cell. They are composed of overlapping thick and thin filaments. These structures are responsible for contraction of muscle and a high proportion of water is held within them. Water is in the muscle fiber as a lubricant, as well as a medium to transport metabolites in the fiber. The mechanism by which drip is lost from meat is influenced by both the pH of the tissue and by the amount of space in the muscle cells particularly the myofibril that exists for water to reside [6].

Research has led to a general agreement that the water can exist in three forms (1) bound, (2) immobilized and (3) free as shown in Fig. 2. Bound water is tightly bound to proteins and is not free to move around, cannot be frozen, is not affected by changes in pH and is also unavailable to partake in reactions. It is therefore possible to say that this water remains tightly bound to the meat proteins even during the processing of the meat, including even during severe mechanical (or physical) forces being applied. This however is the smallest amount of water overall, accounting for approximately 5–10 g per 100 g of protein. Immobilized water has also strong attraction to the bound protein molecules, but these forces become weaker the further one moves away from the proteins as binding occurs in the form of layers. This water is not necessarily lost easily, however this is dependent on factors such as exerted physical force, and in total this type of water accounts for approximately 50–60 g per 100 g of protein.

Finally there is the so-called free water, of which there is typically a large amount (approximately 300/100 g of protein). This water is held loosely in the capillary space between and within proteins. It is very loosely held and very dependent upon the capillary space between the interfibrillar strands of muscle proteins, meaning that muscle structure becomes an important determinant in WHC. Anything which alters the protein structure and/or spacing will affect the ability of the meat to retain water. Processing that reduces the amount of protein denaturation during the conversion of muscle to meat and factors that increase

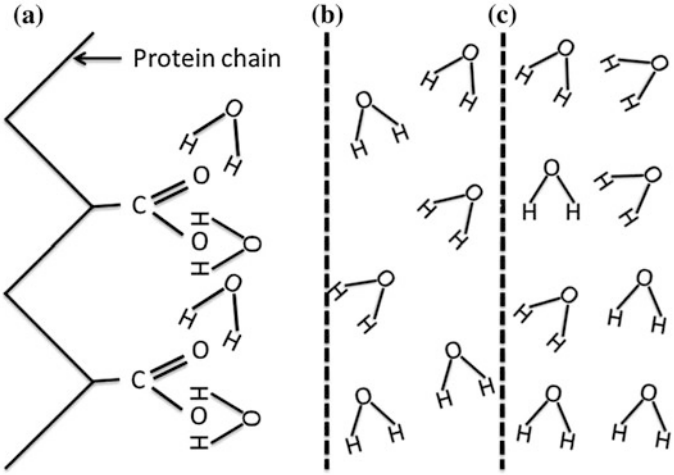

Fig. 2 Different forms of water in meat: **a** bound, **b** immobilized and **c** free; the further the water is from the protein chains, the easier it is lost

muscle pH, the electrostatic repulsion of the proteins, increasing sarcomere length, minimizing damage of the muscle structure, maintaining low storage temperatures, and avoiding freezing pre-rigor, will help maintain water immobilization and minimize the movement of water to become "free".

1.2 Meat Tenderness

A major factor in determining consumer satisfaction with meat is tenderness. Degradation of the muscle proteins in post-mortem muscle is associated with indices of meat tenderness. Muscle protein degradation may also be associated with drip loss. Research has suggested that reduced degradation of proteins that tie the myofibril to the cell membrane (such as desmin) may allow shrinkage of the myofibril to result in shrinkage of the muscle cell. This shrinkage opens drip channels and results in increased drip loss [7–9].

Postmortem factors, such as temperature, sarcomere length and proteolysis, which affect the conversion of muscle to meat, do contribute to meat tenderness. However, variation in other factors such as the muscle fiber type composition and the buffering capacity of the muscle together with the breed and nutritional status of the animals may also contribute to the observed variation in meat tenderness [10].

In 2010 a patent was granted for an apparatus and method for predicting meat (particularly raw meat) tenderness [11]. The invention does not require the removal or destruction of any cuts of meat from the carcass to which the method is applied. The method allows for the identification of tender meat products that might not be identified as tender using the conventional United States Department

of Agriculture quality grading method. The method includes the insertion of one or more, blunt flat-tipped blades into a meat sample, measuring values such as stress, force, or energy upon insertion of the blade, and calculating a tenderness factor based on a tenderness threshold.

1.3 Pre-Slaughter Stress

Another major effect of WHC in meat is the state of the level of stress of the animal pre-slaughter. Animals are susceptible to stress and respond in different ways to it. They respond by increasing their heart rate, respiratory rate, and muscle metabolic rate, all of which have negative effects on rigor mortis, protein denaturation, WHC, and meat functionality. Hence, all animals should be properly handled ante-mortem, so that these negative effects reduced or eliminated.

A research by Hambrecht et al. on the effect of stress on pork quality. The study was on physiological changes elicited in response to stress in the immediate pre-slaughter period and to link them to pork quality characteristics. Crossbred, halothane-free pigs ($n = 192$) were processed in eight groups (24 pigs per group) on various days at one of two commercial processing plants operating different stunning systems (electrical and CO_2 stunning in Plants A and B, respectively). In each group, half the pigs were exposed to either minimal or high pre-slaughter stress. Blood samples were taken at exsanguination, and lactate, cortisol, and catecholamines, as well as blood pH and temperature, were assessed and linked to various longissimus muscle quality attributes. The research team concluded that stress immediately before slaughter has severe, negative consequences on pork quality attributes, such as drip loss and pork color, both after electrical and CO_2 stunning [12].

Recently a team of scientists based in Ireland has explored possible molecular factors in a proteomics study of pork. The wanted to identify proteins and peptides associated with drip loss in order to try and gain a better understanding of the process. Stress-related proteins were found in high drip loss samples. When the high and low drip loss phenotypes were compared, triosephosphate isomerase, creatinine kinase M-type, serum albumin and transferrin were less abundant in the high group, while β-tropomyosin was more abundant [13].

2 Factors Affecting WHC

2.1 Net Charge Effect

The pH of meat affects WHC enormously. During the conversion of muscle to meat, the pH of muscle changes from neutral ($pH \approx 7.0$) to about 5.5–5.7, the normal pH of post-rigor meat. Lactic acid, the by-product of anaerobic metabolism, is

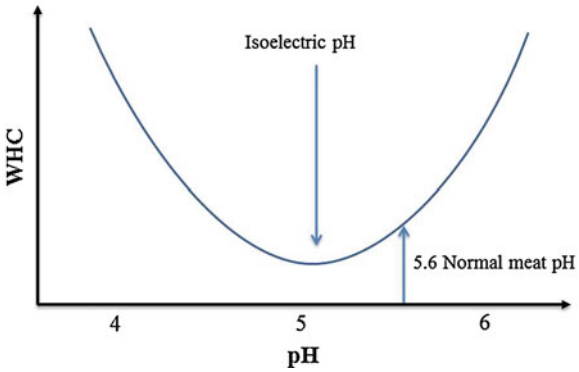

Fig. 3 Relationship between WHC and pH

responsible for the decline in pH. The energy required for muscle activity in the live animal is obtained from sugars (glycogen) in the muscle. In the healthy and well-rested animal, the glycogen content of the muscle is high. After the animal has been slaughtered, the glycogen in the muscle is converted into lactic acid, and the carcass becomes firm (rigor mortis). This lactic acid is necessary to produce meat, which is tasteful and tender. If the animal is stressed before and during slaughter, the glycogen is used up, and the lactic acid level that develops in the meat after slaughter is reduced. This will have serious adverse effects on meat quality [14].

The formation of lactic acid and the resultant drop in pH in the post-mortem period are responsible for an overall reduction of reactive groups on proteins available for water binding. This change results in varying amounts of denaturation and loss of solubility in proteins. The reduction in numbers of reactive groups occurs because the pH approaches the isoelectric point of myofibrillar proteins. Consequently, these groups tend to be attracted to each other, and only those free groups are available to attract water. This influence of pH is called the net charge effect and is illustrated in Fig. 3.

Proteins have an electronic charge that changes as the pH changes. The rule of thumb is that the higher the meat pH, the higher the net negative charge on the proteins and the higher the WHC. If proteins become more closely packed because they lack repulsive charges, water is excluded, driving the immobilized water into the free water compartment. All proteins have a characteristic pH where the net electronic charge on the protein is zero (the number of positive and negative charges are equal). This occurs for most meat proteins at a pH level of 5.1. This pH is called the isoelectric pH where the WHC is the lowest because there is minimal attraction between the proteins and water. Unless a meat product needs to lose water such as with dried processed products, the meat should always have a pH above or below the isoelectric pH so that the proteins carry an electronic charge to attract water.

Figure 4 shows the relation between bound water as a percentage of muscle weight and pH level for salted and unsalted meat. Salt slightly increases muscle pH. It also increases muscle filament spacing by providing ions that are attracted to

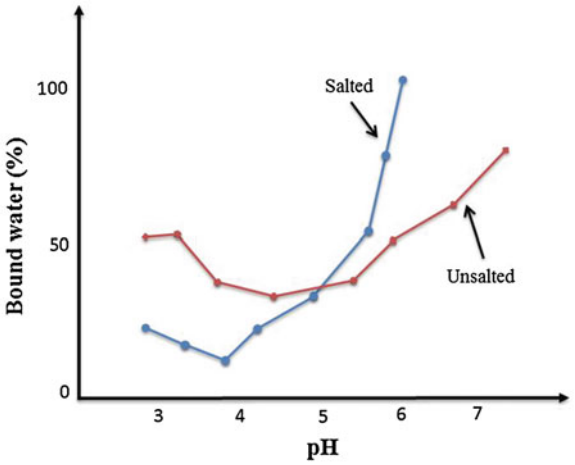

Fig. 4 Bound water as percentage of muscle weight versus pH

charges on the protein surfaces. This widens the structural spacing between filaments, and allows the filaments to swell, providing more room for water molecules to flow into the spaces. Monovalent sodium ions replace some tightly bound divalent positive ions, thus increasing the ability of the filaments to swell. Finally, salt frees more reactive groups on protein to hold to water. Detailed theoretical explanation of the effect of salt and proteins on water-structure and consequently on amount of water in meat can be found in [15]. Also the effect of ion distribution on muscle protein system and its water-holding is discussed.

2.2 Steric Effect

Changes associated with the onset of rigor mortis reduce WHC. At the beginning of rigor mortis, some chemical changes occur in the muscle structure so that a muscle contraction takes place. Some divalent cations (Ca^{2+} and Ca^{2+}) have the ability to combine with negatively charged reactive groups on proteins. As a consequence of these bonds, protein chains pack closely together. The lack of space for water molecules within protein structures is known as a steric effect on water binding.

2.3 Ion Exchange

Some of the loss of protein hydration caused by pH decline and rigor mortis is recovered during the subsequent storage of meat. A change of fiber membrane permeability allows some monovalent ions (such as sodium, Na^{+}) to replace some

divalent ions on protein chains. Consequently, for every divalent cation replaced, one reactive group of a protein is released so that it may react again with water. This exchange of ions in muscle proteins results in improved WHC. However, this improvement accounts for only a small proportion of the total change.

3 Current Methods to Measure WHC

3.1 Manual

Over the past 50–60 years, a number of authors have worked toward protocols which are generally accepted as methods for the determination of WHC. Loosely these methods can be grouped via the method used to encourage water loss from the meat; external pressure, gravity, centrifugal force or material absorption. It is notable that although the methods described below are utilized in industry, and WHC (or drip loss) have been measured for many years, an international procedure is not available. Perhaps the closest has come in the form of work by Honnikel [16]. However, this work will use the EZ-Dripless method as a reference standard.

3.1.1 EZ-Dripless Method

The day after slaughter the muscles to be analyzed are taken from the carcass. Within 1 h, a 25 mm slice is cut at a right angle to the muscle fiber direction. The sample is then cut using a 25 mm cork borer in the fiber direction. The sample is cylindrical, 25 mm in diameter and 25 mm in length. It is then placed in a special container equipped with a lid to avoid evaporation and loss of meat juice. The container is stored for 24 h at 4–6 °C before the drip loss is determined by weighing. The weight of the sample is taken before and after the 24 h period [17].

3.1.2 Filter Paper Press Method

This method was originally developed by Grau and Hamm in 1953, but a number of modifications to the technique have been suggested. In most of them the application of a defined pressure is recommended or the amount of released water is determined by weighing the meat sample or the filter paper before and after pressing. Hamm suggested a more rigorous protocol in 1972, which involves small meat samples (0.3 g) being pressed onto a filter paper at 35 kg cm^{-2} between two plates. 5 min later, meat samples are removed. The areas covered by the flattened meat sample and the stain from the meat sample are marked and measured [18, 19].

3.1.3 Centrifuge Method

Methods of centrifugation can be used for measuring the WHC of intact (unground) tissue. In this method a weighed muscle sample (3–4 g) is centrifuged at 100.000 g for 1 h in stainless steel tubes. The juice released from the meat is decanted off as quickly as possible (in order to avoid re-absorption of water). The meat sample is removed from the tube with forceps, dried with tissue paper, and then reweighed to determine liquid loss. If the residue is dried in the tube at 105 °C, the total water content of the sample can be determined, and WHC can be expressed as released or bound water as a percentage of total water. The need for a high-speed centrifuge makes it almost impossible to use this type of method in a slaughterhouse [20].

3.1.4 Bag Method

Meat samples are cut from a carcass and immediately weighed. The samples are then placed in a bag and hung in an airtight container using a hook under the lid. After the required storage time at the temperature under investigation (usually 24–48 h at +1 to +4 °C) samples are weighed again. A weight of about 100 g is recommended [16].

3.1.5 Absorption Method

This relatively new method consists of inserting cotton-rayon material in the longissimus muscle through the subcutaneous fat layer. This material is inserted into a " + " shaped incision approximately 2.4 in. deep at a well-defined place (e.g. 12th rib) and period of time (15 min at 15 min post-mortem or 15 min at 24 h post-mortem). Absorption is calculated as the difference between the final weight plus exudates and the initial dry weight of the material. This technique offers a rapid means of predicting WHC and could be a useful and accurate means of predicting this capacity during the early post-mortem period [21].

3.2 Automated

The methods described above are manual processes. However it is clear that the use of some equipment or methods is difficult or impossible in during the processing of meat products. There are a number of reasons for this: some equipment is impractical for use in a slaughter house, all testing procedures are destructive, and all involve some handling of meat such that water may be lost as a result of the testing itself. In addition, these processes are time consuming, and therefore mean that they cannot be used for timely sorting of meat products or to implement real-time changes in the

processing itself. Therefore, automated non-destructive testing (NDT) would present a significant improvement for the industry and is the purpose of this work.

3.2.1 Near-Infrared Spectroscopy

Progress on new methodologies for WHC evaluation is assisted by improved instrumentation coupled to computers with faster and better analytical capabilities than humans. Methods using near infrared spectroscopy (NIRS) have been successfully used for more than 30 years, providing rapid determination of moisture, fat, and protein of many food products. About 10 years ago, similar instruments were developed for meat and meat products for chemical analyses and these instruments are widely used today. Reports of adaptations of NIRS technology for meat WHC have considerable promise although the methodology still needs refinement to increase accuracy and precision.

NIRS involves the region of the electro-magnetic spectrum from about 700–3,000 nm. NIRS measures the difference between the composition of the instrument's light source and the composition of the light after it is exposed to a sample. The resulting spectrum of the sample is then evaluated. In general, the sample's molecular bonds absorb specific wavelengths (energy) for their vibrations and overtones.

NIRS technology involves exposing samples to known qualities of light. The reflected light is measured and converted into units of absorbed light, which reflects the chemical properties of the sample's composition. The goal is to find absorption patterns that are highly related to chemo-metric determinations of the samples inherit chemical and/or physical properties so that prediction equations can be developed.

The complex absorption bands in the NIR region can reveal information pertaining to meat quality, WHC, and numerous other traits. For these tests to be successful it is important to create datasets which contain large variations in the reference trait of interest. With all "natural" variation included, the chemo-metric comparisons utilizing computer software can determined if significant relationships exist between measured reference parameters and the complex NIRS absorption bands.

Calibration for the NIRS methods has been a major hurdle. In fact, nearly every individual product needs its own calibration, and this requires considerable attention to detail, a large number of observations (sometimes into the thousands), and validation of prediction equations. Once established, NIRS data can often provide data on many different chemical, physical, and sensory properties of meat, which would be extremely useful, making NIRS a powerful tool for automated, higher volume systems that need continuous feedback.

Correlations with cross-validation studies often range from about 0.25–0.68, with some studies obtaining correlations in the mid to upper 0.70s. If prediction equations for WHC can be validated with high accuracy using independent data sets, successful industry applications could be tested. However, additional refinement is needed because these correlations only account for about 50 % of the

variation in WHC. Nevertheless, NIRS measurements can sort meat into WHC categories of high WHC (less than 2 % losses) or low WHC (more than 4 % losses).

3.2.2 Nuclear Magnetic Resonance

Nuclear Magnetic Resonance (NMR) works on the principle of determining the electronic spin of a nucleus and low-field NMR T_2 relaxometry, which is used for determining WHC. The relaxometry is based on differences in the relaxation time of protons depending on their environment. The signals have been ascribed to hydration water closely associated to macromolecules, myofibrillar water and extra-myofribrillar water.

NMR measures relative "freedom" of water molecules to move in magnetic field. NMR method has potential for rapid, non-invasive quantitative analysis of the distribution and mobility of water in meat as well as to detect certain metabolic intermediates (metabonomics), which correlate to factors important for WHC. NMR analysis of water distribution and mobility correlates reasonably well to established methods for determining WHC. Metabonomic analysis, although promising, needs further investigation to demonstrate its usefulness in the meat industry.

NMR could provide reasonably rapid, non-invasive analysis of the distribution and mobility of water in meat, and at the experimental level, the method correlates well to established methods for determining WHC. The NMR technology could be at-the-line and possibly even on-line at slaughter plants, but smaller, faster, more economical NMR-equipment must be developed before its potential can be exploited by industrial meat operations [22].

3.2.3 Biomarkers

Biomarkers are genes or gene products formed via interactions between an animal's genes and its production and ante-mortem environments. One limitation of biomarkers is that they represent only a portion (mainly before slaughter) of the factors that affect WHC, and finding biomarkers that relate to the complexity and variability of the post-mortem environment is a challenge. However, since meat quality is the result of interactions of both antemortem and post-mortem conditions, this methodology could create new ways to evaluate and improve WHC.

Apart from applying metabonomics, the identification of biomarkers that reflect certain meat quality traits are also being pursued by using other "omics" methods like genomics, transcriptomics, and proteomics where detailed treatment and analysis of the data are needed.

Often biomarkers are not associated with NDT methods specifically, as particularly in the medical field a laboratory based assay might be used. However technologies such as NMR, when combined with other techniques, could identify biomarkers that could differentiate meat properties associated with WHC. The NMR technique suitable for this approach is high-field NMR where metabolites are

identified (metabonomics). Presently, the search for biomarkers and the validation of these markers is receiving considerable attention. Sophisticated techniques are being used for identifying changes in genes (genomics), gene-transcripts (transcriptomics), proteins (proteomics), and metabolites (metabonomics), which may correlate with meat quality parameters, including WHC.

All of these are potential biomarkers, but in reality, several biomarkers will need to be combined to obtain sufficiently strong correlations to WHC. The advantage of these "omics" techniques is that they are exploratory; a very large number of biological mixtures at different levels are analyzed to establish a huge base for the correlation analysis. Finding biomarkers often results from one technology and within one genetic and production scheme, so additional work would need to verify that they work with other methodologies and genotypes. Once appropriate correlations are obtained, other more simple, robust, and rapid analysis approaches, such as antibody-based systems, could be developed using identified biomarkers. Meat industry personnel can then use optimized assays to help adjust genetic lines, animal production systems, and meat industry practices that improve WHC in industrial settings.

3.2.4 Online Color Measurements for WHC Prediction

It was suggested that objective color measurements taken on the striploin and topside muscles after boning out may be useful in the prediction of WHC of cooked hams [23]. Despite some improvements over recent decades, the incidence of PSE (pale, soft, exudative) meat in pork industry remains a serious economic problem for producers, processors and retailers alike. A number of factors contribute to the quality status of a pork carcass including genetics, nutrition, seasonality, handling procedures on the farm and during transit to the packing plant, method of stunning, method of dehairing, and method and time of chilling after slaughter. The PSE condition is characterized by a rapid drop in meat pH after slaughter and a low final pH, resulting in meat which is pale in color, has a soft texture and is exudative or watery. Color is one of the most important quality attributes as it influences the attractiveness of pork at purchase.

There are many points on a carcass at which industry personnel can take readings with hand-held probes for pH, conductivity and color. Predicting meat quality from a single on-line measurement has great commercial potential if measurement at one site can predict the status of the whole muscle or even of the entire carcass.

Two measurements of color, namely reflectance and CIE L*, have displayed potential as predictors of pork topside quality prior to the production of hams, providing objective threshold values for acceptance or rejection of the raw material. Pork reflectance values may be measured using an Optostar Intelligent Color Gauger (SFK Technology A/S, Transformervej 9, 2730 Herlev, Denmark) while the CIE L* value of color may be determined using a portable HunterLab Miniscan XE (Hunter Associates Laboratory, 11491 Sunset Hills Road, Reston, VA 20190). Both instruments are portable for efficient on-line use.

4 Electromagnetic Wave Theory

The principle of real-time monitoring using microwaves is based on the interaction of the electromagnetic (EM) waves with the matter under test. The test object changes the velocity of the signal, attenuates or reflects it. The major advantages with microwave sensors are the capabilities to measure non-destructively, without contact from a short distance, using penetrating waves, without health hazards to the personnel. EM waves are waves of energy that travel through a vacuum at the speed of light. EM waves consist of two primary components, an electric (E) field and a magnetic (H) field. The electric field and magnetic field oscillate in phase perpendicular to each other and perpendicular to the direction of energy propagation.

If one considers a hollow structure with conducting walls (i.e. a cavity), it will resonate when it is excited at an appropriate electromagnetic (EM) frequency if one places a small antenna inside with the purpose of launching the EM energy. Any number of such antennae may be placed inside the cavity for the purposes of transmission and reception of EM energy, however the most typical configurations involve one or two port (one or two antennae) devices since often the materials placed within them are relatively homogenous and therefore further ports serve little purpose.

In a one port configuration it is possible, using a Vector Network Analyzer (VNA), to measure the power which is reflected from the cavity; this is often referred to simply as an S_{11} measurement. In a two port configuration, one can also measure power transmitted through the cavity; this is referred to as an S_{21} measurement. This is illustrated further in Fig. 5.

A cavity will resonate when it is excited at an appropriate frequency. The resonant modes occur when the electric and magnetic fields form standing waves, which depend on the internal dimensions of the cavity and the dielectric properties of the test sample. Therefore, its relative permittivity (ε_r) will change. The resonant frequency for TE_{nml} and TM_{nml} modes in a rectangular waveguide can be calculated using the following equation [24].

$$f_{mnl} = \frac{c}{2\pi\sqrt{\mu_r \varepsilon_r}} \sqrt{\left(\frac{m\lambda}{a}\right)^2 + \left(\frac{n\lambda}{b}\right)^2 + \left(\frac{l\pi}{d}\right)^2} \tag{1}$$

where;

- c is the speed of light
- μ_r is of the relative permeability
- ε_r is the relative permittivity
- p_{nm} is the value of the Bessel function for the TE or TM modes of a rectangular waveguide
- a is the width of the cavity
- b is the height of the cavity
- d is the depth of the cavity

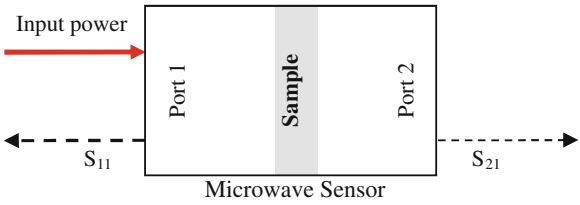

Fig. 5 Illustration of a microwave cavity structure, showing where measurements of S_{11} and S_{21} may be acquired

All EM modes therefore have the same dependence upon $\sqrt{\varepsilon_r}$, so when the cavity is excited by an appropriate range of frequencies and the resulting spectrum is captured, the resonant peaks corresponding to these modes will shift to lower frequencies as the permittivity is increased. Permittivity is commonly defined by;

$$\varepsilon_r = \varepsilon_r' - j\varepsilon_r'' \tag{2}$$

Permittivity is a measure of how an electric field is affected by a dielectric medium, which is determined by the ability of a material to polarize in response to the field, and reduce the total electric field inside the material. Therefore, permittivity relates to a material's ability to transmit an electric field and is a complex value which varies with changing frequency, and accounts for both the energy stored by a material (ε') as well as any losses of energy (ε'') which might occur. It is assumed that properties such as permittivity and conductivity (i.e. the ability of a material conduct electric current) will vary in relation to its WHC. Microwave spectroscopy, based upon these principles, has become well known as a technique which can be implemented cheaply, yet be used for a wide range of applications in a robust manner. The technique is non-ionizing and utilizes very low power in the order of 1 mW.

5 Experimental Methodology

5.1 Microwave Resonator Modelling

A cavity has been designed and modeled using the Ansys High Frequency Structure Simulation Software (HFSS). HFSS is a 3D full wave EM field simulation package which can be used to design microwave structures. It allows complex geometries to be created, which is particularly useful in these sorts of applications. The outputs of HFSS include S-parameters, Full-Wave SPICE extraction and 3D electromagnetic field simulation. The basic model created is shown in Fig. 6. The cavity has been designed such that the sample is located in the center of the cavity and is thus exposed completely to the TE_{101} mode, where the electric field is at a maximum as shown in Fig. 7.

Figure 8 shows some of the configurations for the TM modes in the designed rectangular cavity. The red color in this figure represents the maximum field intensity and the blue color represents the minimum field intensity.

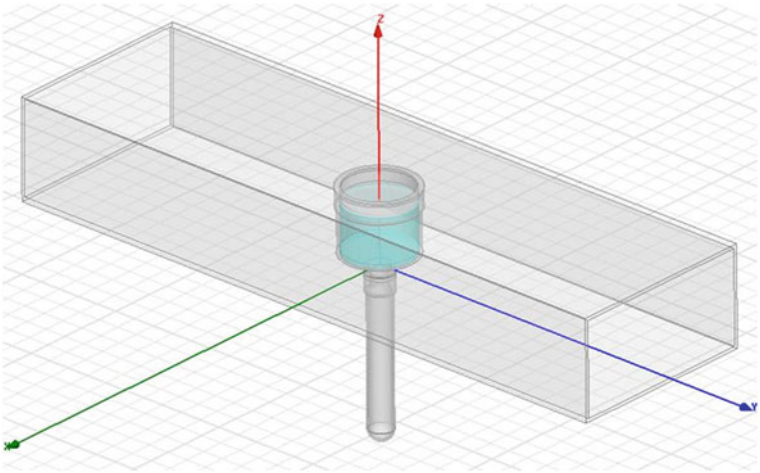

Fig. 6 Model of EZ-Driploss container placed inside a rectangular microwave cavity

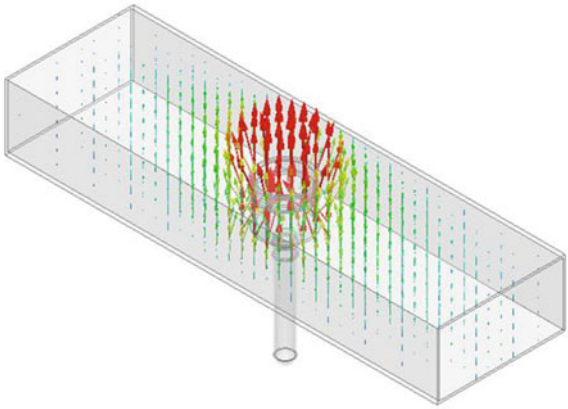

Fig. 7 Resonant cavity showing the TE_{101} mode, where the electric field interaction is maximized at the EZ-Driploss container location

5.2 Microwave Resonator Construction

The EZ-Driploss container is constructed from a polyethylene material based on the successful simulation of the cavity model shown above. This has been tested briefly to ensure that it does not change the microwave spectrum within a cavity significantly when comparing the case of an empty cavity and one with a drip loss container inserted. It is notable that at low frequencies very little change is apparent which is likely due to low permittivity $(\varepsilon_r \approx 2.25)$ and low loss (≈ 0.0001). A removable plate is incorporated to seal the cavity (i.e. to contain the

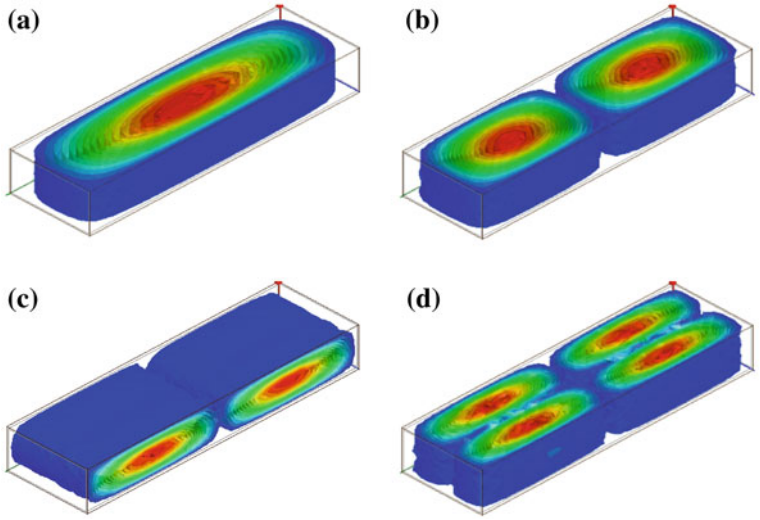

Fig. 8 **a** TE_{101}, **b** TE_{102}, **c** TE_{012} and **d** TE_{202} inside the rectangular cavity

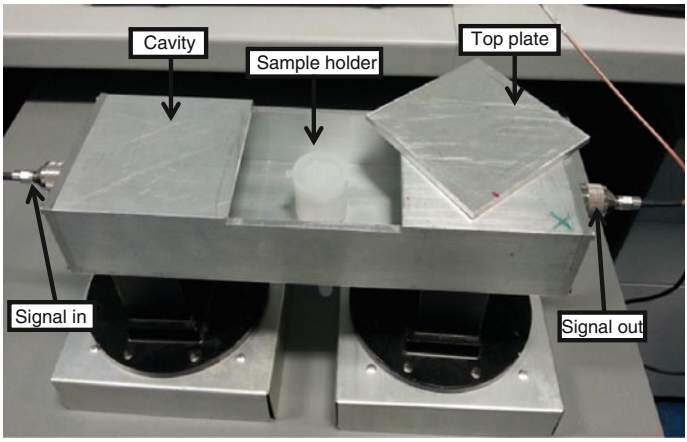

Fig. 9 Cavity for measurements with EZ-Dripless container

microwave energy) while also allowing access to insert an EZ-Dripless container. Ports are available at either end of the cavity to connect to a VNA, allowing for S_{11} and S_{21} measurements to be acquired as shown in Fig. 9.

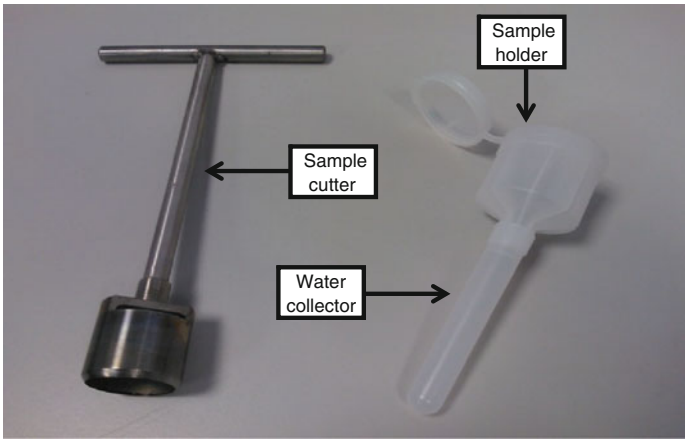

Fig. 10 Meat sample cutter (*left*) and sample holder with water collector (*right*)

5.3 Procedure

The following meat samples are used in this work; lamb, chicken, beef and pork. Each meat sample of 20 mm thickness is excised with the circular knife in accordance with the EZ-Driploss method procedure [17] as shown in Fig. 10.

The sample is then placed into the polypropylene tube (EZ-Driploss container), also shown in Figs. 10, 11 and 12. The sample container is weighed when empty (W_c) and weighed again with the meat sample inside (W_t). It is then placed inside the rectangular microwave cavity, with the container being placed such as to maximize interaction with the fundamental TE_{101} resonant mode. The container is left in the cavity for 24 h.

Reflection and transmission measurements are taken every 30 min over the course of 24 h. Water lost from the meat is collected in the cylinder beneath the sample aperture which thus allows for drip loss measurement. After 24 h the container with the collected liquid is weighed (W_l) and the drip loss of the meat sample of interest is calculated using the following formula;

$$Drip\ loss(\%) = \frac{W_l - W_c}{W_t - W_c} \times 100 \tag{3}$$

where;

- W_c is the weight of the empty EZ-Driploss container only.
- W_t is the weight of the EZ-Driploss container with the meat and liquid.
- W_l is the weight of the EZ-Driploss container with the liquid only.

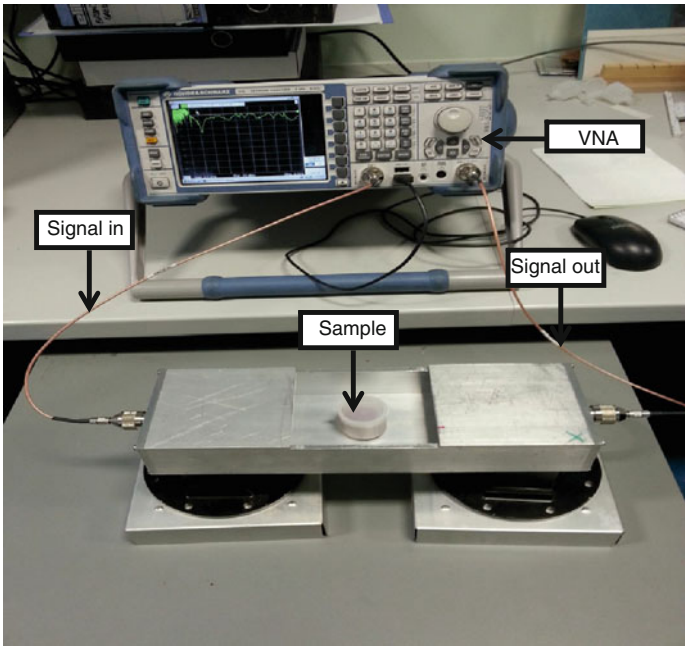

Fig. 11 Experimental setup for WHC measurement

Fig. 12 Close-up view of meat sample inside the rectangular cavity

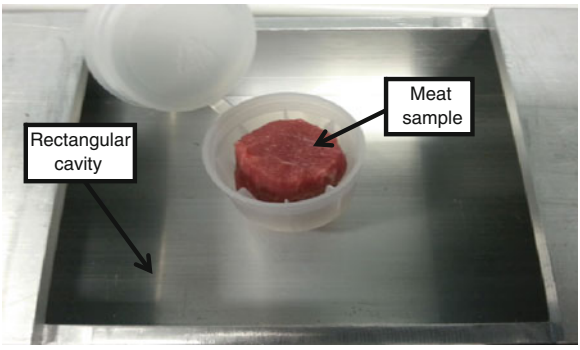

6 Results

Figures 13, 14, 15, 16, 17, 18, 19, 20 show the reflection and transmission measurements, i.e. S_{11} and S_{21} respectively. As can be seen from the reflection and transmission measurements, as the amount of water in the sample decreases over time both the transmission and reflection coefficients change. We can see that there is a magnitude shift in both reflection and transmission coefficients as time passes. This shift corresponds to the amount of water lost from the sample since the

sample in untouched and all other conditions remain the same. This trend is the same for all meat samples tested so far.

The results presented so far show that major changes to the reflection and transmission signals occur in the first 8 h. However, it is possible to predict the WHC within 30 min as shown in Figs. 19 and 20. Major changes do occur within 30 min especially when the WHC is lower, i.e. water is purged at a faster rate in meats with lower WHC.

6.1 Lamb

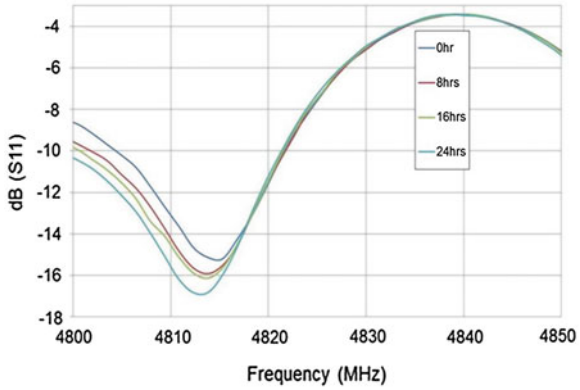

Fig. 13 Reflection measurements of lamb meat

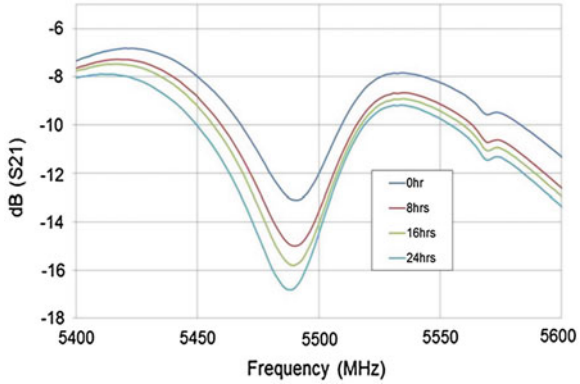

Fig. 14 Transmission measurements of lamb meat

6.2 Beef

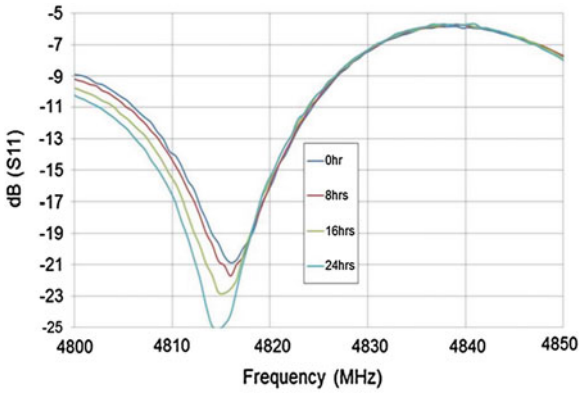

Fig. 15 Reflection measurements of beef meat

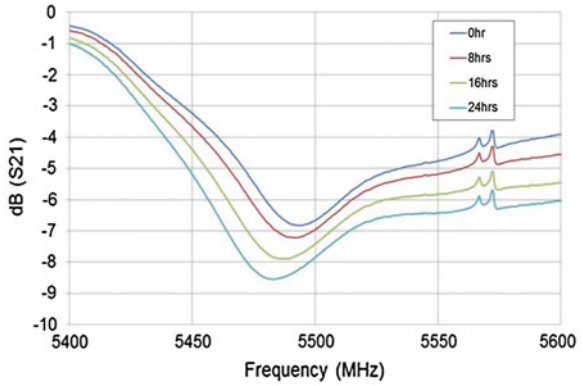

Fig. 16 Transmission measurements of beef meat

6.3 Chicken

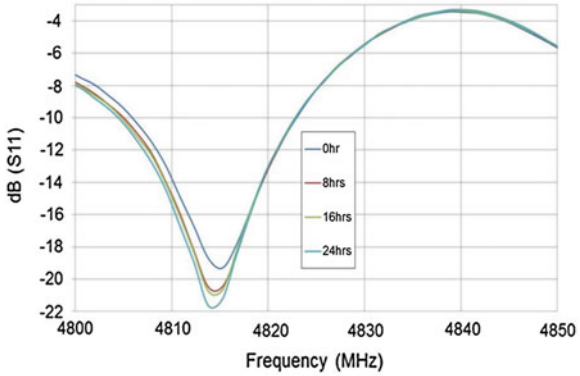

Fig. 17 Reflection measurements of chicken meat

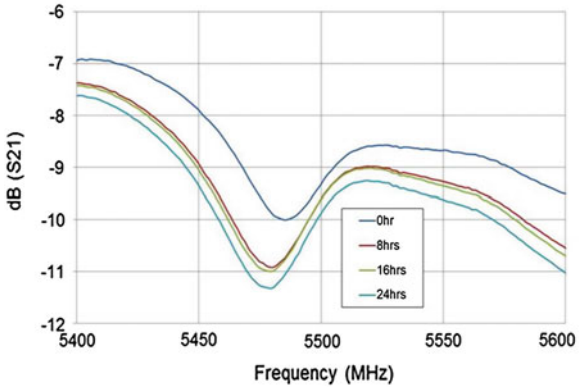

Fig. 18 Transmission measurements of chicken meat

6.4 Pork

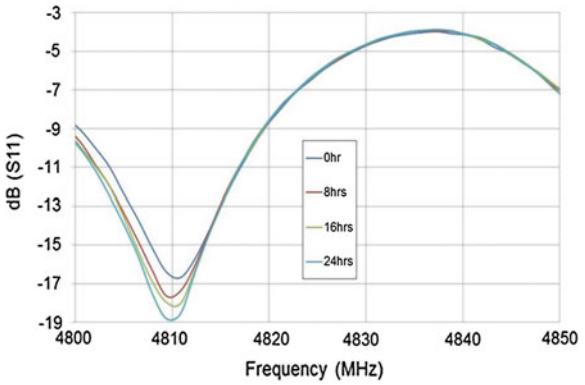

Fig. 19 Reflection measurements of pork meat

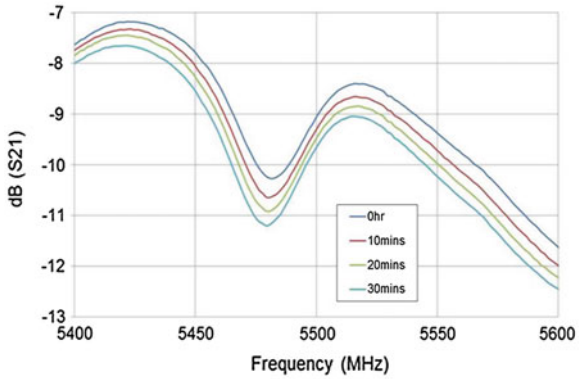

Fig. 20 Transmission measurements of pork meat

7 Conclusion

Several methods are currently applied in meat industry to determine WHC such as the bag drip method and EZ-Driploss method. An extensive review of such existing methods and work in the area of drip loss/WHC measurement has been conducted. It has been evidenced that there is little in the way of a practical solution to the issue of real-time measurement of WHC. Current methods require much work and time and ultimately they are not always practical or affordable.

This work is conducted based on an alternative and novel method using microwave spectroscopy. The need to build up an understanding of what happens to the properties of the meat, from a microwave spectroscopy point of view, as it undergoes changes during the EZ-Driploss 24 h testing procedure is investigated comprehensively throughout this project and presented in this chapter. Design and development of a rectangular cavity resonator is presented along with reflection and transmission measurements of four types of meat.

Results show that major changes to the reflection and transmission signals occur in the first 8 h. The changes to the spectra are highly dependent on the amount of water lost from the meat sample. Therefore, microwave measurements can be correlated with the amount of water recorded to be lost using the EZ-Driploss method. Furthermore, it is possible to predict the WHC within 30 min. Major changes do occur within 30 min especially when the WHC is low, i.e. water is purged at a faster rate in meats with lower WHC.

Acknowledgments This work has been conducted as part of the EUREKA project entitled "Increased Efficiency: Moving from Assumed Quality to Online Measurement and Process Control" (INFORMED, Project Number 6748).

References

1. R. Hamm, Biochemistry of meat hydration. Adv Food Res **10**, 355–436 (1960)
2. G. Offer, J. Trinick, On the mechanism of water holding in meat: the swelling and shrinking of myofibrils. Meat Sci **8**, 245–281 (1983)
3. T.R. Baechle, R.W. Earle, *Essentials of Strength Training and Conditioning* (Human Kinetic, Champaign, 2008)
4. K.L. Pearce, K. Rosenvold, H.J. Andersen, D.L. Hopkins, Water distribution and mobility in meat during the conversion of muscle to meat and ageing and the impacts on fresh meat quality attributes—a review. Meat Sci **89**, 111–124 (2011)
5. S. Ke, Effect of pH and salts on tenderness and water-holding capacity of muscle foods, 3215890 Ph.D., University of Massachusetts Amherst, Massachusetts, 2006
6. E. Huff-Lonergan, S. Lonergan, Mechanisms of water-holding capacity of meat: The role of postmortem biochemical and structural changes. Meat Sci **71**, 194–204 (2005)
7. L. Kristensen, P.P. Purslow, The effect of ageing on the water-holding capacity of pork: role of cytoskeletal proteins. Meat Sci **58**, 17–23 (2001)
8. J.L. Melody, S.M. Lonergan, L.J. Rowe, T.W. Huiatt, M.S. Mayes, E. Huff-Lonergan, Early postmortem biochemical factors influence tenderness and water-holding capacity of three porcine muscles. J Anim Sci **82**, 1195–1205 (2004)
9. P. McClain, M. Mullins, Relationship of Water Binding and pH to Tenderness of Bovine Muscles. J Anim Sci **29**, 268–271 (1969)
10. C. Maltin, D. Balcerzak, R. Tilley, M. Delday, Determinants of meat quality: tenderness. Proc Nutr Soc **62**, 337–347 (2003)
11. M.J.-F. Charles, Apparatus and method for predicting meat tenderness, 20100221395, 2010
12. E. Hambrecht, J.J. Eissen, R.I. Nooijent, B.J. Ducro, C.H. Smits, L.A. den Hartog, M.W. Verstegen, Preslaughter stress and muscle energy largely determine pork quality at two commercial processing plants. J Anim Sci **82**, 1401–1409 (2004)

13. A. Di Luca, G. Elia, R. Hamill, A.M. Mullen, 2D DIGE proteomic analysis of early post mortem muscle exudate highlights the importance of the stress response for improved water-holding capacity of fresh pork meat. Proteomics **13**, 1528–1544 (2013)
14. P.G. Chambers, T. Grandin, G. Heinz, T. Srisuvan, *Guidelines for Humane Handling, Transport and Slaughter of Livestock*. RAP Publication 2001/4. Food and Agriculture Organization of the United Nations and Humane Society of the United States, 2001
15. E. Puolanne, M. Halonen, Theoretical aspects of water-holding in meat. Meat Sci **86**, 151–165 (2010)
16. K. Honnikel, Reference methods supported by OECD and their use in Mediterranean meat products. Food Chem **54**, 573–582 (1996)
17. A. Rassmussen, M. Andersson, New method for determination of drip loss in pork muscles. Presented at the 42nd International congress of meat science and technology, Lillehammer, Norway, 1996
18. R. Hamm, Kolloidchemie des Fleisches—das Wasserbindungsvermoegen des Muskeleiweisses, in *Theorie und Praxis*, ed Berlin: Paul Parey, 1972
19. R. Grau, G. Hamm, Eine enfache Methode zur Bestimmung der Wasserbindung im Muskel, *Die Naturwissenschaften,* **40**, 29–30 (1953)
20. P. Bouton, P. Harris, W. Shorthose, The effect of ultimate pH on bovine muscle: mechanical properties. J Food Sci **37**, 351 (1972)
21. C. Walukonis, T. Morgan, D. Gerrard, J. Forrest, A technique for predicting water-holding capacity in early post-mortem muscle, in *Purdue Swine Research Reports* ed West Lafayette: Purdue University, 2002
22. H.C. Bertram, H.J. Andersen, NMR and the water-holding issue of pork. J Anim Breed Genet **124**, 35–42 (2007)
23. A.M. Mullen, C. McDonagh, D.J. Troy, Technologies for detecting PSE in pork, Research report, 2003
24. D. M. Pozar (ed.), *Microwave Engineering*, 2nd edn. Wiley, New York, 1998

Chapter 8
Microwave Tomography in Timber Processing: Two Examples

I. Platt, I. Woodhead, M. Hagedorn and S. Richards

Abstract The determination of moisture content in raw timber is an important parameter to determine its processing life cycle. In this paper two novel methods are presented to measure this, one using the radiant electric field from a pair of parallel transmission lines and the other the capacitance built up between contact electrodes. Both methods are arranged to provide a tomographic solution to the distribution to improve either resolution (parallel line) or volume coverage (capacitance). It is shown that while improvements can be made to each technique both have the potential to accurately provide a measure of the required parameters.

Keywords Tomography · Timber processing · Time domain reflectometry · Electromagnetic waves · Microwave sensors · Impedance measurements · Transmission line

1 Introduction

For the forestry industry, it is important to reliably grade raw timber as close to harvesting as possible so that it can be directed toward the most efficient product directed processing. Poor grading decisions at any stage along the processing cycle can lead to handling inefficiency and reduced product worth. There are a number of sensors developed for measuring parameters important in grading including those based upon optical, microwave and sound propagation.

It is of course important that the chosen sensor can perform accurately within the environment in which it is required to operate—no mean feat for industries employing heavy equipment with highly varying operating conditions, such as

I. Platt (✉) · I. Woodhead · M. Hagedorn · S. Richards
Lincoln Agritech Ltd, PO Box 133Lincoln, Christchurch 7640, New Zealand
e-mail: ian.platt@lincolnagritech.co.nz

A. Mason et al. (eds.), *Sensing Technology: Current Status and Future Trends I*, Smart Sensors, Measurement and Instrumentation 7, DOI: 10.1007/978-3-319-02318-2_8,

those experienced by timber harvesting and processing. For this sensor robustness and operation tolerance are critical and this criteria provides a unique opportunity for the development of new sensors and techniques.

In this work two new sensing techniques currently under development are detailed, designed specifically for the timber industry they initially target moisture content and density of raw timber, but have been chosen such that other important grading parameters will be accessible.

Important parameters for grading timber include:

- moisture content
- density
- defects—knots, splits, rot, resin pockets
- taper—changes in diameter along length
- sweep—curvature along length

Of these parameters, the moisture content is the most readily measured by the presented tomographic processes, with density and defects derivable directly via some manipulation. In fact in both techniques, it is the water component that dominates the measurement. Water has a particularly large dielectric constant compared to many other common molecules due a large polar moment resulting from its hydrogen—oxygen bonding properties. For example the relative permittivity of water is $\varepsilon_r \sim 80$ while for other commonly found dry biological material $\varepsilon_r = 2 - 5$. Thus an electromagnetic waves interaction with timber is dominated by its interaction with its free water component. It is this contrast in ε_r that allows water content to be measured directly (i.e. percentage moisture content of material) or used as a surrogate to image properties of the material (e.g. splits and knots in timber) that have different water content form the background.

Section 2 starts with a discussion of the method of moments, an integral technique adapted for posing the mathematical forward model of the dielectric composition and its interaction with an imposed electric field. Both tomography techniques use this formulation. Section 3 is devoted to the use of non invasive parallel transmission lines to reconstruct a timber samples moisture content distribution while Sect. 4 illustrates the same determination using a contact impedance measurement.

2 Method of Moments in Dielectric Materials

Both tomography methods discussed here infer the relative permittivity of the material under test by measuring the polarization field that dielectric molecules radiate after they have been disturbed by an incident electric field. To calculate this polarization field the sample space is discretized into finite grids with the required permittivity in each grid determined via an integral over the electromagnetic constitutive equations [1]. One of the most utilized methods for solving these discretized integral equations is the Method of Moments (MoM). A brief outline of this method as applied to both tomographic measurement methods is given below.

The interaction of radio waves travelling through materials such as wood is largely determined by the dielectric properties of the medium. For example, the velocity, v of a wave propagating through any material can be given in terms of its permittivity and permeability (e.g. [2]) by (1).

$$v = \frac{1}{\sqrt{\varepsilon_r \mu_r}} \tag{1}$$

where ε_r is the relative permittivity and μ_r is the relative permeability of the material. Note that for the material discussed here $\mu_r \sim 1$. This equation will become of more interest in Sect. 3 where it is applied to determine the propagation time of TDR signals along a transmission line.

When a dielectric material is subject to an incident electric field, E_i the polar molecules give up the random orientation of their magnetic moments and attempt to align with the external field, thus producing a net electric field polarization, E_p in opposition. The total electric field experienced in the region is then [3]:

$$\boldsymbol{E_t} = \boldsymbol{E_i} + \boldsymbol{E_p} \tag{2}$$

An explicit expression for E_p can be obtained by considering a small volume of the dielectric. For such a region the extent of material polarization, P is given in terms of the relative permittivity as:

$$\boldsymbol{P} = \boldsymbol{E_t}\varepsilon_0(\varepsilon_r - 1) \tag{3}$$

where ε_0 is the permittivity of free space.

The polarization electric field resulting from this volume is then:

$$\boldsymbol{E_p} = -\nabla \iiint \frac{P.r}{4\pi\varepsilon_0 r^3} \mathrm{dv} \tag{4}$$

where v is the volume of the polarized material and r is the distance between this region and the point at which the resulting polarized field is measured.

Combining Eqs. (2–3):

$$\boldsymbol{E_i} = \nabla \iiint \frac{\mathbf{P}.\mathbf{r}}{4\pi\varepsilon_0 r^3} \mathrm{dv} + \frac{\mathbf{P}}{\varepsilon_0(\varepsilon_r - 1)} \tag{5}$$

And this may be conveniently rewritten in terms of a linear operator L acting upon the polarization P [3] as:

$$-\boldsymbol{E_i} = \boldsymbol{LP} \tag{6}$$

The solution to this equation forms the central thesis of the MoM in dielectric theory and has been extensively developed by Harrington. In discretized form (see Fig. 1) the polarization (4) becomes:

$$E_{P_m} = -\nabla \sum_{\mathrm{n}=1}^{N} \frac{\mathbf{P}.\mathbf{r}}{4\pi\varepsilon_0 r^3} \Delta v \tag{7}$$

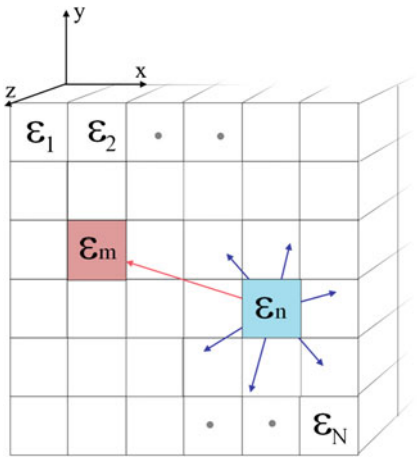

Fig. 1 Cells representing the discretized form of the dielectric sample. for the case depicted here cell n is the source cell and cell m is the cell for which the measurement of the polarization field is sought

With components given by [4]:

$$\boldsymbol{E}_{P_m} = \sum_{\mathrm{n}=1}^{\mathrm{N}} \left[\frac{1}{4\pi\varepsilon_0} \begin{pmatrix} \frac{3x_{mn}^2 - r_{mn}^2}{r_{mn}^5} & \frac{3x_{mn}y_{mn}}{r_{mn}^5} \\ \frac{3x_{mn}y_{mn}}{r_{mn}^5} & \frac{3y_{mn}^2 - r_{mn}^2}{r_{mn}^5} \end{pmatrix} \right] \mathbf{P}_{\mathrm{n}} \tag{8}$$

When $m \neq n$ and

$$\boldsymbol{E}_{P_m} = \frac{1}{4\pi\varepsilon_0} \begin{pmatrix} \frac{1}{3\varepsilon_0} & 0 \\ 0 & \frac{1}{3\varepsilon_0} \end{pmatrix} \mathbf{P}_{\mathrm{m}} \tag{9}$$

When $m = n$.

So applying the MoM (with a sub sectional basis function which is non zero only for the source cell) to these equations determines the value of the operator L of (6) to be those inside the brackets [ ] of (8) when $m \neq n$ and by:

$$\frac{1}{4\pi\varepsilon_0} \begin{pmatrix} \frac{1}{3\varepsilon_0} & 0 \\ 0 & \frac{1}{3\varepsilon_0} \end{pmatrix} + \frac{1}{\Delta\varepsilon} \tag{10}$$

When $n = m$ (6) represents the forward transform of the model with the required permittivity value ε_{r} buried with the operator L. For a more thorough discussion see [4, 5]. As in many problems of physical significance, this forward function requires its inverse to be found so that the value ε_{r} can be found. This inverse solution can be potentially accomplished via a number of optimisation techniques, though because the matrix L is ill conditioned extreme care must be taken. Platt [4] developed a robust method based on pre-calculated Monte Carlo Markov Chain (MCMC) Bayesian techniques [6–8] that will be used in various forms for the required solution.

3 TDR Tomography Using Transmission Lines

Time Domain Reflectometry (TDR) has been used for many years in a number of applications, most notably fault finding on both electrical and optical transmission waveguides that extend over long distances. In this application a break, or degradation of guiding capability in the waveguide, causes the signal inserted at the beginning of the line to be reflected back. In the cases of an electrical signal on a coaxial line the point of an open or short (or any damage that does not match the characteristic impedance of the cable) will cause a reflection the magnitude of which is given by:

$$\rho_0 = \frac{Z_t - Z_0}{Z_t + Z_0} \tag{11}$$

where Z_t is the terminating impedance at the point of discontinuity and Z_0 is the characteristic impedance of the coaxial cable and is given by (e.g. [2]);

$$Z_0 = \frac{1}{2\pi}\sqrt{\frac{\mu}{\varepsilon}} Log_{10}\frac{D}{d} = \frac{138}{\sqrt{\varepsilon_r}} Log_{10}\frac{D}{d} \tag{12}$$

Where D, d are the outer and inner conductor radii respectively.

Since both the relative permittivity, ε_r and relative permeability, μ_r of the cable are known the velocity of propagation is easily determined by (1). Thus measuring the time of flight of a pulse reflected from the discontinuity can be used to determine its distance along the cable from the point of insertion, with the value of ρ_0 available to give some indication of the type of fault.

The basic theory of TDR used in this communications cable fault finding has since been extended to many other applications including deterioration of power lines [9], structural cables [10], ground movement [11, 12] and ground moisture content [13, 14].

3.1 The Parallel Transmission Line

The basic TDR method discussed above has been extended over many years to measuring moisture content in soils references [15–17]. In this application two parallel probes, acting as a transmission line, are inserted into the soil. The soil and water surrounding the probe interact with the electric field generated by a pulse travelling along the inserted probes and modify its velocity by an amount given by (1). By rearranging this equation a measure of the propagation time t_p along a line length of d can give a value for ε_r by:

$$\varepsilon_r = \frac{1}{\mu_r}\frac{t_p^2}{d^2} \tag{13}$$

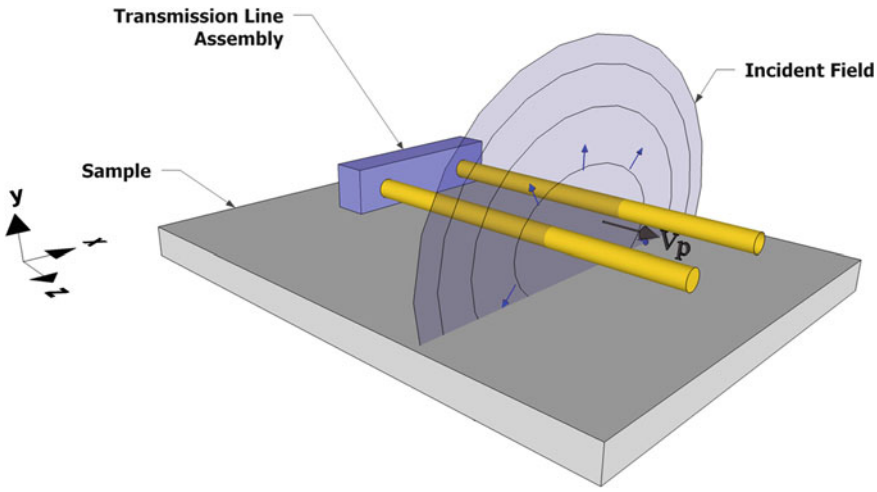

Fig. 2 Geometry of the parallel transmission lines in air over the timber sample. The pulse travels down the transmission lines to be reflected at their end. Interaction of the incident electric field with the sample moisture content slows the pulse velocity down

Once ε_r is determined, the volumetric moisture content of the soil can be estimated by using one of the well known soil mixing model functions [15, 17].

While this application of TDR has proved useful, the sensing is invasive in that the probes have to be inserted into the material for which a moisture measurement is sought. To provide for quicker and non-invasive applications [1, 18] developed a method whereby the parallel transmission lines are placed adjacent to the material to be measured. This non invasive technique clearly has a number of advantages the most important being that it can be used on material where inserting probes is not practical, such as in timber discussed here. Another important advantage is that since no mechanical interaction with the sample is required, measurements can be made as the transmission lines move along the measurand at relatively high speed. For this setup the incident electric field E_i penetrates the material surface and invokes a polarization response (see Fig. 2) for which the total electric field between the transmission lines, E_l (i.e. that part of E_t between the transmission lines) is determined via the MoM outlined in Sect. 2.

Note that in this non-invasive setup most of the surrounding cells, as depicted in Fig. 1, contain air with a known $\varepsilon_r = 1$.

The total field, E_l, between the transmission lines can then be used in the telegrapher's equation to provide a measure of the expected pulse propagation time, t_p for a relative permittivity of the material surrounding the transmission lines of ε_r.

$$v = \frac{2d}{t_p} = \sqrt{\frac{\pi V_l}{\rho\,\mu\,cosh^{-1}\left(b/a\right)}} \tag{14}$$

where $V_l = \int E_l dl$ and l is the distance between the surface charges of the lines (i.e. outside surface of lines) and E_l is the total electric field across this; d is the length of the transmission line; t_p is the propagation time of the pulse from the beginning of the line to its reflection at the end and back to the beginning; ρ is the line charge density; μ is the magnetic permeability; b is the spacing between the *center* of the parallel lines, and a is the diameter of the transmission lines.

The forward model process may thus be viewed as the composition:

$$t_p = g(E_l) \circ h(\varepsilon_r) \tag{15}$$

where the function g is defined by (14) and that of h by (6).

The above discussion on TDR has focussed upon using the measured pulse propagation time in (14) to estimate the relative permittivity via a process described in (15). An example of the signal characteristics of a pulse travelling down a parallel transmission line and reflecting from the end is shown in Fig. 3. The case is for two samples with different moisture levels placed beneath the lines, with the dashed trace having the higher moisture content and thus exhibiting a longer propagation time, t_p.

In reality the permittivity of the material is complex, with the imaginary part representing the electric field energy loss within the material. This energy loss results in an amplitude change of the signal and this can also be seen in Fig. 3. This amplitude change has been exploited by [19] to image knots and other timber features down to a depth of several centimetres below the surface as shown in the example of Fig. 4.

As yet there is no model available to relate the dielectric loss to the imaginary part of the permittivity so measurements so far have relied entirely on the contrast between various features. In future applications it is possible that, for a specific material, an empirical relationship can be developed to estimate the degree of parameter (i.e. moisture content) change with amplitude loss.

3.2 Tomography

The non-invasive TDR measurement strategy using transmission lines described above can be put to good use in determining some of the timber grading parameters, particularly moisture content variation and the extent of structurally significant features such as knots, sap pockets and splits. Since no contact or timber preparation prior to measurement is required the transmission lines can be placed rapidly about the timber sample chosen for tomographic reconstruction. Fig. 5 describes the principle behind collecting the data for the inversion. At each angle a

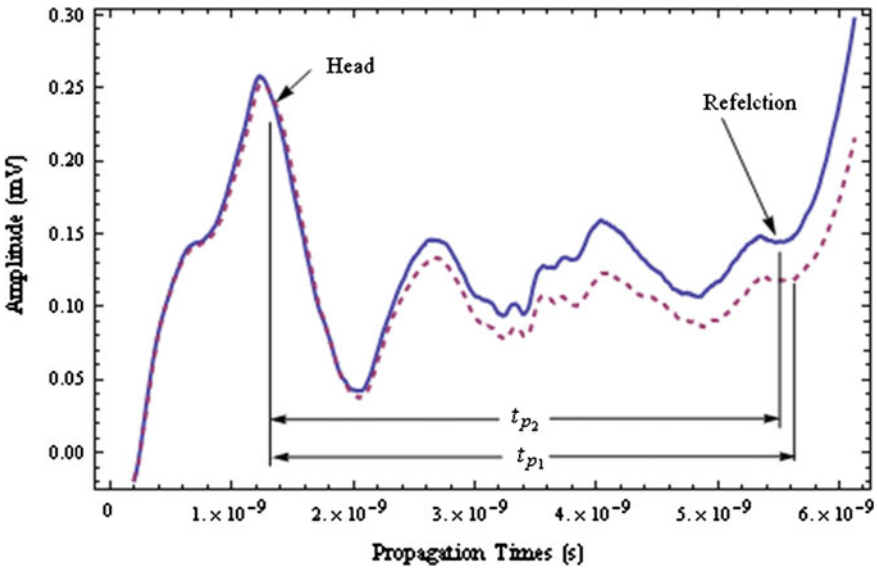

Fig. 3 The time versus amplitude trace for a pulse when the transmission lines are surrounded by air only (*solid curve*) and placed over a moist piece of timber (*dashed curve*). Note the difference in both propagation time and amplitude

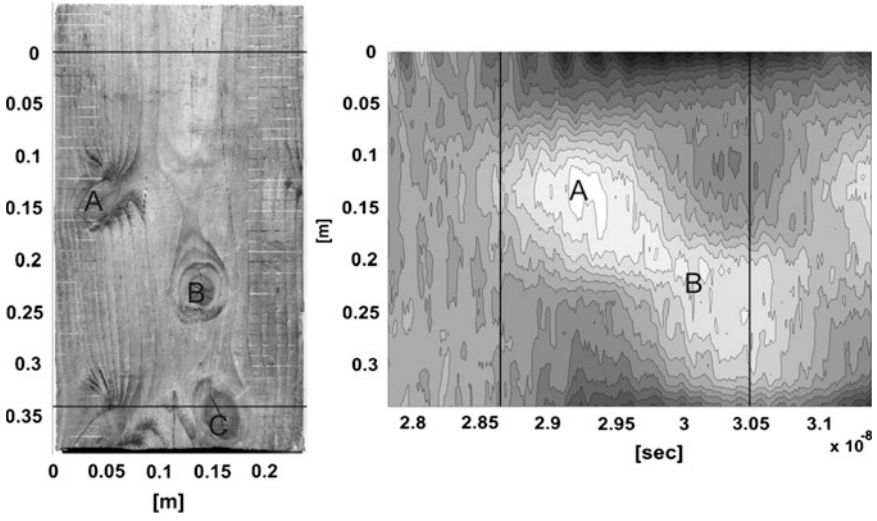

Fig. 4 After [19], showing how knots can be imaged with the parallel transmission lines by using moisture content as a surrogate

set of measurements are made as the transmission lines move linearly across the sample. Assuming that the property being measured at each point x, y of the sample is given by $f(x, y)$ each projection represents the integrated path [20].

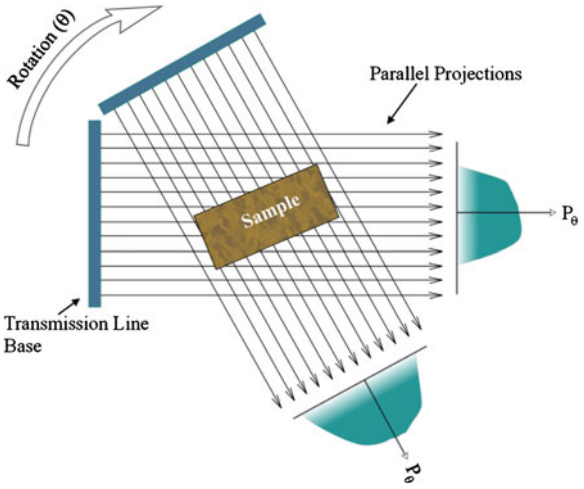

Fig. 5 Tomography measurement arrangement for the transmission line and timber sample. Note the projection plots resulting from each of the parallel projections. An actual projection for the sample to be used here is shown in Fig. 8

$$P_\theta(r) = \int_{line} f(x,y)ds \tag{16}$$

Where r is the parameterization of one of the parallel lines at angle, θ to the chosen x, y coordinate system:

$$r = x\cos\theta + y\sin\theta \tag{17}$$

The sum of all the parallel line integrals at the same angle produces a parallel projection of the required parameter. Repeating this for several different values of θ then produces a series of projections which may be inverted to find the value of the function $f(x, y)$ at some grid spacing determined by the distance between parallel projection lines and the number of rotation angles. The inversion in the case described here is usually referred to as back projection and can be accomplished by using an inverse Radon transform, since the extension of (16) using the delta function:

$$P_\theta(r) = \int_{-\infty}^{\infty}\int_{-\infty}^{\infty} f(x,y)\delta(x\cos\theta + y\sin\theta - r)\,dx\,dy \tag{18}$$

is referred to as a Radon transform. The seemingly complicated explanations above belie the simplicity of the actual calculation which in its essence is proportional to the mean of projection amplitudes that intersect a common grid region of the sample.

Note that the intention of this tomography as applied to the timber samples is to provide an increased resolution of the moisture distribution near the surface of the sample, not to provide a 3D reconstruction of the moisture throughout it.

Fig. 6 Photo of timber sample used in the tomographic reconstruction

3.3 Experimental Setup

For the experiment discussed here 116 parallel projection lines are used for every angle, θ between 0°–180° in 15° steps with the function f being the propagation time δt_p over each 3 × 3 mm segment. Since 116 projection lines are used, each with a spacing of 3 mm the grid size resolution across the scanning area is 3 × 3 mm with a total of 116 × 116 = 13, 456 gridded segments across the sample. Fig. 6 is a photo of the naturally dried section of macrocarpa sample used.

An example of the parallel projections at $\theta = 0°$ is shown in Fig. 7, where P_θ of (18) is the total propagation time, t_p and the $f(x, y)$ relates to the value of δt_p of each x, y grid. The corresponding projection plot of P_θ is shown in Fig. 8.

To transform δt_p into a value for the relative permittivity ε_r at each grid point, (6) is solved using a Markov Chain Monte Carlo (MCMC) technique [4]. The step to convert this ε_r into θ_v requires some sort of theoretical mixing model or an empirical data driven transform. Fortunately, extensive measurements of timber properties for different species have been accumulated by Torgovnikov [21]. These detailed data include the value of ε_r for different dry basis moisture content over many frequencies.

The flow chart in Fig. 9 describes the steps taken in the moisture content reconstruction described above.

Note that in practice it is much more efficient to transform the propagation time t_p, into the relative permittivity ε_r, before applying the inverse Radon function, since this reduces the number of optimization calculations performed by the MCMC process (i.e. there are only 116 × 12 (*angles*) = 1,392 values to convert before inversion but 116 × 116 (*grids*) = 13,456 after inversion). In fact for any operational system it would be best to transform each t_p measurement to $t_p \xrightarrow{g \circ h^{-1}} \varepsilon_r \xrightarrow{w^{-1}} \theta_v$ (where ε_r and θ_v are the line integral values) before the inverse Radon transform, though here we will stick to the computation at a segment level to highlight the process.

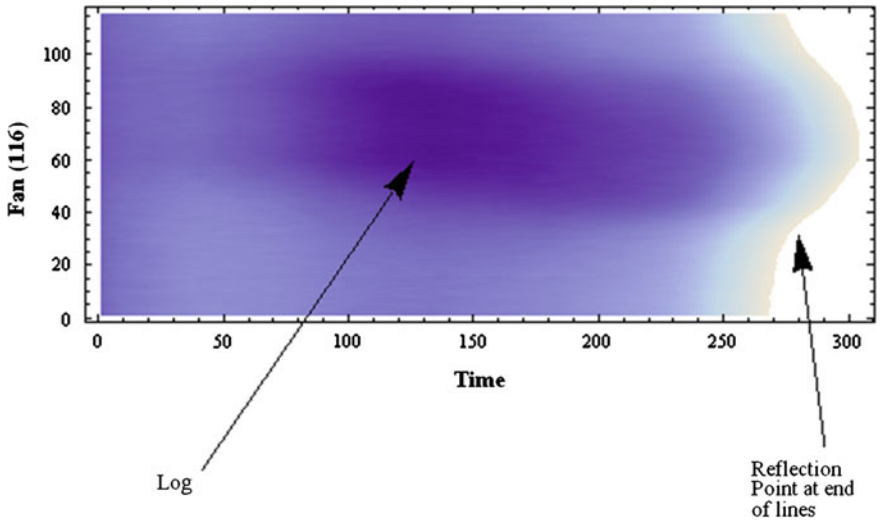

Fig. 7 Amplitude of characteristics of the log for 116 fans at a table rotation angle of 15°. The value of t_p for each scan is at the reflection point at the end of the transmission line. In this is unprocessed data the outline of the log sample can be seen

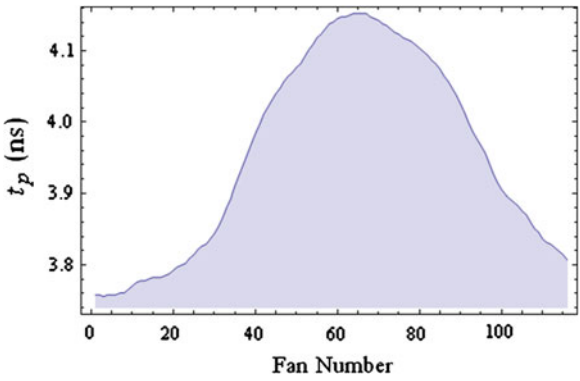

Fig. 8 The projection plot resulting from the measurement taken in Fig. 7. (i.e. Align with the right hand total time in Fig. 7)

3.4 Experimental Results

The full parallel projection of each angle is applied to the inverse Radon transform to reconstruct δt_p for each segment and the unprocessed result of this is shown in Fig. 10.

A close look at this figure will reveal that there is a large amount of blurring around the edges of the reconstructed image. This is caused by the influence of the electric field gradient along the x-direction of the transmission lines (Fig. 2 for axis orientation) and the combined effects of the pulse rise time and frequency dispersion in the propagation direction (z-axis). After converting the value of δt_p in

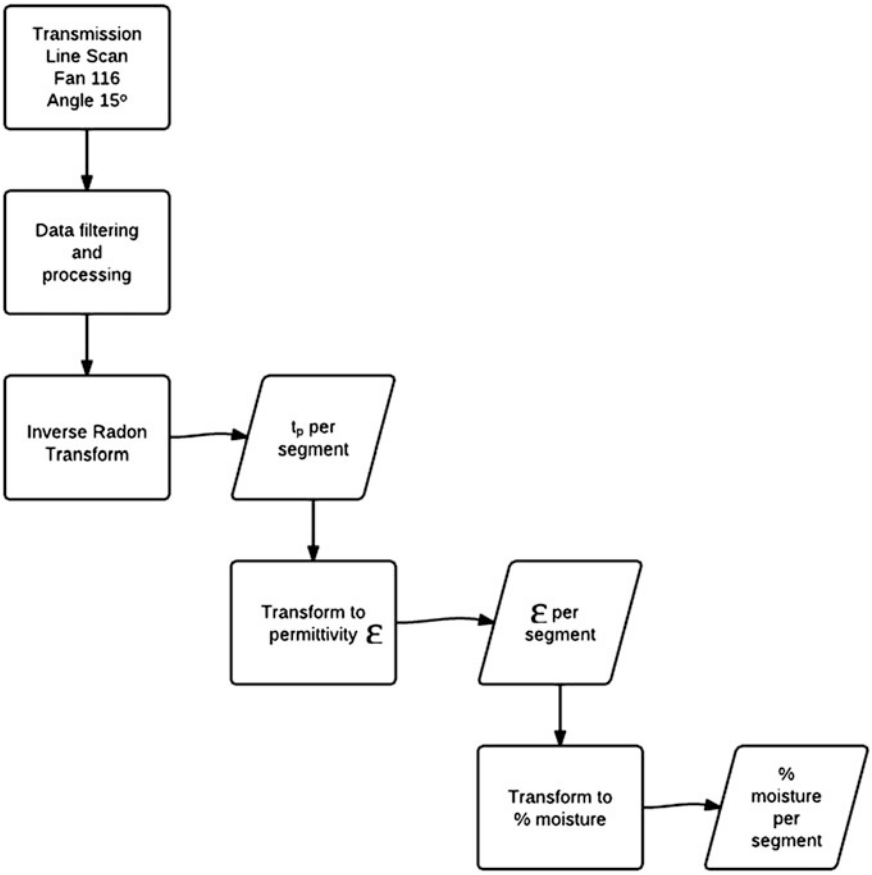

Fig. 9 Flow diagram representing the process of reconstructing measurements of t_p to give a high resolution moisture distribution cross section of a log sample. Note that the TDR imaging includes data up to some 200 mm below the sample surface

each cell to its associated ε_r, the cellular grid of relative permittivity is as given by Fig. 11.

The data plotted in this figure has undergone some filtering (e.g. Gaussian, Threshold, Quantization) and because of the gradients observed in Fig. 10 has thus introduced a "ragged" edge to the boundary.

To provide the desired moisture content, θ_D, on the 3 mm square grid, a mapping from the actually measured relative permittivity, ε_r is required. Torgovnikov [21] generated a large number of tables for this mapping over several different wood species and operational frequencies. The macrocarpa is taken to have a density $\rho_0 = 0.7$–0.8 g/cm^3 at high frequencies ($f = 2$–5 GHz range); a range corresponding to the high end frequency spectrum of the TDR pulse. The maximum value of ε_r shown in Fig. 11 is $\varepsilon_r \sim 5.9$ thus giving a maximum value of moisture content of $\theta_D \sim 30$ %. Since the minimum value $\varepsilon_r \sim 1$ the value of

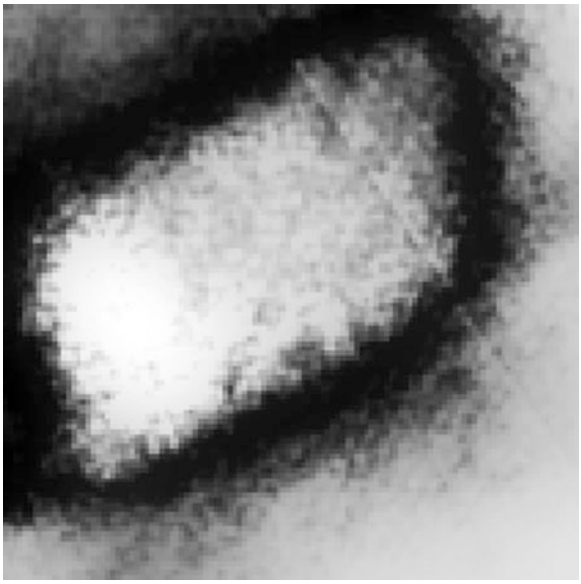

Fig. 10 Tomography Reconstruction showing the contrast between t_p for each 3 mm square grid. The *dark band* around the log is due to gradients caused by the "shape" of the incident electric field

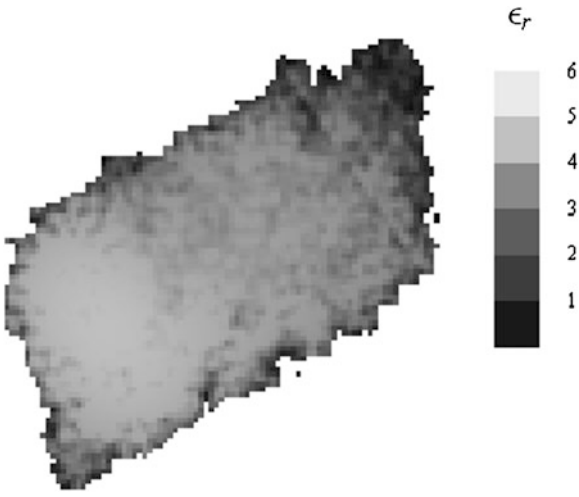

Fig. 11 Tomography reconstruction for ε_r

θ_D can be effectively scaled assuming a linear relationship between ε_r and θ_D. The results of this are shown in Fig. 12.

While the absolute value and variation of θ_D over this sample is within the limits expected from this type of timber sample, there are a number of obvious features which require some explanation. Principal among these is the appearance of noise like peaks (near the rear of the sample) that have no apparent visual correspondence and are hard to accept as naturally occurring variations. The mostly likely source for this error is an inaccuracy in rotating table and sample

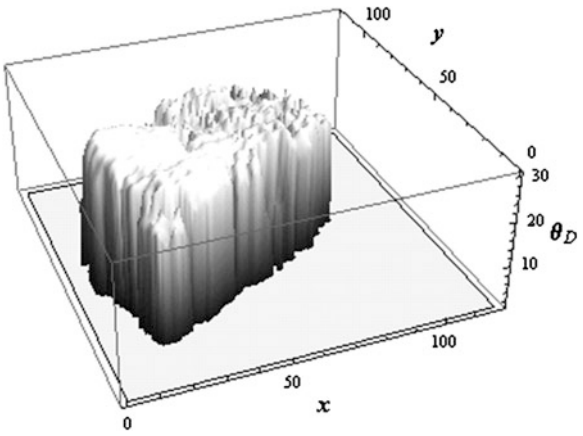

Fig. 12 Tomography reconstruction for θ_D

placement coordinates, causing misalignment of the required common sample cells for different angles. As already alluded to above, the fact that the electric field generated between the transmission lines has a considerable smoothing effect on the signal response means that sharp boundaries corresponding large variations in ε_r will also be considerably smoothed. One way to overcome this problem, caused by the convolution between transmission lines electric field and the sample, is to use the fields shape to provide a deconvolution function at the end of the permittivity processing phase. Such functions are notoriously difficult to construct when significant noise is present, especially if some adaptability is required.

4 Impedance Tomography

The moisture content θ_D determined in the TDR tomography above is essentially a 2D parametric representation of the moisture content integrated to a distance of approximately 2 cm below the surface. For this case the tomography was used to increase the resolution of the near surface measurements but does not supply the distribution accuracy in the third spatial (height or z-axis) coordinate. While there is potential for the TDR to do this, another method utilizing the combined dry mater and water timber impedance of the timber can be used to estimate the full 3D moisture content distribution.

As already mentioned the actual permittivity of a moist sample is complex, where the real part represents the stored energy of the system and the imaginary part corresponds to the energy dissipation:

$$\varepsilon_r = \varepsilon_r' f_o - j\left(\varepsilon_{relax}'' + \frac{\sigma_{dc}}{2\pi f_o \varepsilon_0}\right) \tag{19}$$

where ε_r' is the stored energy of the system, σ_{dc} is the electrical conductivity between the probes, ε_{relax}'' is the molecular relaxation of the water molecules and f_o

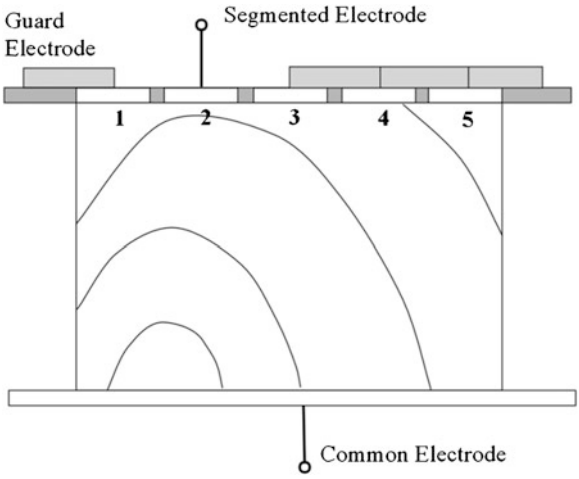

Fig. 13 Geometry of the segmented electrodes used in the capacitance impedance measurements

is the frequency of the probe signal. Equation (19) shows that both parts of the permittivity depend upon the frequency and ideally this should be chosen to maintain a low loss component since a large value for this compared to ε_r' leads to inaccuracies [22]. The mechanical set up for the experiment is shown in Fig. 13 where each segmented electrodes at the top of the sample is in turn attached to the impedance meter allowing current between this small surface to the large common electrode at the sample base. The capacitance field at each combination can then be measured and used to determine both the real and imaginary part of the permittivity.

The real part of the permittivity, ε_r' can be calculated by discretizing the sample and developing the forward model in terms of the MoM described in Sect. 2 and with the incident field given in terms of the displacement current [23]. Woodhead et al. [24] have also described a similar technique for the imaginary (loss) component of the permittivity. The inverse of both is via a Monte Carlo method using an a priori distribution given by the forward model with $\varepsilon_r = 7$.

The predicted relative permittivity distribution is then converted to moisture content with the sample cells by using a dielectric model [4] configured for the Aspen-Birch [21].

The measurements were carried out with HP4277A LCZ meter at a frequency of 1 MHz [25]. A photo of the 200 mm long and 100 $\times$ 100 mm square sample of *pinus radiate* is shown in Fig. 14. The electrodes were placed along the length of cells 1–5 (i.e. back of sample shown in Fig. 14 with the common electrode placed along the opposite face (i.e. front of sample shown in Fig. 14. The second set of measurements were then conducted by successively placing the electrodes along the length of cells 1, 6, 11, 16 and 21 (left face in Fig. 14 with the common electrode on the opposite face. After this series of impedance and phase measurements the sample was sliced longitudinally by a band saw and each cell weighed. After being dried at 100 °C for 50 h, each cell was again weighed from which the volumetric moisture content θ_v was determined.

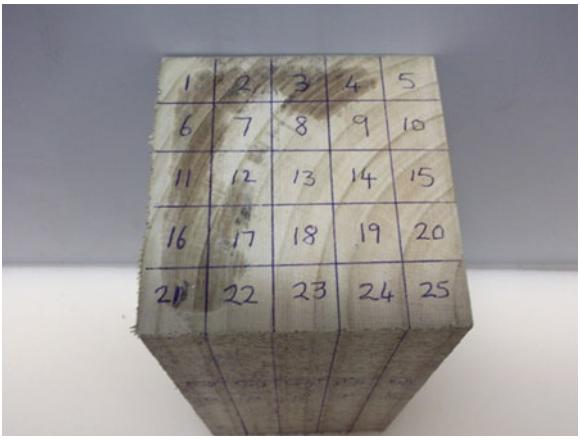

Fig. 14 100 by 100 by 200 mm Pinus radiata block used for impedance measurements. The 5 by 5 cells for which a value of moisture content is sought are marked

4.1 Experimental Results

Table 1 shows the results of the moisture calculated by the weighing–drying–weighing process and is reproduced in Fig. 15 (right) for visual comparison. Table 2 gives the impedance and phase measurements taken directly from the HP4277A for each of the electrode measurements.

The capacitance from the measurement readings were then used in the inversion procedure outlined above to provide an estimate for the volumetric moisture distributed within each cell and this is shown in Fig. 15 (right).

By comparing the plots in Fig. 15 it can be seen that the impedance derived measurement differs from the gravimetrically (weighed) calculated results near the centre to rear of the sample but are otherwise reasonably similar. The discrepancies are most likely due to the forward model inaccurately representing the

Table 1 Cell moisture content measured by weighing wet and dried sample

Cell	MC	Cell	MC
1	0.52	14	0.52
2	0.76	15	0.35
3	0.80	16	0.98
4	0.77	17	0.81
5	0.24	18	0.42
6	0.84	19	0.54
7	0.59	20	0.43
8	0.65	21	0.73
9	0.51	22	0.62
10	0.27	23	0.37
11	0.82	24	0.40
12	0.61	25	0.32
13	0.37		

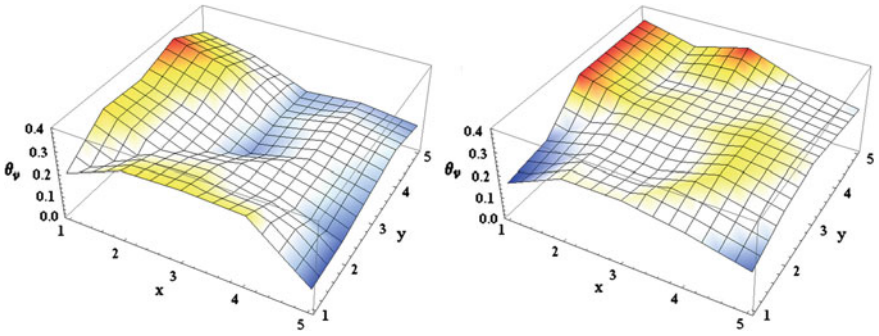

Fig. 15 Plot of moisture content determined by (*left*) inverting the 10 measurements of capacitance and (*right*) gravimetric measurements using pre and post drying weight

Table 2 Measured impedance and determined capacitance for two adjacent sides of the cells

Cell	Z	Angle	C(F) × 10^{12}
1	54.5	−64.5	2.64
2	48.6	−61.1	2.87
3	54.4	−61.0	3.07
4	53.0	−64.1	2.70
5	105.4	−68.8	1.41
21	59.2	−60.5	2.34
16	45.1	−61.2	3.09
11	46.4	−58.7	2.93
6	45.8	−57.1	2.92
1	48.9	−58.3	2.77

capacitance linkage with the permittivity, possibly due to the level of discretization involved and accuracy in modeling of the loss component. There may also be some smaller contribution due to equipment error, especially with the ability of the electrodes to maintain good contact with the sample.

5 Concluding Remarks

This chapter has presented two examples of employing tomography on timber samples to determine the distribution of their moisture content. Moisture content and an estimate of timber density arising from its determination are the most important factors in ultimately determining the processing grade of raw timber, since they indicate its structural strength and drying requirements. The two techniques are under development, but offer potential for a much greater range of grading parameters such as defects outlined in Sect. 1. Both methods have their

advantages but the parallel transmission line ability to conduct non contact, rapid measurement through unprepared surfaces seems attractive for application early on in the harvest/processing cycle. On the other hand this process has limited penetration depth, so to measure the full volume of a larger sample would best be suited to the impedance tomography, a method more readily applied further down the handling cycle.

Certainly neither method is without its difficulties, with error contributions that can be categorized, as can many processes of type, as due to, (1) Physical representation—primarily inaccuracies in the model that relates one parameter to another. In this cases the moisture content θ_v to the measured relative permittivity ε_r, (2) Physical process—to accurately model the interaction of the sensing component to the sample material. Here the ability to represent the response of the sample to the impressed electric field E_i and (3) Measurement errors—due to equipment interpretation for one reason or another. This includes poor reading, noise, signal processing etc.

While both the presented tomography techniques suffered to some extent from all of these errors it is clear that different sources dominated each. For example in the parallel transmission line tomography the precise mechanical positioning of the lines required for the resolution sought was suspect, leading to the apparent noise ripples evident in Fig. 12. Also, even though the values given by Torgovnikov [21] cover an excellent range for the transform $\varepsilon_r \xrightarrow{w^{-1}} \theta_v$over species and frequencies, the values do not provide high enough resolution for the application described here. For the impedance tomography measurements are perhaps more reliable but the discrepancies in Fig. 15 between the actual and predicted values of θ_v have been largely attributed to modelling inaccuracies [25].

Both these applications were chosen for their robust deployment potential in a very harsh working environment—both sensing probes having the ability to perform well when constructed from highly durable material. This is an important consideration for many practical systems where some equipment or measurement requirements will simply not work.

References

1. I. Woodhead, G. Buchan, D. Kulasiri, Pseudo-3-D moment method for rapid calculation of electric field distribution in a low-loss inhomogeneous dielectric. IEEE Trans. Antennas Propag. **49**, 1117–1122 (2001)
2. J D Kraus, K.R Carver, *Electromagnetics* (McGraw-Hill, New York, 1981)
3. R.F, Harrington, R.E Kreiger, (ed.), *Field Computation by Moment Methods* (Wiley-IEEE, New York 1987)
4. I.G. Platt, I.M. Woodhead, A bayesian approach to solving the non—invasive time domain reflectometry inverse problem. Sens. Transducers J **6**, 27–42 (2009)
5. I.G Platt, I.M Woodhead, A 1D inversion for non-invasive time domain reflectometry. Meas. Sci. Technol. **19**, (2008)

6. J. Kaipo, E. Somersalo, Statistical inverse problems: descritization, model reduction and inverse crimes. J. Comput. Appl. Math. **198**, 493–503 (2007)
7. J. Kaipo, E. Somersalo, *Statistical and Computational Inverse Problems*, vol 160 (Springer, New York, 2005)
8. S.R Arridge, J.C Schotland, Optical tomography: forward and inverse problems. Inverse Probl. **25**, (2009)
9. Y.J. Shin, E.J. Power, T.S. Choe, C. Hong, E.S. YSong, E.S. Yook, J.B. Park, Application of time-domain reflectometry for detection and localizarion of a fault on coaxial cable. IEE Trans. Instru. Meas. **54**, 2493–2500 (2005)
10. C.H, Dowding, K.M O'Connor, Real Time Monitoring of Infrastructure using TDR Technology. Structural Materials Technology NDT Conference 2000, (2000b)
11. C.H Dowding, K.M O'Connor, Comparison of TDR and Inclinometers for Slope Monitoring, in *Geotechnical Measurements— Proceedings*, Denver, CO 2000, vol 80–81, (2000a)
12. S.P, Farrington, S.M Sargand, Advanced Processing of Time Domain Reflectometry for Improved Slope Stability Monitoring, in *Proceedings of the Eleventh Annual Conference on Tailings and Mine Waste*, Oct, 2004
13. K. Noborio, Measurement of soil water content and electrical conductivity by time domain reflectometry: a review. Comput. Electron. Agric. **31**, 213–237 (2001)
14. D.A. Robinson, S.B. Jones, J.M. Wraith, D. Or, S.P. Friedman, A review of advances in dielectric and electrical conductivity measurements in soils using time domain reflectometry. Vadose Zone J. **2**, 444–475 (2003)
15. G.C. Topp, J.L. Davis, A.P. Annan, Electromagnetic determination of soil water content: measurements in coaxial transmission lines. Water Resour. Res. **16**, 574–582 (1980)
16. G.C. Topp, J.L. Davis, A.P. Annan, The early development of TDR for soil measurements. Vadose Zone J **2**, 492–499 (2003)
17. J.R. Wang, The dielectric properties of soil-water mixtures at microwave frequencies. Radio Sci. **15**(5), 977–985 (1980)
18. I.M. Woodhead, G.D. Buchan, J.H. Christie, K. Irie, A general dielectric model for time domain reflectometry. Biosyst. Eng. **86**, 207–216 (2003)
19. M. Hagedorn, M, I.G. Platt, I.M. Woodhead, Log Condition Scoring using a Non-Invasive TDR Sensor,in *IEEE Sensors Conference*, Christchurch, New Zealand, 2009
20. A.C, Kak, M. Slaney, Principles of computerized tomographic imaging. siam, classics in appliead mathematics, (1988)
21. G.I. Torgovnikov, *Dielectric properties of wood and wood-based materials*, ed. by T.E. Timel, (Springer , Berlin 1993)
22. W. Leschnik, U. Schlemm, Measurement of the moisture and salt content of building materials, in *Third workshop on electromagnetic wave interaction with water and moist substances*, *USDA*, Athens, Georgia, 1999
23. I.M. Woodhead, N. Sobue, I.G. Platt and J.H. Christie, A forward solution for RF impedance tomography in wood. Sens. Transducers J. Special Issue on Modern Sensing Technologies, April, **90**, 294–301 (2008)
24. I.M. Woodhead, G.D. Buchan, I.G. Platt, J.H. Christie, in *Seventh Conference on Electromagnetic Wave Interaction with Water and Moist Substances*, Hamamatsu, Japan, 2007
25. I. Woodhead, G. Buchan, D. Kulasiri, Pseudo-3-D moment method for rapid calculation of electric field distribution in a low-loss inhomogeneous dielectric. IEEE Transactions on Antennas and Propagation **49**, 1117–1122 (2001)

Chapter 9
A Novel Method for Monitoring Structural Metallic Materials Using Microwave NDT

B. M. Abdullah, J. Cullen, A. Mason and A. I. Al-Shamma'a

Abstract This book chapter describes a preliminary study carried out using EM wave technology within the microwave region to detect defects in metallic materials, such as materials used in building structures and vehicle platforms. The measurement system used in this research study makes use of the low power microwave energy over the frequency range of 300 MHz and 6 GHz. Main metallic defects such as cracking and corrosion in metal sheets are studied extensively in this research study. However, the system can also be used to detect other defects such as weld bead defects. The proposed EM wave NDT (Non-Destructive Testing) system will be integrated into a wide variety of structural elements (e.g. automotive and construction) and will provide continuous real-time structural health monitoring of the materials. The system will be able to provide information related to the presence, type and location of damage or defects. Two sensors are presented here for defect detection and monitoring; a rectangular patch structure and an interdigitated electrode structure. Experimental results demonstrate that the presence of defects such as cracks near the surface of the sensor elicit a change in sensor response.

Keywords Microwave NDT · Corrosion · Cracking · Structural monitoring · Patch sensor · Interdigitated electrode (IDE) sensor · Microwave sensor · Metallic defects

1 Introduction

The NDT of metals is a vast subject covering a large number of NDT methods and a wide range of defects. During the 1950s, the NDT of raw metals dominated the proportion of NDT carried out by end users and totaled as much as all the other

B. M. Abdullah · J. Cullen · A. Mason (✉) · A. I. Al-Shamma'a
Built Environment and Sustainable Technologies (BEST) Research Institute,
Liverpool John Moores University, Byrom Street, Liverpool L3 3AF, UK
e-mail: A.Mason1@ljmu.ac.uk

A. Mason et al. (eds.), *Sensing Technology: Current Status and Future Trends I*,
Smart Sensors, Measurement and Instrumentation 7, DOI: 10.1007/978-3-319-02318-2_9,

industrial sectors put together. However, the market for NDT of raw metals has declined since then due to the decline of heavy industry, but NDT of metallic material in sectors such as automotive, construction and aerospace has grown exponentially in recent years.

NDT of change in material state such as cracks, corrosion and fatigue is widely reported in literature [1–5]. By definition NDT of materials is the testing for surface or internal flaws or metallurgical condition without interfering in any way with the integrity of the material or its suitability for service. The methods employed for detecting such defects vary according to the type of defect or change that is being tested for and the material type. The most well-established of the NDT methods are; eddy current testing, acoustic emission, dye penetration, magnetic particle testing, visual testing, radiography and ultrasonic testing. Each method has its own advantages, disadvantages and specific applications. Some of these methods are time consuming because a point-by-point inspection is needed. This contributes to the rising costs of NDT of metallic structures. In the UK, expenditure on NDT of naval ships and submarine components and structures at build, during re-fit and in-service is considerable. It is also reported that corrosion in structures costs the UK around 4 % of its gross national product per annum [6]. Therefore methods of reducing the overall costs are constantly under review. The proposed NDT method using microwave techniques will provide high-speed real-time inspection.

Microwave NDT techniques have been around for more than 50 years. However, they are still not as widely known as other techniques such as eddy current in the NDT community. Microwave NDT methods are becoming popular in a wide number of areas such as medical [7], food [8] and construction applications [9]. Moreover, lighter, stronger and more durable electrically insulating composites are replacing metals in many applications. This will increase the popularity and diversify applications of microwave methods since microwave signals can penetrate dielectric materials and interact with their surface and inner structure. However, for metals, microwave signals mostly reflect at the surface. Hence, changes in the reflection coefficient properties of microwave sensors are of prime concern. In this study, the idea is that the sensor will be embedded within the metallic structure and the entire resultant system will be used as a unique sensor to detect changes to any part of the structure, whether internal or external.

2 Principle of EM Technology in NDT

Electromagnetic (EM) waves are waves of energy that travel through a vacuum at the speed of light. They consist of two primary components, an electric (E) field and a magnetic (H) field. The electric field and magnetic field oscillate in phase perpendicular to each other and perpendicular to the direction of energy propagation. Analysis using microwaves is non-ionizing with a low power output of 1 mW (0 dBm). The multi-parameter nature of wide band microwave analysis can

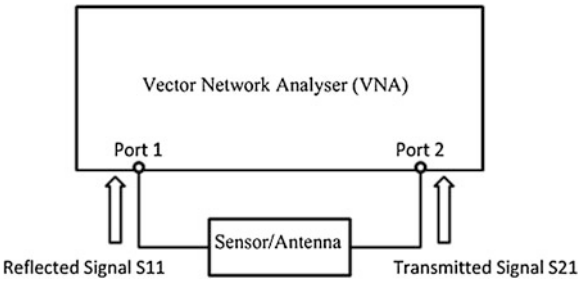

Fig. 1 Block diagram of a typical microwave system

provide unique signal spectrum signatures. Typically these would be in the form of a reflected signal (reflection coefficient) S_{11} and a transmitted signal (transmission coefficient) S_{21}, which are influenced by parameters such as conductivity and permittivity. Fig. 1 shows a block diagram of a typical microwave system. Reflected signal is of paramount importance in this study. A microwave sensing system is constructed of a microwave sensor, an oscillator and a detector. The purpose of the oscillator is to provide a microwave signal to the sensor, while the detector measures the response of the sensor. This functionality is embodies in a typical vector network analyzer (VNA) such as the Rohde and Schwarz ZVL-6 which is used throughout this study.

The system presented in in this chapter proposes to utilize EM wave technology within the microwave region (300 MHz–300 GHz) in order to characterize defects in conductive materials such as aluminum and steel. These materials are widely used in many important industrial sectors, e.g. construction, automotive, aerospace and military. Section 3 of this chapter talks more on the topic of microwave sensors used in a wide range of applications, but the basic operating principle can be found in consideration of transmission lines (e.g. two pair and coaxial), where we know that the impedance of such a transmission line varies with parameters such as resistance (R), inductance (L), conductance (G) and capacitance (C). These can be represented as in Fig. 2. () shows how these parameters are linked to give characteristic transmission line impedance (Z_0), where ω is the angular frequency and j is the imaginary unit.

$$Z_o = \sqrt{\frac{R + j\omega L}{G + j\omega C}} \tag{1}$$

From (1) it is evident that characteristic impedance will change based upon the defined parameters (R, L, G and C). From the perspective of a microwave device (i.e. a sensor or antenna) which is exposed to a real world environment, changes which occur in this environment can be measured as they influence the device characteristic impedance, and therefore its response at varying frequencies. This is the basic principle upon which this work is founded; the challenge is to prove this principle can be applied for real-time continuous NDT of metallic materials. The system will operate at various frequencies within the microwave region. Changes

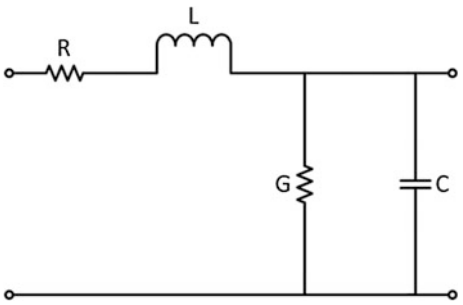

Fig. 2 Key parameters of a transmission line

in response (e.g. frequency, amplitude, phase, etc.) as a result of phenomena such as corrosion, cracking and penetration will be measured. The excitation frequency will depend upon the physical properties of the materials and the fabric responses at various frequency bands. The process of excitation will be segmented such that individual sheets or components are treated separately, thus allowing the system to detect and report localized damage. When a change in response is detected, the system can be designed to have various outputs to suit the operators need. For example, an output could be in the form of an alert mechanism that suggests the component requires some attention in a particular area, thus encouraging targeted maintenance.

3 Current Technologies

3.1 Microwave NDT

Detection of cracks on metal surfaces using microwave NDT was first reported by Feinstein et al. in 1967 using a waveguide [10]. Feinstein et al. used the mode conversion that takes place when an electromagnetic wave of a given polarization impinges on a planar metal surface with a crack. The method used was based on rotating the polarization of the incident wave and associating a particular polarization component in the scattered signal with the crack signature. The crack, in other words, converts parts of the incident wave to an orthogonally polarized wave.

A coupled-stripline crack detector built by Gysel et al. in used two coupled striplines to support two orthogonal modes [3]. The two striplines are excited in one mode and a crack in the metal surface couples energy into the other mode. The crack supplies a coupling mechanism between two modes that are orthogonal. In the absence of cracks, the system is balanced, so that no signal reaches the detector. When a crack unbalances the system, a small signal reaches the detector. Bahr in 1981 used an electromagnetic scattering model in conjunction with microwave measurement to predict the dimension of cracks [11].

The use of an open-ended coaxial probe has received great attention in microwave testing for its distinct advantages, including wide frequency band, ability to inspect hard-to-reach areas, and high sensitivity compared to other microwave probes. Several methods using microwaves were investigated by, Zoughi, Yeh, Qaddoumi and Huber [12–14]. The basis of most of these methods was either using an open-ended rectangular waveguide probe or an open-ended coaxial line probe. The idea behind their work is that without a crack the metal surface behaves like a short circuit. However, if a crack is present high order modes will be generated, i.e. the surface current is disrupted. In an open-ended rectangular waveguide, only the dominant TE_{10} mode may propagate, all other modes are evanescent and decay exponentially. When no crack is present, only the TE_{10} mode exists in the waveguide. However, when a crack is present, the field distribution will be perturbed, thus higher-order modes are generated.

Kharkovsky et al. used the near-field millimeter-wave imaging technique, utilizing a flange-mounted rectangular waveguide probe and a phase-sensitive reflectometer to detect exposed and covered fatigue cracks [15]. A recent study by the same research team used a microwave dielectric-loaded rectangular waveguide resonator sensor to evaluate shallow flaws in metals [16, 17]. The resonator consisted of a rectangular waveguide loaded with a transversely and longitudinally finite dielectric insert that concentrates the electromagnetic field within it and effectively creates a quarter-wavelength resonator. The resonator is short-circuited at one end and the other end is formed by tapering the dielectric insert.

Other work using microwaves for detecting cracks has been presented by researchers such as, F. Mazlumi, J. Kerouedan and G. Ponchak [4, 18, 19]. J. Kerouedan et al. [4] demonstrated how micro-cracks at the surface of metals can be detected and imaged by near-field microwave from the crack-induced variations of the resonance frequency. Two resonant sensors are used, a quarter wavelength micro-strip line resonator, terminated by an electric dipole and a dual-behavior resonator (DBR) band-pass filter probe. They used the reflection and transmission coefficients of the DBR probe interacting with a metal sample to detect and image surface defects. Ponchak et al. used an evanescent field microwave imaging probe (EMP) using two resonators; a coplanar waveguide resonator and a strip-line resonator to obtain images of metal lines with 2.6 μm spatial resolution and a minimum detectable line width of 0.4 μm at 1 GHz.

Microwave NDT method is also widely used to detect corrosion in metals. Corrosion will in most cases be hidden under paint and cannot be visually detected. Thus detection will only be possible when corrosion is severe. The initiation of corrosion is preceded by the presence of corrosion precursor pitting. One method to detect corrosion is to detect the presence of precursor pitting [20]. Detection of precursor pitting yields information about the susceptibility to corrosion initiation. When a precursor pitting becomes relatively large, the corrosion process has already initiated.

Tapered rectangular waveguides can also be used in corrosion detection to investigate the interaction of electromagnetic waves with a layer of dielectric structure with known properties as a replacement of the standoff layer (air) to

obtain higher spatial resolution [21]. An E-plane linear tapered rectangular waveguide was constructed from a standard rectangular waveguide by flaring the narrow dimension of the waveguide linearly in the direction of propagation. By tapering the waveguide the probes sensing area reduces and the spatial resolution improves, and consequently images of high fidelity for concealed entities can be obtained.

3.2 Vision Systems

The advance of high speed computers and cameras has increased the use of vision systems in many applications such as weld monitoring and nuclear decommissioning. Vision systems are particularly useful in hazardous and hard to reach environments since they can be operated remotely. One of the major advantages of using a visual sensing technology to monitor welding operations is the fact that the visual sensor is not touched or interfered with during the welding process and visual images of the weld pool contain more abundant and accurate information about the welding dynamics. B. M. Abdullah developed a vision system for monitoring of arc welding in real-time. The system uses a camera, an illumination source and a combination of filtering and illumination-camera synchronization techniques. Arc light (noise) is totally eliminated and a substantial amount of information is obtained in real-time, e.g. metal transfer and weld pool geometry [22, 23]. Fig. 3a shows the block diagram of the main components of the vision system. Meanwhile, Fig. 3b shows an image of a TIG welding process obtained by the system in real-time. As can be seen the interference from the arc light is totally eliminated and the image is of very high quality.

3.3 Conformal Load-bearing Antenna Structure

Conformal Load-bearing Antenna Structure (CLAS) functions as an antenna while at the same time being part of the structure. Conventional antennas are very expensive and difficult to manufacture. Furthermore, their subsequent mounting or housing aboard vehicle platforms requires extensive structural modifications. The use of CLAS technology is therefore an attractive alternative to existing systems especially in the aerospace industry where conventional antennas have protruding aerials, which are weak and increase drag and weight. The approach using CLAS instead of the conventional antennas reduces weight, drag and also enhances electromagnetic performance, damage resistance and structural efficiency. In the aerospace industry, it will also allow aircrafts to be designed around mission requirements rather than platform limitations.

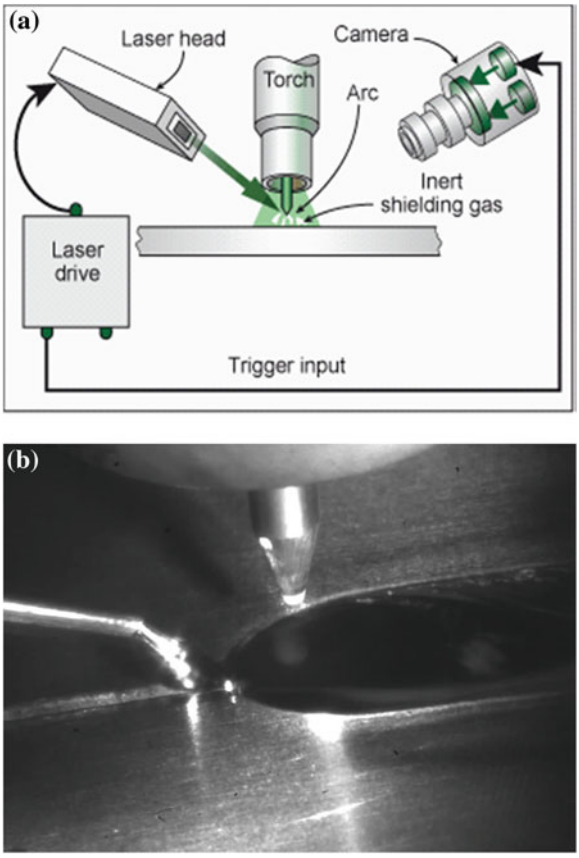

Fig. 3 Block diagram of weld monitoring vision system (**b**) Image of a TIG welding process obtained in real-time

CLAS technology is used more for communications rather than NDT. However, since the antenna forms part of the structure, the sensor can be designed to test for defects in the structure that it is part of. A literature review by Paul J. Callus for the Australian Department of Defense was conducted with a focus on ongoing research activities by the United States Air Force [24]. The study concentrated on the advantages and limitations of CLAS to help decide whether to incorporate CLAS into Australian Defense Force aircraft. In the study, it is hypothesized that many systems could contribute to structural integrity, and similarly parts of the airframe structure could contribute to functionality. For example many of the constituents of ballistic armor would have sufficient mechanical stiffness and strength to act as load-bearing structure. Thus, a multifunctional aircraft structure is an airframe structure that serves the dual purpose of providing for structural integrity as well as a functional system.

3.4 Traditional Methods

A great deal of research work on NDT of metals in the NDT community is carried out using techniques other than microwave testing. The most popular of these methods include; radiography, magnetic particle inspection, dye penetrant testing, ultrasonic and eddy current. Radiography is suitable for the detection of internal defects in ferrous and non-ferrous materials. Radiography can also provide real-time diagnosis such as computerized tomography. Information can also be presented pictorially. Advantages also include its suitability for any material. However, there are quite a few disadvantages of using radiography such as; inability to cope with thick sections, possible health hazards, not suitable for surface defects and no indication of depth of defects. Magnetic particle inspection is suitable for the detection of surface and near surface discontinuities in only magnetic materials. Dye penetrant is frequently used for the detection of surface breaking flaws in non-ferromagnetic materials. The operation is simple and suitable for automatic testing. However, it uses a considerable amount of consumables and suffers decreased sensitivity. Ultrasonic techniques are used for the detection of internal and surface defects in sound conducting materials. The main advantage of this method is its ability to detect flaws deep inside materials and it can be extremely sensitive if required. Eddy current testing is used mainly for the detection of surface or subsurface flaws, conductivity measurements and coating thickness measurements.

Other methods also exist, some of which are developments of the aforementioned methods and some are specialized methods. Brudar used electromagnetic NDT to distinguish surface cracks from subsurface cracks. The method is based on determining changes in the amplitude and phase of the magnetic flux over a cross-section in a metal bar containing defects. It was shown that for surface and subsurface cracks, the resultant magnetic fields have phases which lead and lag respectively the field from a bar with no defects [2]. Hirao et al. in their review article on electromagnetic acoustic resonance techniques (EMAR) highlighted the wide applications this technique can be used for, e.g. stress measurement and fatigue damage [25]. This method relies on the use of electromagnetic-acoustic transducers (EMATs) and the super-heterodyne circuitry for processing the received reverberation signals excited by long radio-frequency bursts. Kalyanasundaram et al. used ultrasonic techniques for defect detection in weld elements of austenitic stainless steel and for fatigue crack growth in 316 stainless steel [26]. Another ultrasonic technique is used by Murayama et al. to evaluate the formability of zinc-coated steel sheets [27]. The technique is based on the dispersion relation, which correlates the velocity anisotropy of the S_0-mode Lamb wave to the texture defined by orientation distribution coefficients.

Thermal NDT of materials for defects is another crack detection method, in which propagation of thermal waves in solids are studied and analyzed. Active thermography usually employs a pulse or sinusoidal thermal stimulus. An alternative approach in which the thermal stimulus is frequency modulated was proposed by Tuli et al. [28]. In Frequency Modulated Thermal Wave Imaging

(FMTWI), a specimen is heated for launching thermal waves into the sample, not at a single frequency (lock-in), or at all frequencies (pulsed), but in a desired range of frequencies in a decided time span.

Infrared (IR) imaging technique can be used to detect defects in metals. It is usually used to detect the temperature of a surface, and sometimes used to detect anomalies due to temperature profiles in the sample under study. Qidwai et al. used IR imaging technique in conjunction with image deconvolution algorithms to detect defects in metallic plates [29]. Heat distribution remains fairly homogenous in a healthy metal and can be seen as a flat surface under an IR imaging camera. However, things change drastically if there is a discontinuity in the homogenous metal, such as cracks. This change is exploited as an output of a defect function.

4 Methodology and Sensor Design

4.1 Patch Sensor

In the near-field mode, a patch antenna (or sensor) has been developed as a resonant sensor for microwave NDT. The resonant frequency of the sensor is indicated by the minimum in the return loss. The resonance frequency and amplitude of the sensor shifts depending on the permittivity of its environment and, in this way, degradation or anomalies in conductivity materials can be detected. A patch antenna operating at microwave frequencies was chosen for this work as such devices are flat with a reasonably large contact area. They can be pressed uniformly against an artificially damaged piece of metal, which will be used to represent a small piece of a sheet metal. A software model is constructed using the Ansys High Frequency Structure Simulator (HFSS) package to ascertain appropriate dimensions for the patch sensor, and this model is shown in Fig. 4. Once appropriate dimensions were attained, the software model was then constructed on double sided FR4 substrate.

Only the top layer is routed, the under layer is left untouched and acts as a ground plane. The patch has a single SMA connector to allow measurements to be taken using a Vector Network Analyzer (VNA) via a coaxial connection. Figure 5 shows the return loss of both the HFSS software model and the constructed sensor with a reasonable similarity displayed between the two. This gives confidence that the software model gives a good approximation of the real world for future use.

Figure 6 shows the Rhode and Schwarz ZVL-6 VNA connected to the patch sensor with a defective aluminum plate and a PMMA layer on top. All measurements are acquired in the form of S-Parameters, specifically measuring changes in reflected signature (EM wave spectrum) back from the antenna when interacting with the material under test.

The sensor and defective metallic layer are separated by a thin (1.5 mm) layer of polymethylmethacrylate (PMMA) to prevent short circuiting the patch. Multiple

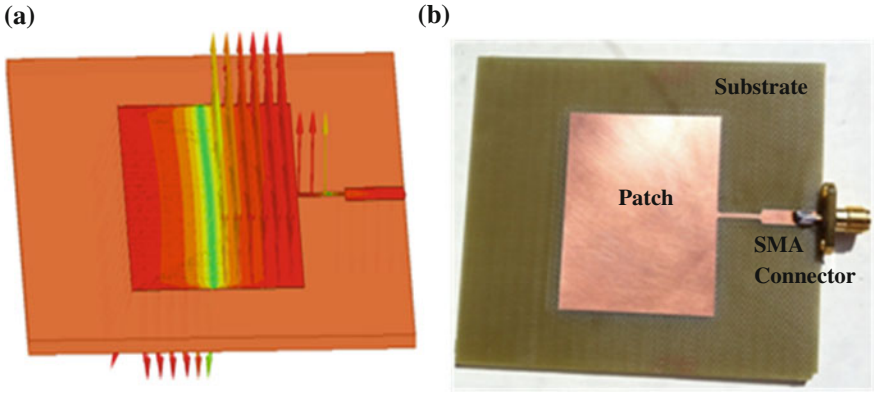

Fig. 4 **a** Ansys HFSS model showing electric field and **b** actual patch sensor

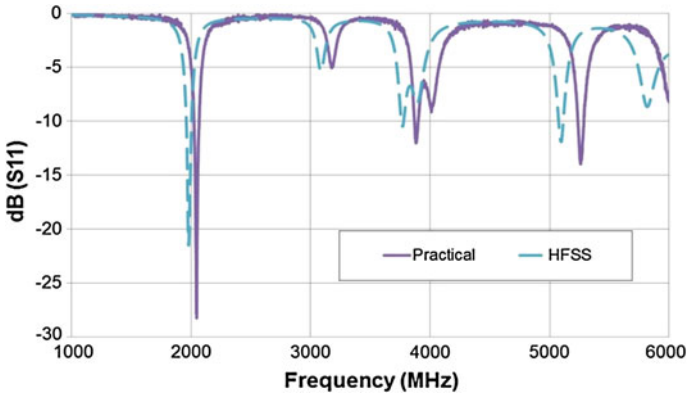

Fig. 5 Ansys HFSS software model and real world sensor S_{11} comparison, showing a good match between the reality and simulation

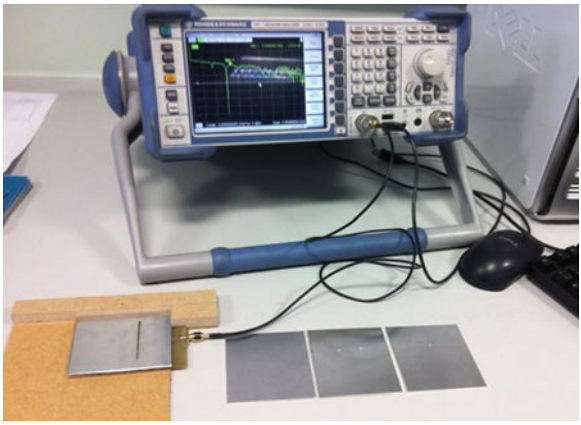

Fig. 6 Experimental apparatus, sensor with PMMA layer and an artificially damaged aluminum piece

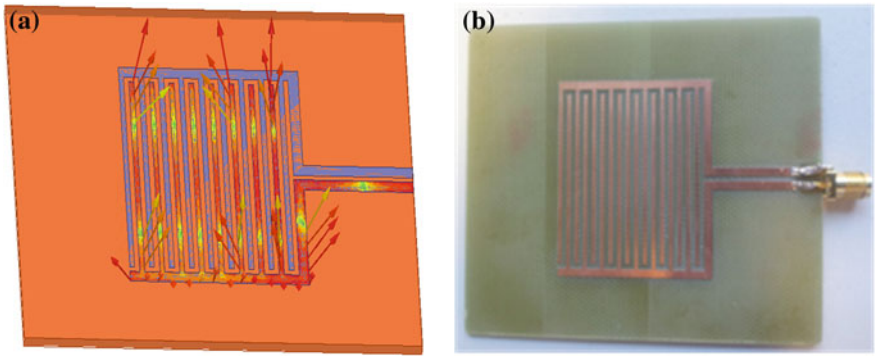

Fig. 7 **a** Ansys HFSS model showing electric field and **b** Constructed interdigitated sensor

measurements were taken from the sensor and averaged in the following configurations:

1. Sensor without any metal plates.
2. Sensor exposed to a defect free metal plate.
3. Sensor exposed to a metal plate with a slot (2 × 50 mm) cut into it, emulating a large crack.
4. Sensor exposed to a metal plate with a longitudinal crack.
5. Sensor exposed to a metal crack with a vertical crack.

4.2 Interdigitated Electrode Sensor

IDE sensors have been used for a number of years for monitoring changes in dielectric materials, but have seen limited application for sensing purposes outside of this domain and are rarely used at frequencies greater than 1.0 GHz. The extraordinary feature of IDE sensors is their excellent sensitivity to change close to the sensor surface, with this sensitivity decaying rapidly as one moves further away. This is advantageous as it reduces significantly the chance of undesirable factors influencing sensor response.

Another notable feature, and one which encouraged experimental work in this project, is the multiple elements available. The addition of elements to the sensor changes significantly the spectral response. When elements are individually exposed to some change, this gives a unique spectral change, which may give the opportunity to exploit such behavior for the detection of damage location. The IDE sensor was designed and constructed as shown in Fig. 7. To test this sensor, a similar methodology was undertaken to that of the patch sensor, primarily so that the patch and IDE sensors can be compared like for like.

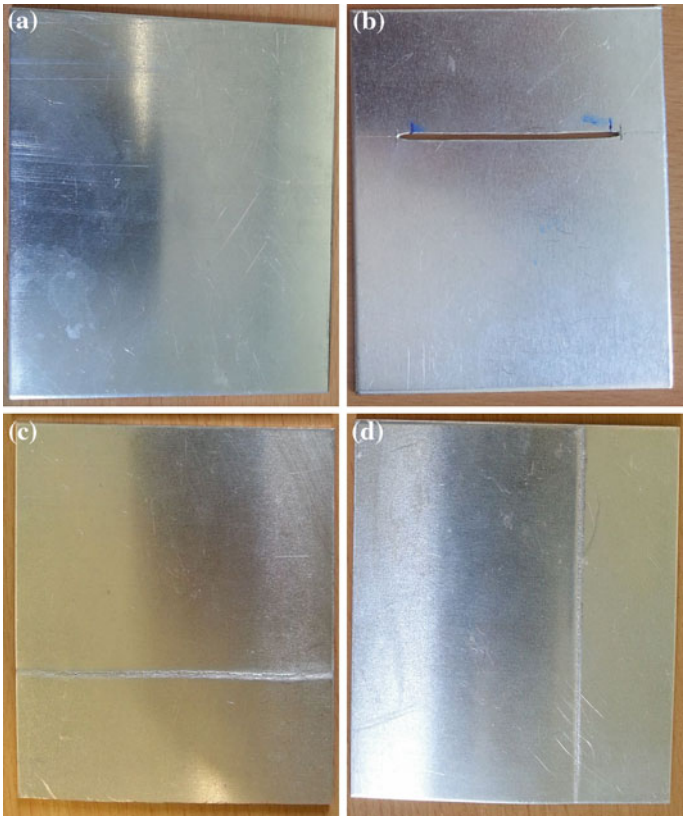

Fig. 8 Aluminum plates with **a** no defect, **b** horizontal defect, **c** horizontal crack, and **d** vertical crack

5 Results

5.1 Crack Monitoring

5.1.1 Patch Sensor

Figure 8 shows the four different aluminum plates used; (a) Non-defective plate, (b) Horizontal slot plate, (c) Horizontal crack plate and (d) Vertical crack plate. The different defects were introduced into the three aluminum plates so that the sensor can be used to detect them. The non-defective plate here is used as a comparison guide. Crack detection using a patch sensor excited in the frequency range 1–6 GHz with a variety of defect types are shown in Fig. 9. Figure 9a shows the full spectrum response between 1–6 GHz, while Fig. 9b highlights a region in the spectrum where there is notable response as a result of the metal defects.

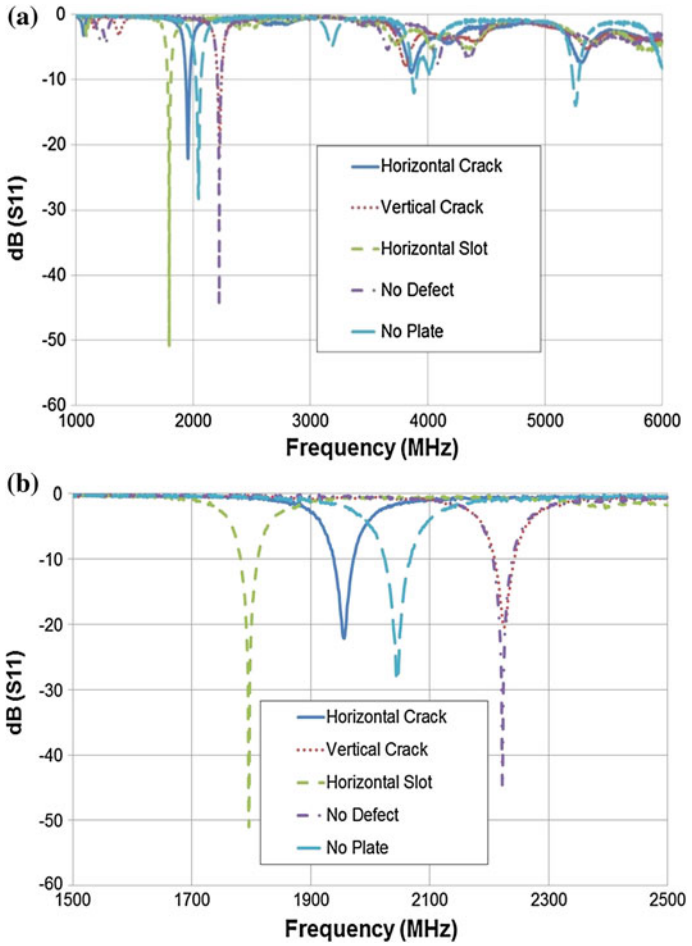

Fig. 9 Spectral response of the patch sensor for each aluminum plate **a** Spectral response between 1000–6000 MHz and **b** A notable response to the defective metallic plates between 1500–2500 MHz

Interestingly, the slot defect encourages a far greater response from the sensor than other defects. The major response from the sensor due to defects on the test plates is centered on the resonant frequency of 2.0 GHz. Each plate has a distinctive frequency shift as can be seen. This is a significant result as prediction of the type and orientation of defects can be easily determined. The purpose of this initial phase of the research project work has been to prove the principle of the idea underpinning this study: will a defect elicit a change in response in an EM wave sensor system? As shown, defects presented to the sensor do indeed elicit a response or change in the measured S_{11} reflection coefficient spectrum. Therefore

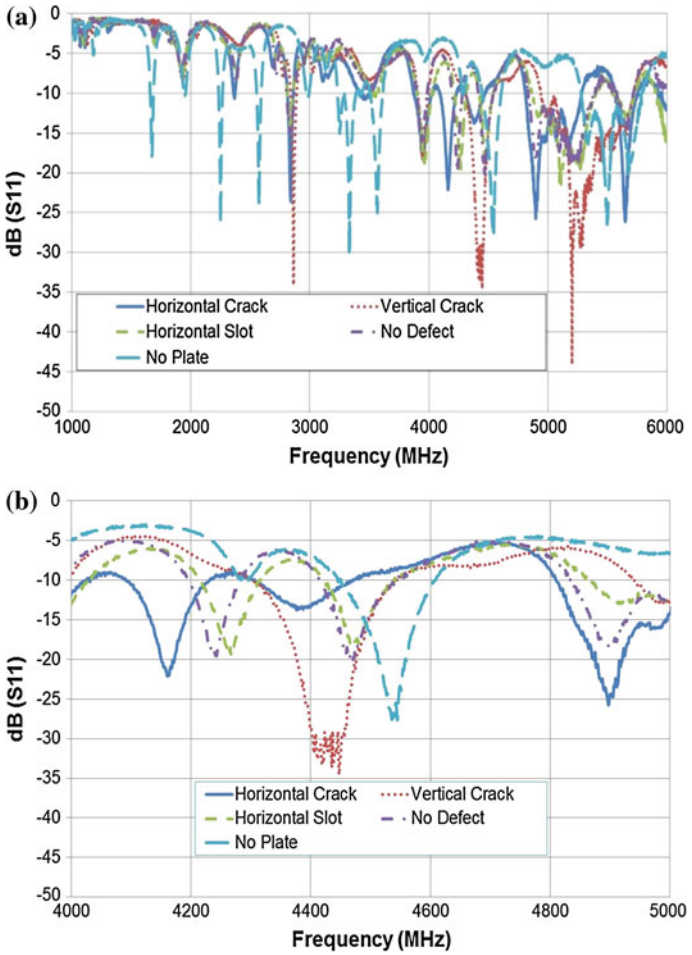

Fig. 10 Spectral response of the IDE sensor **a** Spectral range, 1000–6000 MHz **b** A notable response to the defective metallic plates between 4000–5000 MHz

it is possible to say that the underlying principle is sound, and the challenge lies in developing a sufficiently capable sensor system to satisfy the target requirements.

5.1.2 Interdigitated Electrode Sensor

Crack detection using an IDE sensor excited in the frequency range 1 GHz-6 GHz with a variety of defect types are shown in Fig. 10. Figure 10a shows the spectrum response between 1,000–6,000 MHz, while Fig. 10b highlights a region in the spectrum where there is notable response as a result of the metal defects. The most notable feature is the significant number of resonant peaks available with the IDE

sensor, which indicates that the various sensing elements (or digits) each influence the obtained spectrum (or signature). This gives a different characteristic performance when compared with the patch antenna since it means that we now have multiple frequencies where one could expect a change to occur. It is believed that this will give significant advantages in terms of identifying the defect type present with greater sensitivity, selectivity and high resolution. It is shown in Fig. 10 for example that each scenario tested gives a significantly different spectral signature, and we see that this is not isolated to a changing response at a single frequency. These changes manifest as both frequency and amplitude changes in the measured spectra.

The results presented for the IDE device show that it has favorable characteristics when compared to the patch. The availability of broadband response (in the cases shown here up to 6 GHz) allows for more information to be revealed from the captured spectrum. The results shown so far give an indication that that this type of structure has a good potential for exploitation in terms of being able to assess damage type, size and location.

The measurements taken and presented in this chapter are designed to consider the types of crack defect which could be detected by the EM wave sensor used in this project. It is evident from the different obtained spectra that the technique shows quite different responses depending upon the defect type (i.e. slot, crack). Note that all measurements were repeated six times and the results shown represent the average of these repeated measurements.

From the spectra shown so far it would be feasible to suggest that the method could detect:

1. Defect types of cracks, since cracks and slots give different spectral signatures.
2. Defect orientations of cracks, since at lower frequencies the sensor responds most to horizontally orientated defects, but shows an apparent increasing sensitivity to vertically orientated defects at higher frequencies (i.e. > 3 GHz).

Another advantage for this type of monitoring is the possibility of revealing concealed defects, which current methods cannot detect. The sensor can also be integrated onto other devices and can be used remotely as a real-time monitoring smart system. Progression of defects, their types, size and location can be monitored in real-time and appropriate actions can be taken. Hence, detection of major defects before it progresses to an unsafe level would be of huge interest to numerous industries.

5.2 Corrosion Monitoring

Aluminum has a very high resistance to corrosion. One reason for this is that aluminum is covered by a thin but effective coating of oxide which protects it from further oxidation. The aluminum oxide is impermeable and is integral with the

Fig. 11 Electrolysis to accelerate corrosion

base metal. If the coating of oxide is damaged mechanically this coating will be renewed immediately. The coating of oxide is a main reason for the good corrosion characteristics of aluminum. Different types of corrosion, more or less visible to the naked eye, can occur on aluminum, such as uniform corrosion, pitting corrosion, stress corrosion, etc. The predominant type of corrosion will depend on a certain number of factors that are intrinsic to the metal, the medium and the conditions of use.

The aim here is to utilize a similar methodology as adopted for the crack monitoring measurements to determine whether or not the EM wave system could be utilized to monitor corrosion of aluminum sheets. Five aluminum plates (7 cm by 8 cm) are monitored using the patch sensor. Four plates are corroded, whilst the fifth plate is left untouched mainly since it is useful to show the results of a non-defective plate alongside those which were corroded. Electrolysis is used to accelerate corrosion. Sea water corrosion mixture is first dissolved in water; cathode and anode electrodes of the voltage supply are then immersed into the solution as shown in Fig. 11.

The plates are divided into two sets; plate 1 and plate 4 were corroded together for the same length of time and in the same solution and plate 2 and plate 3 were corroded together. It is clear in Fig. 12 that the measurements taken from the corroded plates show a good level of reproducibility; i.e. each set of plates give similar results. All results shown in this report are repeated numerous times and an average result given. In Fig. 12, it is evident that there are changes in the spectra corresponding to the four corroded plates. Each plate behaves differently due to the amount of corrosion it endured and produces a unique spectrum which can be used to identify the level of corrosion.

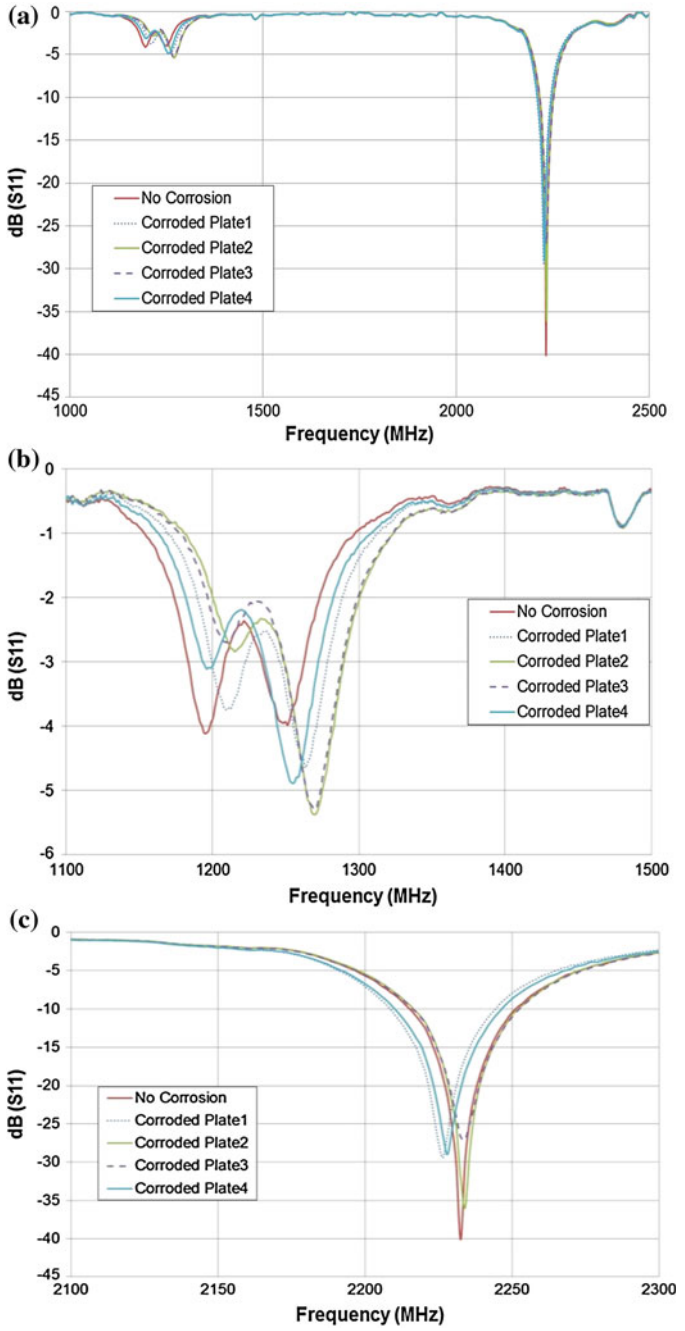

Fig. 12 Spectral response of the patch sensor **a** Spectral range, 1000–6000 MHz **b** A notable response to the corroded metallic plates between 1100–1500 MHz **c** A notable response to the corroded metallic plates between 2100–2300 MHz

6 Conclusion

There are a number of NDT methods available for inspection of metallic materials. However, many of these are expensive, not applicable in real-time and time-consuming as point-by-point inspection is needed. Literature relating to microwave technologies applied to these areas suggest that damage detection of conductive materials is possible, although many of the techniques applied are not applicable in the given scenario but rather as a tool for manual inspection. The use of microwave technologies presents a novel addition to the current suite of NDT tools, while giving the possibility for being cost-effective to implement, operating as an integral part of the target area to be sensed and providing the potential to operate truly in real-time.

In this chapter a novel method based on the use of EM waves to detect non-destructively the presence of defects in metallic materials is presented. The method is mainly concentrated on the interaction of EM waves with metallic material when they are in the vicinity of the EM sensor. The following sensors are developed and presented in this chapter; a patch sensor and an IDE sensor.

Results of the work showed that defects were detectable using EM wave sensors. The presence and type of defects in a conductive material elicit a change in the sensor spectral response and a unique sensor signature is obtained. In addition, the sensor utilized in this work showed that it responded to horizontally orientated cracks at lower frequencies than cracks aligned in a vertical direction; this suggests that the method could be applied to determine defect orientation. Thus the challenge for the subsequent phases of this work is to develop a system which can be applied and be robust enough to operate in the toughest of environments without an operator. The sensor can be integrated with the structure of platforms such as ships or building structures. Such integration appears to be the way forward for structural systems with them no longer simply providing a single function but rather a variety of functions, therefore becoming intelligent.

Furthermore, aluminum plates were corroded using sea water corrosion mixture to simulate varying corrosion aggressiveness. It was found that the patch sensor exhibited a shift in resonant frequency in response to the corrosion which took place and repeatability of the sensor measurements was confirmed.

References

1. BDM Federal, Inc. corrosion detection technologies, sector study, final report, prepared for North American Technology and Industrial Base Organization (NATIBO), March (1998)
2. B. Brudar, How to distinguish surface and subsurface cracks using electromagnetic ndt methods. NDT Int. **17**, 221–223 (1984)
3. U.H. Gysel, L. Feinstein, *Design and Fabrication of Stripline Microwave Surface-Crack Detector for Projectiles* (Stanford Research Institute, California, 1974)

4. J. Kerouedan, P. Quéffélec, P. Talbot, C. Quendo, S. De Blasi, A. Le Brun, Detection of micro-cracks on metal surfaces using near-field microwave dual-behavior resonator filters. Meas. Sci. Technol. **19**, 105701 (2008)
5. J. Jongwoo, K. Jungmin, L. Jinyi, P. Youngmin A hand held magnetic camera system for real time crack inspection, in *Sensors Applications Symposium (SAS), 2011 IEEE*, 2011, pp. 298–301
6. Günter Schmitt, Michael Schütze, George F. Hays, Wayne Burns, En-Hou Han, Antoine Pourbaix, Gretchen Jacobson, World corrosion organization global needs for knowledge dissemination, research, and development in materials deterioration and corrosion control, May (2009)
7. J. H. Goh, A. Mason, A. I. Al-Shamma'a, S. R. Wylie, M. Field, P. Browning, Lactate detection using a microwave cavity sensor for biomedical applications, in *Sensing Technology (ICST), 2011 Fifth International Conference on*, 2011, pp. 436–441
8. S.C. Mukhopadhyay, C.P. Gooneratne, A novel planar-type biosensor for noninvasive meat inspection. Sens. J. IEEE **7**, 1340–1346 (2007)
9. R. Zoughi, S. Ganchev, Microwave nondestructive evaluation, *State of the art review,* Colorado State University, Ft. Collins, CO 80523 February (1995)
10. L. Feinstein, R. J. Hruby, Surface Crack Detection by Microwave Methods, in *6th Symposium on Nondestructive Evaluation of Aerospace and Weapons Systems Components and Materials*, San Antonio, Texas, 1967
11. A. J. Bahr, Microwave Eddy-Current Techniques for Quantitative Nondestructive Evaluation, *American Society for Testing and Materials,* pp. 311–331, 1981
12. R. Zoughi, C. Huber, N. Qaddoumi, E. Ranu, V. Otashevich, R. Mirshahi, S. Ganchev, T. Johnson, Real-time and on-line near-field microwave inspection of surface defects in rolled steel, in *Microwave Conference Proceedings, 1997. APMC '97, 1997 Asia-Pacific*, vol. 3, 1997, pp. 1081–1084
13. C. Huber, H. Abiri, S.I. Ganchev, R. Zoughi, Modeling of surface hairline-crack detection in metals under coatings using an open-ended rectangular waveguide. Microwave Theory Tech. IEEE Trans. **45**, 2049–2057 (1997)
14. N. Qaddoumi, S. Ganchev, R. Zoughi, A novel microwave fatigue crack detection technique using an open-ended coaxial line, in *Precision Electromagnetic Measurements, 1994. Digestivas, 1994 Conference on*, 1994, pp. 59–60
15. S. Kharkovsky, M.T. Ghasr, R. Zoughi, Near-field millimeter-wave imaging of exposed and covered fatigue cracks. Instrum. Measur. IEEE Trans. **58**, 2367–2370 (2009)
16. S. Kharkovsky, A. McClanahan, R. Zoughi, D.D. Palmer, Microwave dielectric-loaded rectangular waveguide resonator for depth evaluation of shallow flaws in metals. Instrum. Measur. IEEE Trans. **60**, 3923–3930 (2011)
17. A. McClanahan, S. Kharkovsky, A.R. Maxon, R. Zoughi, D.D. Palmer, Depth evaluation of shallow surface cracks in metals using rectangular waveguides at millimeter-wave frequencies. Instrum. Measur. IEEE Trans. **59**, 1693–1704 (2010)
18. F. Mazlumi, S.H.H. Sadeghi, R. Moini, Analysis technique for interaction of rectangular open-ended waveguides with surface cracks of arbitrary shape in metals. NDT E Int. **36**, 331–338 (2003)
19. E. Ponchak, D. Akinwande, R. Ciocan, S. R. LeClair, M. Tabib-Azar, Evanescent microwave probes using coplanar waveguide and stripline for super-resolution imaging of materials, in *Microwave Symposium Digest, 1999 IEEE MTT-S International*, vol. 4, 1999, pp. 1859–1862
20. M.T. Ghasr, S. Kharkovsky, R. Zoughi, R. Austin, Comparison of near-field millimeter-wave probes for detecting corrosion precursor pitting under paint. Instrum. Measur. IEEE Trans. **54**, 1497–1504 (2005)
21. N. Qaddoumi, M. A. Khousa, W. Saleh, Near-field microwave imaging utilizing tapered rectangular waveguides, in *Instrumentation and Measurement Technology Conference, 2004. IMTC 04. Proceedings of the 21st IEEE*, vol. 1, 2004, pp. 174–177
22. B. M. Abdullah, Monitoring of Welding Using Laser Diodes, in *Semiconductor Laser Diode Technology and Applications* ed, 2012, p. 22

23. B. M. Abdullah, J. S. Smith, W. Lucas, J. Lucas, F. Malek, Monitoring of TIG welding using laser and diode illumination sources: a comparison study, in *Electronic Design, 2008. ICED 2008. International Conference on*, 2008, pp. 1–4
24. P. J. Callus, Conformal Load-Bearing Antenna Structure for Australian Defence Force Aircraft, 2007
25. M. Hirao, H. Ogi, Electromagnetic acoustic resonance and materials characterization. Ultrasonics **35**, 413–421 (1997)
26. P. Kalyanasundaram, B. Raj, T. Jayakumar, Characterization of microstructures in metallic materials using static and dynamic acoustic signal processing techniques, in *Advances in Signal Processing for Non Destructive Evaluation of Materials*, Quebec City, Canada, 2006
27. R. Murayama, K. Fujisawa, M. Hirao, H. Fukuoka, Non-destructive evaluation of formability of zinc-coated steel sheets using electromagnetic acoustic transducer. NDT E Int. **30**, 377–382 (1997)
28. S. Tuli, R. Mulaveesala, NDE for metals, composites and semiconductors by frequency modulated thermography, in *Indian Society for NDE*, Hyderabad, India, 2006
29. U. Qidwai M. Maqbool, Image deconvolution for enhancing IR images in order to detect defects in metallic plates, in *Signal Processing and Information Technology (ISSPIT), 2009 IEEE International Symposium on*, 2009, pp. 230–235

Chapter 10
Nanostructured Nickel Oxide by Hydrothermal Route for Gas Sensing Applications

D. V. Ahire, G. E. Patil, D. D. Kajale, V. B. Gaikwad and G. H. Jain

Abstract A hydrothermal process was used for the synthesis of nanostructured Nickel Oxide (NiO) with and without capping reagent (surfactant). Nickel Chloride ($NiCl_2$) a precursor of Nickel and Thioglycerol, a capping reagent, was used for this preparation. The structure, morphology and crystalline phase of the nickel oxide nanocrystal have been investigated by scanning electron microscopy (SEM), transmission electron microscopy (TEM) and X-ray diffraction (XRD). TEM images showed that the nickel oxide nanoparticles have hexagonal structure with uniform size distribution around 20–38 nm for NiO with capping agent and 23–100 nm for NiO without capping agent. Phase pure, cubic nickel oxide formation was identified from the XRD data. The thick films of NiO were prepared by screen-printing technique to study their gas sensing properties. The gas sensing performance of NiO thick films (with and without surfactant) were tested to H_2S, LPG, H_2, NH_3, Ethanol, CO, CO_2, and O_2, to operating temperature ranging from 100 to 450 °C, they showed maximum response to H_2S for 10 ppm gas concentration at 150 °C. The response and recovery values upon the exposures to 10 ppm H_2S gas and air were 4 and 58 s for NiO (with surfactant) thick film sensor, while those were 10 and 64 s for NiO (without surfactant) thick film sensor respectively. The NiO thick films have potential applications in H_2S gas sensor applications. The results are discussed and presented in this paper.

Keywords Hydrothermal route · Ni-doped ZnO nanorods · Gas sensor

D. V. Ahire · G. E. Patil · G. H. Jain (✉)
Materials Research Laboratory, K. T. H. M. College, Nashik 422002, India
e-mail: gotanjain@rediffmail.com

D. D. Kajale
Materials Research Laboratory, Arts, Commerce and Science College, Nandgaon 423106, India

V. B. Gaikwad
B. C. U. D., University of Pune, Pune 411007, India

A. Mason et al. (eds.), *Sensing Technology: Current Status and Future Trends I*, Smart Sensors, Measurement and Instrumentation 7, DOI: 10.1007/978-3-319-02318-2_10,

1 Introduction

In the twenty-first century, hydrothermal technology, on the whole, will not be just limited to the crystal growth, or leaching of metals, but it is going to take a very broad shape covering several interdisciplinary branches of science. Therefore, it has to be viewed from a different perspective. Further, the growing interest in enhancing the hydrothermal reaction kinetics using microwave, ultrasonic, mechanical, and electrochemical reactions will be distinct [1]. Also, the duration of experiments is being reduced at least by 3–4 orders of magnitude, which will in turn, make the technique more economic. With an ever-increasing demand for composite nano-structures, the hydrothermal technique offers a unique method for coating of various compounds on metals, polymers and ceramics as well as for the fabrication of powders or bulk ceramic bodies. It has now emerged as a frontline technology for the processing of advanced materials for nanotechnology. On the whole, hydrothermal technology in the twenty-first century has altogether offered a new perspective which is illustrated in Fig. 1. It links all the important technologies like geotechnology, biotechnology, nanotechnology and advanced materials technology. Thus it is clear that the hydrothermal processing of advanced materials is a highly interdisciplinary subject and the technique is popularly used by physicists, chemists, ceramists, hydrometallurgists, materials scientists, engineers, biologists, geologists, technologists, and so on.

The hydrothermal processing of materials is a part of solution processing and it can be described as super heated aqueous solution processing. Figure 7.2 shows the pressure temperature (PT) map of various materials processing techniques [2]. According to this, the hydrothermal processing of advanced materials can be considered as environmentally benign. Besides, for processing nanomaterials, the hydrothermal technique offers special advantages because of the highly controlled diffusivity in a strong solvent media in a closed system. Nanomaterials require control over their physico-chemical characteristics, if they are to be used as functional materials. As the size is reduced to the nanometer range, the materials exhibit peculiar and interesting mechanical and physical properties: increased mechanical strength, enhanced diffusivity, higher specific heat and electrical resistivity compared to their conventional coarse grained counterparts due to a quantization effect [3].

Further, the technique facilitates issues like energy saving, the use of larger volume equipment, better nucleation control, avoidance of pollution, higher dispersion, higher rates of reaction, better shape control, and lower temperature operations in the presence of the solvent. In nanotechnology, the hydrothermal technique has an edge over other materials processing techniques, since it is an ideal one for the processing of designer particulates. The term designer particulate refers to particles with high purity, high crystallinity, high quality, mono-dispersed and with controlled physical and chemical characteristics. Today such particles are in great demand in the industry. In this respect hydrothermal technology has

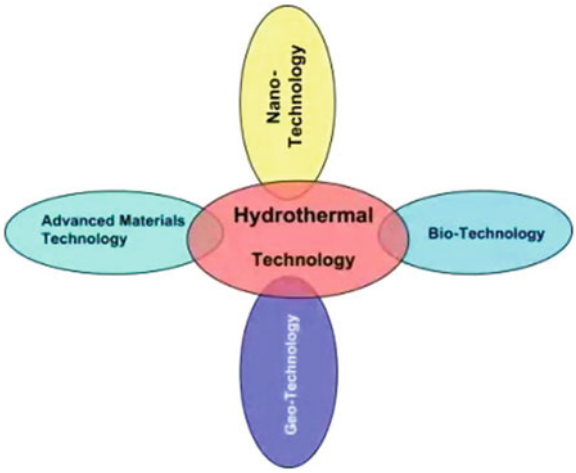

Fig. 1 Hydrothermal technology in the twenty-first century [1]

witnessed a seminal progress in the last decade in processing a great variety of nanomaterials ranging from microelectronics to micro-ceramics and composites.

Synthesis of size and shape controlled metal oxide nanostructures is very important in controlling their physical and chemical properties, and crucial for their potential uses. Recently, considering the properties of the materials are greatly affected by their morphologies, wide range of metal oxide with different morphologies providing great opportunities for the discovery of new properties and potential uses have been synthesized via different methods. Among these methods, hydrothermal approach [4, 5] has great advantages in synthesizing metal oxide crystals through relative low temperature and simple equipment, which makes the method more suitable and economic for large-scale production.

Semiconductor metal oxides as gas sensing materials have been extensively studied for a long time due to their advantageous features, such as good sensitivity to the ambient conditions and simplicity in fabrication [5–7]. Nevertheless, there are still some critical limitations to be overcome for the commercial sensors based on particulate or thin-film semiconductor metal oxides, such as limited maximum sensitivity, high working temperatures and lack of long-term stability.

In the last decade, nanostructured materials display more attractive physical and chemical properties than conventional bulk materials, due to their small particle size, large surface to volume ratio and high surface energy. These properties cause metal oxides with high porosity and nanostructure considered promising candidates in the development of gas sensor with high performance. Nanoscale oxide particles of transition metals are gaining continuous importance for various applications such as catalysts, passive electronic components and ceramic materials [8]. Due to their small size, nanoparticles exhibit novel material properties that are significantly different from those of their bulk counterparts.

Nickel oxide (NiO) nanoparticles with a uniform size and well dispersion are desirable for many applications in designing ceramic, magnetic, electrochromic

and heterogeneous catalytic materials [9]. Several researchers have prepared NiO nanoparticles by various methods like sol-gel [10], surfactant-mediated synthesis [11], thermal decomposition [12], polymer-matrix assisted synthesis [13] and spray-pyrolysis [14]. Some of the above methods suffer from the difficulty in size-homogeneity and well dispersion of NiO nanoparticles. Among them hydrothermal method has more advantages, such as its simple process, low cost and facility to obtain high purity products. Hence, it is quite promising and easy to use for industrial applications. Up to now, many methods have been developed to synthesize NiO nanoparticles and nanorods, but few attempts have been made to prepare porous NiO nanosheet [15, 16]. In this chapter, we report a simple and novel approach to the fabrication of nanostructured NiO cubes by hydrothermal method. It is expected to explore a more extensive potential application of transitional metal oxides.

2 Experimental

2.1 Preparation of Materials

A hydrothermal process was used for the synthesis of nanostructured NiO with and without capping reagent (surfactant). All reagents were purchased from Sigma-Aldrich and used as received. First, 0.1 M of the Nickel Chloride ($NiCl_2$) a precursor of Nickel was dissolved in 20 mL of deionised water–ethanol (1:1 volume ratio), a 5 M NaOH solution was prepared in deionised water for maintaining pH of the reaction, a 0.2 M Thioglycerol, a capping reagent, solution was prepared in isopropyl alcohol with constant stirring to make clear solution.

2.2 NiO With Surfactant

The solution of Thioglycerol was added slowly in the solution of NaOH with continuous stirring for 1 h. Add Nickel chloride solution slowly in as prepared solution of Thioglycerol with constant stirring and maintained pH = 11 by addition of more NaOH solution, say this is solution ‘A’.

2.3 NiO Without Surfactant

The solution of NaOH was slowly added in the solution of Nickel chloride solution with continuous stirring and maintained pH = 11, say this is solution ‘B’.

Then these prepared homogeneous solutions (25 mL each A and B separate) were transferred in 50 mL capacity autoclaves with Teflon liner by uniform heating at 200 °C for 15 h. These reaction mixtures were heated at a rate of 5 °C min^{-1}. After completion of the reaction, it was cooled to room-temperature and powdered samples were collected by centrifugation. Powdered sample was thoroughly washed with deionised water and ethanol. Samples were dried at 80 °C for 12 h. The materials were characterized by XRD, UV, SEM and TEM techniques.

2.4 Preparation of Thick Films

The thixotropic paste was formulated by mixing the fine powder of as prepared NiO (with and without surfactant) with the solution of ethyl cellulose (a temporary binder) in a mixture of organic solvents such as butyl cellulose, butyl carbitol acetate and terpineol etc. The ratio of inorganic part to organic part was kept at 75:25 in formulating the paste. This paste was screen printed [17, 18] on glass substrate in the desired pattern. The films were fired at 550 °C for 30 min.

3 Characterization Results

3.1 Structural Analysis Using XRD

Figure 2 shows the X-ray diffractograms of the as prepared NiO nanopowder with and without surfactant. All the peaks can be indexed to hexagonal NiO, with the lattice. The observed peaks match well with the standard JCPDS data of NiO [19]. The broad peaks are due to the nanocrystalline nature of NiO. The average grain size calculated from Scherrer's formula was about 13 and 19 nm for NiO with and without surfactant. The surfactant controls the size of the particles due to its surface passivation [20, 21].

3.2 Surface Morphology

Figure 3a, b depicts the SEM images of nanostructured NiO (with and without surfactant) thick films fired at 550 °C with equal magnifications. The particles get agglomerated due to firring process which was done for removal of organic binder.

It is clear from the SEM images that the average particle size of the NiO (with surfactant) thick film was smaller than the particle size associated with the NiO (without surfactant) thick film. Figure 3b is the SEM image of the NiO (without surfactant) thick film. It shows a high degree of agglomeration of particles with a

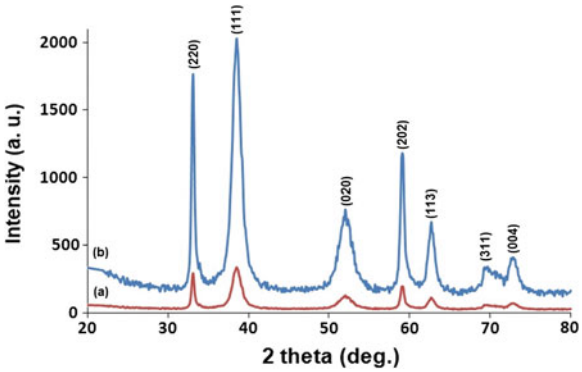

Fig. 2 X-ray diffractogram of pure nanocrystalline NiO **a** with and **b** without surfactant

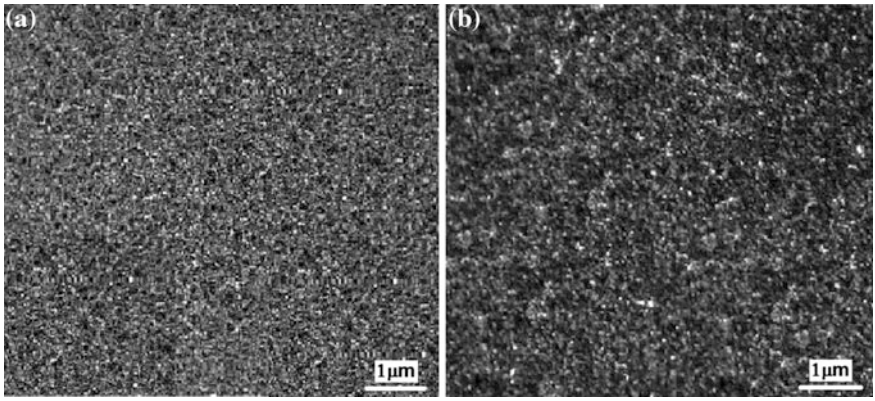

Fig. 3 SEM images of the nanocrystalline NiO **a** with and **b** without surfactant thick films

wide range of particle size distribution. Due to the high degree of agglomeration the porosity of the film was observed to be decreased, which in turn decreased the in-pore adsorption of gas, leading to a smaller surface to volume ratio, in turn less gas response (without surfactant) compared to NiO (with surfactant) thick film.

3.3 Transmission Electron Microscopy

Figure 4(a–d) shows the TEM images of NiO (with and without surfactant) powders with different magnifications. The average particle size of the NiO with surfactant is 28 and 58 nm for NiO without surfactant. The surfactant plays important role in controlling the growth of the NiO particles. The TEM images clearly indicate spherical and cubic particles distributed uniformly.

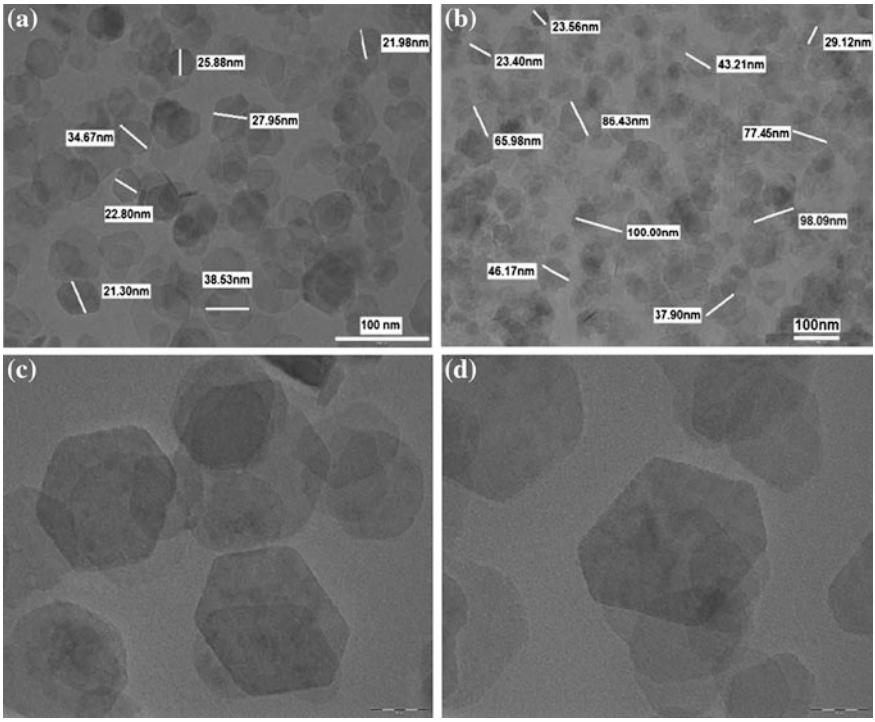

Fig. 4 TEM images of the nanocrystalline NiO **a**, **c** with and **b**, **d** without surfactant thick films

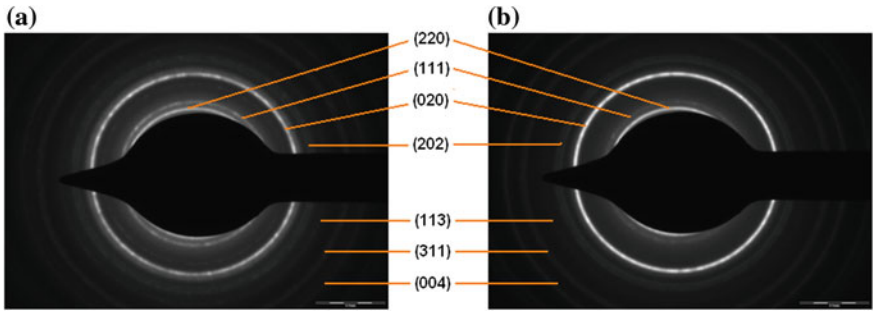

Fig. 5 SAED pattern of NiO nanoparticles **a** with and **b** without surfactant

3.4 Electron Diffraction Pattern

Figure 5a and b show the selected area electron diffraction (SAED) patterns of NiO (with and without surfactant) powders. It is clear from the figures that the NiO particles are crystalline in nature. The electron diffraction patterns show diffuse but

continuous ring patterns without any additional diffraction spots and rings of secondary phases revealing their crystalline structure.

Seven fringe patterns corresponding to planes: (220), (111), (020), (202), (113), (311), and (004) are consistent with the peaks observed in XRD patterns. XRD and TEM studies confirmed pure hexagonal structure of NiO as evidenced from Figs. 2 and 4 respectively.

4 Gas Sensing Performance

4.1 Gas Response with Operating Temperature

The gas sensing performance of NiO thick films (with and without surfactant) was tested to H_2S, LPG, H_2, NH_3, Ethanol, CO, CO_2, and O_2, at the operating temperature ranging from 100 to 450 °C, they showed maximum response to H_2S for 10 ppm gas concentration, as shown in Fig. 6.

Wang and co-workers [22, 23] suggested that the gas response was mainly dependent upon two factors. The first is the amount of active sites for oxygen and the reducing gases on the surface of the sensor materials. The more active sites the surface of nanosensor contain, the higher sensitivity the sensor exhibits. The second is the reactivity of the reducing gases. The bond energy of H–SH is 381 kJ/mol [24], so that it is easy to open the bond H–SH at lower temperature compared to other interfering gasses. It is clear from the figure that nanocrystalline NiO showed largest response to H_2S ($S = 154$, with surfactant and $S = 89$, without surfactant) at 150 °C as compared to responses of other gasses.

4.2 Selectivity

Figure 7 shows the selectivity profile of nanocrystalline NiO (with and without surfactant) for different gases at 150 °C. It is observed from Fig. 7 that the sensor is highly selective to H_2S gas against other gasses.

4.3 Response and Recovery Time

Figure 8 shows the response and recovery of the nanocrystalline NiO (with and without surfactant) based thick films sensors to 10 ppm H_2S gas at an operating temperature 150 °C.

The times to reach 90 % variation in resistance upon exposure to H_2S gas and the air were defined as response and recovery times, respectively. The response

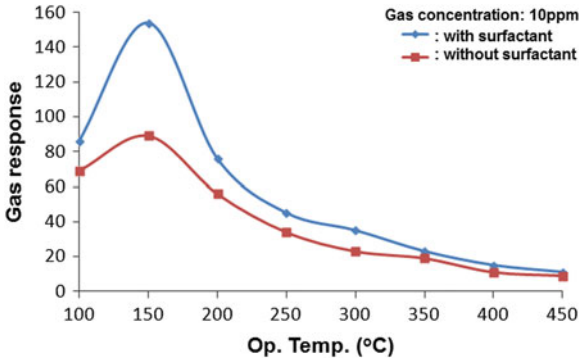

Fig. 6 Variation of H_2S gas response with operating temperature

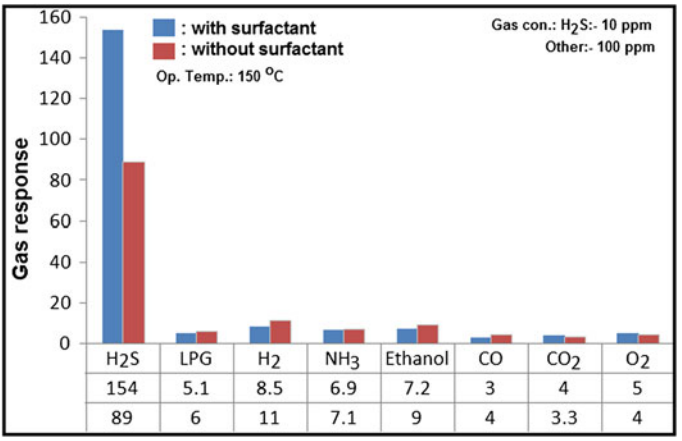

H_2S	LPG	H_2	NH_3	Ethanol	CO	CO_2	O_2
154	5.1	8.5	6.9	7.2	3	4	5
89	6	11	7.1	9	4	3.3	4

Fig. 7 Selectivity of nanocrystalline NiO (with and without surfactant) thick films

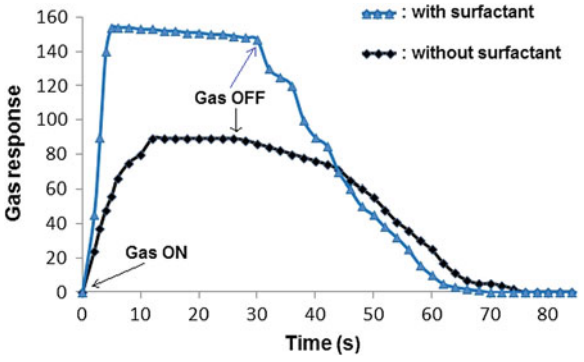

Fig. 8 Response and recovery time of nanocrystalline NiO thick film sensors

and recovery values upon the exposures to 10 ppm H_2S gas and air were 4 and 58 s for NiO (with surfactant) thick film sensor, while those were 10 and 64 s for NiO (without surfactant) thick film sensor respectively.

When a reducing gas is detected using p-type oxide semiconductors, the response time is usually shorter than the recovery time [24]. This reflects that the in-diffusion of reducing gas to the sensor surface and its oxidation with negatively charged surface oxygen during the gas sensing reaction is faster than the serial surface reactions regarding the adsorption, dissociation, and ionization of oxygen during the recovery reaction.

Accordingly, the shorter response time (4 s) for NiO (with surfactant) in comparison to that in NiO (without surfactant) sensor (10 s) can be attributed to the faster diffusion of analyte gases through the less agglomerated hierarchical structures. And this is consistent with the literature data that the gas responding speed of well-ordered and less-agglomerated configuration of hierarchical structures is significantly faster than that of agglomerated nanoparticles [25]. This indicates the possibility that two sensor specimens with different preferred orientations may show the different oxygen adsorption–desorption behaviours during response and recovery process.

4.4 Variation of H_2S Gas Response with Gas Concentration

Figure 9 shows the response of the sensors exposed to different concentrations of H_2S for NiO nanoparticles (with and without surfactant) thick films. For both the samples, the response values were observed to increase continuously with the gas concentration up to 40 ppm at 150 °C temperature. The rate of the increase in response was relatively larger up to 20 ppm, smaller during 20–50 ppm and then approximately saturated after 50 ppm. Thus, the active region of the sensor would be between 5 and 20 ppm. The results clearly indicate that even the lowest concentration of H_2S, i.e., 5 ppm, can be detected with (Gas response = 49 and 54 for with and without surfactant NiO), which is an acceptable response value, for both the sensors.

For both the senors, the response goes on increasing with gas concentration up to 40 ppm, then becomes saturation and beyond it decreases. At lower gas concentrations, a monolayer of the gas molecules would be expected to be formed on the surface, which could interact with the surface more actively, giving larger responses. There would be multilayers of gas molecules on the sensor surface at the higher gas concentrations, resulting in saturation in response.

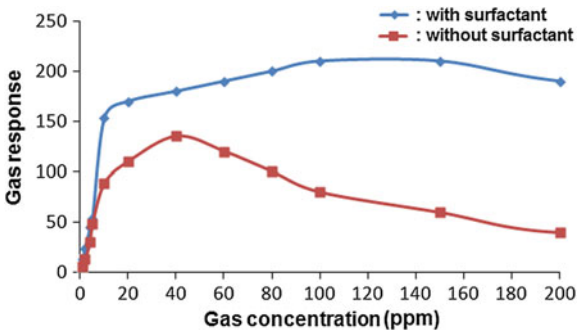

Fig. 9 Variation of H_2S gas response of NiO (with and without surfactant) thick film sensor with concentrations

5 Discussion

The moderate sensitivity observed in the NiO thick film sensor without surfactant can be attributed to the surface morphology of the films consisting of tightly packed crystallites with less porosity and less surface to volume ratio due to more particle size, on the other hand high sensitivity of the NiO thick film sensor with surfactant can be undoubtedly ascribed to the nanostructure that provides high surface to volume ratio for gas–solid reaction. As a result, it is easy for the gas molecule to adsorb on the surface of the film and to diffuse through the film. Hence it is necessary to synthesize starting powders with small grain size rather than large grain size with high degree of crystallinity. Nanostructures with less agglomerated configuration have been reported to show very high gas responses due to their high surface area and nano-porous structures.

The sensing reaction that governs the process of gas detection is the oxidation of H_2S. The possible reaction in the oxidation of H_2S would produce SO_2 and water.

$$2H_2S_{(g)} + 3O^-_{2(g)} \rightarrow 2SO_{2(g)} + 2H_2O_{(g)} \quad (1)$$

As explained in [26] the oxygen is adsorbed on the surface of NiO (p-type semiconductor) increasing the quantity of reactive sites, because the metal ions of the lattice can be oxidised from Ni^{2+} to Ni^{3+}. The oxygen species capture electrons from the material (conduction band) leading to a rise in the concentration of charge carriers (holes) [29]

$$O_{2(g)} \leftrightarrow O_{2(ads)} \quad (2)$$

$$O_{2(ads)} + e^- \leftrightarrow O^-{}_{2(ads)} \quad (3)$$

$$O^-{}_{2(ads)} + e^- \leftrightarrow 2O^-{}_{(ads)} \quad (4)$$

$$O^-_{(ads)} + e^- \leftrightarrow O^{2-}_{(ads)} \quad (5)$$

Once the conductance is established, the material is exposed to H_2S gas so the molecules react with the adsorbed oxygen. This reaction gives rise to transfer of electrons to the material, so the conductance diminishes, due to a reduction in the density of holes. The possible reactions are the following ones:

$$2H_2S_{(g)} + 3O^-_{2\,(ads)} \rightarrow 2SO_{2(g)} + 2H_2O_{(g)} + 6e^- \quad (6)$$

$$H_2S_{(g)} + 3O^-_{(ads)} \rightarrow SO_{2(g)} + H_2O_{(g)} + 3e^- \quad (7)$$

$$H_2S_{(g)} + 3O^{-2}_{(ads)} \rightarrow SO_{2(g)} + H_2O_{(g)} + 6e^- \quad (8)$$

Hence, regarding (7) and (8) the concentration of H_2S molecules is related to the increment of resistance.

6 Conclusions

Based upon the work presented here, the following conclusions can be made:

- Nanostructured NiO material with and without surfactant could be prepared by simple and inexpensive hydrothermal technique.
- Hydrothermal technique may be useful for the large scale production of nanostructured NiO material.
- The XRD pattern of nickel oxide material confirmed the formation of NiO with hexagonal structure having crystallite size in the range of 23–100 nm.
- The crystallite sizes of NiO were observed to be decreased with surfactant.
- The thick films of nanostructured NiO showed remarkable improvement of H_2S gas response over the reported sensors.
- The sensor showed good selectivity to H_2S gas against CO_2, H_2, NH_3, C_2H_5OH, CO and O_2.
- The nanostructured NiO thick films exhibit rapid response–recovery which is one of the main features of NiO based sensor.

Acknowledgments The author (DVA) is grateful to U.G.C., WRO, Pune and BCUD, University of Pune for financial assistance to this project. Authors are very much thankful to Principal, Arts, Commerce and Science College, Nandgaon and Principal, KTHM College, Nashik for providing experimental facilities.

References

1. R. Roy, Accelerating the kinetics of low-temperature inorganic syntheses. J. Solid State Chem. **111**, 11–17 (1994)
2. M. Yoshimura, W. Suchanek, K. Byrappa, Soft processing for advanced inorganic materials. MRS. Bull. Spec. Issue **25**(9), 17–25 (2000)

3. S.C. Tjong, H. Chen, Nanocrystalline materials and coatings. Mat. Sci. Eng. R **45**, 1–88 (2004)
4. K. Byrappa, M. Yoshimura, *Handbook of Hydrothermal Technology* (Noyes Publications, New Jersey, 2001)
5. T. Siyama, A. Kato, A new detector for gaseous components using semiconductor thin film. Anal. Chem. **34**, 1502–1503 (1962)
6. J.Q. Xu, Q.Y. Pan, Y.A. Shun, Z. Li, Emulsion synthesis structure and gas sensing properties of nanometer ZnO. J. Inorg. Chem. **14**, 355–359 (1998)
7. A.A. Tomchenko, G.P. Harmer, B.T. Marquis, J.W. Allen, Semiconducting metal oxide sensor array for the selective detection of combustion gases. Sens. Actuators B **93**, 126–233 (2003)
8. B. Wu, C. Guo, N. Zheng, Z. Xie, G.D. Stucky, Nonaqueous production of nanostructured anatase with high-energy facets. J. Am. Chem. Soc. **130**, 17563–17567 (2008)
9. D. Tao, F. Wei, New procedure towards size-homogeneous and well-dispersed nickel oxide nanoparticles of 30 nm. Mater. Lett. **58**, 3226–3228 (2004)
10. K.C. Liu, M.A. Anderson, Porous nickel oxide/nickel films for electrochemical capacitors. J. Electrochem. Soc. **143**, 124–130 (1996)
11. Y.D. Wang, C.L. Ma, X.D. Sun, H.D. Li, Preparation of nanocrystalline metal oxide powders with the surfactant-mediated method. Inorg. Chem. Commun. **5**, 751–755 (2002)
12. L. Xiang, X. Y. Deng, Y. Jin, Experimantal study on synthesis of NiO nano-particles. Scripta Materialia **47**, 219–224 (2002)
13. S. Deki, H. Yanagimito, S. Hiraoka, NH_2-terminated poly (ethylene oxide) containing nanosized NiO particles: synthesis, characterization, and structural considerations. Chem. Mater. **15**, 4916–4922 (2003)
14. P. Ngo, P. Bonville, M.P. Pileni, Nanoparticles of $CoxFeyzO_4$: synthesis and superparamagnetic properties. Euro. Phys. J. B **9**, 583–592 (1999)
15. X.M. Sun, X. Chen, Z.X. Deng, Y.D. Li, A CTAB-assisted hydrothermal orientation growth of ZnO nanorods. Mater. Chem. Phys. **78**, 99–10 (2002)
16. E.R. Beach, K.R. Shqaue, S.E. Brown, S.J. Rozesveld, P.A. Morris, Solvothermal synthesis of crystalline nickel oxide nanoparticles. Mater. Chem. Phys. **115**, 373–379 (2009)
17. D.D. Kajale, G.E. Patil, V.B. Gaikwad, S.D. Shinde, D.N. Chavan, N.K. Pawar, S.R. Shirsath, G.H. Jain, Synthesis of $SrTiO_3$ nanopowder by sol-gel hydrothermal method for gas sensing application. Int. J. Smart Sens. Intell. Syst. **5**(2), 382–400 (2012)
18. S.D. Shinde, G.E. Patil, D.D. Kajale, V.B. Gaikwad, G.H. Jain, Gas sensing performance of nanostructured ZnO thick film resistors. Int. J. Nanopart. **5**(2), 126–135 (2012)
19. JCPDS data card no. 47-1049
20. S.D. Shinde, G.E. Patil, D.D. Kajale, V.B. Gaikwad, G.H. Jain, Synthesis of ZnO nanorods by hydrothermal method for gas sensor applications. Int. J. Smart Sens. Intell. Syst. **5**(1), 57–70 (2012)
21. Y.D. Wang, C.L. Ma, X.D. Sun, H.D. Li, Preparation of nanocrystalline metal oxide powders with the surfactant-mediated method. Inorg. Chem. Commun. **5**, 751–755 (2002)
22. H. Sato, T. Minami, S. Takata, T. Yamada, Transparent conducting p-type NiO thin films prepared by magnetron sputtering. Thin Solid Films **23**, 27–31 (1993)
23. K.C. Liu, M.A. Anderson, Porous nickel oxide/nickel films for electrochemical capacitors. J. Electrochem. Soc. **143**, 124–130 (1996)
24. D. Adler, J. Feinleib, Electrical and optical properties of narrow-band materials. Phys. Rev. B **2**, 3112–3134 (1970)
25. A. Gorschluter, H. Merz, Localized d–d excitations in NiO (1 0 0) and CoO (1 0 0). Phys. Rev. B **49**, 17293–17302 (1994)
26. K. Anandan, V. Rajendran, Structural, optical and magnetic properties of well-dispersed NiO nanoparticles synthesized by CTAB assisted solvothermal process. Nanosci. Nanotechnol. Int. J. **2**(4), 24–29 (2012)

Chapter 11
Preparation of Ni-doped ZnO Nanorods by Hydrothermal Route for Gas Sensor Applications

G. H. Jain, G. E. Patil, G. J. Mogal, D. V. Ahire, R. L. Patil, D. D. Kajale, S. D. Shinde and V. B. Gaikwad

Abstract In this work, we propose a novel method for the synthesis Ni-doped ZnO nanorods, analytical grade zinc acetate dehydrate [$Zn(Ac)_2.2H_2O$], nickel acetate [$Ni(Ac)_2.4H_2O$], sodium hydroxide (NaOH) and poly vinyl alcohol (PVA) were used. All the reagents were used as received (Sigma Aldrich, USA) without further purification. Various $(Zn_{1-x}Ni_x)O$ ($x = 0.01$, 0.06, and 0.10) nanorods were obtained via a facile hydrothermal method. This work aims at preparing sensing material of Ni-doped ZnO nanorods by hydrothermal process, and testing their sensing properties for detection of toxic gases. The growth mechanism, morphology, as well as the gas sensor applications of the Ni-doped ZnO nanorods were systematically studied in this chapter.

Keywords Hydrothermal route · Ni-doped ZnO nanorods · Gas sensor

1 Introduction

Nanostructured ZnO has been widely exploited due to good semiconducting and electronic properties. These properties drive micro device applications such as thin film transistors, high power LED, gas sensors, and spintronic devices [1–4]. Due to

G. H. Jain (✉) · G. E. Patil · G. J. Mogal · D. V. Ahire · R. L. Patil
Materials Research Laboratory, K. T. H. M. College, Nashik 422002, India
e-mail: gotanjain@rediffmail.com

D.D. Kajale
Materials Research Laboratory, Arts, Commerce and Science College, Nandgaon 423106, India

S. D. Shinde
Department of Physics, H. P. T. Arts and R. Y. K. Science College, Nashik 422013, India

V. B. Gaikwad
B. C. U. D, University of Pune, Pune 411007, India

A. Mason et al. (eds.), *Sensing Technology: Current Status and Future Trends I*, Smart Sensors, Measurement and Instrumentation 7, DOI: 10.1007/978-3-319-02318-2_11,

its high surface area, nanostructured ZnO was able to detect the sub ppm range of volatile gases such as acetone and ethanol in gas sensor applications [5, 6]. Room temperature sensing can expand the application of metal oxide based gas sensors to areas such as explosive and flammable gas detection, and the biomedical field [7]. Nevertheless, metal oxide gas sensors are commonly operated at an elevated temperature to overcome the energy required for the chemisorptions between gas molecules, which allows for high sensitivity with a short response time. To overcome the limits of high operating temperature, noble metals such as platinum, palladium, and gold have been doped. This has improved sensing properties at relatively lower temperatures by enhancing interactions between dopants and gas molecules [8–10].

Doping of transition metals in ZnO has been mostly investigated in modifying ferroelectric properties [11–13], but few studies have focused on transition metal doping for enhancing gas sensing properties. Nickel was chosen as a dopant for ZnO nanorods because of similar ionic radius with zinc ions [14] and facile incorporation of Ni into ZnO without altering ZnO morphology.

Solid-state gas sensors make use of the chemical sensitivity of semiconductor surfaces to different adsorbed gases. Appropriate donor doping can produce the electronic defects that increase the influence of oxygen partial pressure on the conductivity. Doped zinc oxide films have a number of attractive applications, such as: gas sensor devices [15], transparent electrodes [16], and piezoelectric devices [17]. Several techniques have been used to produce many distinct zinc oxide films: chemical vapor deposition [18], radio frequency magnetron sputtering [19], sol–gel [20], spray pyrolysis [21–23], hydrothermal [24–28].

The aim of the present chapter is the investigation of structures, optical properties and gas sensing properties of Ni-doped ZnO hexagonal nanorods, which is very important for both fundamental and applied points of view. Furthermore, Ni^{2+} ion with the smaller radius (0.069 nm) compared to Zn^{2+} ion (0.074 nm) is facile to implant the critical nuclei of ZnO during the nano-crystalline growth.

2 Experimental

2.1 Synthesis of ZnO and Ni-doped ZnO Nanorods

ZnO was prepared as per the procedure mentioned in the Chap. 5 and used as it is. For the synthesis of Ni-doped ZnO nanorods, analytical grade zinc acetate dehydrate [$Zn(Ac)_2.2H_2O$], nickel acetate [$Ni(Ac)_2.4H_2O$], sodium hydroxide (NaOH) and poly vinyl alcohol (PVA) were used. All the reagents were used as received (Sigma Aldrich, USA) without further purification. Various $(Zn_{1-x}Ni_x)O$ ($x = 0.01$, 0.06, and 0.10) nanorods were obtained via a facile hydrothermal method. In this, 1 mmol zinc acetate [$Zn(Ac)_2.2H_2O$] and required amount nickel acetate [$Ni(Ac)_2.4H_2O$] were dissolved in absolute ethanol to form a 25 ml

solution. A 3.0 g of PVP were dissolved in 50 ml deionized water and stirred for 30 min. Simultaneously, a 10 ml NaOH (10 M) was added drop wise into this aqueous zinc acetates, nickel nitrate and PVP solution under vigorous stirring. During the addition of NaOH into aqueous solution, the solution was heated at 80 °C to avoid the immediate precipitation of zinc and nickel ions. At last, the final solution was transferred into a 100 ml Teflon-lined stainless steel autoclave. The autoclave was sealed and maintained at 200 °C for 12 h, and then allowed to cool to room temperature naturally. After terminating the reaction in desired time, the resulted solid projects were centrifuged, washed with distilled water and ethanol to remove the ions possibly remaining in the final product, and finally dried in air at 60 °C for 4 h. The synthesized Ni-doped ZnO nanorods were characterized in terms of their structural, optical and gas sensing performances.

2.2 Preparation of Thick Films

The thixotropic paste was formulated by mixing the fine powder of as prepared ZnO and $Zn_{1-x}Ni_xO$ (x = 0.01, 0.06 and 0.10) nanorods with the solution of ethyl cellulose (a temporary binder) in a mixture of organic solvents such as butyl cellulose, butyl carbitol acetate and terpineol etc. The ratio of inorganic part to organic part was kept at 75:25 in formulating the paste. This paste was screen printed [29, 30] on glass substrate in the desired pattern. The films were fired at 550 °C for 30 min.

3 Characterization Results

3.1 X-ray Diffraction Patterns of the ZnO and Ni-doped ZnO Samples

Figure 1 displays X-ray diffraction patterns of the as-prepared ZnO and Ni-doped ZnO samples. The XRD spectra of Ni-doped ZnO rod arrays consist of (100), (002), (101), (102), (110), (103), (200), (112), (201), (004), (202), and (103) peaks, and all the observed diffraction peaks can be indexed to ZnO wurtzite structure. The strong (101) peak proves that ZnO rods with wurtzite structure were obtained in both undoped and Ni-doped ZnO samples. No diffraction peaks of other structures were detected in these samples, indicating that the Ni ion successfully occupied ZnO lattice site and there were no secondary phases or precipitates in the samples. The crystallites sizes of the ZnO and Ni-doped ZnO are estimated using the Scherrer formula. The average values of grain sizes are 27, 23, 15 and 6 nm for the ZnO, $(Zn_{0.99}Ni_{0.01})O$, $(Zn_{0.94}Ni_{0.06})O$, and $(Zn_{0.90}Ni_{0.10})O$ respectively.

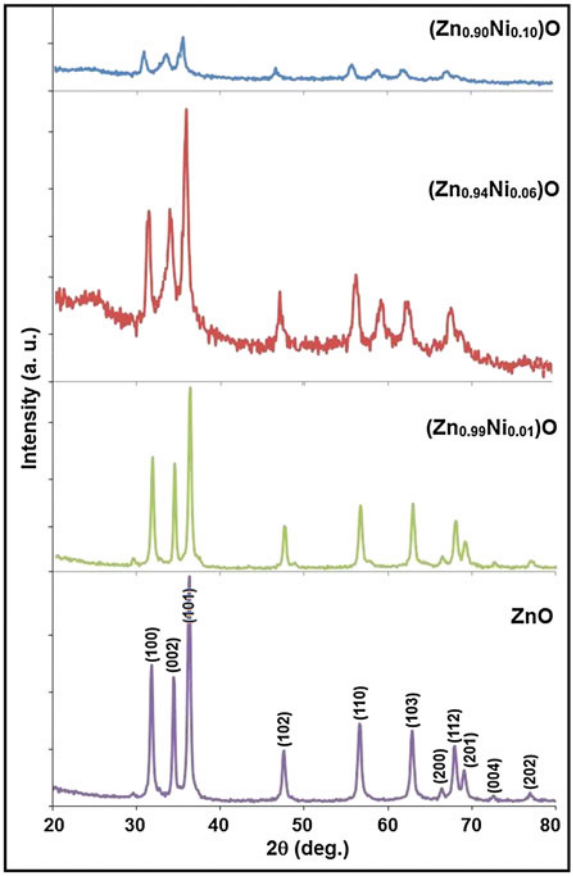

Fig. 1 X-ray diffraction patterns of the ZnO and Ni-doped ZnO samples

The prepared undoped and Ni-doped ZnO were demonstrated to be preferential orientation along the (101) peak direction. The all diffraction peaks of Ni-doped ZnO were obviously higher than that of undoped ZnO. However, $(Zn_{0.99}Ni_{0.01})O$ XRD spectrum has the same height of diffraction peaks as ZnO, which might be due to lower Ni_2^+ concentration. Due to the higher bond energy of Ni^{2+}–O_2^- compared to that of Zn^{2+}–O_2^-, the more energy is required to make Ni^{2+} ions enter into lattice and form the bond of Ni^{2+}–O_2^-.Therefore, of Ni^{2+} substituting for Zn^{2+} has higher stability relative to the Zn–O structure, and more energy is required for the substituted samples to complete crystallization. In addition, because of the larger radius of Zn^{2+} (0.74 Å) [31] compared to Ni^{2+} (0.69 Å), the replacement of Zn^{2+} by Ni^{2+} will cause only slight decrease in lattice parameters. Although doping does not alter the crystal structure, it causes the lattice constant to change as evidence of the (101) peak position shift. Although the change is very little, the concentration of dopant plays a role in the c-axis constant.

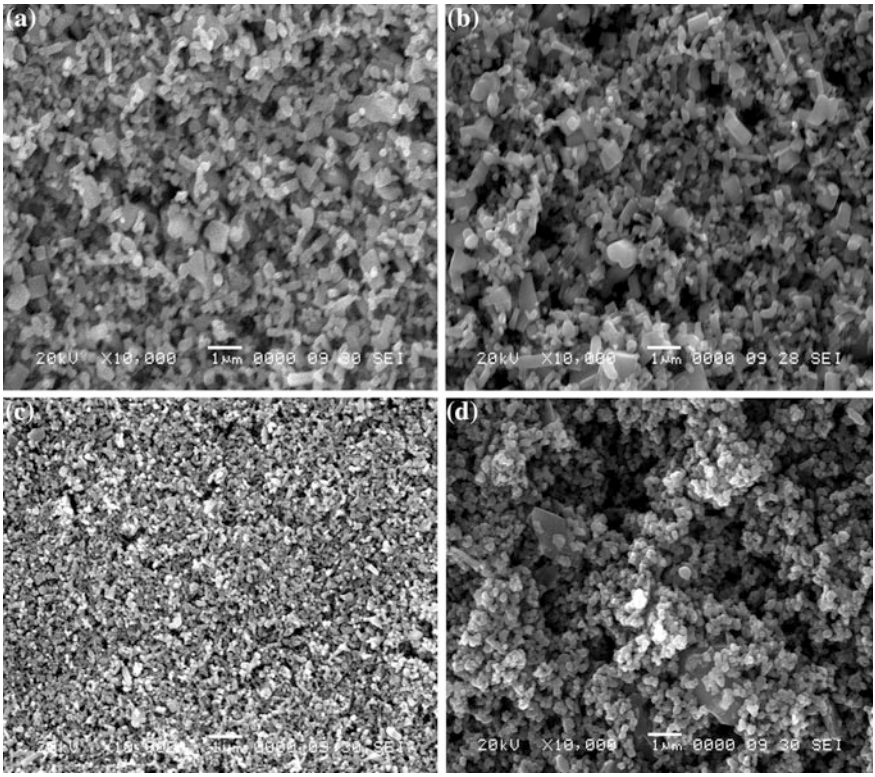

Fig. 2 SEM images of: **a** ZnO, **b** $(Zn_{0.99}Ni_{0.01})O$, **c** $(Zn_{0.94}Ni_{0.04})O$, and **d** $(Zn_{0.90}Ni_{0.10})O$ thick films

The capping ligand, polyvinyl pyrolidone (PVP) was used in the preparation of Ni-doped ZnO nanorods. The PVP can change the surface energy of different crystal facets, the side facets may possess higher energy than the top-down surfaces, and thus ultimately leading to the formation of Ni-doped ZnO nanorods. Matysina [32] determined that hexagonal metals with c/a ratios greater than 1.633 have {101} and {100} surface energy 1.5 times larger than those for {001} facets [33]. Ni-doped ZnO has a c/a ratio of 2.6 and should have even higher surface energy on the {101} and {100} surfaces. As a result, the Ni-doped ZnO nanorods grow more rapidly along these facets and the [110] direction is the long axes of the nanorod while the [001] direction is the short axis. On the other hand, Muthukumar et al. [34] found that the Ni-doped into the ZnO could control the surface morphology by lowering the surface energy. It may be speculated that the Ni element doped into the crystal lattice of the Zn embryos lowers the surface energy of the (10–10) planes, resulting in an isotropic oxidation growth of the Zn embryos instead of the preferred growth at (10–10). At the same time, the completely oxidized embryos may coalesce Ni each other with the definite direction (10–10) and the regularly hexagonal Ni-doped ZnO nanoparticles are synthesized Fig. 2.

Therefore, the formation of the Ni-doped ZnO nanoparticles may be controlled by the Ni-doped into the lattice of the Zn embryos. This is also observed in the XRDs and TEM images of Ni-doped ZnO reported in this work.

4 Transmission Electron Micrograph

Figure. 3a–d shows the TEM and SAED images of (a) ZnO, (b) $(Zn_{0.99}Ni_{0.01})O$, (c) $(Zn_{0.94}Ni_{0.04})O$ and (d) $(Zn_{0.90}Ni_{0.10})O$ powders respectively. The images clearly indicate that the average crystallite size is decreasing with an increase Ni concentrations. The clarity of the rings in the SAED pattern goes on decreasing with Ni-dopant concentration which reveals that the particle sizes of Ni-doped ZnO particles are decreasing. The $(Zn_{0.90}Ni_{0.10})O$ powder shows the diffuse ring pattern which indicates the more decrease in particle size compared with others.

The ZnO rods length ranges from 50 to 120 nm and showing crystalline nature Fig. 3a, while the lengths of rods for $(Zn_{0.99}Ni_{0.01})O$ changes slightly but not remarkably (Fig. 3b). The remarkable decrease in length of the rods was observed in $(Zn_{0.94}Ni_{0.04})O$ and $(Zn_{0.90}Ni_{0.10})O$ powders, Fig. 3c, d. The range of rods length for $(Zn_{0.94}Ni_{0.04})O$ is about 40–80 nm and for $(Zn_{0.90}Ni_{0.10})O$ is about 10–40 nm, with some agglomeration, which might be the reason for decrease in surface area of this powder.

5 Gas Sensing Performance

5.1 Gas Response of ZnO and Ni-doped ZnO Rods

Thick films of ZnO and Ni-doped ZnO nanorods were tested to various gases such as: LPG, CO, CO_2, ethanol, O_2, NH_3, H_2S and Cl_2 etc. at operating temperatures ranging from 25 to 300 °C. The ZnO rods film showed maximum response to H_2S gas at 25 °C (RT) and to ethanol vapors at 300 °C as reported in previous chapter. Ni-doped ZnO rods thick films were tested to various gases at various temperatures from 25(RT) to 300 °C and showed maximum response to H_2S gas for lower gas concentration (1 ppm).

Figure 4 shows the gas response as a function of sensor operating temperature for ZnO and Ni-doped ZnO thick films for H_2S gas in air atmosphere. The response to H_2S gas of Ni-doped ZnO thick films was found to be enhanced with increase in Ni concentrations and decreases for further increase in Ni concentrations as shown in Fig. 4. The lower temperature H_2S gas sensing would be due to nano-crystalline particle sizes of the sensor element, which offers more surfaces to volume ratio causes the oxidation of H_2S gas at room temperature.

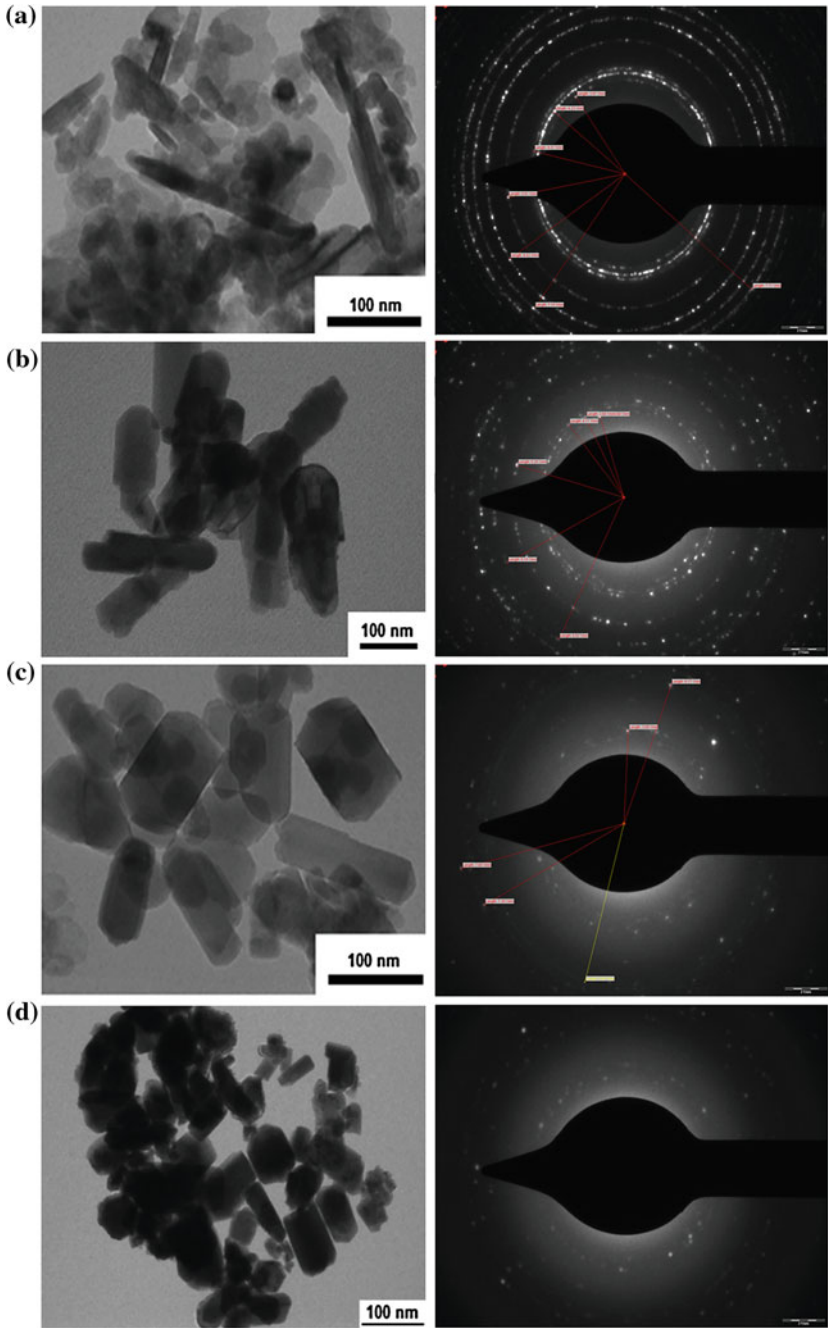

Fig. 3 TEM and SAED images of: **a** ZnO, **b** $(Zn_{0.99}Ni_{0.01})O$, **c** $(Zn_{0.94}Ni_{0.04})O$ and **d** $(Zn_{0.90}Ni_{0.10})O$ powders respectively

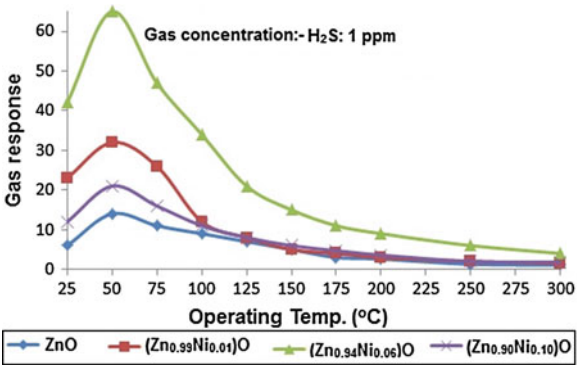

Fig. 4 Variation of H_2S gas response with operating temperature

From Fig. 4 H_2S gas response increases with operating temperature, attains maximum at 50 °C and decreases with further increases in temperature. But the sensor has potential to detect H_2S gas at lower temperature 25 °C (RT).

5.2 Selectivity of ZnO and Ni-doped ZnO Rods Thick Films

The selectivity is the important feature of the gas sensor. The Fig. 5 shows the bar diagram of the selectivity of the ZnO and Ni-doped ZnO thick films sensor to H_2S gas against the other interfering gases. Thick films of ZnO and Ni-doped ZnO nanorods showed maximum selectivity to H_2S gas against the other gases. The $(Zn_{0.94}Ni_{0.06})O$ thick film was found to be most selective to H_2S gas compared to the other gases Fig. 6.

5.3 Response and Recovery Time

The Table 1 shows the response and recovery times of the ZnO and Ni-doped ZnO thick film sensors. The response time of ZnO sensor was quick but comparatively its response is less ($S = 6$) and recovery time was more. But the Ni-doped ZnO sensors showed improved response values but recovery time was more. This would be due to more response values and the energy required to oxidize the H_2S gas was less at lower operating temperature (25 °C). But the $(Zn_{0.94}Ni_{0.04})O$ based sensor has quick response and speedy recovery and showed high response ($S = 42$). This sample has potential to satisfy all sensor specifications requirements.

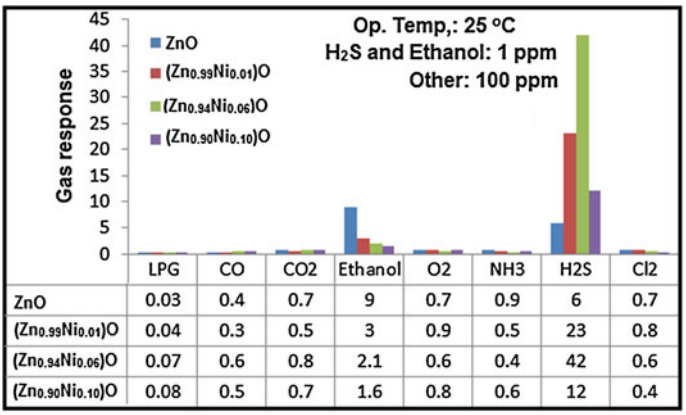

	LPG	CO	CO2	Ethanol	O2	NH3	H2S	Cl2
ZnO	0.03	0.4	0.7	9	0.7	0.9	6	0.7
$(Zn_{0.99}Ni_{0.01})O$	0.04	0.3	0.5	3	0.9	0.5	23	0.8
$(Zn_{0.94}Ni_{0.06})O$	0.07	0.6	0.8	2.1	0.6	0.4	42	0.6
$(Zn_{0.90}Ni_{0.10})O$	0.08	0.5	0.7	1.6	0.8	0.6	12	0.4

Fig. 5 Selectivity of the ZnO and Ni-doped ZnO thick films sensor to H_2S gas at 25 °C (RT)

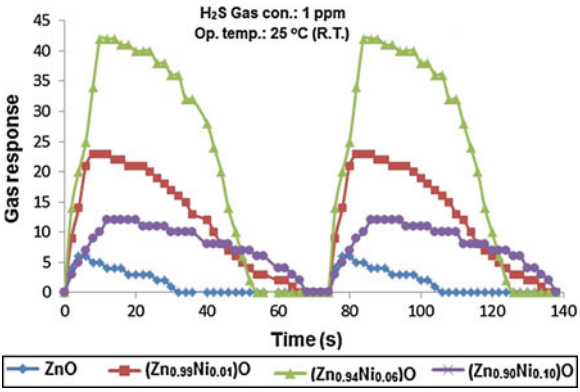

Fig. 6 Response and recovery times of the ZnO and Ni-doped ZnO thick films sensor to H_2S gas at 25 °C (RT)

Table 1 Response and recovery times of the ZnO and Ni-doped ZnO thick film sensors

Samples	Response time	Recovery time
ZnO rods	3 s	24 s
$(Zn_{0.99}Ni_{0.01})O$	8 s	44 s
$(Zn_{0.94}Ni_{0.04})O$	6 s	40 s

5.4 Gas Sensing Mechanism

When reducing gas such as H_2S is inleted, the interaction of this gas with the surface chemisorbed oxygen, O_2^-, can take place. The reducing gas readily releasing electrons back to the conduction band and the electrical conductance of the semiconductor increases.

$$2H_2S + 3O_2^-(ads) \rightarrow 2SO_2(g) + 2H_2O(g) + 6e^- \quad (1)$$

As per earlier reports by many authors, the liberation of water saturates the surface and unless desorbed completely, affects the response of the surface. And hence, after each measurement, the chamber was flushed thoroughly and the sensor was heated to overcome the effect of humidity. But in this experiment, we observed that, this was not essential for these samples. The reason may be due to nonstoichiometry, lattice distortion, smaller grain size, and highest surface activity, which result in stronger interaction between H_2S molecules and the surface active sites [35]. The manifestation of the maximum response at optimal operating temperature is also allied to the formation of charged oxygen ions on the oxide surface. It is possible that Ni-doping not only decreases the particle size but also increases the catalytic activities of the powder. The decrease in particle with optimum Ni-doping is due to the dispersion of the crystallites avoiding the agglomeration. One of the probable explanations for shift in optimal operating temperature towards lower side by 25 °C may be the reduction in the particle size with doping concentration. This can be explained as: in nano-sized particles surface-to-bulk ratio is much larger than that of coarse micro-grained materials, which yields a large interface between the oxide and the gaseous medium. The larger surface area generally provides more adsorption–desorption sites, which can enhance the reactivity at lower temperature. However, the improved response of a nanostructured gas sensor cannot be explained only by reference to the increase in the specific reactive surface; the full depletion of the metal oxide semiconductor as the nanoparticles size approaches the thickness of the space charge region is also important. In a semiconductor metal oxide with grains of diameter D, each grain has an electron-depleted surface layer, also known as the space-charge layer of the depth L [36]. The depth of this layer is determined by both the Debye length of the material and the strength of oxygen chemisorption. The reduction in the grain size allows the space charge to cover large volume of the grain and the large number of grain boundaries and periphery, hence, large variation in the barrier resistance, which helps to significantly enhance gas detection [37–39]. Furthermore, the size-dependent gas-sensing properties are linked to the density of surface states induced by the chemisorbed oxygen species which leads to a lower degree of Fermi level pinning [40]. So the other possibility may be the Fermi level pinning, which may reduce with doping. The Fermi level pinning can help in lowering the temperature and less Fermi level pinning can help in lowering the temperature and less Fermi level pinning means that the surface barrier and accordingly, the overall resistance, can undergo large variations [41]. This may lead to the response of Ni-doped ZnO sensor elements fabricated from nanosized particles with lowering in the optimal operating temperature.

6 Conclusions

From this work, the following conclusions can be drawn:

- The Ni ion successfully occupied ZnO lattice site and there were no secondary phases or precipitates in the samples.
- The size of ZnO decreases with the Ni-concentrations in ZnO and is confirmed by XRD and TEM analysis.
- The response to H_2S gas increases with Ni-dopant concentrations attains maximum and decreases on further increase in dopant concentrations.
- The improvement in H_2S gas response is due to increase in the surface to volume ratio of the Ni-doped ZnO samples.
- The response and recovery times of Ni-doped ZnO samples were quick and fast compared to pure ZnO.
- The $(Zn_{0.94}Ni_{0.6})O$ thick film showed maximum response to H_2S with fast response and recovery time characteristics.

Acknowledgments The author (GHJ) is grateful to U. G. C., New Delhi and BCUD, University of Pune for financial assistance to this project. Authors are very much thankful to Principal, Arts, Commerce and Science College, Nandgaon and Principal, K. T. H. M College, Nashik for providing experimental facilities.

References

1. P.F. Carcia, R.S. McLean, G. Nunes, Transparent ZnO thin-film transistor fabricated by rf magnetron sputtering. Appl. Phys. Lett. **82**, 1117–1120 (2003)
2. J.H. Lim, C.K. Kang, K.K. Kim, I.K. Park, D.K. Hwang, S.J. Park, UV electroluminescence emission from ZnO light-emitting diodes grown by high temperature radiofrequency sputtering. Adv. Mater. **18**(20), 2720–2724 (2006)
3. H.-U. Lee, Kyun Ahn, S.-J. Lee, J.-P. Kim, H.-G. Kim, S.-Y. Jeong, C.-R. Cho, ZnO nanobarbed fibers: fabrication, sensing NO_2 gas, and their sensing mechanism. Appl. Phys. Lett. **98**, 193114–193116 (2011)
4. C. Ronning, Manganese-doped ZnO nanobelts for spintronics. Appl. Phys. Lett. **84**, 783–785 (2004)
5. Q. Wan, Fabrication and ethanol sensing characteristics of ZnO nanowire gas sensors. Appl. Phys. Lett. **84**, 3654–3656 (2004)
6. Q. Qi, Selective acetone sensor based on dumbbell-like. ZnO with rapid response and recovery. Sens. Actuators B Chem. **134**, 166–170 (2008)
7. L.Y. Zhang, L.W. Yin, C.X. Wang, N. Lun, Y.X. Qi, D. Xiang, Origin of visible photoluminescence of ZnO quantum dots: defect-dependent and size-dependent. J. Phys. Chem. **114**, 9651–9658 (2010)
8. Z. Zhou, K. Kato, T. Komaki, M. Yoshino, H. Yukawa, M. Morinaga, K. Morita, Effects of dopants and hydrogen on the electrical conductivity of ZnO. J. Europian Ceram. Soc. **24**, 139–146 (2004)
9. N. Hongsith, C. Viriyaworasakul, S. Choopun, Ethanol sensor based on ZnO and Au-doped ZnO nanowires. Ceram. Int. **34**, 823–826 (2008)

10. J.K. Song, J.M. Szarko, S.R. Leone, S.H. Li, Y.P. Zhao, Ultrafast carrier dynamics and wavelength-dependent lasing-time characteristics in single ZnO nanotetrapod and nanowire lasers. J. Phys. Chem. B **109**, 15749–15753 (2005)
11. C. Cheng, G. Xu, H. Zhang, Y. Luo, Hydrothermal synthesis Ni-doped ZnO nanorods with room-temperature ferromagnetism. Mater. Lett. **62**, 1617–1620 (2008)
12. G. Huang, Synthesis, structure, and room-temperature ferromagnetism of Ni-doped ZnO nanoparticles. J. Mater. Sci. **42**, 6464–6468 (2007)
13. H. Wang, ZnO-based light-emitting metal-insulator-semiconductor diodes. Appl. Phys. Lett. **90**, 0525–0527 (2007)
14. R. Shannon, Revised effective ionic radii and systematic studies of interatomic distances in halides and chalcogenides. Acta Crystallogr. A **32**, 751–767 (1976)
15. C.H. Kwon, H.K. Hong, D.H. Yun, K. Lee, S.T. Kim, Y.H. Roh, B.H. Lee, Thick-film zinc-oxide gas sensor for the control of lean air-to-fuel ratio in domestic combustion systems. Sens. Actuators B Chem **24**, 610–613 (1995)
16. S. Major, S. Kumar, M. Bhatnagar, K.L. Chopra, Effect of hydrogen plasma treatment on transparent conducting oxides. Appl. Phys. Lett. **49**, 394–396 (1986)
17. M.G. Ambia, M.N. Islam, M. Obaidul Hakim, Studies on the seebeck effect in semiconducting ZnO thin films. J. Mater. Sci. **27**, 5169–5176 (1992)
18. J. Hu, R.G. Gordon, Textured aluminum-doped zinc oxide thin films from atmospheric pressure chemical-vapor deposition. J. Appl. Phys. **71**, 880–884 (1992)
19. O. Takai, M. Futsuhara, G. Shimizu, C.P. Lungu, J. Nozue, Nanostructure of ZnO thin films prepared by reactive rf magnetron sputtering. Thin Solid Films **318**, 117–119 (1998)
20. M. Ohyama, H. Kozuka, T. Yoko, Sol-gel preparation of ZnO films with extremely preferred orientation along (002) plane from zinc acetate solution. Thin Solid Films **306**, 78–85 (1997)
21. S.D. Shinde, G.E. Patil, D.D. Kajale, V.B. Gaikwad, G.H. Jain, Synthesis of ZnO nanorods by spray pyrolysis for H_2S gas sensor. J. Alloy. Compd. **528**, 109–114 (2012)
22. G.E Patil, D.D. Kajale, P.T. Ahire, D.N. Chavan, N.K. Pawar, S.D. Shinde, V.B. Gaikwad, G.H. Jain, Synthesis, characterization and gas sensing performance of SnO_2 thin films prepared by spray pyrolysis. Bull. Mater. Sci. **34,** 1–9 (2011)
23. G.E. Patil, D.D. Kajale, V.B. Gaikwad, G.H. Jain, Effect of thickness on nanostructured SnO_2 thin films by spray pyrolysis as highly sensitive H_2S gas sensor. Adv. Sci. Lett. **18**, 199–207 (2012)
24. F. Paraguay, W. Estrada, D.R. Acosta, E. Andrade, M. Miki-Yoshida, Growth, structure and optical characterization of high quality ZnO thin films obtained by spray pyrolysis. Thin Solid Films **350**, 192–202 (1999)
25. S.D. Shinde, G.E. Patil, D.D. Kajale, V.B. Gaikwad, G.H. Jain, Synthesis of ZnO nanorods by hydrothermal method for gas sensor applications. Int. J. Smart Sens. Intell. Syst. **5**, 57–70 (2012)
26. S.D. Shinde, G.E. Patil, D.D. Kajale, V.B. Gaikwad, G.H. Jain, Gas sensing performance of nanostructured ZnO thick film resistors. Int. J. Nanoparticles **5**, 126–135 (2012)
27. Y. Zuo, S. Ge, Z.Q. Chen, L. Zhang, X.Y. Zhou, S. Yan, Morphology, optical and magnetic properties of $Zn_{1-x}Ni_xO$ nanorod arrays fabricated by hydrothermal method. J. Alloy. Compd. **470**, 47–50 (2009)
28. T. Al-Harbi, Hydrothermal synthesis and optical properties of Ni doped ZnO hexagonal nanodiscs. J. Alloy. Compd. **509**, 387–390 (2011)
29. G.H. Jain, L.A. Patil, M.S. Wagh, D.R. Patil, S.A. Patil, D.P. Amalnerkar, Surface modified $BaTiO_3$ thick film resistors as H_2S gas sensors. Sens Actuators B Chem **117**, 159–165 (2006)
30. G.H. Jain, L.A. Patil, Gas sensing properties of Cu and Cr activated BST thick films. Bull. Mater. Sci. **29**, 403–411 (2006)
31. R. Viswanatha, S. Sapra, B. Satpati, Synthesis and characterization of Mn-doped ZnO nanocrystals. J. Phys. Chem. B **108**, 6303–6310 (2004)
32. Q.H. Li, Q.Y. Wang, X. Liang, T.H. Wang, Electronic transport through individual ZnO nanowires. Appl. Phys. Lett. **84**, 4556–4560 (2004)

33. A.C. Wang, J.Y. Dai, J.Z. Cheng, M.P. Chudzik, T.J. Marks, R.P.H. Chang, C.R. Kannewurf, Charge transport, optical transparency, microstructure, and processing relationships in transparent conductive indium–zinc oxide films grown by low-pressure metal-organic chemical vapor deposition. Appl. Phys. Lett. **73**, 327–329 (1998)
34. K.R. Kittilstved, N.S. Norberg, D.R. Gamelin, Chemical manipulation of high-Tc ferromagnetism in ZnO diluted magnetic semiconductors. Phys. Rev. Lett. **94**, 1472–1475 (2005)
35. N. Xinshu, Z. Haoxiang, W. Xinjun, J. Kai, Sensing properties of rare earth oxide doped In2O3 by a sol–gel method. Sens. Actuators B Chem. **115**, 434–438 (2006)
36. C. Xu, J. Tamaki, N. Miura, N. Yamazoe, Grain size effects on gas sensitivity of porous SnO_2-based elements. Sens. Actuators B Chem. **3**, 147–155 (1991)
37. P. Serrini, V. Briois, M.C. Horrillo, A. Traverse, L. Manes, Chemical composition and crystalline structure of SnO_2 thin films used as gas sensors. Thin Solid Films **304**, 113–122 (1997)
38. A. Galkidas, A. Mironas, A. Setkus, Peculiarities of surface doping with Cu in SnO_2 thin film gas sensors. Sens. Actuators B Chem. **26**, 29–33 (1995)
39. Q. Pan, J. Xu, X. Dong, J. Xang, Gas-sensitive properties of nanometer-sized SnO_2. Sens. Actuators B Chem. **66**, 237–239 (2000)
40. G.E. Patil, D.D. Kajale, S.D. Shinde, V.G. Wagh, V.B. Gaikwad, G.H. Jain, Synthesis of Cu-Doped SnO_2 thin films by spray pyrolysis for gas sensor application. Adv. Sens. Technol. Smart Sens. Measurement Instrum. **1**, 299–311 (2013)
41. D.D. Kajale, G.E. Patil, V.B. Gaikwad, S.D. Shinde, D.N. Chavan, N.K. Pawar, S.R. Shirsath, G.H. Jain, Synthesis of $SrTiO_3$ nanopowder by sol-gel hydrothermal method for gas sensing application. Int. J. Smart Sens. Intell. Syst. **5**(2), 382–400 (2012)

Chapter 12
Studies of Microstructure Properties and Gas Sensing Performance of $(Sn_{0.3}Ti_{0.7})O_2$ Thick Film Resistors

P. D. Hire, V. B. Gaikwad, N. U. Patil, M. K. Deore and G. H. Jain

Abstract In this work we report the synthesis, microstructure, electric properties and sensing performance of $(Sn_{0.3}Ti_{0.7})O_2$ powder, were prepared by wet chemistry route. Thick films were prepared by screen-printing technology. The surfaces of the films were modified by dipping them into an aqueous solution of copper chloride for different intervals of time, followed by firing at 550 °C for 30 min. pure film showed response to CO_2 at 300 °C and cupricated films have been found to be highly selective towards H_2S at 200 °C. The surface modification, using dipping process, altered the adsorbate–adsorbent interactions, which gave the unusual gas response and selectivity effect. The characterization of the films was done by Scanning Electron microscopy, X-ray diffraction, Thermal gravimetric analysis and UV spectrophotometer. Single peaks of the X-ray diffraction pattern reveals that the formation of compound of $(Sn_{0.3}Ti_{0.7})O_2$. Average crystallite size was found to be 41 nm of pure film. The role played by surface copper species in the gas sensing performance is discussed. Grain size, electric properties and gas sensitivity of the films were measured and presented.

Keywords $(Sn_{0.3}Ti_{0.7})O_2(ST_{30})$ · Thick films · H_2S gas sensor · Gas response · Selectivity

P. D. Hire · N. U. Patil · M. K. Deore · G. H. Jain (✉)
Material Research Lab, K.T.H.M. College, Nashik 422002, India
e-mail: gotanjain@rediffmail.com

V. B. Gaikwad
B.C.U.D, University of Pune, Pune 411007, India

A. Mason et al. (eds.), *Sensing Technology: Current Status and Future Trends I*,
Smart Sensors, Measurement and Instrumentation 7, DOI: 10.1007/978-3-319-02318-2_12,

1 Introduction

Gas sensors are used for monitoring and controlling of industrial processes, analysis of gas compositions, for surveillance and many other applications. The development of gas sensor devices with optimized sensitivity and selectivity has been gaining prominence in recent years [1]. Since the demonstration almost 50 years ago, it has been noted that the adsorption of gas on the surface of metal oxides can bring about a significant change in the electrical resistance of the material. There has been a sustained and successful effort to make use of this change for purposes of gas detection. Hydrogen sulphide is a toxic gas, often produced in coal, coal oil and natural gas manufacturing. Therefore, reliable sensors with low cost, low energy consumption, having high sensitivity, selectivity, and operable in a sub ppm range of H_2S are in high demand for environmental safety and industrial control purposes.

Among the metal oxides, tin dioxide and titanium dioxide, due to their chemical and electrical properties, are particularly appealing both for basic research and for a wide variety of possible applications [2]. Tin dioxide is the most common material in gas sensing [3], but it is widely used as transparent conductor and in heterogeneous catalysis. Titanium dioxide is used as a photocatalyst in solar cells, as an optical coating, in gas sensing, etc. Tin dioxide and titanium dioxide are both wide-gap semiconductors, showing several similarities in structural as well as in electronic properties.

One of the most active fields in the sensor research is the exploration of new materials that enable enhanced gas-sensing properties of all the materials currently examined, semiconducting oxides, for example, SnO_2 and TiO_2. These materials are of strong interest, largely because their physical properties are important for promising application as a gas sensor [4–7]. The gas-sensing property for the SnO_2-based sensors is found to be affected dominantly or even controlled by their surfaces [8]. Above 400–500 °C (oxygen losses), the low temperature SnO_2-sensors suffer from a structure instability and poor selectivity [9], while that for the TiO_2-based sensors by their bulk constituents as well and are suited to work at high temperature (1000–1200 °C)[10]. Since the two oxides have distinct gas-sensing behaviors, a combination of them would presumably initiate a new system [11], which might have the gas sensing properties that are not present in either of their bulk oxides was reported in literature [12–14]. The ST_{30} material could be more selective and stable.

The goal of this chapter is the synthesis of ST_{30} materials. More specifically, we aim at better information on: (i) the structure and morphology of the powder (ii) electronic properties and their changes in contact with different gases. Scanning Electron microscopy (SEM), X-ray diffraction (XRD), Thermal gravimetric analysis (TGA) and UV spectrophotometer measurements were adopted to analyze the morphology, the crystalline structure, crystallite size, thermal stability and band gap of sample. Finally, electrical properties and gas sensing properties have been studied.

2 Experimental

2.1 Preparation of Material

The $(Sn_{0.3}Ti_{0.7})O_2$ powder was synthesized via wet-chemistry route from AR-grade starting materials and solvents, used without any further purification [14]. Tin (II) dichloride dihydrate ($SnCl_2.2H_2O$) (0.3 M) (99.8 %, Aldrich) was dissolved in distilled water. Further Titanium chloride III ($TiCl_3$) (0.7 M), containing 15 % HCl (99.8 %, Aldrich) was introduced dropwise into the solution with constant stirring followed by slowly heating it in air at 80 °C. The dried powder was calcinated at 1,000 °C for 6 h to obtain base material ST_{30} [15–17]. Then this powder was ground in an agate pastle–mortor to ensure sufficiently fine particle size.

2.2 Preparation of Thick Films

The thixotropic paste was formulated by mixing the fine powder of ST_{30} with temporary binder as a mixture of organic solvents. The ratio of the inorganic to organic part was kept at 75:25 in formulating the paste. This paste was screen printed on a glass substrate in a desired pattern (1.5 × 0.5 cm) to prepare thick films [18–20]. The films were fired at 550 °C for 30 min in an air atmosphere to remove the residual.

2.3 Modification of Thick Films

The CuO-modified ST_{30} thick films were obtained by dipping them in a 0.01 M aqueous solution of copper chloride ($CuCl_2$) for different intervals of dipping time of 5, 10 and 20 min. These films were dried at 80 °C, followed by firing at 550 °C for 30 min. The films so prepared are termed as 'cupricated' films [21–23].

2.4 Thickness Measurement

The thickness (t) of the film was calculated using a weight-difference method using (1),

$$t = \frac{m}{\rho \times A} \tag{1}$$

where, m is the mass of the film deposited on the substrate in gm, '*A*' the surface area of the film in cm^2 and 'ρ' is the density of deposited material. Average thickness of the film was observed to be 75 μm. The reproducibility of the film thickness was achieved by maintaining the proper rheology and thixotropy of the paste.

3 Structural Properties

3.1 X-ray Diffraction Analysis

To identify the structure and phase purity of the prepared sample, X-ray diffraction analysis (XRD) measurement was carried out. XRD analysis of these powders were carried out in the 20–80° (2θ) range using Cu-Kα (with $\lambda = 1.542$ Å, 40 kV, 30 mA) radiation. Figure 1 showed the X-ray diffraction patterns of ST_{30} thick film. X-ray diffraction analysis at room temperature was carried out to recognize the crystalline phase of ST_{30} powder. ST_{30} solid solution exhibited a rutile-like single phase. It has been possible to observe that the ST_{30} peak position well matched with JCPDS data of rutile TiO_2 (JCPDS No.: 76–0649), allowing us to indirectly verify that the synthesis of the material correctly occurred. The prepared sample shows single phase of the solid solution ST_{30} at calcinations temperature 1,000 °C. This temperature is lower than that required to prepare the material by the solid-state reaction (1,500 °C) [24]. The sharpness of the peaks indicates the polycrystalline nature of the film material.

Table 1 depicts X-ray diffraction analysis of pure ST_{30} Thick Film. The d values were in good agreement with those in the JCPDS for TiO_2 possessing tetragonal structure. The average crystallite size was determined by using Scherrer formula for various identified diffraction peaks [25] and crystallite size was found to be nearly 41 nm.

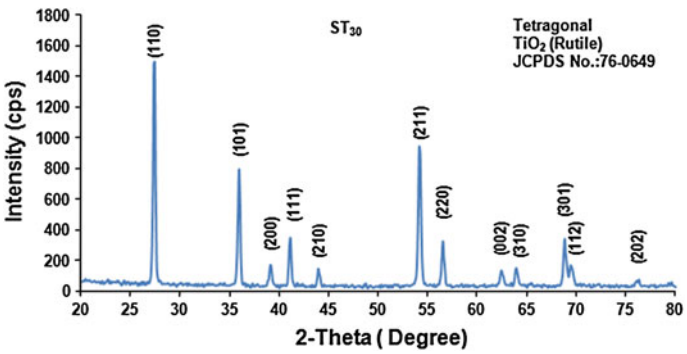

Fig. 1 XRD pattern of pure ST_{30} film

Table 1 X-ray diffraction analysis of pure ST_{30} thick film

Angle (2θ) (°)	d spacing (Å)	FWHM	Peak intensity in %	Crystallite size (nm)	hkl plane
27.40	3.252	0.278	100	42	110
35.87	2.501	0.272	53.1	36	101
39.17	2.298	0.334	11.6	34	200
41.09	2.194	0.280	23.2	42	111
43.89	2.060	0.354	9.8	32	210
54.10	1.693	0.330	62.9	40	211
56.47	1.628	0.274	21.8	48	220
62.32	1.487	0.355	9.1	49	002
63.88	1.445	0.363	10.2	35	310
68.79	1.363	0.291	22.9	49	301
69.42	1.352	0.290	11.3	49	112
76.27	1.247	0.301	4.6	48	202

4 Microstructural Analysis

4.1 Pure ST_{30} Films

Figure 2 depicts a SEM image of a pure ST_{30} thick film fired at 550 °C. The film consists of voids and a wide range of particles with particle sizes ranging from 200 to 840 nm distributed non-uniformly.

4.2 Cupricated ST_{30} Films

Figure 3a–c consist of SEM images of cupricated ST_{30} thick films for the dipping time interval of 05, 10 and 20 min fired at 550 °C, respectively. The micrograph shows a number of small particles distributed uniformly between the larger grains

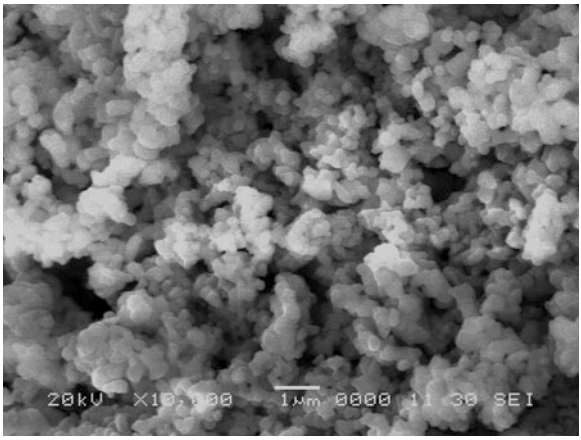

Fig. 2 SEM image of pure ST_{30} films

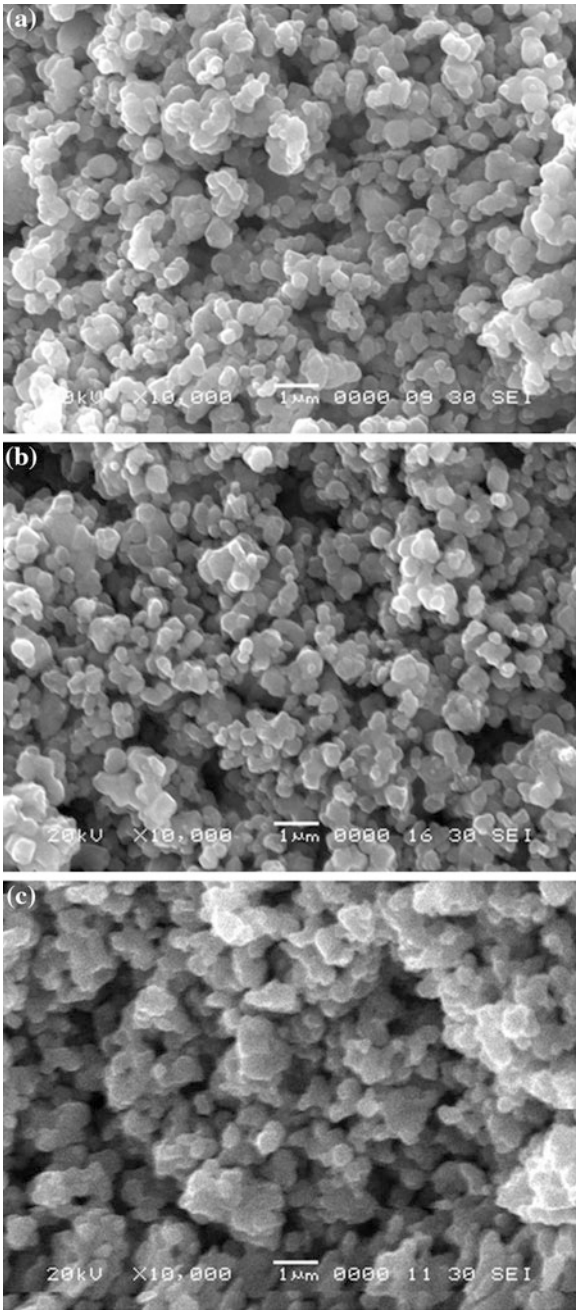

Fig. 3 SEM image of cupricated **a** ST_{30} (05 min), **b** ST_{30} (10 min), and **c** ST_{30} (20 min) films

around the ST_{30} which may be attributed to the presence of CuO. The change in dipping time of the film changes the particle sizes. The particle sizes ranging from 151 to 350 nm (Fig. 3a), 145 to 220 nm (Fig. 3b), and 175 to 500 nm (Fig. 3c) were observed. The micrograph (10 min dipping) appears to consist of a number of small particles distributed uniformly between the larger grains of the ST_{30} film. The smaller particle may be attributed to the presence of CuO. The film seems to be highly porous with a large effective area for oxygen adsorption.

Table 2 depicts the variation of average particle size (d) and specific surface area (SSA) with dipping time of the film. Average particle size (d) was estimated from the SEM images of ST_{30} samples and SSA from (2),

$$A = \frac{6}{\rho \times D} \tag{2}$$

where, ρ is the density of sample and D is the particle size of the films.

5 Elemental Analysis

Figure 4a shows the EDAX spectra of pure ST_{30} film and Fig. 4b shows the EDAX spectra of cupricated ST_{30} films. The quantitative elemental composition of the film and wt % of CuO analysed using an energy dispersive spectrometer are presented in Table 3. It has been observed that the weight percentage of copper increased with dipping time. The film with the dipping time of 10 min was observed to be more oxygen deficient (23.37 wt %). This oxygen deficiency may make the sample possible to adsorb a large amount of oxygen species.

6 Structural Parameters and Their Analysis

6.1 Texture Coefficient

The texture coefficient (Tc) of the film was determined using (3). From that, it was observed that T_C approaches unity for randomly distributed samples whereas T_C is larger than unity for a preferentially oriented (hkl) plane. The lower value of T_C reveals that the films have poor crystallinity. It has been observed that the preferred orientation is the (110) plane for ST_{30} sample. Texture coefficient of the film was found to be 1.13.

Texture coefficient of (hkl) plane,

$$Tc(hkl) = \frac{I(hkl)/Io(hkl)}{\frac{1}{N} \times \sum I(hkl)/Io(hkl)} \tag{3}$$

where, N–No. of planes in XRD pattern.

Table 2 Variation of specific surface area with dipping time of films

Sample	Av. particle size, d nm (SEM)	Specific surface area (SSA) m^2/g
Pure ST_{30} film	520	5.77
Cupricated ST_{30} (05 min)	240	12.50
Cupricated ST_{30} (10 min)	200	15.00
Cupricated ST_{30} (20 min)	337	8.90

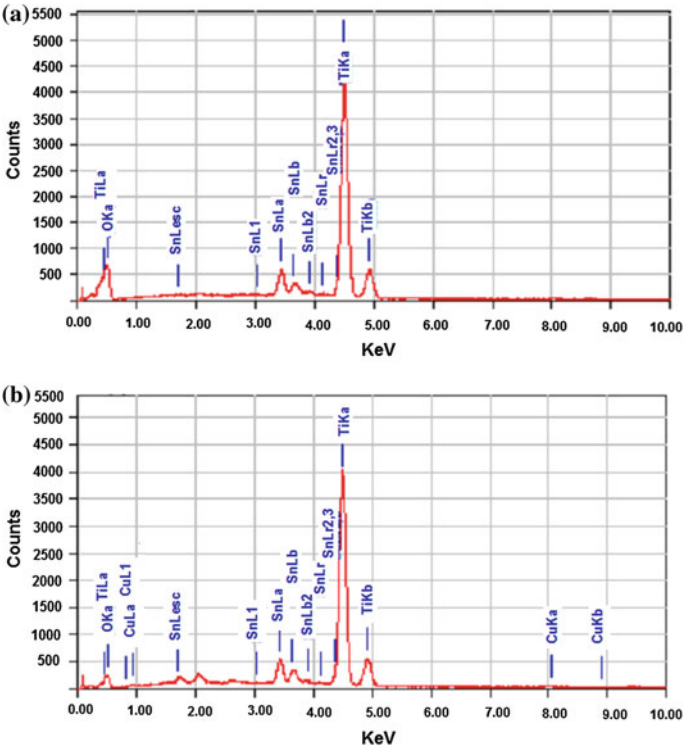

Fig. 4 EDAX spectra of **a** pure ST_{30} and **b** cupricated ST_{30} films

Table 3 Elemental composition of pure and cupricated ST_{30} thick films

Samples	Wt. % of			
	Sn	Ti	O	Cu
Pure ST_{30} film	20.59	49.71	29.70	0.00
Cupricated ST_{30} (05 min)	22.29	51.44	25.91	0.36
Cupricated ST_{30} (10 min)	22.50	52.62	23.37	1.51
Cupricated ST_{30} (20 min)	21.57	51.57	25.25	1.61

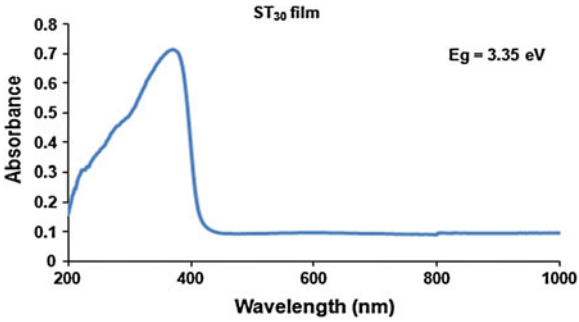

Fig. 5 Diffuse absorbance UV–Vis–NIR spectra of ST_{30}

6.2 UV–Vis–NIR Spectrum Analysis

Figure 5 shows the absorbance spectra of ST_{30} sample. UV analysis of the prepared ST_{30} powder was carried out using JASCO UV–Vis-NIR Spectrophotometer (V-670). The energy band gap, Eg, of the prepared powder was determined using the absorption UV–VIS—NIR spectra. The optical energy band gap was found to be 3.35 eV, using the relationship [26, 27]:

$$Eg = \frac{h \times c}{\lambda} \tag{4}$$

H–Planck's constant, $h = 4.135 \times 10^{-15}$ (eV·s), *c*–speed of light (m/s), $c = 3 \times 10^{8}$ (m/s),

λ–wavelength of light (nm).

7 Thermo Gravimetric Analysis/Differential Thermal Analysis

Figure 6 shows the TGA/DTA profiles of pure ST_{30} sample. Thermogravimetric (TGA) analysis of the samples was carried out using a Mettler Toledo Star system-851 under similar conditions in static air. Thermal stability of pure ST_{30} was examined by a thermo gravimetric analyzer (TGA), using α-Al_2O_3 powder as the reference in air and at a heating rate of 10 °C/min. About 6.008 mg of powders were used for the test. Weight loss ST_{30} material was observed to be nearly 1 %.The small weight loss may be contributing to its larger stability of the prepared material.

The DTA showed the endothermic nature of reactions for pure ST_{30}. The heat absorbed by the samples may be due to the non-stoichiometry of ST_{30} and oxygen deficiency.

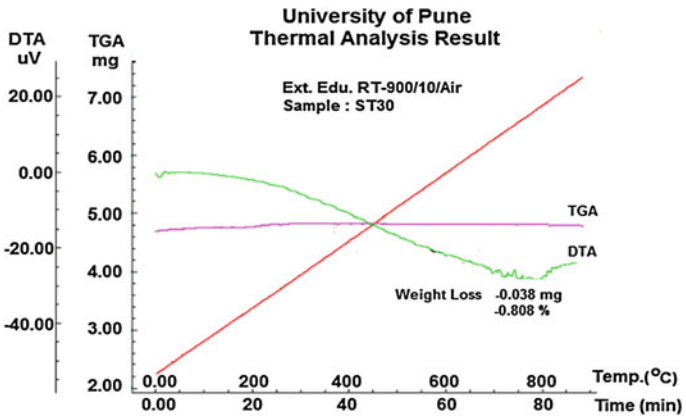

Fig. 6 TGA/DTA of pure ST_{30} material

8 Electrical Properties

8.1 I–V Characteristics

Figure 7 shows the I–V characteristics of pure and cupricated ST_{30} thick films in air atmosphere. The linearity in the graphs indicates the ohmic nature of the pressure contacts.

8.2 Temperature Coefficient of Resistance

Temperature coefficient of resistance for metal is positive, whereas for semiconductors TCR is negative. The relation for resistance and temperature is given by (5),

$$RT = R0[1 + \alpha T] \tag{5}$$

where,

R_T = resistance of sample of temperature T
R_O = resistance of sample at room temperature
T = temperature under consideration
α = TCR of the sample

$$\therefore TCR(\alpha) = \frac{1}{R_o}\left(\frac{\Delta R}{\Delta T}\right) \Big/ {}^{\circ}\mathrm{C}$$

$$\therefore TCR(\alpha) = \frac{\text{slope}}{R_o} \Big/ {}^{\circ}\mathrm{C} \tag{6}$$

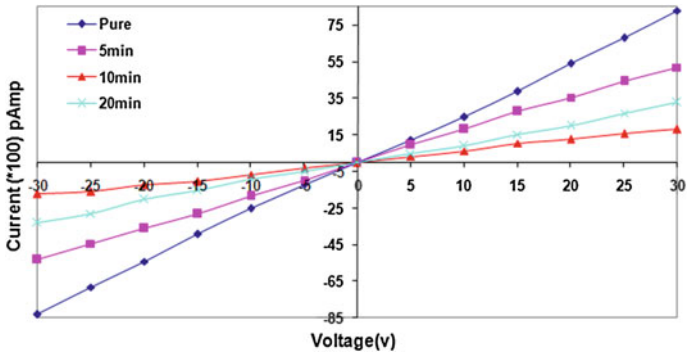

Fig. 7 I-V characteristics of pure and cupricated ST_{30} films

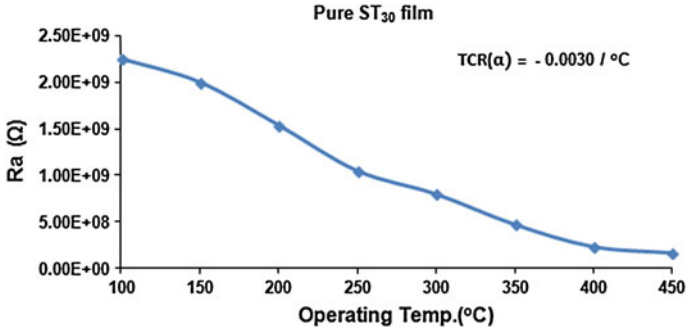

Fig. 8 Variation of resistance of the film with operating temperature

TCR (α) of the pure ST_{30} film was calculated from the slope of the graph of resistance of the film in air (Ra) versus operating temperature (Fig. 8) using (6) and found to be negative. This shows the semiconducting nature of the film.

8.3 Electrical Conductivity

Figure 9 shows the variation of conductivity with temperature for the pure and cupricated samples. The legends suffixed 'a' are the graphs for samples tested in air atmosphere, while the legends suffixed 'g' represent the graphs for the conductivities in the presence of H_2S gas. The graph shows the nonlinear variation of conductivity with temperature for all samples. This shows the semiconducting nature of the films. The conductivity of particular cupricated sample, upon exposure of gas, was larger than that in air. The conductivity of the sample cupricated for 10 min was largest of all. The conductivities of cupricated ST_{30}

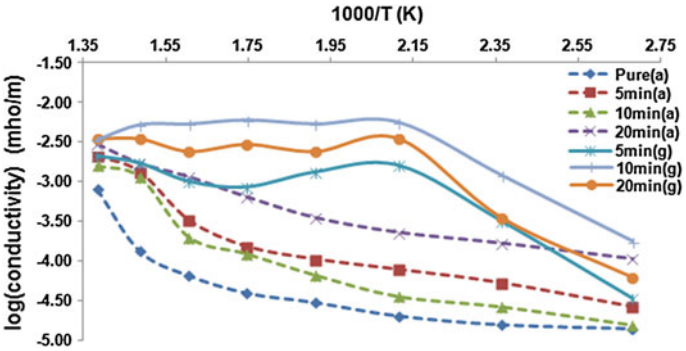

Fig. 9 Variation of electrical conductivity with temperature of pure and cupricated ST_{30} films

Table 4 Variation of activation energy with dipping time ST_{30} thick films

Sample	Activation energy(eV)
Pure ST_{30} film	0.242
Cupricated ST_{30} (05 min)	0.172
Cupricated ST_{30} (10 min)	0.140
Cupricated ST_{30} (20 min)	0.148

samples were larger than that of pure ST_{30} at particular temperature in the presence of gas or in air.

Table 4 represents the activation energy with dipping time of the film, which is calculated from the slope of the graph of log (conductivity) versus 1/T. It has been observed that the activation energy of most sensitive film (10 min.) (0.140 eV) is less than the pure film (0.242 eV) at 300 °C. This reveals that the surface cuprication of the films improves the gas response of the film; since less amount of energy is require to change the one stable state to other state of sensor.

9 Gas Sensing Properties

9.1 Pure ST_{30} Films

9.1.1 Gas Response with Operating Temperature

Figure 10 depicts the response to CO_2 gas with operating temperature of the pure ST_{30} thick films fired at 550 °C.The gas response values of pure thick films were determined at various operating temperatures ranging from 100 to 450 °C for CO_2 gas. The response increases with increasing the operating temperature, attains its maximum at 300 °C and then decreases with a further increase in operating temperature. It has been noted that the optimum operating temperature of pure film is 300 °C.

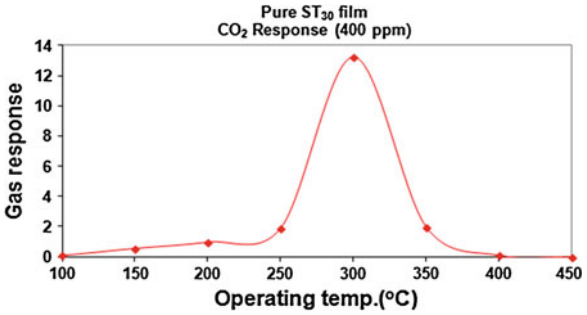

Fig. 10 Variations in response to CO_2 gas with operating temperature of pure ST_{30} film

9.1.2 Selectivity

Figure 11 shows the bar diagram indicating the selectivity of the pure ST_{30} sensor operated at 300 °C to CO_2 gas against other gases. It is evident that the pure sensor is selective to CO_2 at 300 °C gas against the other gases.

9.2 Modified ST_{30} Films

9.2.1 Gas Response with Operating Temperature

The response to H_2S gas with operating temperature of the cupricated ST_{30} thick films for the dipping time interval of 05, 10 and 20 min. fired at 550 °C are represented in Fig. 12.The gas response values of surface cupricated ST_{30} films were determined at various operating temperatures ranging from 100 to 450 °C to H_2S gas. The modified film suppresses gas response of CO_2 gas of pure film and enhances the response to H_2 S gas. The films dipped for 10 min. was most sensitive H_2S gas. The response increases with increasing the operating temperature attains its maximum (at 200 °C) and then decreases with a further increase in operating temperature. It is clear that the optimum operating temperature of cupricated film is 200 °C.

9.2.2 Variation of Gas Response with Dipping Time

Figure 13 shows the variation of the gas response of the cupricated films treated for different intervals of dipping time. It is clear that the response to H_2S goes on increasing with an increase in the dipping time interval. H_2S gas response attains its maximum at 10 min dipping and decreases with further dipping.

9.2.3 Selectivity

Figure 14 depicts the selectivity of the cupricated (10 min) ST_{30} film operated at 200 °C to H_2S gas against other gases. The cupricated film suppresses response of

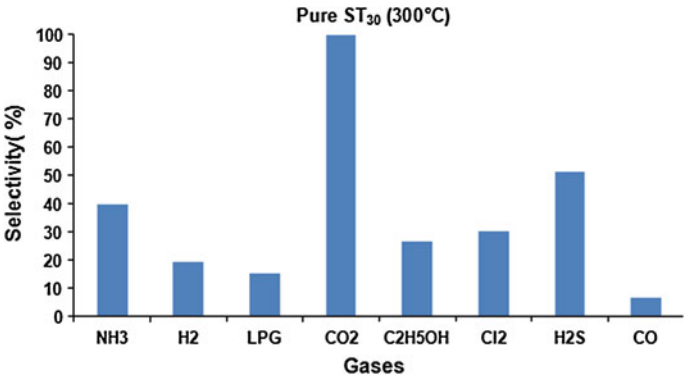

Fig. 11 Selectivity of pure ST_{30} film to CO_2 against other gases

Fig. 12 Variations in response to H_2S gas with operating temperature of cupricated ST_{30} film

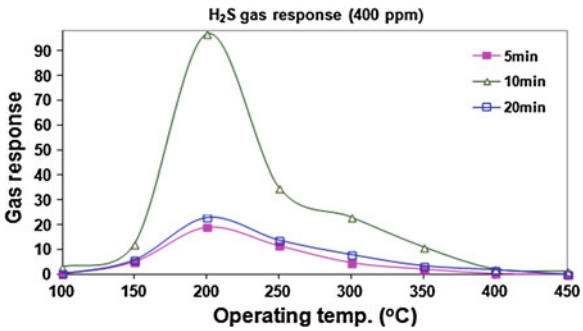

Fig. 13 Variation in H_2S gas response with dipping time of ST_{30} film

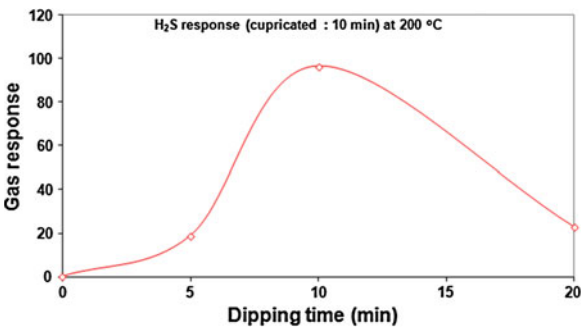

the gases selected at 300 °C operating temperatures of pure film and enhances the response to H_2S gas. It is evident that the cupricated sensor was highly selective to H_2S gas at 200 °C.

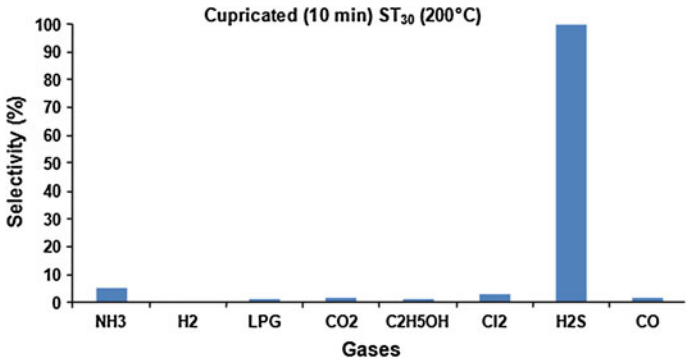

Fig. 14 Selectivity of cupricated ST_{30} film to H_2S against other gases

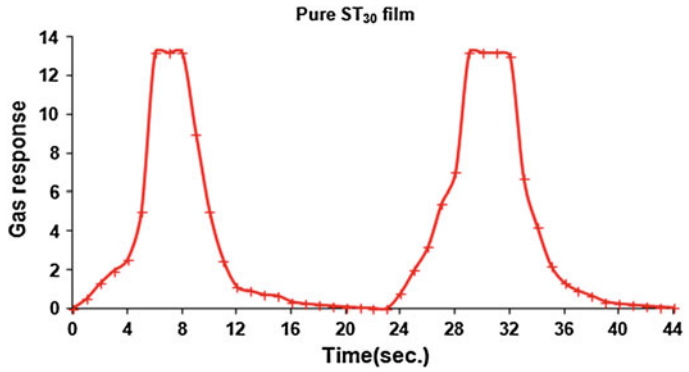

Fig. 15 Response and recovery time of pure ST_{30} film

10 Response and Recovery Time of Sensors

10.1 Pure ST_{30} Film

The response and recovery time of pure ST_{30} film are represented in Fig. 15. The response time of pure ST_{30} film was 5 s. and recovery time was 22 s. at operating temperature 300 °C.

10.2 Cupricated ST_{30} Film

Figure 16 shows the response and recovery time of cupricated (10 min.) ST_{30} film. The response time of the film was 3 s and recovery time was 20 s at operating temperature 200 °C. This indicates that surface cuprication of the film reduces the

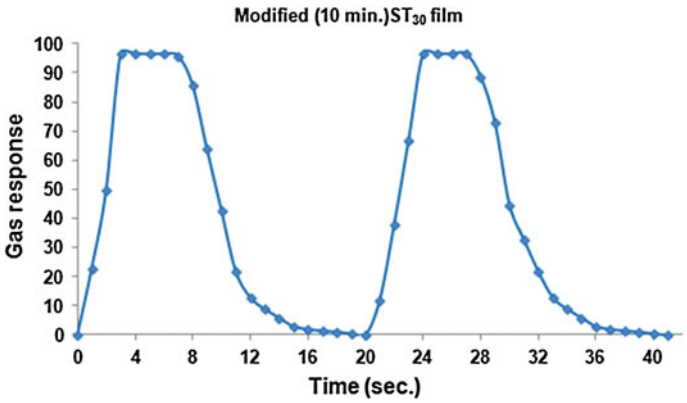

Fig. 16 Response and recovery time of cupricated (10 min) ST_{30} film

response and recovery time of the sensor. The small response and recovery time are the remarkable features of the cupricated ST_{30}.

11 Long-Term Stability of Sensor

11.1 Pure ST_{30} Film

Figure 17 shows the long term stability of pure ST_{30} film. It was observed that the over a long period (2 month) the response of the sensor was found to be nearly same.

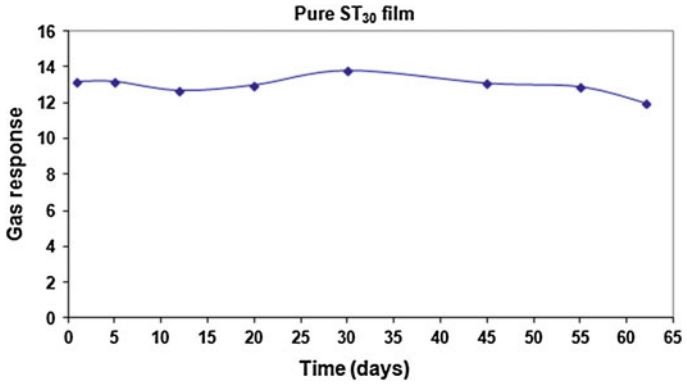

Fig. 17 Long time stability of pure ST_{30} film

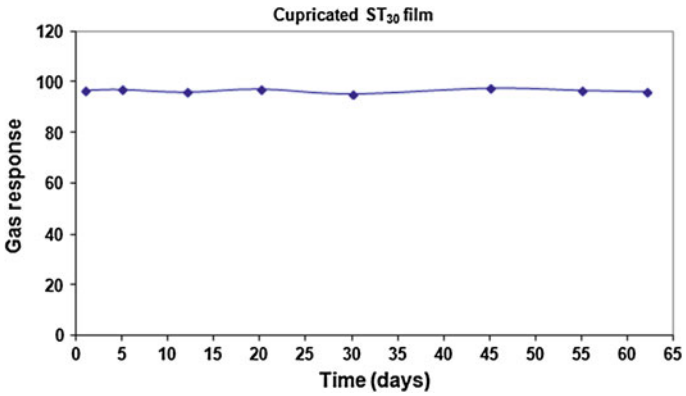

Fig. 18 Long time stability of cupricated (10 min) ST_{30} film

11.2 Cupricated ST_{30} Film

Long term stability of cupricated ST_{30} film is shown in Fig. 18. It was observed that due to cuprication of the films the long time stability of gas response of the sensor is found to be improved.

12 Gas Response to Different Gas Concentrations

Figure 19 exhibits response to H_2S gas for various gas concentrations ranging from 100 to 800 ppm at 200 °C operating temperature. It observed that sensitivity increases linearly from 100 to 400 ppm after that, film shows nearly constant response. This may be due to the masking of sensor surface and not responding further increasing gas concentration. So sensor would be used in active region (100–400 ppm).

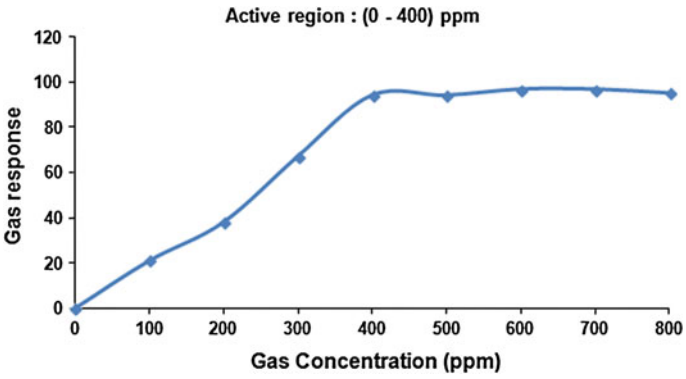

Fig. 19 Response to H_2S gas for different gas concentration of cupricated (10 min) ST_{30} film

13 Error Measurement

The standard deviation (σ) is calculated from the squares of the deviations from the mean using the following formula (7):

$$\sigma = \sqrt{\frac{\sum \left[(x_i - \bar{x})^2 \right]}{n-1}} \tag{7}$$

Measurement of % error in gas response of ST_{30} film of pure and most gas sensitive cupricated ST_{30} film is depicted in Table 5.

It is observed that the maximum error is less than 10 %. It means the measurement method carried in this work is correct. It is also observed that error decreases with surface modification that indicates the method of surface modification is correct.

14 Summary Table

Samples	Optimum operating conditions			Gas sensing performance			
	Dipping time	Temp. (°C)	Gas conc. (ppm)	Max. sensitive to gas	Gas response	Res. time (s)	Rec. time (s)
Pure ST_{30} film	–	300	400	CO_2	13.20	6	24
Cupricated ST_{30} film (10 min)	10 min	200	400	H_2S	96.70	3	20

ST_{30} :$(Sn_{0.3}Ti_{0.7})O_2$, Conc.: concentration, Max.: Maximum, Res.: Response, Rec.: Recovery

15 Discussion

Gas response (S) is the device characteristic of perceiving a variation in physical and/or chemical properties of the sensing material under gas exposure. The sensitivity, in the case of resistive gas sensors, is defined as the relative change in

Table 5 Measurement of % error in gas response

Sample	Temp.	Gas response	Standard Deviation (σ)	% Error
Pure ST_{30} film	300	13.20	0.79	6
Cupricated ST_{30} film (10 min.)	200	96.70	0.63	1

resistance of the thick film. It is the ratio of the change in the resistance of the thick film in air to the change in resistance in particular gas atmosphere. The sensitivity is given by (8) [22]:

$$\text{Gas response (S)} = \left|\frac{R_a - R_g}{R_a}\right| = \frac{\Delta R}{R_a} \tag{8}$$

where, R_a–resistance of a thick film sensor in air

R_g–resistance of a thick film sensor in a sample gas

It is the ability of a sensor to respond to a certain gas in presence of other gases is known as selectivity. A good sensor will discern a particular signal by allowing adsorption of the desired gas while remaining insensitive to others.

The % selectivity of 'target gas' to another gas is defined as:

$$\%\text{Selectivity} = \frac{S_A}{S_B} \times 100 \tag{9}$$

where, S_A and S_B are the sensitivities of sensors in 'target gas' and B gas, respectively.

It is known that atmospheric oxygen molecules are adsorbed on the surface of ST_{30} semiconductor oxide in the forms of O^-, $O_2{}^-$ and O^{2-}, thereby decreasing the electronic conduction. Atmospheric oxygen molecules take electrons from the conduction band of ST_{30} to be adsorbed as O^- ST_{30}. The reaction is as follows:

$$O_2\{g\} + 2e^- \rightarrow 2O^- ST_{30} \tag{10}$$

When reducing gas molecules like CO_2 react with negatively charged oxygen adsorbates, the trapped electrons are given back to conduction band of ST_{30}. The energy released during decomposition of adsorbed CO_2 molecules would be sufficient for electrons to jump up into conduction band of ST_{30}, causing an increase in the conductivity of sensor.

For oxidation of CO_2, some amount of activation energy has to be provided thermally. An increase in operating temperature surely increases the thermal energy so as to stimulate the oxidation of CO_2. The reducing gas (CO_2) donates electrons to ST_{30}. Therefore, the resistance decreases, or the conductance increases. This is the reason why the gas response increases with operating temperature. The point at which the gas response reaches maximum is the actual thermal energy needed for the reaction to proceed. However, the response decreases at higher operating temperatures, as the oxygen adsorbates are desorbed from the surface of sensor [28]. Also, at high temperatures the carrier concentration increases due to intrinsic thermal excitation and the Debye length decreases. This may be one of the reasons for the decreased gas response at high temperatures [11].

The interaction between a semiconductor surface and H_2S may be explained in terms of reaction of H_2S molecules with pre-adsorbed oxygen. Oxygen adsorbs at the surface in several forms such as : O^-, $O_2{}^-$ and O^{2-}.

The H_2S gas is reducing in nature. It can reduce CuO into CuS which are metallic in nature and is more conducting. This can be represented as:

$$CuO + H_2S \rightarrow CuS + H_2O \quad (11)$$

Upon subsequent exposure of sensor to air ambient at elevated temperature, sulphides got oxidized and could be recovered back to oxides as

$$2CuS + 4O_2 \rightarrow 2CuO + 2SO_3 \quad (12)$$

When oxygen is adsorbed on the surface of ST_{30} film, abstracting electrons, and thus an increase in potential barrier at the grain boundaries. When reducing gas such as H_2S is adsorbed between the grains of ST_{30} film, the potential barrier decreases as a result of oxidative conversion of the H_2S gas. H_2S reacts with adsorbed oxygen ions as:

$$H_2S + 3O^- \rightarrow H_2O + SO_2 + 3e^- \quad (13)$$

The amount of oxygen adsorbed on the surface of cubricated ST_{30} films is more, since copper oxide form misfit regions between the grains of ST_{30} film and act as efficient catalysts for oxygenation.

When the optimum amount of copper oxide is incorporated on the surface of the ST_{30} film, copper species would be distributed uniformly throughout the surface (Fig. 3b). Due to this not only the initial resistance of the film is high but this amount would also be sufficient to promote the catalytic reaction effectively and the overall change in resistance on exposure of the test gas larger leading to high sensitivity to gas.

When the amount of copper oxide on the surface of the film is less than the optimum, the surface dispersion would be poor and amount may not be sufficient to promote the reaction more effectively leading to decreased sensitivity.

The nonlinearity of the electrical conductivity-temperature profiles of the samples reveals the semiconducting nature of pure and cupricated ST_{30}. The semiconducting nature may be attributed to oxygen deficiencies in ST_{30}. Cupri-cation of ST_{30} has enhanced the electrical conductivity. This may be due to the bridging of intergranular gaps between ST_{30} particles by small particles of CuO segregated around the grain boundaries of ST_{30}.

Fast recovery and response to H_2S gas may be due to faster adsorption–desorption reactions on the surface of the cupricated films. A large number of oxygen ions would be adsorbed on the misfit regions of copper in ambient air. The larger the misfits on the surface, the larger would be the number of oxygen ions adsorbed on the surface leading to high resistance. The larger the number of oxygen ions adsorbed on the surface, the faster would be the oxidation of the exposed gas and the response time. ST_{30} was observed to be highly oxygen deficient. The larger the oxygen deficiency, the faster would be the adsorptions of oxygen ions and in turn the faster the recovery of the sensor.

16 Summary and Conclusions

Following statements can be made from the experimental results.

- The thick films of pure ST_{30} were sensitive to CO_2 gas at 300 °C.
- Surface cupication process was employed to modify only the surface of the film and not the bulk portion of the base material ST_{30}.
- The thick films of pure and cupricated ST_{30} was observed to be semiconducting in nature and showed a negative temperature coefficient of resistance.
- The cuprication alters morphology and shifts response of the films towards H_2S gas at temperature (200 °C).
- Cupricated films were found to be more porous film. As porosity increases of the film, the gas response of the film would be increases.
- Average crystallite size from XRD using Scherrer formula of pure film was 41 nm.
- Response and recovery time of cupricated film was reduced due to surface modification.
- Cupricated films showed the good long time stability compare to pure film.
- The optical energy band gap of prepared ST_{30} sample was found to be 3.35 eV.

Acknowledgments The author would like to thank UGC (WRO), Pune for the financial support to research work. The authors also thank to university of Pune for the help in the characterization of the films. A special thanks goes to the Principal of the K.T.H.M. College, Nashik for providing the facility of laboratory for research work.

References

1. K. Zakrzewska, Mixed oxides as gas sensors. Thin Sol. Films **391**, 229–238 (2001)
2. R. Moos, A brief overview on automotive exhaust gas sensors based on electroceramics. Int. J. Appl. Ceram. Technol. **2**, 401–413 (2005)
3. W. Schmid, N. Barsan, U. Weimar, Sensing of hydrocarbons with tin oxide sensors: possible reaction path as revealed by consumption measurements. Sens. Actuat. B Chem. **89**, 232–236 (2003)
4. E. Traversa, M. Miyayama, H. Yanagida, Gas sensitivity of ZnO/La_2CuO_4 heterocontacts. Sens. Actuat. B Chem. **17**, 257–261 (1994)
5. J. Tamaki, T. Maekawa, N. Miura, N. Yamazo, Gold-loaded tungsten-oxide sensor for detection of ammonia in air. Sens. Actuat. B Chem. **9**, 197–203 (1992)
6. X. Zhou, Q. Cao, Y. Hu, J. Gao, Y. Xu, Sensing behavior and mechanism of La_2CuO_4-SnO_2 gas sensors. Sens. Actuat. B Chem. **77**, 443–446 (2001)
7. X. Zhou, Q. CaO, H. Huang, P. Yang, Y. Hu, Study on sensing mechanism of CuO–SnO_2 gas sensors. Mater. Sci. Eng. B **99**(1–3), 44–47 (2003)
8. R. Kumar, A. Khanna, P. Tripathi, R. Nandedkar, S. Potdar, S. Chaudhari, S. Bhatti, CuO SnO_2 element as hydrogen sulfide gas sensor prepared by a sequential electron beam evaporation technique. J. Appl. Phys. **36**, 2377–2381 (2003)

9. F. Edelman, H. Hahn, S. Seifried, C. Alof, H. Hoche, A. Balogh, P. Werner, K. Zakrzewska, M. Radecka, P. Pasierb, A. Chack, V. Mikhelashvili, G. Eisenstein, Structural evolution of SnO_2–TiO_2 nanocrystalline films for gas sensors. Mater. Sci. Eng. B **69–70**, 386–391 (2000)
10. M. Radecka, K. Zakrzewska, M. Rgkas, SnO_2–TiO_2 solid solutions for gas sensors. Sens. Actuat. B Chem. **47**, 194–204 (1998)
11. J. Mizsel, How can sensitive and selective semiconductor gas sensors be made? Sens. Actuat. B **23**, 173–176 (1995)
12. L. Kong, J. Ma, H. Huang, Preparation of the solid solution $Sn_{0.5}Ti_{0.5}O_2$ from an oxide mixture via a mechanochemical process. J. Alloy. Compd. **336**, 315–319 (2002)
13. Y. Park, H. Song, C. Lee, J. Jee, Fabrication and its characteristics of metal-loaded TiO_2/SnO_2 thick-film gas sensor for detecting dichloromethane. J. Ind. Eng. Chem. **14**, 818–823 (2008)
14. M. Carotta, A. Cervi, S. Gherardi, V. Guidi, C. Malagu, G. Martinelli, B. Vendemiati, M. Sacerdoti, G. Ghiotti, S. Morandi, S. Lettieri, P. Maddalena, A. Setaro, (Ti, Sn)O_2 solid solutions for gas sensing: a systematic approach by different techniques for different calcination temperature and molar composition. Sens. Actuat. B Chem. **139**, 329–339 (2009)
15. G. Jain, V. Gaikwad, L. Patil, Studies on gas sensing performance of $(Ba_{0.8}Sr_{0.2})(Sn_{0.8}Ti_{0.2})O_3$ thick film resistors. Sens. Actuat. B Chem. **122**, 605–612 (2007)
16. J.D. Lee, *Concise In-organic Chemistry,* 5th edn. (Wiley India, New Delhi, 2008), p. 698
17. G.S. Manku, *In-organic Chemistry* (TMG Co, New York, 1984), pp. 465–467
18. T. Ishihara, K. Kometani, Y. Nishi, Y. Takita, Improved sensitivity of CuO–$BaTiO_3$ capacitive type CO_2 sensor by additives. Sens. Actuat. B Chem. **28**, 49–54 (1995)
19. C.A. Harper, *Hand Book of Thick Film Hybrid Microelectronics* (McGraw-Hill Co, New York, 1974)
20. M. Wagh, L. Patil, T. Seth, D. Amalnerkar, Surface cupricated SnO_2-ZnO thick films as a H_2S gas sensors. Mater. Chem. Phys. **84**, 228–233 (2004)
21. S. Patil, L. Patil, D. Patil, G. Jain, M. Wagh, CuO-modified tin titanate thick film resistors as H_2-gas sensors. Sens. Actuat. B Chem. **123**, 233–239 (2007)
22. G. Jain, L. Patil, Gas sensing properties of Cu and Cr activated BST thick films. Bull. Mater. Sci. **29**, 403–411 (2006)
23. V. Choudhary, I. Mulla, K. Vijaymohan, Comparative Studies of doped and surface modified tin oxide towards hydrogen sensing: synergistic effects of Pd and Ru. Sens. Actuat. B **50**, 45–51 (1998)
24. H. Naidu, A. Virkar, Low-temperature TiO_2–SnO_2 phase diagram using the molten-salt method. J. Am. Ceram. Soc. **81**, 2176–2180 (1998)
25. B. Cullity, *Elements of X-ray Diffraction*, 2nd edn. (Addison Wesley, Reading, 1978), p. 107
26. K. Porkodi, S. Arokiamary, Synthesis and spectroscopic characterization of nanostructured anatase titania: a photocatalyst. Mater. Charact. **58**, 495–503 (2007)
27. Molea, V. Popescu, The obtaining of titanium dioxide nanocrystalline powders. Optoelectron. Adv. Mater. Rapid Commun. **5**(3–4), 242–246 (2011)
28. H. Wndichamann, P. Mark, A model for the operation of a thin film oxide (snOx) conductance-modulation carbon monoxide sensor. J. Electrochem. Soc. **126**, 627–633 (1979)

Chapter 13
Synthesis, Characterization and Ammonia Gas Sensing Properties of Cr_2O_3 Doped ZrO_2 Thick Film Resistor

S. B. Deshmukh, R. H. Bari and G. H. Jain

Abstract Aqueous solution of zirconium oxychloride octohydrate in appropriate volumetric amounts, were used as the starting chemicals in the synthesis of pure ZrO_2 powder. ZrO_2 thick films were prepared by standard screen printing technique. Pure ZrO_2 films were activated with Cr^{3+} by dipping them into an aqueous solution (0.1 M) of chromium trioxide CrO_3 for different interval of time 5, 10, 20, 30 min and fired at 550 °C for 30 min The CrO_3 is known to be unstable above 197 °C and transform into Cr_2O_3 upon firing above 197 °C. The grain of Cr_2O_3 would disperse around the grains of ZrO_2 base material. The films were characterized by XRD, SEM, EDAS, UV, FTIR techniques. The gas sensing performance of different target gases was tested and the chromium activated films dipped in 10 min was observed to be sensitive. And highly selective 1,000 ppm of NH_3 gas at operating temperature 300 °C. The elemental composition were discussed and effect of Cr^{3+} concentration on sensitivity, selectivity, response and recovery time of the sensor in the presence of different gases were studied. Reaction mechanism were discussed with better performance could attributed to an optimum number of surface misfits in terms of Cr_2O_3 on the ZrO_2 films. It was first time observed that crominated surface modified film have reduction in bandwidth and observed activation energy were reported. Observation of FTIR spectra for both pure and activated ZrO_2 predicts the existence of Zr–O–Zr bond with proper stretching and bending.

Keywords Cr_2O_3 activated · Dipping · Sensitivity · Response and recovery time

S. B. Deshmukh (✉)
Arts Science and Commerce College, Nampur, Maharashtra 423203, India
e-mail: mesudhakar_deshmukh@rediffmail.com

R. H. Bari
GDM Arts KRT's Commerce and MD Science College, Jamner,
Maharashtra 424206, India

G. H. Jain
Material Research Lab, K.T.H.M. College, Nashik, Maharashtra 422002, India

A. Mason et al. (eds.), *Sensing Technology: Current Status and Future Trends I*,
Smart Sensors, Measurement and Instrumentation 7, DOI: 10.1007/978-3-319-02318-2_13,

1 Introduction

In the recent past thick film sensors have attracted a great deals of attention because of several advantages such as simple construction, portable size, good sensitivity and selectivity, quick response and fast recovery time, low operating temperature, high stability with good accuracy, easy processing, reproducibility, better repeatability and life cycle, low cost and consumption [1–3]. Classification of thick film sensor is represented in Fig. 1. According to the International Union of Pure and Applied chemistry (IUPAC), "chemical sensor is a device that transforms chemical information, ranging from the concentration of specific sample components to total composition analysis into an analytical useful signal", these conventional gas sensors are based on change in electrical quantity of the active material used. This change is either adsorption or absorption of chemical species at the surface of the active material. In present work Zirconia is used as an active material.

Gas sensors are also classified into metal oxide, Ceramic semiconductor oxide, solid electrolyte potentiometric, capacitive, resistive (conductive), calorimetric, Gravimetric, optical gas sensors. Electronic structure of material is responsible for most of its properties [4]. The chemical information is transduced through the electronic structure of the material. Gas sensing performance especially sensitivity, are controlled by three independent factors: the receptor function, transducer function, utility work function. Receptor function concerns the ability of the oxide surface to interact with the target gas. Chemical properties of the surface oxygen of the oxide itself is responsible for this function in a oxide device, but this function can be largely modified to induce a large change in usually loaded on the oxide surface. Transducer function concerns the ability to convert the signal caused by chemical interaction of the oxide surface (work function change) into electrical signal [5, 6]. The function is played by each boundary between grains, to which a double schottky barrier model can be applied. The utility depends on the barrier height, pore size of sensing work body, diffusion depth, film thickness, doping of the material and concentration of the target gas. Decrease in grain size below critical value can lead to appearing quantum size effects and dramatically increase in the sensitivity of the sensor. ZrO_2 has high refractive index, high melting point, and high resistance to oxidation, good biological properties, oxygen ion conductivity, low thermal conductivity and high coefficient of thermal expansion. ZrO_2 is considered as an important ceramic material due to its superior chemical, thermal, and mechanical properties in a wide range of applications such as catalysts, oxygen sensors, thermal barrier coating on metal surface, high temperature electrolytes in fuel cells, magneto hydrodynamic electrodes, heat resistance lining in high temperature furnaces, biomaterials, biosensors and electrochemical gas sensors [7–9]. At atmospheric pressure Zirconia exist, depending on temperature in three polymorphic forms namely monoclinic, m-ZrO_2 (baddeleytie a = 0.5121 nm, b = 0.5196 nm, c = 0.5316 nm, β = 98.83 °C), tetragonal t-ZrO_2 (a = 0.3632 nm, c = 0.5075 nm) and cubic c-ZrO_2 (a = 0.5128 nm).Transition temperature is not accurately known but it is assumed that the monoclinic form is stable up to approximately 1,100 °C, while

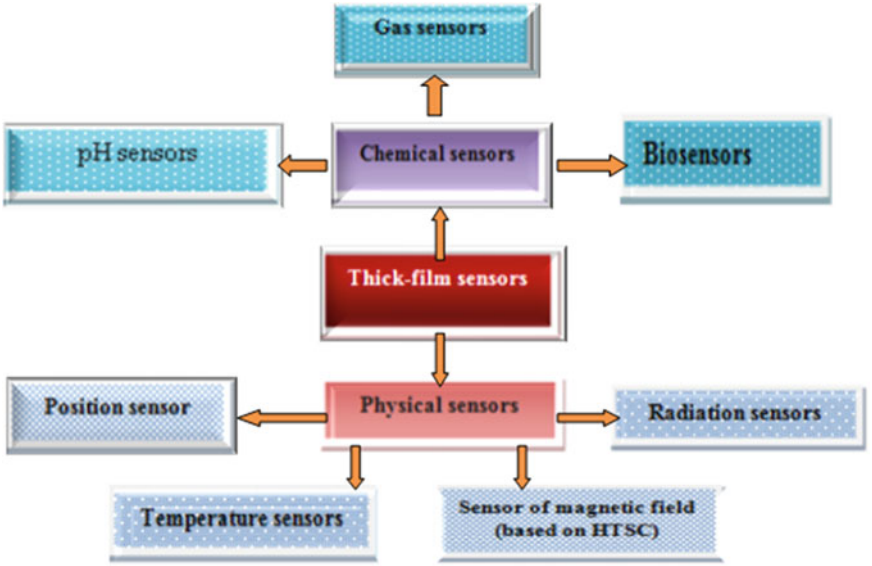

Fig. 1 Thick film sensor classification

above 2,300 °C the stable form is cubic one [10–12]. However appearance of both cubical and tetragonal metastable phases at low temperature [LTP] has been observed by numerous authors, depending on the precursor and condition of preparation, the particle size and the presence of impurity and dopants are important for evaluation of the crystal structure of the films obtained as a function of the temperature of their deposition has been studied in the present study. The Zr^{4+} ion, in ZrO_2 because of its small ionic radius prefers a seven fold coordination's. For this reason pure ZrO_2 is adopts the monoclinic baddelyte structure. Pure ZrO_2 is a ionic conductor. However, when divalent (Ca^{2+}, Ba^{2+}, Mg^{2+}, Cd^{2+} Cu^{2+}) and/or trivalent (Gd^{3+}, Y^{3+}, Yb^{3+}, Sc^{3+}, Ce^{3+}, Cr^{3+}) cations impurities are added to this material, these locate substitution ally on the Zr^{4+} sites and consequently a fraction of the oxygen sites becomes empty to retain overall charge neutrality. The effect of this doping is twofold, one hand doping ZrO_2 with bigger cations stabilizes the fluorite phase at lower temperature and for this reason these materials are usually dubbed stabilized zirconia [13–15]. On the other hand, the introduction of oxygen vacancies increases the mobility of the remaining anions and leads to exceptional value of the ionic conductivity, thus playing an important role in gas sensing. ZrO_2 is thus n-type oxides being stable material for gas sensing and in present work film is modified using dipping technique. Chromium trioxide CrO_3 aqueous solution of 0.1 M was used. Chromium was discovered in 1780 by Nicolas Vanquelin It is a transitional metal having density 7.19 g/cm^3. The metal forms a thin protective oxide coating in air and burns when heated to form green chromium oxide (Cr_2O_3). Cr_2O_3 is a P-type semiconducting material oxide

which has been proposed as a potentially attractive electrode material for resistive sensors due to high melting point, excellent corrosion resistance, and good high temperature electrical conductivity. Cr_2O_3 was selected as a model oxide because its stability and electrical properties have been well documented in literature. Its electrical conductivity of about 5×10^{-3} S/cm at 600 °C and is independent of oxygen pressure changes the oxygen diffusion coefficient is of the order of 10^{-9} μm/s at 1,000 °C, which leads to poor oxygen ion conduction in Cr_2O_3 [16–19]. Ammonia is a colorless gas with a characteristic pungent odor. It is both caustic and hazardous to human especially when its concentration exceeds TLV value of 25 ppm [20]. Decrease of temperature and decrease of humidity decreased ammonia concentrations and emissions. Water vapor pressure had a stronger correlation to ammonia than relative air humidity. The air flow rate affects concentrations of odor and ammonia but had a limited effect on emissions. Control of temperature and humidity potentially decreases generation and emission of ammonia. It is a byproduct from industrial "cracking "of hydrocarbons. It is used as a raw material in fertilizer industry and also applied directly as a fertilizer. It is a gas at normal atmospheric pressure. It is easy to liquefy and readily dissolves in water. It has a vapor pressure of 8.5 bars at 20 °C and a boiling point of 33.4 °C at normal atmospheric pressure. It is usually available at a very high degree of purity (99.8 %).Storage and distribution in liquid state requires containers able to resist high pressure. Ammonia is produced and utilized extensively in many chemical industries, fertilizer factories, refrigeration system, food processing, medical diagnosis, fire power plants etc. [21–27]. Therefore detection and measurement study at low, as well as high, concentration is necessary. In the present work sensing performance except oxygen and H_2S gas were tested.

2 Experimental Techniques

2.1 Preparation of the Thick Film

Zirconium dioxide was prepared using 25 gm Analytical grade Zirconyl (IV) oxychloride octohydrate ($ZrOCl_2.8H_2O$) [Aldrich] in 200 ml deionized water. The solution was stirred at 98 °C for 2 h. into which was added drop wise aqueous ammonia solution until a PH value of 9.3 with subsequent filtration and washing to formation $Zr(OH)_4$ precipitate. It was followed by heating at 600 °C to form ZrO_2 as reported in literature [28, 29] and it was dried, grinded for formation of small grains and calcinated at 800, 900 and 1,000 °C in a muffle furnace for few hours. Glass Substrate used were ultrasonically cleaned with acetone and thereafter deionized water and stored in hot oven at 80 °C temperature for few minutes to remove volatile and moisture impurities. Thixotropic Paste was formulated by mixing dried (calcinated at 1000 °C)ZrO_2 powder with ethyl cellulose (temporary binder), butyl carbitol acetate (organic solvent) and alpha terpineol depending on mixture

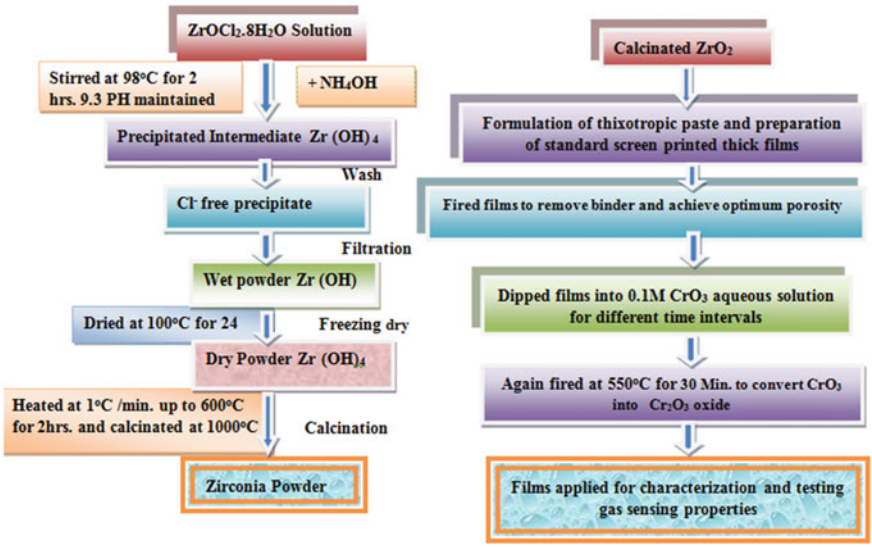

Fig. 2 Flowcharts represent the synthesis and formulation of thick films for gas sensing application

proportion. Permanent binder glass frit was not used since glass substrate utilized. Inorganic to organic compound ratio maintained with 75:25 percentage to achieved desired viscosity and rheology of the paste. This thixotropic paste was kept in bowel for few minutes to good settlement. Thickness of the film is controlled by squeegee stroke. The screen printed thick films were dried in IR light source and sintered at 550 °C to burn organic binder to produce desired porosity [29, 30]. Details steps of film synthesis and formulation is represented in flowcharts as shown in Fig. 2.

2.2 Thickness Measurement

The thickness of the films was measured using the Taylor Hobson (Talystep, UK system). It was observed in the range from 35-55 μm. The Various thicknesses of the films were possible by controlling number of squeeze strokes. It was achieved considering substrate and functional material cracking limit at working temperature and shear stress [30].

2.3 Temperature Coefficient of the Thick Film

The temperature coefficient of the film was determined using following formula and it was observed NTC.

$$TCR = \frac{1}{R}\frac{\Delta R}{\Delta T}\Big/{}^{\circ}K \tag{1}$$

TCR also can be defined and derived as

$$\mathrm{TCR} = -\frac{\mathrm{E_a}}{\mathrm{K}}\left[\frac{1}{\mathrm{T}^2}\right] \tag{2}$$

where E_a is activation energy, k is Boltzmann's constant and T is temperature in Kelvin. [31].

2.4 Modification of the ZrO_2 Thick Films

The surface modified ZrO_2 thick films were obtained by dipping them in 0.1 M aqueous solution of chromium trioxide (CrO_3) for different intervals of time: 5, 10, 20 and 30 min. The CrO_3 is known to be unstable above 197 °C and transform into Cr_2O_3 upon firing above 197 °C. The grains of Cr_2O_3 would disperse around the grains of ZrO_2 base material. The Cr^{3+} activated ZrO_2 films dipped in 10 min was observed to be sensitive and highly selective for ammonia gas. These films were dried in IR light source, followed by firing at 550 °C for 30 min. The films so prepared are termed as 'chrominated modified ZrO_2 films'.

3 Characterization

3.1 Structural and Morphological Analysis of ZrO_2 Particles

Figure 3 Shows the XRD Pattern of ZrO_2 powder at different calcinated temperatures within range 20 to 80 °C. X-ray diffractogram of the material was confirmed the polycrystalline structures of the ZrO2. It is determined 2θ values and hkl planes corresponding to monoclinic at 35.2° (200), 63.08° (222) and tetragonal at 30.2° (111), 50.4° (220), 60.2° (311), 74.70° (400). The strongest peaks for the tetragonal phase was observed. At higher calcinations temperature 1000 °C the sharp broaden peaks with highest intensities were observed. It was better for gas sensing since broader peaks indicates less particle size and high surface to volume ration. Inspection of X-ray pattern shows that no cubical phases transformation. The observed peaks in the XRD pattern are matched with the standard recorded data (JCPDS 36-020) and (JCPDS 17-0923) [32, 33] during sintering CrO_3 is converted into Cr_2O_3 oxide. Electronegativity of Cr^{3+} (1.7) [34] and ionic radius of Cr^3 (0.62 Å) play important role and because of Cr_2O_3 activated surface of the film have good ability of gas sensing (Fig. 4).

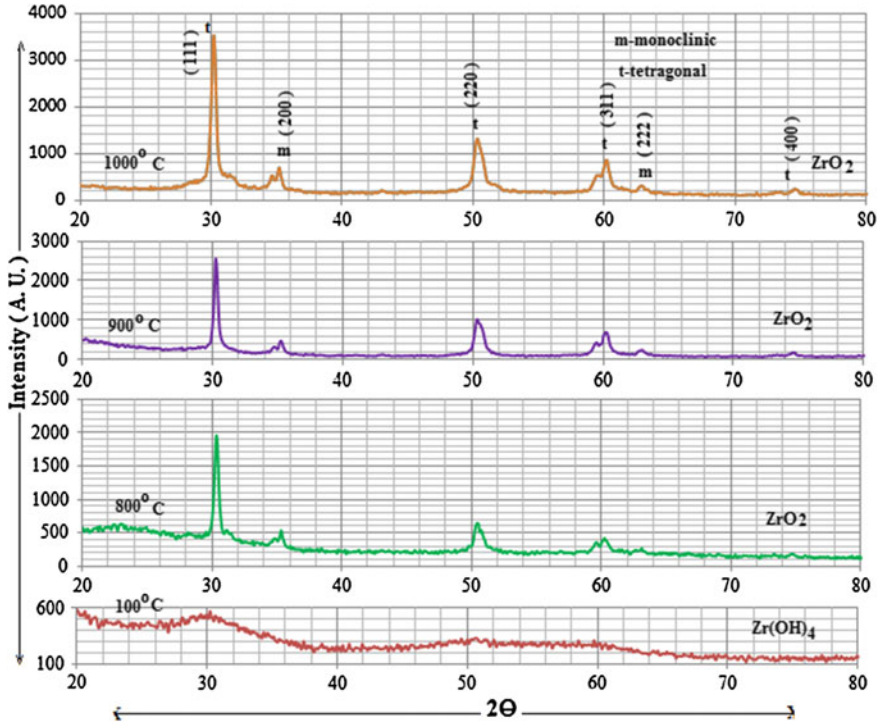

Fig. 3 XRD pattern of ZrO_2 powder

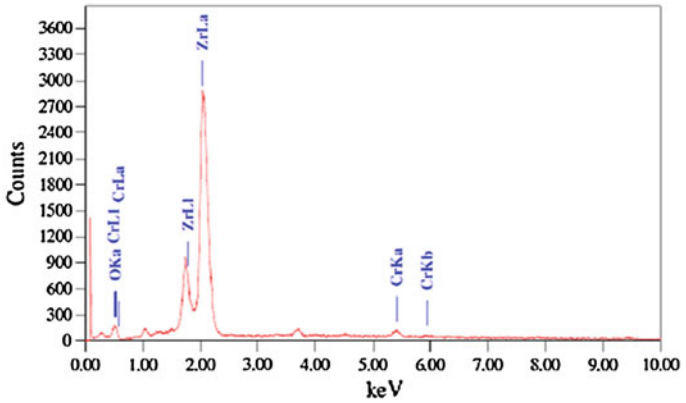

Fig. 4 EDX for Cr^{3+} modified ZrO_2 film (10 min dipped sample)

The average particle grain size of ZrO_2 powder was determined by using Scherrer formula and was estimated 82 nm.

$$D = \frac{0.9\,\lambda}{\beta\cos\theta} \tag{3}$$

$$\beta = \sqrt{\beta m^2 + \beta s^2} \tag{4}$$

where λ-wavelength of X-Ray in Å (1.542 Å) and β is the peak FWHM in radian. It could be calculated from Warren's formula where β_m is measured peak width in radian at half peak height and β_s corresponding width of the standard material.

Texture coefficient was determined using following formula and observed intensities of corresponding peaks and standard values from JCPD data sheet. It was found >1 for (111) peak plane (tetragonal) hence it is crystalline and for others peaks texture coefficient are found <1.

$$T_{c(hkl)} = \frac{I(hkl)/I_0(hkl)}{I/N\sum I(hkl)/I_0(hkl)/I(hkl)/I_0(hkl)} \tag{5}$$

Also volume fraction for monoclinic to tetragonal phase was estimated using formula and it was observed volume shrinkage. Therefore dopant is necessary to stabilize in tetragonal phase.

$$V_m = \frac{1.311\times_m}{1+0.311\times_m} \tag{6}$$

$$V_{t/c} = (100 - V_m) \tag{7}$$

$$\times_m = \frac{1_{m(200)} + 1_{m(222)}}{I_{m(200)} + I_{m(222)} + I_{t(111)} + I_{t(220)}I_{t(311)} + I_{t(400)}} \times 100\,\% \tag{8}$$

Interplaner spacing (d) was determined using Bragg's formula:

$$2d\sin\theta = n\lambda \tag{9}$$

Lattice constants a (Å) interatomic spacing can be estimated for each peaks using the following equation [35]:

$$\frac{1}{d^2} = \frac{h^2 + k^2 + l^2}{a^2} \tag{10}$$

Root mean square (RMS) microstrain (e) can be determined using a Williamson and Hall plot. The slope of the plot of ($2\cos\theta/\lambda$) versus ($2\sin\theta/\lambda$) gives the value of the RMS microstrian [36–38]:

$$\frac{\beta COS\theta}{\lambda} = \frac{1}{D} + e\left(\frac{\sin\,\theta}{\lambda}\right) \tag{11}$$

The dislocation density was calculated using the following equation:

$$p = \frac{\sqrt{12}\langle e^2 \rangle^{1/2}}{dD} \tag{12}$$

where e is the RMS microstrain, d is the interplaner spacing and D is the crystalline size, β is FWHM in radians, a is lattice constant and θ is Bragg's diffraction angle (in degrees). The stacking fault probability was calculated using the following equation:

$$\alpha = \frac{2\pi^2 \Delta(2\theta)}{45\sqrt{3}\tan\theta} \tag{13}$$

3.2 Surface Morphology of the Films

SEM images were observed by JEOL-JSM 6360(LA), JAPAN coupled with EDAX analysis. Figure 5a–d depict the SEM images unmodified (pure ZrO_2) and modified ZrO_2 thick films (5, 10 and 20 min dipped sample). From these surface morphology observation it is seen that an unmodified film consists of larger grains distributed randomly. The Cr-modified film (with dipping time 10 min) consists of smaller particles associated with larger ones, as in Fig. 5c .These particles could be attributed to Cr_2O_3 Particles. Cr_2O_3 grains may reside in the intergranular regions of ZrO_2 thick film. Effective sensing surface area was expected to be increased. Average particle size of the ZrO_2 is observed to be 119–138 nm by SEM and matched with calculated value 82 nm having uniform bulk appearance on film [39, 40] (Tables 1, 2).

3.3 Elemental Composition Analysis of the Thick Films

The quantitative elemental compositions of the film were analyzed using an energy dispersive spectrometer, and mass % values surface modified films are presented in Table 3.

Stoichiometrically (theoretically) expected wt % of cations (Zr) and anions (O) are 66.67 and 33.33 respectively. The wt % of constituent cations and anions in the pure ZrO_2 and surface chrominated ZrO_2 were not as per the stoichiometric proportion and all samples were observed to be oxygen deficient, leading to semiconducting nature of material. It is clear from Table 3 that the weight percentage of Cr different for each dipping time. The film with dipping time of 10 min is observed to be more oxygen deficient (25.99 wt %). The deficiency of oxygen reduces the resistance of the film. This oxygen deficiency would promote the adsorption of relatively larger amount of oxygen species favorable for higher gas

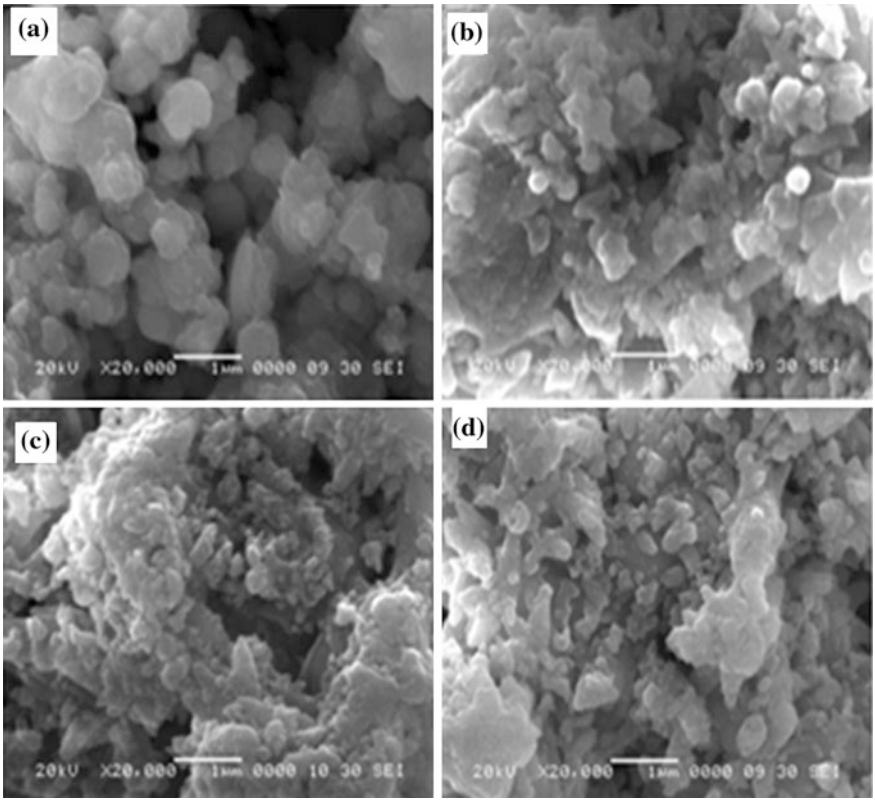

Fig. 5 (**a**) Micrograph of pure ZrO_2 film. Micrograph of (**b**) 5 min dipped (**c**) 10 min dipped and (**d**) 20 min dipped surface chrominated (modified) ZrO_2 thick film

Table 1 Determination of different parameters for material and structure confirmation using XRD pattern

h k l plane miller indices	Peak position 2θ	I/I_o	$1000 * \sin^2\theta$	Peak index $1000 * \sin^2\theta/23.667$	Reflection $(h^2 + k^2 + l^2)$	Inter atomic Spacing d (Å)	Lattice Parameter a (Å)
111	30.2	354.1	67.76	2.86 = 3	3	2.956	5.1199
200	35.2	27.6	91.43	3.875 = 4	4	2.547	5.094
220	50.4	37.75	181.25	7.6598 = 8	8	1.8084	5.1149
311	60.2	18.96	251.513	10.6269 = 11	11	1.5354	5.0923
222	63.08	22.08	213.62	11.5610 = 12	12	1.4720	5.0912
400	74.7	26.13	367.806	15.54 = 16	16	1.2705	5.082

response. Cr_2O_3 %, ZrO_2 % and elemental % of modified film accordingly dipping time is stated in Table 3. Cr_2O_3 is p- type and ZrO_2 on glass substrate act n-type oxide.

Table 2 Structural parameters accordingly (hkl) = 111 plane at particular firing temperature

Firing temperature	V_m (%)	$V_{t/c}$ (%)	Micro strain (e)	Dislocation density (ρ)	Stacking fault probability (α)
550 °C	3.472	96.528	0.52670	1.2×10^{15} lines/cm^2	0.11038

Table 3 Elemental compositional analysis of pure and surface modified films

Type of the film	Zr (Wt %)	O (Wt %)	Cr (Wt %)	Cr_2O_3 (Wt %)	ZrO_2 (Wt %)	Total Cr_2O_3–ZrO_2
ZrO_2 pure	66.66	33.33	0	0	100	100
Surface modified :5 min	70.31	26.25	3.43	5.02	94.8	99.82
: 10 min	73.72	25.99	0.28	0.41	95.59	96
: 20 min	71.01	26.20	2.80	4.09	95.91	100
: 30 min	69.48	26.31	4.20	6.14	93.86	100

4 Electrical and Optical properties

4.1 I–V Characteristics

Figure 6 depicts the I–V characteristics of pure and modified ZrO_2 films, the symmetrical nature of the I–V characteristics for particular samples shows that the contact is ohmic in nature.

4.2 Electrical Conductivity

It is observed from Fig. 7 that the conductivity of pure ZrO_2 film is larger than that of modified film in air because basically zirconia is an ionic conductor, it is famous for oxygen gas response and modified film have less conductivity in air but by exposure of reducing gas modified film responds sudden decrease in resistance resulting increase in conductivity at optimal temperature. This increase in current depends on oxygen species and reaction mechanism. The conductivity of the film dipped for 20 and 30 min is least among all. This could be attributed to an increase in the amount of ZrO_2-Cr_2O_3 intergrain boundaries and hence intergranular potential barriers. Cr_2O_3 modified ZrO_2 film consists of large number of smaller particles of Cr species distributed around the larger particles on the surface of the ZrO_2 film. Cr_2O_3 grains may reside in the intergranular regions of ZrO_2, resulting in developing of intergrain boundaries and intergranular potential barriers. (0.1 to 1.1 eV and for resistive film up to 2 eV) [40].The semiconducting nature of ZrO_2 film is observed from the measurements of conductivity with operating temperature. The semi conductivity in ZrO_2 film must be due to large oxygen deficiency in it. The material would then adsorb the oxygen species at higher temperatures

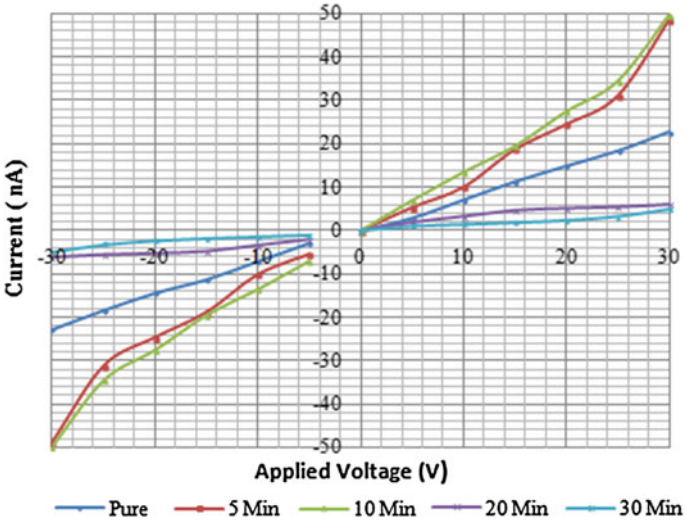

Fig. 6 I-V characteristic of pure and modified ZrO_2 films for different time intervals

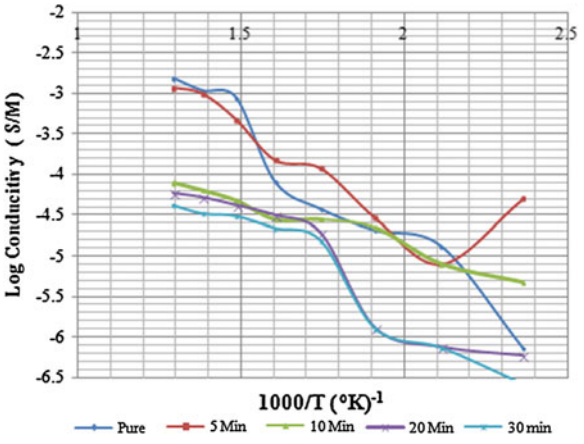

Fig. 7 Conductivity profile for pure and Cr_2O_3 activated sample for different time interval

($O_2^- \rightarrow 2O^- \rightarrow O^{2-}$). The adsorption chemistry of Cr_2O_3-modified ZrO_2 film surface would be different from the pure ZrO_2 thick film surface. The Cr_2O_3 misfits on the surface would be adsorb more oxygen species than the pure ZrO_2 thick film surface.

4.3 Optical Properties of the Film

Plot of $(\alpha h\gamma)^2$ verses photon energy $h\gamma$ is shown in Fig. 8. It is carried out observing absorption spectra using JASCO UV–VIS-NIR Model V-670 Spectrophotometer. The absorption at higher wavelength in the range 320–380 nm at intense absorption can be seen. Absorption coefficient decreases after modification. The absorption coefficient (α) calculated using Lamber's law was found to be in the order of 10^5 cm^{-1}, the high α value ($>10^4$) confirms the existence of direct band gap.

The optical band gap E_g was calculated using Touch's plot $(\alpha h\gamma)^2$ verses $h\gamma$. The photon energy at the point where $(\alpha h\gamma)^2$ is zero represents E_g, which is determined by extrapolation of the linear portion of the curve.

$$\alpha h\gamma = A(\alpha h\gamma - E_g)^n \tag{14}$$

where $h\gamma$ is photon energy and n is a constant. The value of n is ½ or 2 depending on presence of the allowed direct and indirect transition [41, 42]. The nature of the plot suggest direct interband transition. The band gap of the material ZrO_2 without heating treatment was observed between 5.8 and 6.4 eV (here film thickness have not considered, since powder was used) and having high band gap because of non agglomeration. After calcinations, sintering, firing and surface modification grain growth with agglomeration achieved, also particles size have being reduced hence band gap was reduced. It is observed first time band gap reduces after sintering for surface Chrominated ZrO_2 film. The values determined are between 4.8 eV and 4.2 eV, 3.8 eV and 2.8 eV for pure calcinated powder, fired and modified films respectively. Remarkable change in bandwidth was observed. Reduction in band gap enhances sensing response. Electron can easily cross conduction band transfer to sensing oxide film surface. After modification at higher photon energy abortion coefficient increases and then being flat.

4.4 FTIR Spectra of Pure and Modified ZrO_2

FTIR spectra are shown in Fig. 9. Zr–O–Zr bonding lines are observed in the region 400–500 cm^{-1}. During sintering, the Zr–O–Zr bonding peaks in tetragonal of ZrO_2 appears around 460 cm^{-1} Sharp bonds 1,020 cm^{-1} appears which can be attributed to the characteristics bond of monoclinic zirconia [43]. The spectra also exhibits O–H stretching vibration around 3,432 cm^{-1}, this O–H bending vibration in the zirconium alkoxide indicates a certain amount of solvents residues. Residual water and anion in the absorption peaks at 2,350 cm^{-1} are well resolved. Both spectra pure and modified ZrO_2 clear that the bond has been not changed and proper amount of additive doping (Cr_2O_3) has utilized. This surface modification does not changed bulk (microstructure) of base material. Some ions of Zr^{4+} are replaced by Cr^{3+} creating oxygen vacancy, which occurs to restore the electrical charge balance. These oxygen vacancies enable the O^{2-} ions to migrate through the surface.

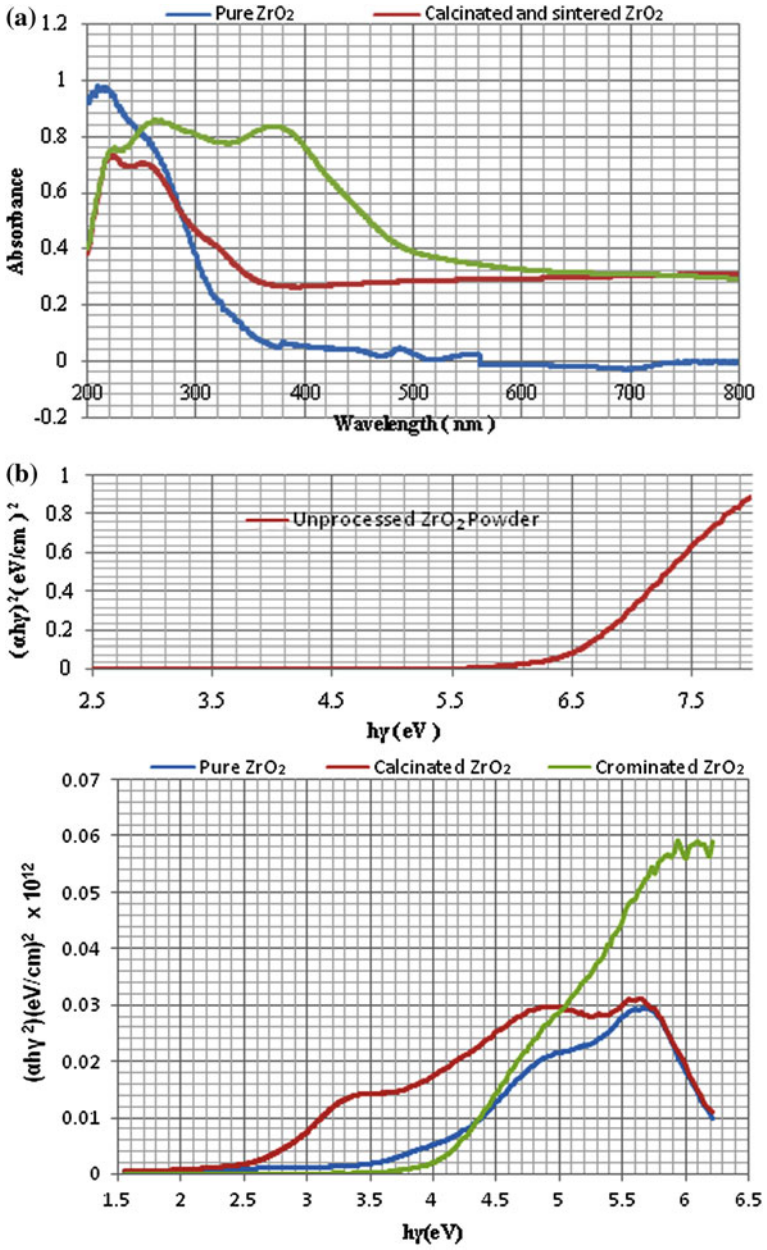

Fig. 8 Plot of $(\alpha h\gamma)^2$ Vs photon energy $(h\gamma)$ for both pure unprocessed, calcinated ZrO_2 powder, fired film and crominated film for 30 min dipped sample

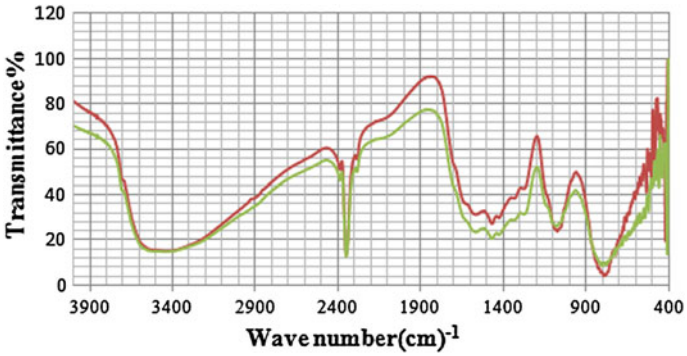

Fig. 9 FTIR spectra of pure and modified ZrO_2

The introduction of Cr_2O_3 in ZrO_2 will create one mobile oxygen vacancy into the compound. It is known as Schotky point defect (non-stoichiometry point defect in material (Crystalline).

5 Results and Discussion

5.1 Gas Sensing Performance

The sensing performance of the films was examined using a' static gas sensing system'. In this system, the sensor element is mounted in an enclosed test chamber of a known volume. In order to measure the sensor resistance in a desired concentration of the analytic gas, a known amount of gas is injected into the housing using micro-syringe. The syringe pipe volume would be varied from 1 to 25 ml for passing different amount of gas concentration. The Chamber is having 25 liter (glass dome) Volume. There were electrical feeds through the base plate. The heater was fixed on the base plate to heat the sample under test up to required operating temperatures. The current passing through the heating element was monitored using a relay operated with electronic circuit with adjustable ON–OFF timer intervals. A Cr–Al Thermocouple was used to sense the operating temperature of the sensor. The output of the thermocouple was used to digital temperature indicator.

A gas inlet valve was fitted at one of the ports of the base plate. A constant voltage was applied to the thick film sensor, and the current was measured by a digital picoammeter. The air was allows to pass into the glass chamber every gas exposure cycle [40]. The temperature dependence of specific conductivity is given by

$$\sigma_{\text{ion}} = \text{KT}^{-1} \exp^{(-\Delta\text{E}/\text{KT})} \tag{15}$$

where K is a material constant. T the absolute temperature, k the Boltzmann constant, and ΔE is the activation energy. From this equation and nature of substrate and its shear stress optimal film thickness and temperature can be calculated for maximum conductivity at film cracking limit. All n- type oxides are thermally stable and have possibility to work at lower oxygen pressure level, It is well known that many p –type oxides are relatively unstable because of the tendency to exchange lattice oxygen easily with air. Besides the interaction with reducing gases decreases the resistance of n-type oxides. This is preferred direction for sensor resistance change during detection of reducing gases. Activation Energy measures the thermal form of energy required to raise electrons from the donor levels to the conduction band or to accept electrons by the acceptor levels from the valance band respectively for n- and p-type materials.

Activation energy corresponds to the energy difference ($E_c - E_d$) and ($E_a - E_v$) respectively for n-type and p-type semiconductor oxides. Activation energy by thermal resistance method can be measure from the variation of σ or ρ and conveniently of R with the temperature and in general activation energy is given by equation [44]:

$$\Delta E = \frac{E_c - E_v}{2} = \frac{Eg}{2} \tag{16}$$

According to Arrhenius activation energy is the threshold energy that the reactant must acquire before reaching the transition state, it is temperature dependent and it was interpreted by equation:

$$Ln\sigma T = \frac{-E_a}{KT} + LnK \tag{17}$$

It is equation of straight line $Y = mX + c$, slope of $Log(\sigma T)$ verses 1000/T is given by $-E_a/K$ which should have somewhat linear trend. The slope of the Arrhenius plot allows the activation energy to be calculated from the equation, the factor 1000 is from the 1000/T [45].

$$E_a = \frac{-2.303 * 1.381 * 10^{-23} * 1000 * slope}{1.602 * 10^{-109}} \tag{18}$$

$$E_a = -0.1984 * slope \tag{19}$$

The activation energy is directly proportional to the curve slope. Negative multiple with negative slope would result positive value of activation energy. It is good agreement that activation energy calculated from bandwidth of crominated film observed 1.4 eV and at room temperature it was observed by arrhenius equation approximately 1.4 eV. At higher temperature it was varied from 1.4 to 0.24 eV, except for pure and 10 min dipping modified crominated film, other films does not have linear trend. From this we predict the temperature dependent reaction, once in the transition state the reaction can go in the forward direction toward products or in the opposite direction toward reactant. Also reaction with a

large activation energy requires much more energy to reach the transition state. Likewise a reaction with a small activation energy doesn't require much energy to reach the transition state.

Some authors have reported that the charge carriers are transported through a material depends on the particle size and charged layers L_s which depends on the surface potential V_s, according to the equation:

$$L_s = L_D \sqrt{\frac{qv_s^2}{KT}} \tag{20}$$

where L_D is the Debys length, q is the electron charge, K is the Boltzmann's constant and T is the temperature. L_D depends on the other physical parameters through the following relation.

$$L_D = \sqrt{\frac{kKT}{2\pi q^2 N}} \tag{21}$$

where k is the dielectric constant and N is the concentration of donor or acceptor impurity, typical values of the L_s are less than 100 nm. If D is the crystalline size, three possible mechanisms are usually proposed.

1. $D \gg 2L_s$, the conductance is limited by Schotky barriers.
2. $D = 2L_s$, the conductivity is controlled by the neck's formed among the particle.
3. $D < 2L_s$, in this case entire volume of each crystalline particle participates in the charge transition.

The third mechanism would be possible explanation of improved gas sensing behavior. Therefore $-E_a/KT$ resembles the Boltzmans distribution law and In overall thermally activated conduction process, the adsorption–desorption gas sensing mechanism depends on temperature as well as Vander Waals weak intermolecular forces within molecules are known as Physisorption and Charge transfer of surface oxygen spices (O_2, O_2^-, O^-,or O^{2-}) and electron sharing with grain boundaries having small and large particle sizes of materials accordingly temperature is known as chemisorption. In air film resistance increases increasing potential barrier height and by exposure of reducing gas resistance decreases decreasing potential barrier height. The voltage dependence of the current is ohmic if the voltage drop is less than KT/q at each intragranular (grain boundary) contact. Gas sensors may present a constant resistance in the air at this time reducing gas form oxidation reaction with the oxygen adsorbed on the surface of semiconductor, isolation effect of gas molecules results in the change of surface potential, consequently the resistance of sensor may change. For reducing gas resistance reduces and conductivity increases while for oxidizing gas, resistance increases and conductivity decreases. Also conductivity increases by increasing in gas concentration [46].

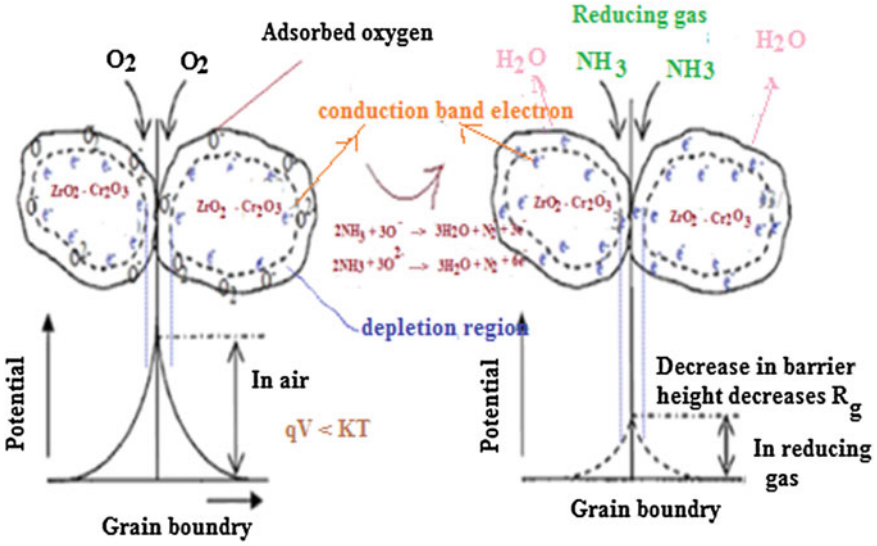

Fig. 10 Oxygen adsorption- desorption mechanism on the film surface with gas sensing mechanism

Gas response is defined as the ratio of change in conductance of the sensor on the exposure of the target gas to the original conductance in air medium. The relation for sensitivity (S) is:

$$\text{Sensitivity} = \frac{\text{Ggas} - \text{Gair}}{\text{Gair}} = \exp\left(\frac{qV_{air} - qV_{gas}}{KT}\right) \tag{22}$$

where G_{air} is the conductance of sensor in air medium, whereas G_{gas} is the conductance of sensors in gaseous medium (Fig. 10).

5.2 Sensing Characteristics of Modified ZrO_2 Film

Figure 11 shows the variation of gas response of the ZrO_2 films (fired at 550 °C) to various gases (1,000 ppm) with Operating temperature ranging from 150 to 500 °C. For NH_3, the response goes on increasing with operating temperature, attains its maximum (12.3) at 300 °C and then decreases with a further increase in operating temperature. From the Fig. 12, it is clear that chrominated surface modified films enhances NH_3 response, it would be 21.2 at 300 °C for 10 min dipping. Further it would be decreases as dipping time goes on increasing.

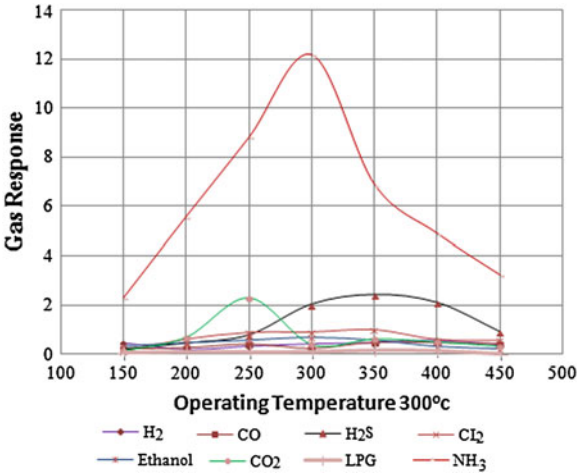

Fig. 11 Variation of gas response at different operating temperature for pure ZrO_2 film with 1,000 ppm concentration

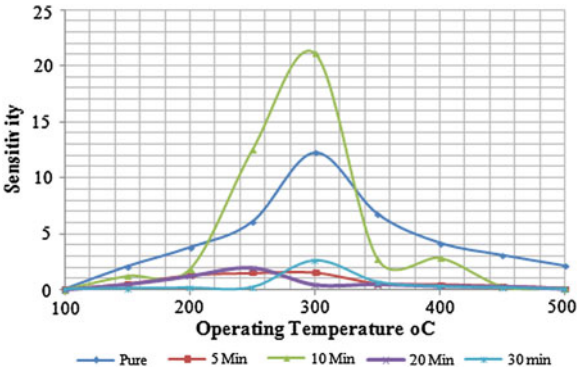

Fig. 12 Variation of gas response at different operating temperature for chrominated ZrO_2 film with 1000 ppm concentration

5.3 Selectivity of NH_3 Gas

Selectivity of a sensor is defined as the ability of a sensor to respond to a certain gas in the presence of other gases. Gas responses of different gases were tested at different temperature and it is selective for NH_3 gas at operating temperature 300 °C as shown in Fig. 13.

$$\text{Selectivity } \% = \frac{\text{S}}{\text{Startget gas}} \times 100\ \% \tag{23}$$

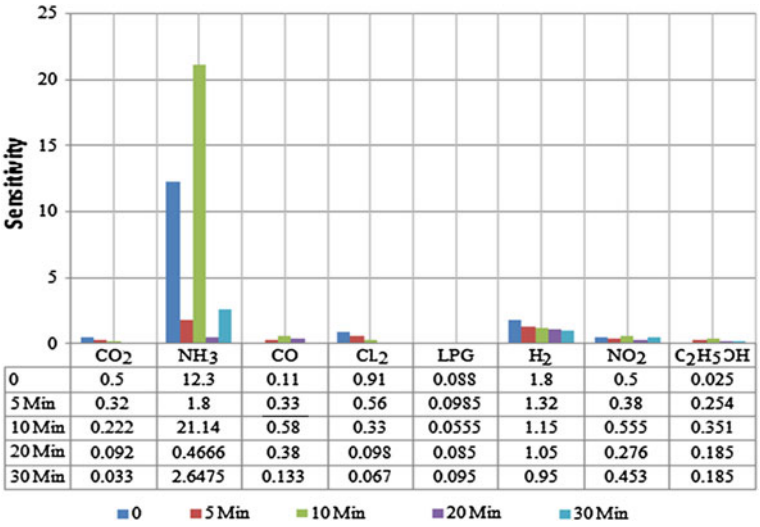

	CO_2	NH_3	CO	Cl_2	LPG	H_2	NO_2	C_2H_5OH
0	0.5	12.3	0.11	0.91	0.088	1.8	0.5	0.025
5 Min	0.32	1.8	0.33	0.56	0.0985	1.32	0.38	0.254
10 Min	0.222	21.14	0.58	0.33	0.0555	1.15	0.555	0.351
20 Min	0.092	0.4666	0.38	0.098	0.085	1.05	0.276	0.185
30 Min	0.033	2.6475	0.133	0.067	0.095	0.95	0.453	0.185

Fig. 13 Selectivity of NH_3 gas among the test target gases for 10 min sample

5.4 Response and Recovery Time

Response time defined as the time required for a sensor to attain the 90 % of the maximum increase in conductance after the exposure of test gas on the film surface, while recovery time (RCT) is defined as the time taken to get back 90 % of the maximum conductance in air. The quick response time (4 s) was observed for both pure ZrO_2 and modified film while fast recovery time (40 s) for pure film and (60 s) for modified film was recorded at 300 °C as shown in Fig. 14. It is well known that the electrical conductivity in ZrO_2 oxide is due to a non-stoichiometric composition as a result of oxygen deficiency. The conductivity is n-type, when the sensor surface is placed in air ambient, the oxygen molecules are adsorbed at the surface resulting in the formation of O_2^-, O^-, O^{2-} ions, thus decreasing the concentration the number of charge carriers near the surface giving rise to a depletion region. When exposed to reducing gas ammonia mutual interaction between the reactant i.e. reducing gas and oxygen species, results in oxidation of reducing gas at the surface. This oxygen phenomenon helps in removal of oxygen ion from ZrO_2 resulting in decrease barrier height, thus increasing conductivity. During the chemisorptions at higher temperature 125 °C, oxygen is adsorbed in ionic form as shown in the following reactions.

$$O_2 + e^- \rightarrow O_2^-$$

$$O_2^- + e^- \rightarrow 2O^-$$

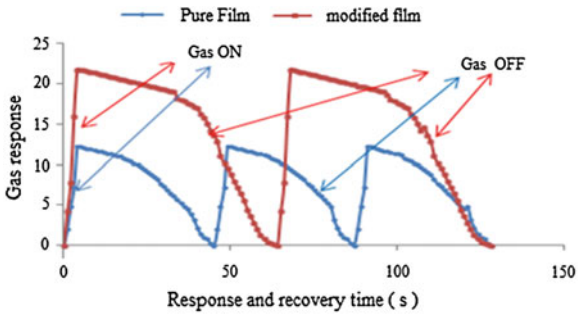

Fig. 14 Gas response and recovery time

Above 175 °C, the reactivity of O^{2-} species is high. The formation of O^{2-} species is also possible as follows:

$$O\ ads^{-} + \rightarrow e^{-}O^{2-}$$

O^{2-} are not adsorbed because these species are not stable and are usually trapped by oxygen vacancies. In case of ZrO_2, the carriers are believed to be due to excess ions at the interstitial position, due to oxygen vacancies, acts as electron donors. Reducing gas like NH_3 reacts with adsorbed oxygen ions. The possible reaction is:

$$2NH_3 + 3O^{-} \rightarrow 3H_2O + N_2 + 3e^{-}$$

$$2NH_3 + 3O^{2-} \rightarrow 3H_2O + N_2 + 6e^{-}$$

The point at which the sensitivity is maximum, is the actual thermal energy needed for the reaction to proceed. However sensitivity decreases at higher operating temperature as the adsorbed oxygen ion desorbed from the surface of the sensor. Hence there would be smaller number of oxygen ions present on the surface of film to react with the reducing gas and the sensitivity would falls at high operating temperature. Gas sensing mechanism is generally explained in terms of conductance either by adsorption of atmospheric oxygen on the surface and/or by direct reaction of lattice oxygen or interstitial oxygen with target gas. In case of former, the atmospheric oxygen adsorbs on the surface by extracting an electron from conduction band, in the form of superoxide or peroxides, which is mainly responsible for the detection of test target gases which is already explained earlier. At higher temperature, it captures the electron from conduction band and it would result in decreasing conductivity of the film, when ammonia reacts with the surface of the film and adsorbed oxygen on the surface of the film, it get oxidized ammonium hydroxide, liberating free electrons in the conduction band. The following reaction takes place:

$$ZrO_2 + 5NH_{3(gas)} + 4O^{2-}(\text{film surface}) \rightarrow Zr(NH_4OH)_{3(\text{film surface})} + 2NO_{2(gas)} + 8e^{-}(\text{Conduction band})$$

This shows n-type conduction mechanism, thus generated electron contribute to sudden increase in conductance of the thick film, which may be due to surface

reaction of ammonia with physisorbed H_2O or by proton conductivity via NH_4^+ cations. Cr_2O_3 may generate the solid acidity on solid base ZrO_2. The acidity on the sensor surface would form NH_4^+ cations, which constitutes the proton conductivity leading to a crucial decrease of the resistance. This would decrease the barrier height among the Cr_2O_3–ZrO_2 grains.

$$NH_{3(g)} + H_2O_{(surface)} \rightarrow NH_4OH_{(g)}$$

Ammonia hydroxide NH_4OH produced during the surface reaction is volatile in nature. The high volatility of NH_4OH influences the quick response and fast recovery of the sensor [47–51].

6 Conclusion

Following conclusion can be drawn from the experimental results:

- Surface modification process was implemented to modify only surface of the film and not the bulk portion of the base material.
- The chrominated film was observed to be semiconducting in nature and showed a negative temperature coefficient of resistance.
- Surface mechanism is based on adsorption–desorption with oxygen vacancies role.
- Chromium trioxide converted into Cr_2O_3 above 197 °C, during firing process.
- Sensing dependent on temperature, gas concentration, film thickness, activation energy, band gap of the material, particle size, grain size, grain boundary, optimum porosity, surface potential, surface to volume ratio and Debye length.
- Quick response and fast recovery time was recorded. It was observed 4 s for both and 40–60 s for pure and modified film respectively.
- Micro strain, dislocation density, staking fault probability was reported and dependent on firing temperatures.

Acknowledgments The authors are grateful to the Principal of concern colleges. Authors are grateful to M. G. Vidyamandir and N. D. M. V. P. Samaj, Nasik Authority, Director BCUD Pune, Head Department of Physics UOP Pune and NMU Jalgaon. Also thanks to Professor Dr. L. A. Patil for their valuable guidance.

References

1. G.H. Jain, L.A. Patil, Gas sensing properties of Cu and Cr activated BST thick films. Bull. Mater. Sci. **29**(4), 403–411 (2006)
2. M. Kleitz, E. Siebert, P. Fabry, J. Fouletier, in *Solid State Electrochemical Sensors, in Sensors a Comprehensive Survey*, vol. 2, ed. by W. Gopel, J. Hesse, J.N. Zemel (VCH, New York, 1991), pp. 341–428
3. S. Roy Morrison, Selectivity in semiconductor gas sensors. Sens. Actuators **12**, 425–440 (1987)

4. J.E. Sundeen, R.C. Buchanan, Electrical properties of nickel-zirconia cermets films for temperature and flow sensors application. Sens. Actuators A **63**(1) 33–40 (1997)
5. C,S. Barret, T.B. Massalstki, Structure of Metals. Pergamon Press, Oxford (1980)
6. M. Francis, D. Helene, L. Claude, Screen printed thick films: from functional material to functional devices. J Europial Ceram Soc **25** 2105–2113 (2005)
7. J. Weissbart, R. Ruka, Oxygen gauge. Rev. Sci. Instrum. **32**, 593–595 (1961)
8. G.Q. Yu, B.K. Tay, Z.W. Zhao, Structure and properties of zirconium dioxide thin films prepare by filtered cathodic vacuum arc. Appl. Phys. B Mater. Sci. Process. A **81**, 405–411 (2005)
9. G. Korotcenkoov, Metal oxides for solid- state gas sensors: what determines our choice? Mater Sci Eng B **139** 1–23 (2007)
10. P. Shuk, E. Bailey, U. Guth, Zirconia oxygen sensor for the process application. State Art Sens. Transducers **90** 174–184 (2008)
11. J. Riegel, H. Neumann, H.M. Wiedenmann, Exhaust gas sensors for automotive emission control. Solid State Ionics **152–153**, 783–800 (2002)
12. S. Meriani, *Zirconia 88* (Advances in Zirconia Science and Technology Elsevier, New York, 1989)
13. S. M. Chang, R. A. Doong, The effect of chemical states of dopants on the microstructures and band gaps of metal- doped ZrO_2 thin films at different temperatures. J. Phys. Chem. B **108**, 18098–18103 (2004)
14. N. Yamazoe, Toward innovations of gas sensors technology (Review). Sens. Actuators **108**, 2–14 (2005)
15. L.P. Martin, A.Q. Pham, R.S. Glass, Effect of Cr_2O_3 electrode morphology on the nitric oxide response of a stabilized zirconia sensor. Sens. Actuators B **96**, 53–60 (2003)
16. G.M. Crosbie, G.J. Tennehouse, R.P. Tischer, H.S. Wroblowa, Electronically conducting doped chromium Oxide. J. Am. Ceram. Soc. **67**, 498–503 (1984)
17. R. Ramamoorthy, S.A. Akabar, P.K. Dutta, Dependence of potentiometric oxygen sensing characteristics on the nature of electrodes. Sens. Actuators B **113**, 162–168 (2006)
18. A. Holt, P. Kofstad, Electrical conductivity and defect structure of Cr2O3 at reduced temperature (1000 °C). Solid State Ionics **69**, 137–143 (1994)
19. Ammonia WWW.en.Wikipedia.org/wiki/Ammonia
20. G.H. Jain, L.A. Patil, P.P. Patil, U.P. Mulik, K.R. Pati, Studies on gas sensing performance of pure and modified barium strontium titanate thick film resistors. Bull. Mater. Sci. **30**(1), 9–17 (2007)
21. D.N. Suryawanshi, D.R. Patil, L.A. Patil, Fe_2O_3 activated Cr_2O_3 thick films as temperature dependent gas sensors. Sens. Actuators B Chem **134**, 579–584 (2008)
22. V.B.Gaikwad, R.L. Patil, M.K. Deore, R.M. Chaudhari, P.D. Hire, S.D. Shinde, G.H. Jain, Gas sensing properties of pure and Cr activated WO_3 thick film resistors. Sens. Transducers. **120**(9), 38–52 (2010)
23. H. Meixner, U. Lampe, Metal oxide sensors. Sens. Actuators B Chem **33**(1–3), 198–202 (1996)
24. K. Wetchakun, T. Samerjai, N. Tamaekong, C. Liewhiran, C. Siriwong, V. Kruefu, A. Wisitsoraat, A. Tuantranont, S. phanichph,Semiconducting metal oxides as sensors for environmentally hazardous gases. Sens. Actuators B Chem **160**, 580–591 (2011)
25. S.H. Lee, T.Y. Song, Kinetics of gas phase oxygen control system and oxygen concentration measurement in liquid Pb and LBE. J. Ind. Eng. Chem. **13**(4), 602–607 (2007)
26. P.T. Mosely, Material selection for semiconductor gas sensors. Sens Actuators B **6**, 149–156 (1992)
27. A. Diaz-Parralejo, A. Macisa-Ciarcia, A.L. Ortiz, E.M. Cureda Correa, Effect of calcination temperature on the textural properties of 3 mol% yttria stabilized zirconia powder. J. Non-Cryst. Solids **356**, 175–179 (2010)
28. S.B. Deshmukh, R.H. Bari, H.G. Jain, G.E. Patil, L.A. Patil, Studies on gas sensing performance of pure and surface modified ZrO_2 thick film resistor. in *ICST-2011 IEEE Conference Publication*, pp. 278–285 (2011)

29. http://www.stanfordmaterials.com/ZrO_2.html
30. G.H. Jain, V.B. Gaikwad, D.D. Kajale, R.M. Chaudhari, R.L. Patil, N.K. Pawar, M.K. Deore, S.D. Shinde, L.A. Patil, Surface modified $BaTiO_3$ thick film resistors as H_2S gas. Sens. Tranducers **90**, 160 (2008)
31. R. Moos, W. Menesklou, H.-J. Schreiner, K.H. Hardtl, Materials for temperature independent resistive oxygen sensor for combustion exhaust gas control. Sens Actuators B **67**, 178–183 (2000)
32. K.M. Garakar, B.S. Shirke, Y.B. Pati, D.R. Patil, Nanostructured ZrO_2 thick film resistors as H_2 gas sensors operable at room temperature. Sens. Transducers **110**(11), 17–25 (2009)
33. JCPDS Data Card (36-020) and JCPD data card (17-0923)
34. http://www.green-planet-solar energy.com/electronegativity-values.html
35. A.H. Ataiwi, A.A. Abdul-Hamead, Study some of the structure properties of ZrO_2 ceramic coats prepared by spray pyrolysis method. Eng. Tech. J. **27**(16), 2918–2930 (2009)
36. E.J. Mittemeijer, U. Wetzel, The state of the art of the diffraction analysis of crystallite size and lattice strain. Z. Kristallogr **223**, 552–560 (2008). doi 10.1524/zkri.1213
37. G.K Williamson, W.H Hall, X-ray line broadening from field aluminium and wolfram. Acta.-Metall. **1**, 22 (1953)
38. T. Mahalingam, V.S. John, L.S. Hsu, Microstructural analysis of electrodeposited zinc oxide thin films. New Mater. Electrochem. Syst. **10**, 9–14 (2007)
39. A. Chaudhari, I.S. Mulla, K. Vijay Mohan, Selective hydrogen sensing properties of surface functionalized Tinoxide. Sens Actuators B **55**, 154–160 (1999)
40. D.H. Aguilar, L.C. Torres-Gonzalez, L.M. Torrres-Martines, Study of the crystallinization of ZrO_2 in sol-Gel system: ZrO_2-SiO_2. J. Solid Chem **5**, 349–357 (2000)
41. G. Reyna Garacia, M. Garacia-Hipolito, J. Guzman-Mendoza, M. Aguilar-Frutis, C. Falcony, Electrical, optical and structural characterization of high-k dielectric ZrO_2 thin films deposited by the pyrosol technique. J. Mater. Sci. Mater. Electron **15**, 439–446 (2004)
42. G.E. Patil, D.D. Kajale, D.N. Chavan, N.K. Pawar, P.T. Ahire, S.D. Shinde, V.B. Gaikwad, G.H. Jain, Synthesis, characterization and gas sensing performance of SnO_2 thin films prepared by spray pyrolysis. Indian Academy of Sciences. Bull. Mater. Sci. **34**(1), 1–9, (2011)
43. Su Meiying, Jing Wang, Preparation and humidity sensitivity of multilayered zirconia thin films by sol-gel method. Sens Lett **9**, 670–674 (2011)
44. Richa Srivastav, Investigation of temperature sensing of nanostructured zinc oxide synthesized via oxalate route. J. Sens. Technol. **2**, 8–12 (2012)
45. Eduarda Maria Soares de Carvalho Tomás, Characterization of the ceria and yttria co-doped scandia zirconia: produced by an innovative sol-gel and combustion process. Ph. D. thesis, University of St. Andrews (2010)
46. N. Yamazoe, Y. Kurokawa, T. Seiyama, Effect of additives on semiconductor gas sensors. Sens. Actuators B **4**(2), 283 (1983)
47. A. Umar, Y.-B. Hahn (Ed.), *Metal Oxide Nanostrucures and Their Applications*, vol. 3. (American Scientific Publishers, Stevenson Ranch, 2010), pp. 31–52
48. G. Sarala Devi, V. Bala Subrahmanyam, S.C. Gakari, S.K. Gupta, NH_3 gas sensing properties of nanocrystalline ZnO based thick films. Anal. Chim. Acta **568**, 41–46 (2006)
49. K. Wetchakun, T. Samerjai, N. Tamaekong, C. Liewhiran, C. Siriwong, V. Kruefu, A. Wisitsoraat, A.Tuantranont, S. Phanichphant, Semiconducting metal oxides as sensors for environmentally hazardous gases. Sens. Actuators B **160**, 580–591 (2011)
50. L.A. Patil, L.S. Sonawane, D.G. Patil, Room temperature ammonia gas sensing using MnO_2-modified ZnO thick film resistors. J. Mod. Phys. **2**, 1215–1221 (2011)
51. M. Bendaha, P. Lauque, J.L. Seguin, K. Aguir, P. Knauth, Development of an ammonia gas sensor. Sens. Actuators B **95**, 170–176 (2003)

Chapter 14
Effectiveness of Argon Nanobubbles in Realizing Enhanced Optical Sensitization for Laser-induced Breakdown Spectroscopy

S. Ikezawa and T. Ueda

Abstract This chapter describes the validity and usefulness of laser-induced breakdown spectroscopy (LIBS) measurements enhanced by argon nanobubbles. The use of argon nanobubbles in the LIBS system revealed higher sensitivity as compared to other conventional methods that are used for LIBS solution measurements. To create the nanobubbles, argon gas was pumped into water, forming bubbles less than 100 nm in diameter. The solution of dissolved argon bubbles was used to measure (1) the atomic spectrum of hydrogen ($\lambda = 656$ nm) from the water molecules (H_2O) in the solution, and (2) the atomic spectrum of nitrogen ($\lambda = 399.5$) from the air bubbles in the solution. These experimental results demonstrated that argon nanobubbles are able to instantaneously retain plasma during the excitation/relaxation period, which is essential for highly sensitive spectral measurements. The intensity of nitrogen spectra (measurement (2)) obtained from the argon-air nanobubbles in water was much higher than that of the spectra obtained from normal LIBS air measurements.

Keywords Laser induced break spectroscopy · LIBS · Argon nanobubbles · Optical sensitization

1 Introduction

Higher sensitivity for the purposes of LIBS measurements is generally obtained by using a microchannel plate (MCP) with time-resolved recordings in order to separate the atomic spectra from plasma emission, which typically involves multiple photoelectron processes. Additionally, a double-pulsed (dual-pulsed)

S. Ikezawa (✉) · T. Ueda
Graduate School of Information Production and Systems, Waseda University, Kitakyushu, Fukuoka, Japan
e-mail: ikezawa@y.fuji.waseda.jp

A. Mason et al. (eds.), *Sensing Technology: Current Status and Future Trends I*, Smart Sensors, Measurement and Instrumentation 7, DOI: 10.1007/978-3-319-02318-2_14,

LIBS [1–7] and a crossed-beam LIBS [8, 9], both of which are alternatives to single-pulsed laser irradiation, have been extensively investigated in previous LIBS research. Many sampling methods have been applied in the LIBS measurements performed on solutions. These methods include nebulizing the solution [10], micronizing the droplets [11–15], and generating a liquid thin film (LTF) [16]. As a result, it was reported that high energy transfer efficiency and successful adjustments of the optimal emission direction could be achieved. After performing the experiments that used several inert gases under various pressures, our research group has found that argon gas has the strongest effect on the LIBS [17, 18]. Apart from these experimental results, evidence that argon gas enhances the signal intensity of the measurements owing to the long-term persistence of thermal insulation properties was also found from the time-resolved analysis that was performed by combining our LIBS system with a microdrop sampling system and an argon-assisted system [19]. Thermal persistence is an important factor for sustaining the laser-heated formation of plasma. The argon nanobubble method is a step forward in the investigation of new methods that allow performing high sensitivity LIBS measurements on solutions. The advantage of this method over conventional methods is that it allows obtaining greater surface area between the solution and argon gas while maintaining the same laser target area. In addition to a greater boundary surface area due to the effects of argon gas, each nanobubble is negatively charged [20–24]. In addition, when the nanobubbles are crushed by pressure, their inner temperature reaches thousands of degrees Celsius. From these reports of nanobubbles and sonoluminescence research [25–28], a synergetic effect between the laser plasma and the nanobubbles is expected.

2 Comparison with Previous LIBS Solution Measurements

To compare the proposed nanobubble LIBS system with conventional LIBS, we briefly discuss previous LIBS measurements on solutions that were performed in our laboratory (see Fig. 1). In the past, LIBS measurements on solutions were carried out using a bulk liquid sample (Fig. 1a, b). For the case of a laser plasma generated inside the bulk liquid (Fig. 1a), the plasma plume narrowed for two reasons: (1) a change in the refractive index that the laser beam experienced when crossing from the air into the liquid, and (2) the darkening of the emission light due to the absorption in the sample solution. Figure 1b shows the case of laser plasma that is generated on the surface of a liquid. The optical lenses were splashed with the sample solution; the splashes were induced by a plasma shockwave that produced bubbles inside the liquid. The schematic of another method to perform the LIBS measurements on solutions is shown in Fig. 1c, and it is based on the microdroplet sampling method. In this sampling method, microdroplets (average diameter: 34 μm) are ejected using the ink-jet technology and then are guided onto the laser beam spot (diameter: 53.4 μm). The problem of splashing of the sample liquid is overcome by using a microdroplet ejection system, resulting in more

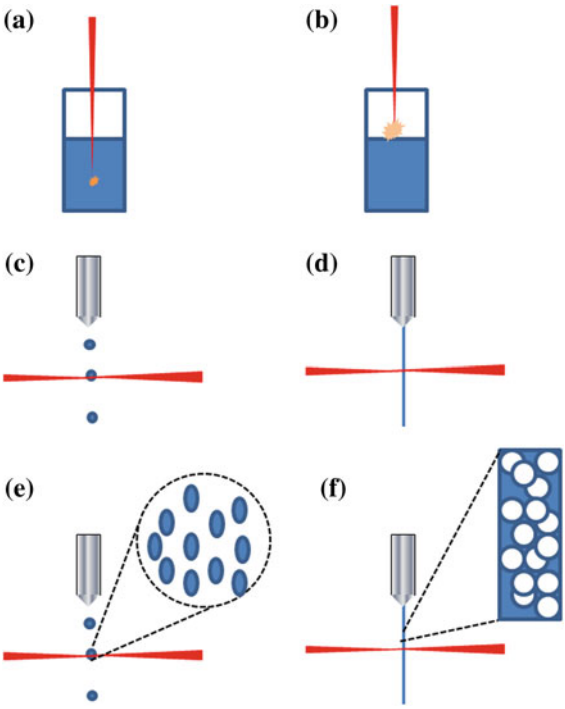

Fig. 1 Different LIBS solution measurement methods

sensitive measurements. While the microdroplet systems are useful, the water-jet method (Fig. 1d) featuring a typical syringe and a dispenser nozzle (orifice diameter: 30 μm, MUSASHI ENGINEERING, INC.) attached to the head of the syringe has been used to reduce the cost and maintenance time of the ink-jet head. In this method, the argon subsystem is attached to the water-jet system to enhance the signal intensity in the measurements. A current issue with the LIBS measurements on solutions pertains to the generation of plasma. Even when the entire volume of the sample liquid is within the beam spot area, the initial point of the vaporization and, subsequently, the generation of plasma occur at the surface of the microdroplet or the micro water-jet. This indicates that the initial point of plasma's growth is the location at which the laser's beam first contacted the liquid's surface. To avoid a large structural refinement, usage of droplets on the nanoscale reduces the dimensionally induced problems. However, because of the reduction in the droplet size, the intensity of the plasma emission is also reduced. Therefore, the nanodroplet cluster (Fig. 1e) and the nanobubble (Fig. 1f) methods are presented in order to tackle these issues. The nanodroplet clusters have a short flying distance after they exit the nozzles and their point of terminal velocity is small. These effects are caused by the resistance due to the viscosity of the ambient gas. Further, the surface of each nanodroplet must be electrically charged. The nanobubble approach is simpler than the nanodroplet cluster method. Thus, in the present study, we adopted the water-jet system that used nanobubbles.

3 Characteristics of Argon Plasma

In the field of chemical analysis, argon is used whenever it is desired to avoid reactions with air. In addition, argon is used as the carrier gas in gas chromatography and in electro spray ionization mass spectrometry. Argon plasma is a prevalent source of ions that can also be looked at as an excitable medium on inductively coupled plasma (ICP-AES/ICP-MS). One of the reasons for which argon plasma is used is its efficiency in plasma generation, which is attributed to its electric potential gradient on breakdown. The ionization potential of argon is higher compared to the potentials of most of other analyte elements, which makes the first ionization potential energy of argon to be 1520.6 kJ/mol. Higher ionization potential of argon contributes to the effective induction of plasma generation of the analyte element. However, helium (with its first ionization potential of 2372.3 kJ/mol) is usually used instead of argon in the analysis that involves elements with higher or comparable ionization energy, such as fluorine (first ionization potential of 1681.0 kJ/mol), chlorine (first ionization potential of 1251.2 kJ/mol), bromine (first ionization potential of 1139.9 kJ/mol), carbon (first ionization potential of 1086.5 kJ/mol), phosphorus (first ionization potential of 1011.8 kJ/mol) and sulfur (first ionization potential of 999.6 kJ/mol). While helium plasma is advantageous, issues such as the cost performance, the low generation efficiency and insufficient amount of plasma for the analysis remain to be addressed. Another reason to use the argon is its low thermal conductivity. Because the argon gas is used in technical scuba diving to inflate a cold dry suit, it is reasonably priced given its effective inert characteristics and low thermal conductivity [29]. While thermal conductivity of nitrogen is 0.024 W/mK, the thermal conductivity of argon is only 0.016 W/mK at a temperature of 273 K. In contrast, the thermal conductivity of helium is 0.142 W/mK at a temperature of 273 K. Because of the easy plasma generation at high atmospheric pressure, a cooling behavior of laser-induced plasma becomes a more important parameter for time resolved analysis in laser induced breakdown spectroscopy.

In our previous research work, we observed a difference between the temporal profiles of laser-induced plasma intensities in argon and air. Figure 2 shows the spectra of air and argon.

These measurements were performed three times for each gas. For each measurement, the number of laser shots was set at one hundred. The time-gate parameter was the same for argon and air. In Fig. 2, the upper set of curves shows the measured argon spectra and the lower set of curves shows the measured air spectra. A signal at the wavelength of 399.5 nm corresponds to the nitrogen's atomic signal. The rest of the spectral peaks correspond to the argon peaks. The graph indicates that the usage of argon gas not only causes an increase in the background level of plasma emission but also enhances the intensity of the peak that is associated with nitrogen.

Figures 3 and 4 show the temporal profile of the intensities of argon and air spectra measured during the first 200 ns from the time of the laser's energy production. In these plots, the values of intensity are normalized by the maximal

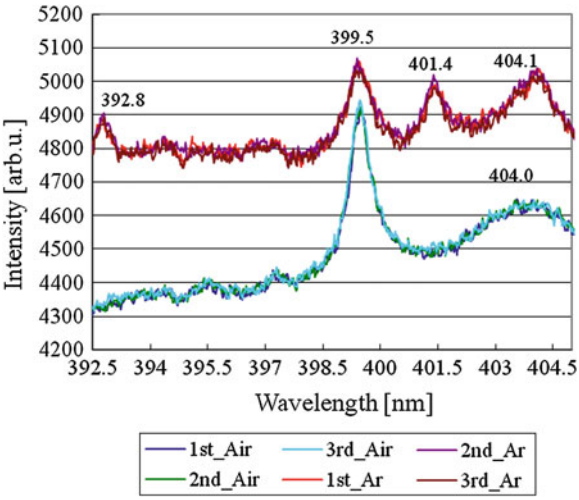

Fig. 2 Air and argon spectra obtained from LIBS operated at 100 laser shots during each of the three measurements

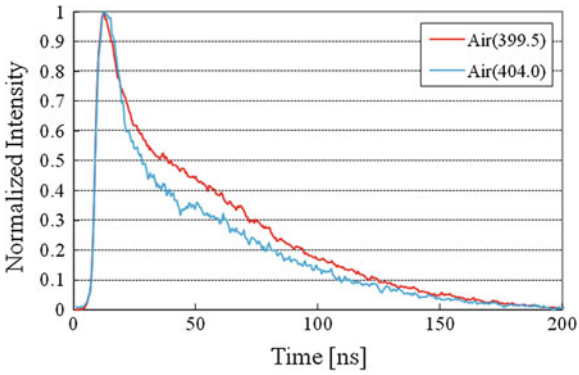

Fig. 3 Temporal profile of air's normalized spectral intensity

intensity. In the measured temporal profile of the air plasma, the characteristic relaxation times differ, depending on the wavelength. In the measured temporal profiles of the argon and nitrogen plasma in argon atmosphere, the characteristic relaxation times are almost the same for all wavelengths under consideration.

Figure 5 shows the combined temporal profile that was obtained by superposing the results from Figs. 3 and 4 and adding the temporal profile of a laser's pulse that was recorded using the same device.

To clarify the difference between the experiments that considered air and argon atmosphere, the same data are shown in Fig. 6 using the logarithmic scale for y axis. From Fig. 6, it is observed that the temporal profiles of all argon spectral intensities under consideration are evidently only moderately attenuated compared with the profiles of air's spectral intensities. This indicates that argon plasma performed adiabatic work. Greater integrated value of intensity during more prolonged

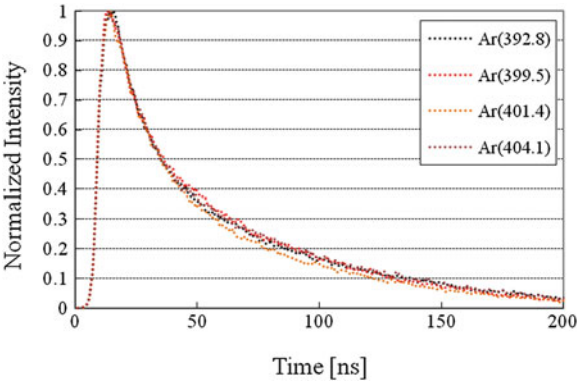

Fig. 4 Temporal profile of argon's and nitrogen's normalized spectral intensity in argon gas atmosphere

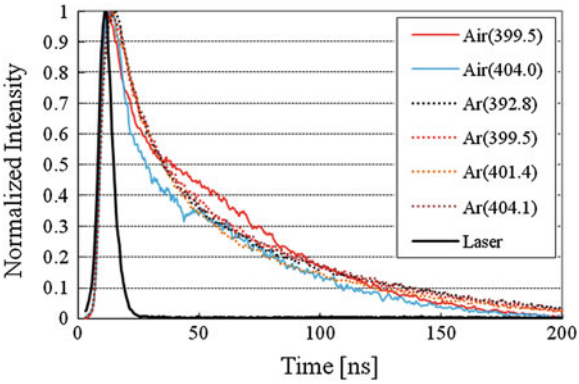

Fig. 5 Temporal profile of normalized spectral intensities for argon and air

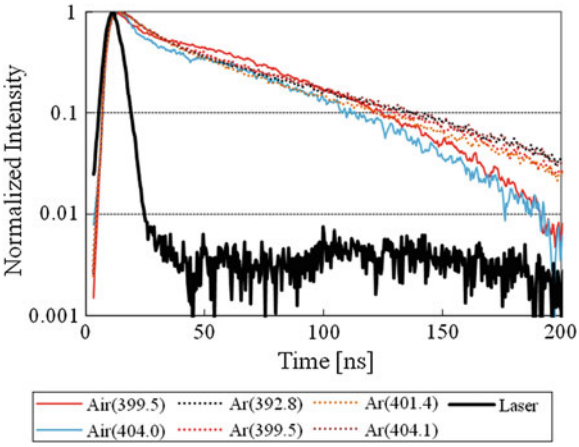

Fig. 6 Temporal profile of normalized spectral intensities for argon and air, plotted using the logarithmic scale for y axis

emission correction causes the measured argon's spectral intensity to be higher than the measured air's spectral intensity when time resolving analysis is used.

4 Experimental Setup of the LIBS System that Uses Nanobubbles

4.1 Nanobubble Liquid

A compact micro/nano bubble generator (MA5S, ASUPU CO., LTD.) that is shown in Fig. 7 was used in these experiments. This device enables the stable generation of a high density of nanobubbles; it is capable of generating more than 2.6 million bubbles per milliliter, and it can constrain the distribution of bubble sizes and the dispersion of density by utilizing a combined system that uses pressure dissolution, gas–liquid shearing, and cavitation. The nanobubbles have the following characteristics: slow bubble levitation, large surface area for the same volume, high inner pressure, negatively charged surface, and creation of hydroxyl radicals. In addition to the production of nanobubbles, the generator forms an LTF, which enables a more effective gas assist for plasma generation (Fig. 8). Two different nanobubble liquids were used in the experiment: (1) an argon nanobubble liquid that was fabricated by dissolving argon gas in water for 10 min using the micro/nano bubble generator, and (2) an argon-air nanobubble liquid that was fabricated by dissolving argon gas and air in water for 10 min each.

4.2 The LIBS System

Figure 9 shows the schematic presentation of the LIBS system. The optical layout of the LIBS system consisted of four subsystems: a Nd:YAG laser, a spectrograph, a streak camera, and a delay pulse generator. The Nd:YAG laser was operated at 1,064 nm to generate a 52.8 mJ Q-switched pulse that had a width of 8 ns (full width at half maximum, FWHM). The sampling system for the micro/nano bubble LIBS measurements consisted of a syringe with a water-jet nozzle. The inner diameter of the nozzle was 30 μm. The water was pushed out of the syringe under pressure from an air compressor. The emissions from the target area in the water-jet stream were guided into the spectrograph and were dispersed by a grating with a groove density of 1,200 lines/mm, and the resulting electrical signal was recorded using the streak camera. The streak camera was operated by directing the light onto a photocathode, where photons produced electrons via the photoelectric effect. The electrons were accelerated in a cathode ray tube and passed through an electric field that was generated by a pair of sweep electrode plates, which deflected the electrons sideways. By modulating the electric potential between the

Fig. 7 Photograph of a micro/nanobubble generator (MA5S, ASUPU CO., LTD.)

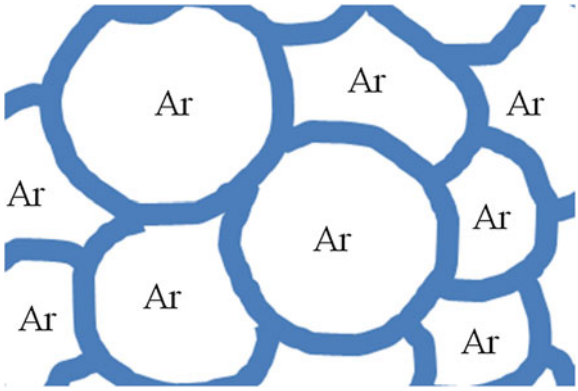

Fig. 8 Structure of the liquid thin film

plates, the electric field was quickly changed to produce a time-varying deflection of the electrons, sweeping the electrons. This was amplified by an MCP across a phosphor screen at the end of the tube. Extraction and relaxation of the spectrum of elements occurred during plasma formation, and the subsequent dissipation of the laser plasma occurred very rapidly. Within 4 μs from the time of plasma initiation, an intense continuum of radiation was observed, along with ionic lines over a broad range of wavelengths; within 20 μs from the time of atomic emission, the spectrum of the elements was observed. The spectra of the plasma that was created within 4 μs was due to the bremsstrahlung radiation and due to the recombination radiation from the plasma, where the latter was caused by free electrons and ions that recombined in the cooling plasma. The intensity of the spectral emission was optimized with respect to the plasma background. Spectral measurements were carried out after an appropriate time delay to allow for the decay of the continuum radiation. Finally, a charge-coupled device (CCD) array was used to measure the streak pattern on the screen and thus the temporal profile of the light pulse; the data were stored in a PC to be processed and analyzed.

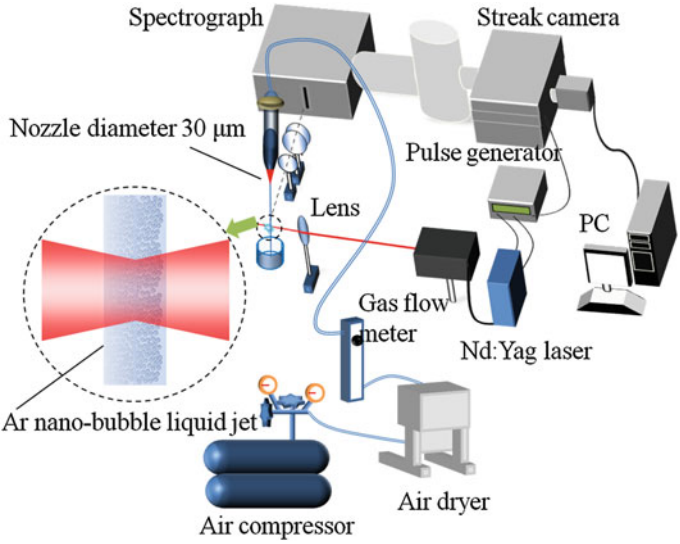

Fig. 9 Schematic of the LIBS system

5 Experimental Results

In the following experiments, the hydrogen and nitrogen spectra were measured five times for each of the following samples: (1) air, (2) pure water, and (3) argon nanobubble liquid. The samples were measured via 100 laser shots with the timing operation for time-resolved analysis; the post-bremsstrahlung gate setting was 1.57 μs.

5.1 Hydrogen Spectrum

In this experiment, the atomic spectrum of hydrogen (H-α, $\lambda = 656$ nm) was recorded; it corresponded to the Balmer series, which was derived from hydrogen atoms in water molecules.

5.1.1 Measurements in Air

Figure 10 shows the variation in the intensities of the hydrogen spectrum obtained from five measurements in air, which corresponds to the atomic spectrum of hydrogen in air's water molecules under the following conditions: humidity of 64 % and temperature of 24 °C.

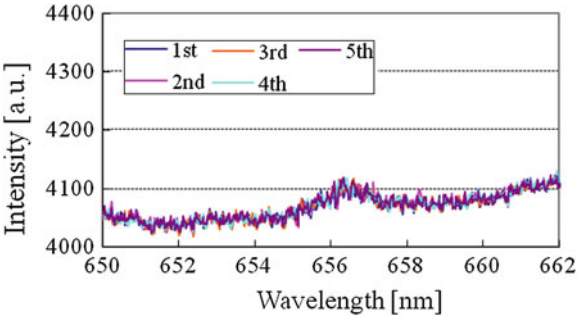

Fig. 10 Hydrogen spectrum obtained from air

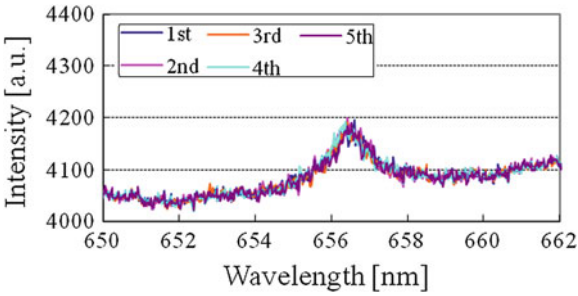

Fig. 11 Hydrogen spectrum obtained from pure water

5.1.2 Measurements in Pure Water

Figure 11 shows the variation in the intensities of the hydrogen spectrum obtained from five measurements in pure water, which corresponds to the atomic spectrum of hydrogen in water molecules of pure water. When the condensed laser beam was irradiated onto the water jet, water molecules were vaporized and hydrogen and oxygen were immediately ionized, creating plasma.

5.1.3 Measurements in Argon Nanobubble Liquid

Figure 12 shows the variation in the intensities of the hydrogen spectrum obtained from five measurements in the argon nanobubble liquid, which corresponds to the atomic spectrum of hydrogen in water molecules of the liquid.

From these experiments, it was found that the intensities obtained from the LIBS measurements of hydrogen spectrum using the argon nanobubble liquid were highest among the three samples. The results indicate that argon in the form of nanobubbles effectively increases the sensitivity of the hydrogen spectrum.

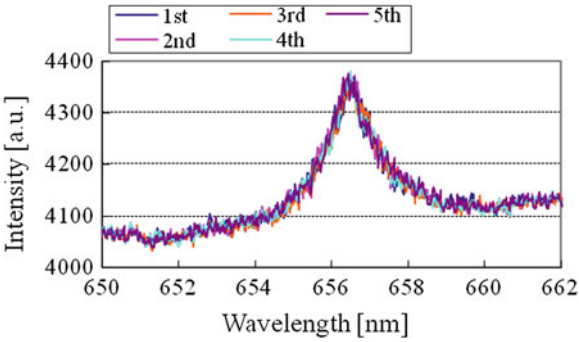

Fig. 12 Hydrogen spectrum obtained from water containing argon nanobubbles

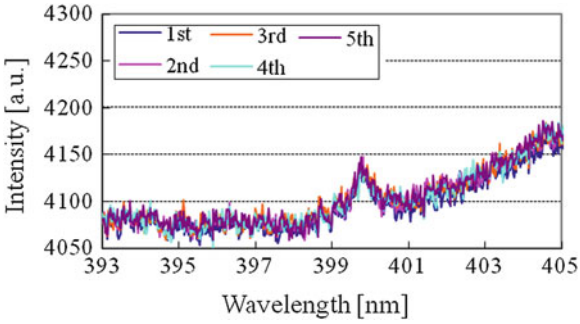

Fig. 13 Nitrogen spectrum obtained from air

5.2 Nitrogen Spectrum

In the following experiments, five measurements for each sample, including air, pure water and the argon-air nanobubble liquid, were carried out to obtain nitrogen spectra ($\lambda = 399.5$) under conditions that were similar to those used in the previous measurements of hydrogen spectra.

5.2.1 Measurements in Air

Figure 13 shows the variation in the intensities of the nitrogen spectrum obtained from five measurements in air, which corresponds to the atomic spectrum of nitrogen from the nitrogen molecules in air. The intensity of the nitrogen spectrum obtained from air is high because the elemental component ratio of air is 78 % nitrogen, 21 % oxygen, 1 % argon, and 0.04 % carbon dioxide.

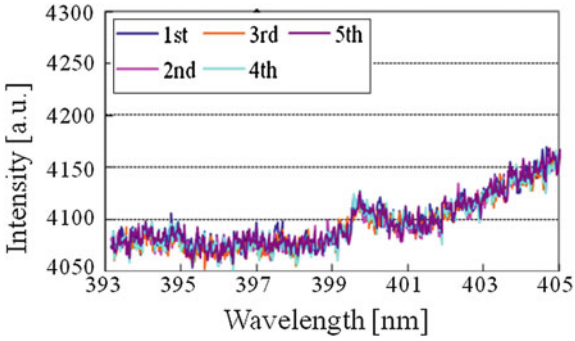

Fig. 14 Nitrogen spectrum obtained from pure water

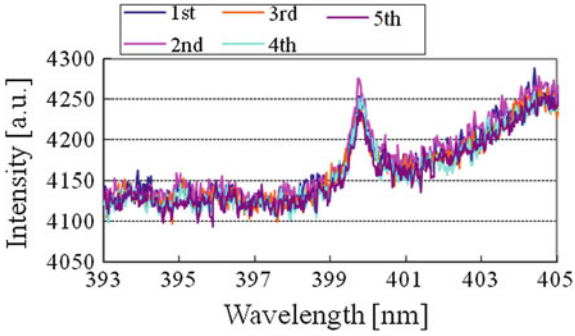

Fig. 15 Nitrogen spectrum obtained from water containing argon-air nanobubbles

5.2.2 Measurements in Pure Water

Figure 14 shows the variation in the intensities of the nitrogen spectrum obtained from five measurements in pure water, which corresponds to the atomic spectrum of nitrogen from ambient air. Ambient air interferes with the measurements on liquids.

5.2.3 Measurements in Argon-Air Nanobubble Liquid

Figure 15 shows the variation in the intensities of the nitrogen spectrum obtained from five measurements in the argon-air nanobubble liquid, which corresponds to the atomic spectrum of nitrogen molecules in air and in the nanobubbles.

The experimental results indicate that the intensities of the nitrogen spectra obtained from the argon-air nanobubble liquid were higher than those of the spectra obtained from air and pure water.

6 Conclusions

In the experiments that were described above, argon nanobubbles enhanced the intensities of the hydrogen and nitrogen spectra that were obtained from the LIBS measurements. By introducing nano-structured argon gas, the adiabatic effect on argon gas (attributed to the lower thermal conductivity as compared with the thermal conductivity of hydrogen) caused not only physical and chemical interactions but also contributed to the structural organization, similar to its function in polystyrene foam materials. These results can find potential applications in the following: (1) highly sensitive LIBS measurements on additional solutions; (2) elemental analyses for new LIBS gas measurements using the nanobubble liquid; and (3) industrial applications of nanobubble LIBS for real-time analyses of commercial products. In order for (1) to become viable, spectra of additional elements and compounds, such as hydrogen, OH radicals, or other elements will need to be measured to obtain evidence for the effects of argon nanobubbles. The benefit of (2) is that the LIBS gas measurements are expected to lower gas consumption because gases of different specific weights have weaker diffusion. As for (3), LIBS bears a promise to become useful in real-time analysis of the amount of nanobubbles that exist in the solution during the production process. With the advancement of a LIBS-based quick analysis, the process can be monitored on site without any requirement of chemical preprocessing or large facilities. Research on nanobubbles is now drawing more attention for their potential applicability in areas such as medical systems for fighting cancer, beauty and healthcare products, soil improvement for agricultural use, long-term storage of food products, prevention of infectious diseases in farmed aquatic animals, and a new fuel form of hydrogen energy. Evaluations of these products will be improved by nanobubble LIBS.

References

1. J. Uebbing, J. Brust, W. Sdorra, F. Leis, K. Niemax, Reheating of a laser-produced plasma by a second pulse laser. Appl. Spectrosc. **45**, 1419–1423 (1991)
2. R. Nyga, W. Neu, Double-pulse technique for optical emission spectroscopy of ablation plasmas of samples in liquids. Opt. Lett. **18**, 747–749 (1993)
3. R. Sattmann, V. Sturm, R. Noll, Laser-induced breakdown spectroscopy of steel samples using multiple Q-switch Nd:YAG laser pulses. J. Phys. D. **28**, 2181–2187 (1995)
4. S. Nakamura, Y. Ito, K. Sone, H. Hiraga, K. Kaneko, Determination colloidal iron in water by laser induced breakdown spectroscopy with two sequential laser pulses. Anal. Chem. **68**, 2981–2986 (1996)
5. A.E. Pichahchy, D.A. Cremers, M.J. Ferris, Elemental analysis of metals under water using laser-induced breakdown spectroscopy. Spectrochim. Acta. B **52**, 25–39 (1997)
6. D.N. Stratis, K.L. Eland, S.M. Angel, Dual-pulse LIBS using a pre-ablation spark for enhanced ablation and emission. Appl. Spectrosc. **54**, 1270–1274 (2000)
7. D.N. Stratis, K.L. Eland, S.M. Angel, Effect of pulse delay time on a pre-ablation dual-pulse LIBS plasma. Appl. Spectrosc. **55**, 1297–1303 (2001)

8. P. Yaroshchyk, R.J.S. Morrison, D. Body, B.L. Chadwick, Quantitative determination of wear metals in engine oils using LIBS: the use of paper substrates and a comparison between single- and double-pulse LIBS. Spectrochim. Acta B Atomic Spectr. **60**, 1482–1485 (2005)
9. A. M. Popov, F. Colao, R. Fantoni, Spatial confinement of laser-induced plasma to enhance LIBS sensitivity for trace elements determination in soils. J. Anal. Atomic Spectr. **25**(6), 837–848 (2010)
10. A. Kumar, F.Y. Yueh, T. Miller, J.P. Singh, Detection of trace elements in liquids by laser-induced breakdown spectroscopy with a meinhard nebulizer. Appl. Opt. **42**, 6040–6046 (2003)
11. C. Favre et al., White-light nanosource with directional emission. Phys. Rev. Lett. **89**, 035002 (2002)
12. V. Boutou, C. Favre, S.C. Hill, Y.L. Pan, R.K. Chang, J.-P. Wolf, Backward enhanced emission from multiphoton processes in aerosols. Appl. Phys. B Lasers Opt. **75**, 145–152 (2002)
13. F. Courvoisier, V. Boutou, C. Favre, S.C. Hill, J.-P. Wolf, Plasma formation dynamics within a water microdroplet on femtosecond time scales. Opt. Lett. **28**, 206–208 (2003)
14. S. Ikezawa, M. Wakamatsu, J. Pawlat, T. Ueda, Improvement of a micro-droplet guiding technique for laser-induced breakdown spectroscopy. IEEJ Trans. Sensors Micromach. **128**, 297–301 (2008)
15. S. Ikezawa, M. Wakamatsu, J. Pawlat, T. Ueda, Sensing system for multiple measurements of trace elements using laser-induced breakdown spectroscopy. IEEJ Trans. Sensors Micromach. **129**, 115–119 (2009)
16. A. Kuwako, Y. Uchida, K. Maeda, Supersensitive detection of sodium in water with use of dual-pulse laser-induced breakdown spectroscopy. Appl. Opt. **42**, 6052–6056 (2003)
17. M. Wakamatsu, T. Ueda, H. Hayashi, Particle element and size measurement using LIBS. Proc. SICE Ann. Conf. **2**, 1191–1195 (2003)
18. M. Wakamatsu, S. Ikezawa, T. Ueda, Particle element and size simultaneous measurement using LIBS. IEEJ Trans. Sensors Micromach. **127**, 397–402 (2007)
19. S. Ikezawa, M. Wakamatsu, Y. L'vovich Zimin, J. Pawlat, T. Ueda, Multi-spectral analytical systems using LIBS and LII techniques, ed. by S.C. Mukhopadhyay, A. Lay-Ekuakille, A. Fuchs, New Developments and Applications in Sensing Technology. Lecture Notes in Electrical Engineering, vol. 83 (Springer, 2011) pp. 207–232
20. M. Takahashi, E. Izawa, J. Etou, T. Ohtani, Kinetic characteristic of bubble nucleation in superheated water using fluid inclusions. J. Phys. Soc. Jpn. **71**(9), 2174–2177 (2002)
21. M. Takahashi et al., Effect of shrinking micro-bubble on gas hydrate formation. J. Phys. Chem. B **107**(10), 2171–2173 (2003)
22. M. Takahashi, The ζ potential of microbubbles in aqueous solutions – Electrical property of the gas-water interface. J. Phys. Chem. B, **109,** 21858–21864 (2005)
23. M. Takahashi, K. Chiba, P. Li, Free-radical generation from collapsing microbubbles in the absence of a dynamic stimulus. J. Phys. Chem. B **111**(6), 1343–1347 (2007)
24. M. Takahashi, K. Chiba, P. Li, Formation of hydroxyl radicals by collapsing ozone microbubbles under strongly acidic conditions. J. Phys. Chem. B **111**(39), 11443–11446 (2007)
25. A.J. Walton, G.T. Reynolds, Sonoluminescence. Adv. Phys. **33**, 595–660 (1984)
26. R.E. Verrall, C.M. Sehgal, Sonoluminescence. Ultrasonics **25**, 29–30 (1987)
27. S.J. Doktycz, K.S. Suslick, Interparticle collisions driven by ultrasound. Science **247**, 1067–1069 (1990)
28. B.P. Barber, S.J. Putterman, Observation of synchronous picosecond sonoluminescence. Nature **352**, 318–320 (1991)
29. M. L. Nuckols, J. Giblo, J. L. Wood-Putnam, Thermal Characteristics of Diving Garments When Using Argon as a Suit Inflation Gas, in *Proceedings of the Oceans 08 MTS/IEEE Quebec, Canada Meeting* (MTS/IEEE), 2009

Chapter 15
Overview of the Development and Applications of a Vision Based Scene Change Detector

A. J. Tickle

Abstract This book chapter discusses the development and applications of a vision based observation methodology called morphological scene change detection (MSCD). This technique uses the differences between successive frames of video or a reference image to a current image so that changes in the scene can be detected. This process is much quicker and requires fewer calculations when undertaken in the binary domain and then processed using mathematical morphology to clean away any noise. Shown here is the development of a system that is implemented via the use of graphical blocks in Simulink for ease of design for deployment on field programmable gate arrays (FPGA). This results in an easy to use system that can be used to detect intruders, faults with piping systems, and if need be, watermark the image digitally to protect against tampering. The FPGA also makes the system easily deployable in many environments either as a static platform or for insertion into an autonomous mobile robot. The uses of this methodology are not simply limited to the applications discussed here but can be applied to a much wider range of problems.

Keywords Morphological scene change detection · Intruder detection · Digital watermarking · Leak detection · Mathematical morphology · Thresholding

1 Introduction

This chapter is an overview of the work undertaken in [1–3], inspired by Elena Stringa, at the Institute for Systems, Informatics, and Safety in Italy [4] where work has taken place on video detection systems. This initial section concentrates

A. J. Tickle (✉)
Faculty of Engineering and Computing, Deptartment of Aviation, Aerospace, Electrical and Electronic Engineering, Coventry University, Priory Street, Coventry CV1 5FB, UK
e-mail: andrew.tickle@coventry.ac.uk

A. Mason et al. (eds.), *Sensing Technology: Current Status and Future Trends I*, Smart Sensors, Measurement and Instrumentation 7, DOI: 10.1007/978-3-319-02318-2_15,

on taking the work from [4] and developing effective graphical user interface circuitry (GUIC) in Simulink for system implementation on field programmable gate arrays (FPGAs). It is envisaged that using this technology would allow security services, armed forces or even the general public to quickly make areas more secure. This methodology is not meant to replace the human in the security progress, whilst it may help to reduce man power required for patrols tasks, its ultimate purpose is to augment existing systems, not replace them. An example of this would be to augment closed circuit TV (CCTV) systems as a means of increasing security, used for surveillance in banks, casinos, airports, military installations, hospitals, private property, etc., the list goes on. The presented system will be simple and inexpensive enough to be used in home security systems, and easily reprogrammed for differing environments via the triggering threshold input. Like CCTV, this system would be most effective not on crime prevention, but on detection and prosecution, when the system is triggered, an output could be a signal sent to the Police, and the onsite security personal telling them that the system has detected a security breach and possibly, start an automated lockdown of the environment.

Video surveillance systems with detection tasks usually include a module aiming at detecting relevant changes in the guarded environment [4–8]. The output of the morphological scene change detector (MSCD) module is further processed, this is necessary to have an MSCD algorithm/circuitry as accurate as possible by removing noise and mismatched between successive frames in the collected image, and jitter in the image comparison. The latter is to make the triggering process more efficient and is done via the use Morphological Operators (MOs) developed previously for noise removal [9, 10]. MSCD techniques presented in the literature can be divided in two classes: pixel-based and region-based algorithms [11].

Pixel-based algorithms compute the output by analyzing the values assumed by the correspondent pixels in the two analyzed images, while region-based algorithms compare features extracted from correspondent regions in the two images. Pixel based methods, such as morphological scene change detection (MSCD) based on binary difference, present the advantage of the simplicity that makes possible real-time applications, whereas region-based techniques such as MSCD based on the illumination model [12], provide results more robust to false alarms introduced by noise. Another class of MSCD algorithms detects changed regions by means of edge comparisons. These methods are quite expensive from the computational point of view, and therefore would not be able to be run on an FPGA and so they are not discussed here. This system also will be immune to many of the techniques used to trick standard security systems, due to the nature of the way it is programmed into the FPGA core. Moving slowly, placing a picture or simply blocking off the camera will be enough to trigger the system and so such a robust system will be vital for anyone wanting to augment their security systems.

Sections 2–5 will then focus on the development of the MSCD system, the logical progression of this would be to develop a digital watermark that could be used in the event that an intruder has been detected and the user wants to prove to the law enforcement agencies that the image has not been tampered with.

This aspect of work continues on from that in [13], were mathematical morphology and the DSP Builder package from Altera were used to hide data within another file or image, a process commonly known as steganography. This is presented in Sects. 6 and 7, a discussion of the watermarking block and how it was designed and applied to the discussed Morphological Scene Change Detection (MSCD) [1] application will be covered.

Much work has been undertaken on digital watermarking in the past decade [14, 15], unlike traditional watermarks on paper, which are visible to our eyes; digital watermarks can be designed to be imperceptible and removable. Throughout this chapter, the term watermark(ing) will be used in reference to a digital watermark. The availability of versatile multimedia processing software and the internet have allowed for flawless copying and manipulations of the digital media. However, abuses of these facilities and technologies pose pressing threats to multimedia security management in general, and multimedia copyright protection and content integrity verification in particular [16].

The idea of digital watermarking is to embed a small amount of imperceptible secret information in the multimedia so that it can be extracted later for the purposes of copyright assertion, copy control, broadcasting, authentication, content integrity verification, etc. For example, a stream of binary bits generated or a binary image, which identifies the owner of an image in the form of text or a company logo, can be taken as a watermark embedded at the Least Significant Bit (LSB) of the pixels or transformed coefficients by adjusting their value according to a predefined algorithm. Since this information is embedded in the content of the media, for the applications related to copyright protection where the watermark is intended to be robust, it does not get erased when the content is manipulated or undergoes format conversions [16].

The robustness of a watermark is vital to its effectiveness to prove if the content of the media has been altered or not. A watermark is called robust if it resists a designated class of transformations; these are used in copy protection applications to carry copy and no access control information. A watermark is called fragile if it fails to be detectable after the slightest modification. Fragile watermarks are commonly used for tamper detection (integrity proof). A watermark is referred to as being semi-fragile if it resists benign transformations, but fails detection after malignant transformations. Fragile watermarks are modifications to original work that are clearly noticeable, more commonly seen as generalized barcodes, whilst semi-fragile watermarks commonly are used to detect malignant transformations. In medical, forensic, intelligence or military applications where content integrity and source authentication are a major concern, more emphases are placed on the schemes' capability of detecting forgeries and impersonations. Therefore, schemes of this type are usually fragile or semi-fragile and are intended to be intolerant to manipulations. Finally, a watermark is classed as imperceptible, if the original media and the marked media are perceptually indistinguishable. On the other side, a watermark is classed as perceptible, if its presence in the marked media is noticeable.

Requirements of digital watermarking vary across applications. The main requirements are low distortion, high capacity, and high security. One issue is that meeting all the three requirements simultaneously is usually infeasible, thus, trade-offs are frequently made to optimize the balance for each specific application [14]. Epson and Kodak have since produced cameras with security features such as the Epson PhotoPC 3000Z and the Kodak DC-290. Both devices added irremovable features to the pictures which distorted the original image, making them unacceptable for some applications such as forensic evidence in court. This paper presents something similar, in that the output from the system will automatically have a watermark in the image, making it more secure than adding one after. A similar secure digital camera (SDC) opposed to a secure digital system (SDS), was proposed by Mohanty et al. in 2003 and published in January 2004, however this was not the first time this was proposed [17]. Blythe and Fridrich also worked on an SDC in 2004 [18] for a digital camera that would use lossless watermarking to embed a biometric identifier together with a cryptographic hash [19]. Advances in the field are occurring all the time in order to combat pirates and forgers.

Finally, Sects. 8 and 9 will deal with how the system can be recalibrated so that it can be used for the detection of leaks rather than intruders, demonstrating the robustness of the system. Traditionally, leak detection uses an externally based system that utilizes a series of dedicated sensors, these systems can be highly sensitive and accurate, but can be expensive, complex to install and limited to one location. As a result, they are usually limited to special high-risk areas. There are several conventional techniques which are briefly discussed below [2]:

- **Infrared radiometric testing:** Infrared thermographic pipeline testing has shown itself to be both accurate and efficient in detecting and locating subsurface pipeline leaks, voids caused by erosion, deteriorated pipeline insulation, and poor backfill. When a pipeline leak has allowed a substance, such as water, to form a plume near a pipeline, the fluid has a thermal conductance different from the dry soil. This will be reflected in a different surface temperature pattern above the leak location, the system measures these patterns based on their grayscale or binary values and allows an operator to determine if the pipe needs attention or not.
- **Acoustic emission detectors:** Escaping liquids creates an acoustic signal as they passes through a hole in the pipe. Acoustic sensors fixed to the outside of the pipeline create a baseline acoustic “fingerprint” of the line from the internal noise of the pipeline in its undamaged state. When a leak occurs, a resulting low frequency acoustic signal is detected and analyzed. Deviations from the baseline “fingerprint” signal an alarm.
- **Vapor-sensing tubes:** The vapor-sensing tube leak detection method involves the installation of a tube along the entire length of the pipeline. This tube comes in the form of a cable and is highly permeable to the substance to be detected in the particular application. If a leak occurs, the substance to be measured comes into contact with the tube in the form of vapor, gas or dissolved in water. In the event of a leak, some of the leaking substance diffuses into the tube. After a

certain period of time, the inside of the tube produces an accurate image of the substances surrounding the tube. In order to analyze the concentration distribution present in the sensor tube, a pump pushes the column of air in the tube past a detection unit at a constant speed. The detector unit at the end of the sensor tube is equipped with the appropriate sensors. A similar method to this is used where the tube is filled with a liquid and the bubbles of the substance escaping the pipe can be detected by sensing the motion of the fluid.

- **Fiber-optic technique:** The fiber-optic sensing technique involves the installation of a fiber-optic cable along the entire length of the pipeline thus making this approach expensive. When the substance to be detected comes into contact with the cable when a leak occurs, it changes the temperature of the cable as a result. The distributed fiber-optical temperature-sensing technique offers the possibility to measure temperature along the pipeline. Scanning the entire length of the fiber, the temperature profile along the fiber can be determined and changes in this thus lead to a leak detection mechanism.

By modifying the MSCD system, it would allow technical staff to help ensure that power stations, nuclear facilities and chemical plants are free from leaks resulting from damage to piping from impacts, decay in piping from age resulting in failed joints or improper welding of the system during construction or repair. Any of the latter could result in high pressure steam, radioactive particles or chemical agents etc, escaping into the atmosphere and causing harm to the work force, the general public and the environment if not properly contained. To additionally assist in this task, small autonomous mobile robots with maintenance routes programmed into them [20, 21] could be devised that could make use this algorithm to hence search automatically for leaks and raise an alert if a leak is indeed detected, thus helping to respond quicker and saving lives. By extracting features here that result from a change due to the substance escaping the piping, this can be shadows caused by the substance, slight movement of the pipes by the momentum of the escaping substance etc, the latter situations can be searched for before the scene detection takes place. As in the original system [1], the output of this augmented MSCD circuitry should undergo a noise reduction filter to assist in removing any unwanted data and helping to improve the accuracy of the counting used to trigger the system. This will be done again using a combination of mathematical morphology [9].

2 Morphological Scene Change Detection

Each MSCD technique is characterized by the metric, introduced in order to quantify the difference between pixels or regions, and by a threshold value allowing the system, to know if the analyzed pixel or region has changed with respect to the reference image. The threshold setting is a crucial step because different threshold values provide extremely different results, and would also have

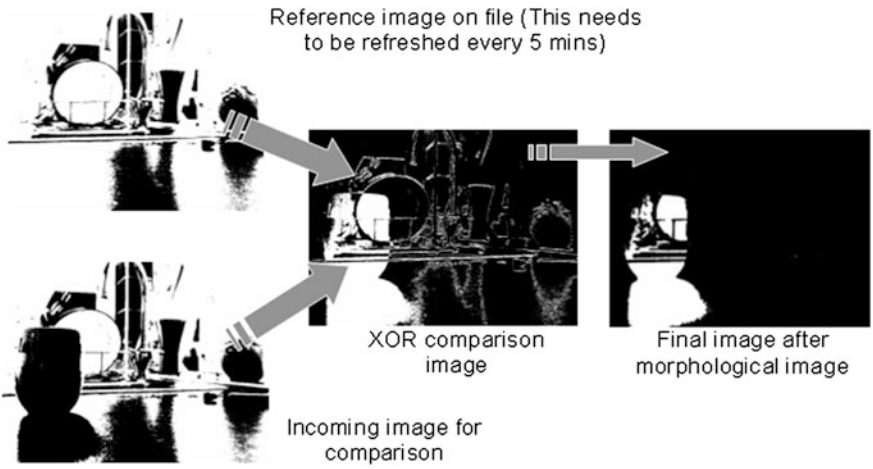

Fig. 1 Basic layout of the morphological scene change detection system

to be calibrated and set for different applications and uses. It would be required that MSCD algorithms/circuits have advantages of both pixel and region based techniques. This goal was reached by considering binary Morphological Operations (MOs), which compute the output value of a pixel according to the values of its neighboring set, which are applied to the output of the binary difference in MSCD systems [22, 23]. The implementation of binary MOs, allows their application to video surveillance systems. MSCD based on binary morphology is performed according to the architecture shown in Fig. 1, with the binary difference in the FPGA performed via a XOR logical function for reasons that will be explained later.

A reference image representing the guarded environment is compared to the image representing the current situation [5–8]. The comparison is based on a pixel-to-pixel binarized difference between the two images, so let $B = B(i)|i = 1...N$ the background image composed of N pixels, and $I_{tk} = I_{tk}(i)|I = 1...N$ the current analyzed frame I_{tk} is the instant at which the current image has been acquired. For each pixel i the result of the binarized difference is obtained by setting to the value '1' the output, if the difference is greater than a threshold value. The threshold indicates the minimal illumination difference to consider two pixels different; in the ideal case, this distance is equal to one gray level, but due to the noise introduced by the acquisition device, the operation is more robust by setting a higher threshold.

When the processed images assumes vector values, for instance they present the R, G, and B color components, then the operation is applied to each image channel and the binary result is obtained by performing a logical OR among the results obtained from each channel. After the binary difference, MOs are introduced in order to eliminate the isolated noisy pixels and to compact into regions pixels belonging to the same changed area. Usually standard or soft openings are applied

because the erosion presents the capabilities of removing isolated noisy pixels and the dilation recompose the regions split by the preliminary erosion. When there are no time constraints and it is necessary to have high accuracy in MSCD operations, it is possible to binarize the difference image and to then subtract the filtered difference.

3 Design of the MSCD in Simulink/Altera DSP Builder

The process of the MSCD used in this proposed method for the FPGA system, was that after the images have been converted from RGB color images to binary images, a XOR logical process is used on the two input images, this is due to the fact that the XOR gate works in a very similar way to the way the comparator works in Simulink environment, as shown via its truth table shown in Table 1. The XOR gate actually turns out to be the better option, because the desired output is to want the none matching areas in the binary image to be white or '0', which is the natural function of the XOR gate. After the current image was then XOR'ed with a reference image, a process of trial and error was used to determine the best combination for noise removal in obtaining the sought after image. This was discovered to be the open operation followed by a series of three successive erosions. Figure 1 also shows the results of this and it was also deemed that the structuring element 8 connectivity (SE8) [9, 10] case would be better than the structuring element 4 connectivity (SE4), due to the greater number of 'active' pixels and so the better the chance to remove the noise.

For the actual system circuitry, the same principles used in [9, 10] are used here with regard to the levels of abstraction. Figure 2 shows the behavioral level of abstraction for the system, there are 5 inputs to the system and 2 main outputs, with a further 2 secondary outputs for checking purposes. The main inputs are the system clock and global reset, which are directed into all the blocks of the RTL level system to trigger the counters and line buffers etc. There are the 2 inputs from the current and reference images, which would come from a real-time camera similar to that shown in [24] and the SDRAM of the FPGA respectively. The final input into the system is a triggering threshold, which can be set anything from 1,000 to 35,000, depending upon the environment to which it is to be deployed; this is covered later in Sect. 5.

Table 1 Exclusive OR (XOR) gate truth table comparison to comparator

Input A	Input B	Comparator out set to equal mode	XOR logical output
0	0	1	0
0	1	0	1
1	0	0	1
1	1	1	0

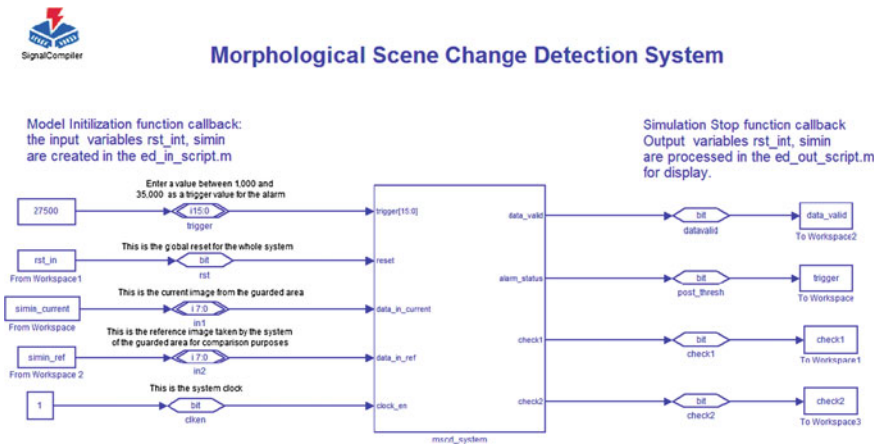

Fig. 2 Behavioral level for MSCD showing system inputs and outputs

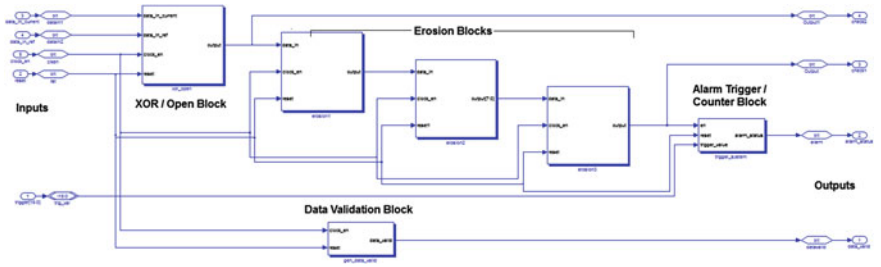

Fig. 3 RTL level for the MSCD system showing the different inter-connections

The register transfer level (RTL) of the system shown in Fig. 3 is fairly standard, the inputs and outputs to this level are the same as those at the behavioral level shown in Fig. 2. The string of blocks are the XOR Open block, which is then connected to the string of 3 Erosion blocks, which are then fed into the alarm trigger block. The current and references are fed into the XOR Open block with just a single output from each successive block, each of these are binary data lines. There are the check signals coming from the blocks directly after the XOR Open block and another after the last Erosion block, this was to ensure that the outputs from these blocks are correct and can be removed in the final version of the system if so desired. The output from the alarm trigger block is either a signal '0' to state that no intruder has been detected, or a '1' to signal that an intruder has been detected, being a 1 bit signal this makes it easy to connect into and augment with existing systems. The block at the bottom of Fig. 3, is the data validator and has been included in all systems to verify the output data, this has always been used as shown in the Altera design example [25, 26]. The latter block produces a signal that is either a '0' or a '1', depending on if the system deems the data to be correct, more information can be obtained from the Altera documentation.

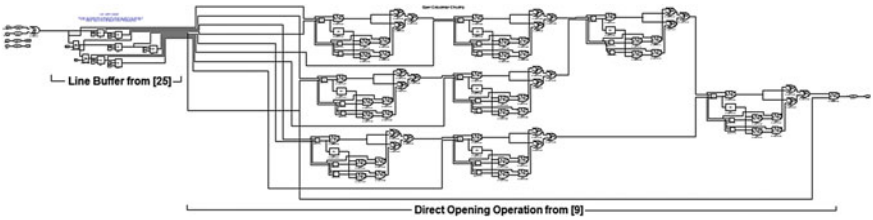

Fig. 4 Gate level circuitry for the XOR and open morphological operation block

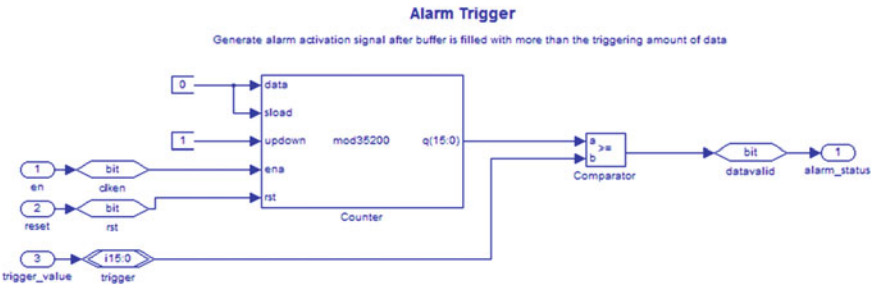

Fig. 5 Gate level circuitry for the alarm triggering block

Figure 4 shows the gate level circuitry for the XOR Open system. The current and references images are fed into the system and then go into the 2 inputs of the XOR gate in the top left corner of the figure. This is why synchronization between the two sets of images is vital, so that the same pixel in each image is being looked at simultaneously and why the comparison takes place before the line buffer circuitry. This latter circuitry has been found to sometimes cause a shift of several pixels, so the best method is to perform the XOR operation first. The output from the XOR gate is then fed into the line buffer, which is set up exactly as in [9, 10] in order to create a 3×3 image segment, which is then fed into the binary opening circuitry of [9]. The output from the opening circuitry is then fed directly into the output port of the block. The gate level circuitry for the Erosion blocks is identical to that discussed in [9] and so no further explanation of this system will be given. The alarm trigger block is essentially a modified counter system; its gate level circuitry is shown in Fig. 5. Here, there is the standard DSP Builder counter block, triggered not off the system clock as with the data validator block, but off the image data that is fed into the system. When the system detects a white pixel (binary '1') in the image, it will trigger the counter and cause the counter value to increase by 1. The counter is set to have a maximum value of 35,200, to account for a case of complete saturation of the count mechanism but this will be extremely unlike unless someone were to shine a bright light source of a laser directly at the camera. The latter would also end up triggering the system before the count process overflows and resets back to zero. The output from the counter block is

then fed into a DSP Builder comparator, if the condition is met then an output becomes a '1' otherwise it is a '0'. Here the triggering value is fed into one input of the comparator and the output from the counter in the other, the comparator is set to "$\geq$" mode. This means that as long as the counter value is less than the triggering value the output stays at '0', but once the counter goes above, it meets the test condition and the output then becomes a '1', thus triggering the alarm. An additional feature, if so desired can be to add a flip flop or an algebraic loop in the form of an OR gate, can be added to hold the output value so the alarm sounds until the system is reset by security personal.

4 Calibration Issues for MSCD

This section of the paper will discuss some of the practical implementation problems that the system encountered during the tests conducted in the laboratory. Each of the three main areas for consideration is covered in the following sections:

4.1 Camera Alignment Problem

One particular problem encountered was the alignment error (λ) of the camera between the two shots or frames of digital video for real world implementation if it is moved slightly. This was present back in Fig. 1, this is seen due to the fact that the taps and dishes in the drier are still slightly visible, caused by the mismatch of their outlines, here $\lambda \approx 1\ mm$. This is usually removed in the noise and post processing stage of the system. If this mismatch becomes too great, then the image is corrupted with too much noise and MSCD will not operate correctly and any useful information is lost and the number of false positive triggers will increase dramatically. This is thus illustrated in Fig. 6, where $\lambda = 5\ mm$, which to the human eye is not much movement, but to the MSCD system, there is too much noise that the post processing cannot compensate for. In the resultant image you can distinctly see two outlines of the corridor, also included in the resultant image is part of the human that would normally trigger the alarm. Therefore, it is vital while conducting such work that the images remain as still and close together as possible, even a slight vibration may cause the system to move too far out of alignment, this may be enough so the alarm could be triggered. This of course could be a good aspect also, meaning that any potential intruder cannot move the camera, to avoid being seen, as this would also trigger the system.

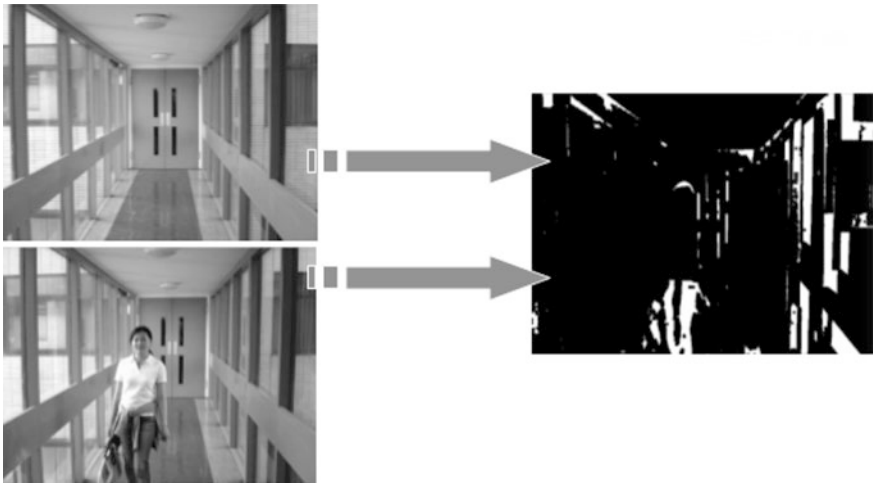

Fig. 6 Effects of mismatched images with an alignment error of $\lambda > 5$ *mm* for the current and reference images after conversion to grayscale

4.2 The Refresh Rate

In the practical system, a counter system would be employed to refresh the reference image in the SDRAM to compensate for environmental factors. These would include events such as lighting conditions and weather, if this system is to be left inside a building even light coming from the windows can be a problem as over time this would cause an overall change in the image, as day becomes night, and if left unaltered, would trigger the alarm. The same is true for weather events, if the system is outdoors, with cloud and changing weather patterns, for changing from a sunny to rainy environment, again if unaltered, would trigger the alarm. The system should be refreshed every 2–5 min to compensate for this, a counter can be used to count the number of clock pulses from the FPGAs onboard clock, when it reaches a certain value, it takes a new image and writes this to the SDRAM and resets itself to start all over again. The counter would have to be a 34 bit counter to reach a value of 9.9 Gig for a refresh time of 5 min using a clock frequency of 33 MHz, likewise, a value of 3.96 Gig would need to be reached for a refresh time of 2 min using the same clock frequency. This can either be coded in DSP Builder in the Simulink environment or in the SOPC processor itself coded from traditional VHDL code. Please note that the overall count value would change depending on the FPGAs onboard clock frequency, this varies from one model of FPGA to the next.

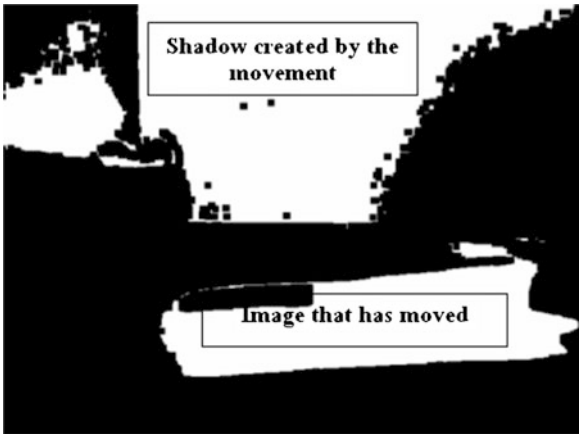

Fig. 7 Effect of shadows and how they can be effectively used

5 Situations and Their Associated Triggering Conditions

An extensive set of simulations were conducted for the triggering levels, to give a rough guide to the user for the differing situations that the system may be placed in. Shadows were found to play a particular role in the system, this is illustrated by Fig. 7 where a close up object being viewed is removed and there is not just the void in the image left by the object, but also by the shadow pattern that has also changed. This will is discussed later in the section, when some of the images used to create this calibration data are discussed in a little more detail. From the analysis conducted, as many as 10,000 pixels in a 640 × 480 are altered minimum when an object is taken and combined with lighting effects, can be increased to greater amounts; the largest was 52,000 pixels which gave a range of 3.26–16.93 %.

The different cases investigated were for both indoors and outdoors, normal, dim and bright lighting conditions that were used for viewing objects both up close and at a distance. These results are shown in Table 2 (averaged results over several tests) and but the triggering level should be tested prior to its deployment as different colored and textured surfaces reflect varying amounts of light. This is again meant to help reduce the number of false positives that are given in practical use. The situation Outdoor, Dim Lighting, Distance was sometimes prone to failure, due to the systems lack of being able to pick out the details in the dark. This will again be pointed out in the resultant images, this was improved however from 100 to 500 (0.03–0.16 % change) pixels to 500–1,000 (0.16–0.33 % change) pixels when the camera used was switched to 'low light' mode. This allowed the image to pick out more information that was able to be used after the image was turned into a binary image along with a slight modification to the binarized parameters, again to allow more data into the binary image that could be used in the MSCD process.

The main result of the system is that the alarm-trigger output changes when there is a corresponding change between the reference image and the current

Table 2 Triggering levels for the various situations

Test situation	Percentage change in image (%)
Indoors, normal light level, close up view, light patterns present	8.46–11.39
Indoors, normal light level, close up view, no light patterns present	3.24–3.26
Indoor, normal light level, distance view	0.16–0.33
Indoor, low light level, close up view	2.28–3.26
Indoor, low light level, distance view	0.16–0.33
Indoor, bright light level, close up view	3.33–3.58
Indoor, bright light level, distance view	1.75–1.95
Outdoors, normal light level, close up view	5.21–5.53
Outdoors, normal light level, distance view	0.33–0.65
Outdoors, low light level, close up view	1.62–2.28
Outdoors, low light level, distance view	0.03–0.16
Outdoors, bright light level, close up	12.12–12.37
Outdoors, bright light level, distance view	0.16–0.33

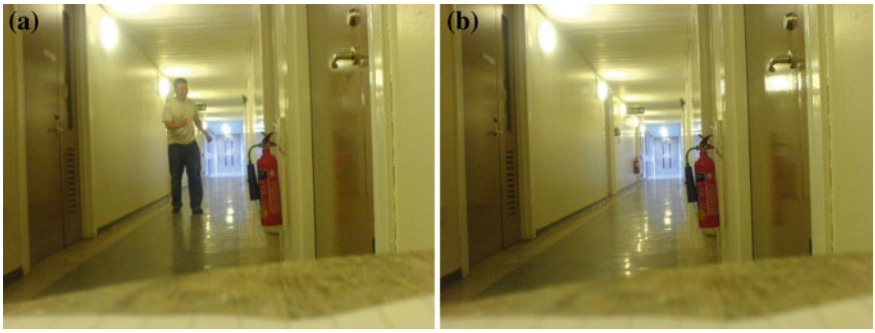

Fig. 8 Simulation reference and current images used in the case for 'Indoor Bright', **a** Current image with person; **b** Reference image of scene

image, which is the case in all of the simulations. The system can be considered to be a success on that front, however, preparing the system for the various situations it will encounter in the real-world, is a different matter. As already discussed, there are errors and environmental factors to take into account. The topic of shadows is an important one, as can be seen in Fig. 8; inside a bright office building, reflections become an important part of the detection process. In this case, as shown in the figure for example, as the person walks down the corridor they not only cause a change due to them simply being there, but also on the reflections in the environment. This is shown in the door to the right of the image as a bright reflective region is blocked via the person. The effect could also be enhanced by the persons clothing if it matches the walls or not, or produces further reflections, this is a topic that could be further investigated in the future.

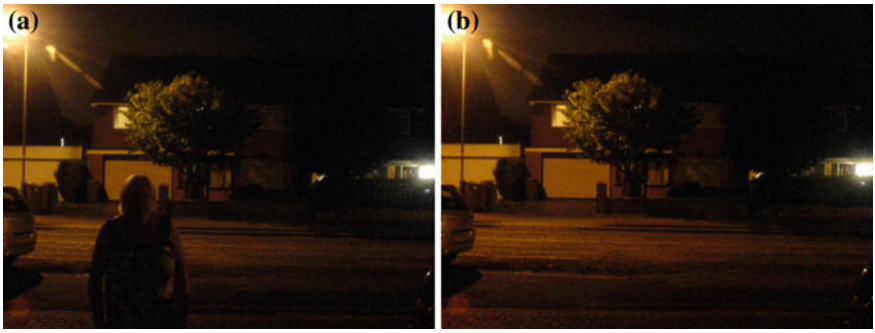

Fig. 9 Simulation reference and current images used in the case for 'Outdoor Low Light', **a** Current image with person; **b** Reference image of scene

Figure 9 shows the effect of using the system outside, without a 'low light' camera capability. The human eye can just make out the outline of a person in the environment, and so it is much more difficult for the system to detect changes like this in a darkened environment, especially when the RGB image is converted to a binary image so information is lost. The 'low light' made on the camera and the binary conversation process modifications help provide more information so that this can be compensated for and so the person can be detected. Another area to consider outside is animal life, cats, dogs, foxes, birds etc, could all potentially wander into the image and the user does not want their security system being triggered by animals and calling the Police. A number of simulations were carried out using a cat and a dog in the environment to see how many pixels the animal occupies in the image and this can be added to the triggering level, to assist in compensating for their possible arrival in the environment. The system would count them, and by themselves would not trigger the system, but the image with a person would still allow the system to be triggered. Figure 10 shows one of the test cases with a dog, the dog occupied approximately 500 pixels in the image with a car occupying approximately 200 pixels. This is 0.06–0.16 % of the image, this value can be either added to compensate for the animals or left as the amounts are so small they can effectively be ignored by the user, the end choice would ultimately fall to the user. Birds or other smaller wildlife would be smaller still and can definitely be considered too small to be able to trigger the system, or cause any difficulties.

The last area for consideration was furniture inside the environment and if the person stands by it, in front of it, behind it or bangs into it (Fig. 11). Standing in front or beside the object in question means that the user can use any of the situations already considered, if they bang into the object if standing in front of the object then this creates a greater mismatch between the images and creates a 700–12,500 (0.22–4.07 %) pixel change as oppose to the 500–1,000 (0.16–0.33 %) pixel change for the standard case. In this situation the normal triggering mechanism will be acceptable as this larger mismatch is still enough to trigger the alarm. The difficulty comes when the user stands behind an object already placed inside

Fig. 10 Simulation reference and current images used in the case for 'Outdoor Animal Calibration', **a** Current image with a dog; **b** Reference image of scene

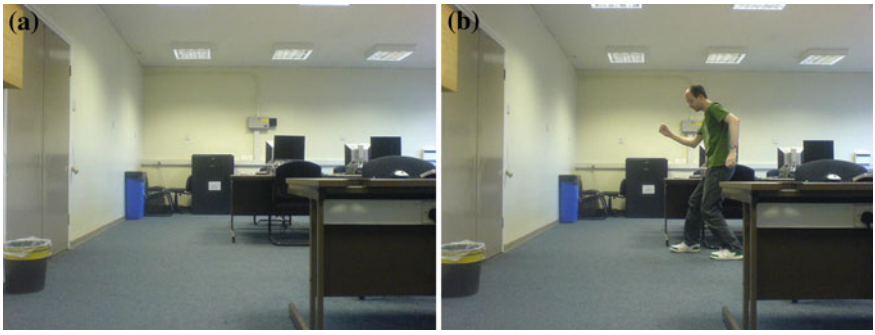

Fig. 11 Simulation reference and current images used in the case for 'Indoor Normal', **a** Current image with person; **b** Reference image of scene

the environment when the reference image was taken, this reduces the amount of pixel change sometimes by as much as a third of its original value. This means that the pixel change falls as low as 150–350 (0.05–0.11 %) at a distance, this becomes a problem as some of this is removed in the noise removal and the triggering threshold for indoor distances is not set to trigger that low. The user would have to make a trade-off of sensitivity for cases such as this to the number of false positives, due to a lower triggering threshold. On the other hand, an intruder would not be able to effectively manipulate or remove anything from the environment with causing a detectable change or coming out of hiding and so the system would eventually be able to detect them, it is just a case of how soon does the user wish to detect them for when they calibrate the system and set up the threshold (Fig. 11).

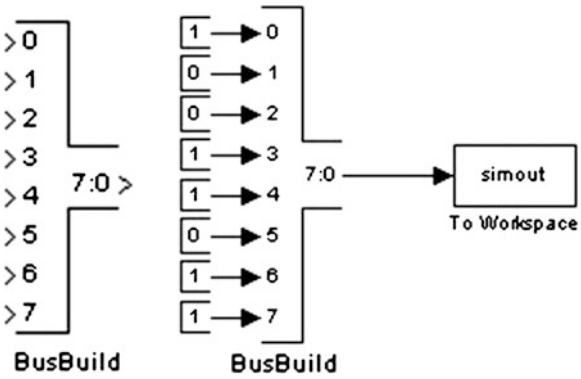

Fig. 12 The busbuild block (*left*) and the application of the block to create a more detailed signal (*right*)

6 Design of the Watermarking Block

The design of the watermarking block, departed from the approach of manipulating the LSB of the pixels as in [13] using mathematics, this is what produced some of the discontinuities in the final images as the mathematics was still subject to the random fluctuations in the LSBs. Instead, the more efficient BusBuild block shown in Fig. 12 (left) was used in DSP Builder that allowed the LSBs to be completely overwritten and could be used afresh. The BusBuild block is used to create a bus of a specified length from a number of single bit inputs, demonstrated in Fig. 12 (right). The length of the output bus is specified in the parameters and by adjusting the number of inputs from 2 to 52. This can allow specific bus configurations to be produced from a variety of different inputs. As an example, the V_{CC} and GND blocks are used to create a bus with the binary output of '10011011' or '155' as a decimal number. This is then connected to the "Simout To Workspace" block on the example system, this produces an output to the MATLAB workspace as the number represented by the binary bus and is a standard Simulink block.

The watermarking block is shown in Fig. 13, here there are two inputs, these namely being the target image (which the watermark will inserted into) and the watermark image itself. The inputs are 8 and 1 bit wide respectively to handle the image data and the watermark. Both of these signals are sent to an Extract Bit block that is used for selecting a specific bit from an input bus which can be of any length up to 52 bits long. The bit to extract is determined in the block parameters and the output will be either '1' or '0' depending on the bits original value in the input bus. Here, each bit of both signals is extracted (this is done to avoid propagation delay issues from the watermark signal already being bit 0) and sent into a product block. This product block has a value tag associated with it, all but bit 0 of the target image is set to '1', this is so that the bits will pass through the product block unaffected and enter the BusBuild. However, bit 0 of the target image on the other hand has its value tag set to '0'; this is so that nothing from that bit can pass through to the BusBuild and it effectively makes that bit 0. When the target is

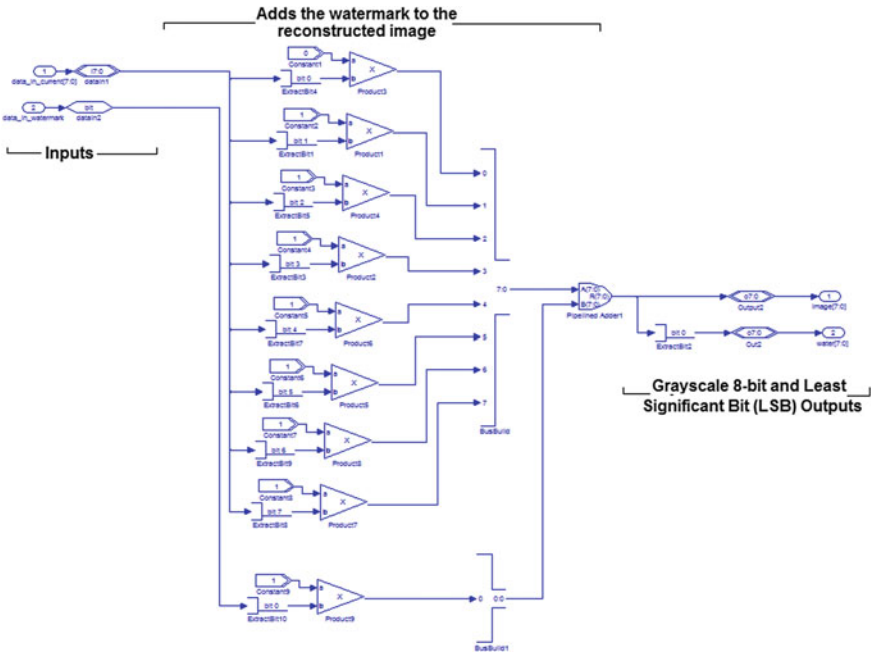

Fig. 13 The DSP Builder watermarking block

reconstructed using the BusBuild, there is no data now at the LSB and so the watermark can simply be added to the LSB by an addition block.

Two signals are seen emerging from the addition block; these are the overall target image and the watermark itself which is visualized with the use of another Extract Bit block. Obviously in the final system there is no need for the latter as this is used to show that the process is a success, the results are shown in Sect. 7.

7 Inclusion of the Watermark into the MSCD System

Figure 14 shows the new Behavioral Level of Abstraction, whilst Figs. 15 and 16 show the new RTL and Gate Level respectively. Figure 14 shows how an extra two inputs have been added to the system, these are the watermark image and a copy of the current image that will be watermarked as it is this that will trigger the system. The current image just mentioned will be in grayscale (along with a binary version of it for triggering) unlike the previous version in Sect. 3 so that the watermark can be easily embedded into, whilst also having greater information contained in it that could be used to identify an intruder. As a result, the outputs which were previously just used to show "check" images for various stages of the process have now been made permanent in order to output the watermarked image,

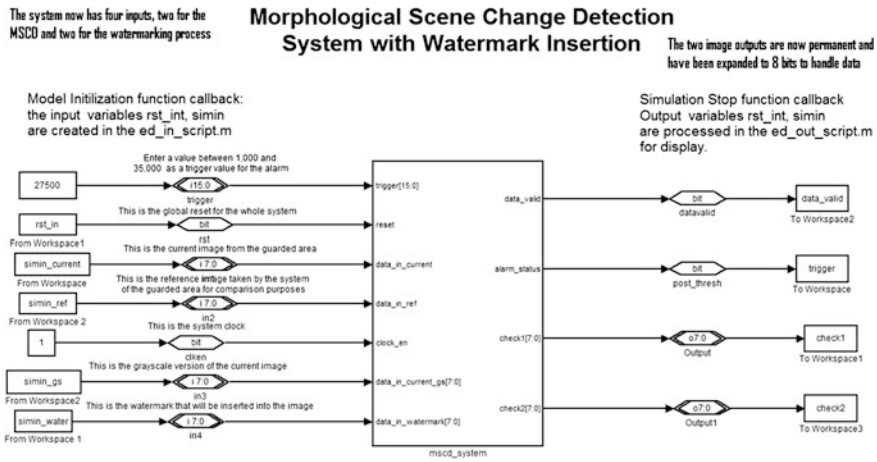

Fig. 14 The behavioral level of the morphological scene change detector with watermarking (MSCD-W)

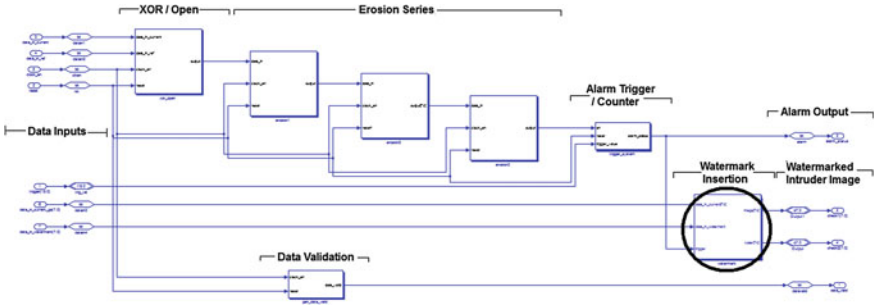

Fig. 15 RTL of the MSCD-W

only a single eight bit port is needed, the other could later be used to output time and date information to say when the image was taken.

The RTL is shown in Fig. 15; the watermark block is highlighted to make it easily identifiable. The block is added at the end of the process after the XOR operation, mathematical morphology strings and the trigger counter. This is as the block will only be required if the system and triggered and so there is no point continuously watermarking the current input image for no reason. As such, the alarm trigger signal is also used to trigger the watermarking block, so that if an intruder is detected and the alarm is triggered, then the block takes a watermark of the current image and outputs it for inspection.

The augmented watermarking block after it has been inserted into the MSCD system is shown in Fig. 16, the system is basically the same as presented in Fig. 13 apart from now there are 3 inputs (one being the alarm trigger signal) and product

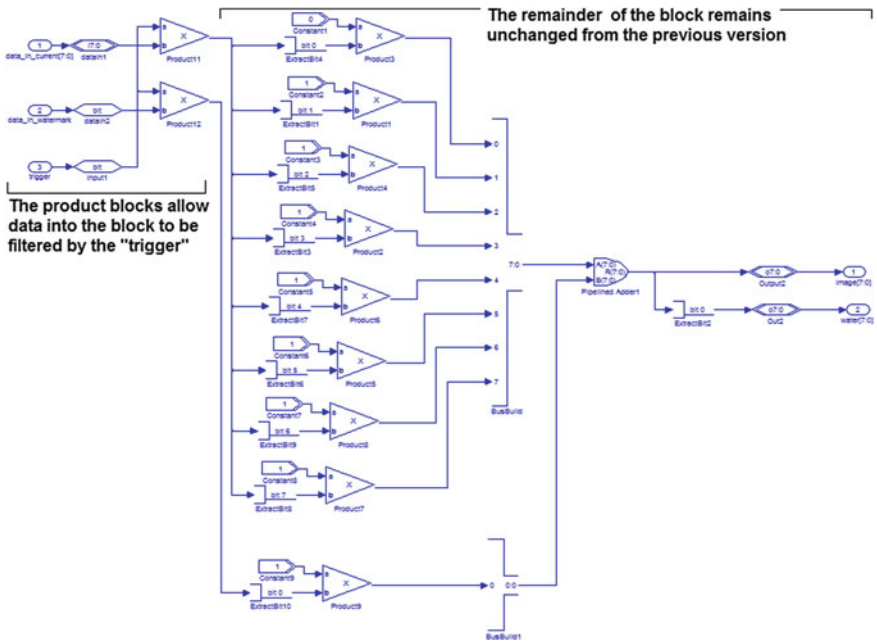

Fig. 16 Gate level of the watermarking block after insertion into the MSCD system

blocks have been added to where the signals enter the block. These product blocks with one input connected to the watermark and current grayscale images, the other input to each block is connected to the trigger. If the trigger is active, the data is multiplied by '1' and allowed to pass into the block where it is processed as before. If the trigger is not active, the data is multiplied by '0' and nothing proceeds into the block and no watermark is produced. It is a simple but effective triggering mechanism that determines if the block is active or not.

Figure 17 shows the results from the first set of test data that were conducted using the watermarking block by itself. These show the original image (a) and its LSB level (b) which shows the random "static" nature of the LSB. It clearly shows that the image has not been watermarked in any way. In Fig. 17c and d, the same image is shown but it has now been watermarked. It is apparent that the watermark has had no visible effect on the image as a whole as Figures (a) and (c) are indistinguishable. The change occurs when you look at Figures (b) and (d), the "static" nature of the image that was present earlier has now been replaced by a watermark made from the Coventry University logo. As no visible signs of alteration are present, the average person would not know the watermark was there and so detection of tampering would be obvious.

The latter is now the topic of the next set of images shown in Fig. 18. The images from Figs. 17 and 18 are also identical except that the USB flash drive seen on the right-hand side of the image in Fig. 17 has now been removed. This was

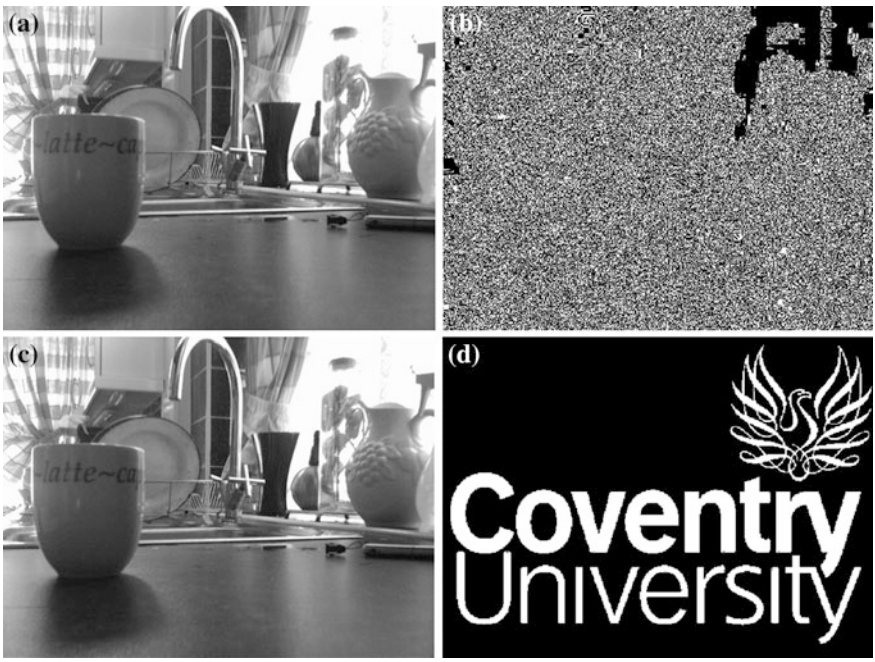

Fig. 17 Output images of the watermarking block; **a** Original grayscale image before watermarking, **b** Original LSB before watermarking, **c** Watermarked grayscale image, and **d** Watermarked LSB

done by copying a section from an un-watermarked image (to produce Fig. 18b) and a watermarked image (to produce Fig. 18c) and pasting it into the watermarked image so it appears as though the cup is sitting on the work surface alone. If you look at the watermark of the image in Fig. 18b, as the section of image pasted over the flash-drive from an un-watermarked image is shown, the "static" nature makes it very obvious to the observer that the image has been tampered with. The same process is visible, if not as obvious, in the watermark of Fig. 18c.

8 Leak Detection Configurations

8.1 Experimental Setup

The experimental set-up for this system is shown in Fig. 19; this shows a simple pipe configuration where corner joints are arranged in such a format that the substance enters at one side, is forced upwards, then travels along the pipe, is forced downwards and then exits the system. The pipes were made of high quality plastic and capable of withstanding four BAR in pressure at 98 C, the corner units

Fig. 18 Evidence of image tampering via the watermark; **a** Watermarked grayscale image, and **b** Watermarked LSB showing signs of tampering with an un-watermarked image, and **c** Watermarked LSB showing signs of tampering with another watermarked image

were pressure sealed and the pipe layout was mounted via brackets onto a piece of medium density fiberboard (MDF). The dotted pipe section would be removed for one test and replaced with a damaged section in order to simulate the situation where the pipe has been damaged by an impact. The other situation will involve not correctly sealing one of the corner joints in order to simulate that a weld has failed or that the joint has degraded over time. During the test where the substance was a liquid, the piping would be connected via flexible plastic tubing to a tap and the output pipe to a drain, the entire mount was positioned in a location as to allow the water that escaped to additionally flow into the drain. For the test where the substance was a gas, steam was used and produced via a steam machine at 3BAR pressure which was pumped into the mount with the output leading an area away from people. A secondary steam test was also conducted where low pressure steam from a kettle was forced into the system and the output closed up with a pressure vice to cause the steam to build up in the pipes and escape, this was carried out with steam from a kettle to reduce the risk of the piping exploding and the excess steam would simply be diverted back to the kettle. Images were taken from a tripod mounted camera located 2 m away from the pipe configurations after the mount has been secured so that it was unable to move, reference images were taken before the substance allowed to enter the system and a further series of

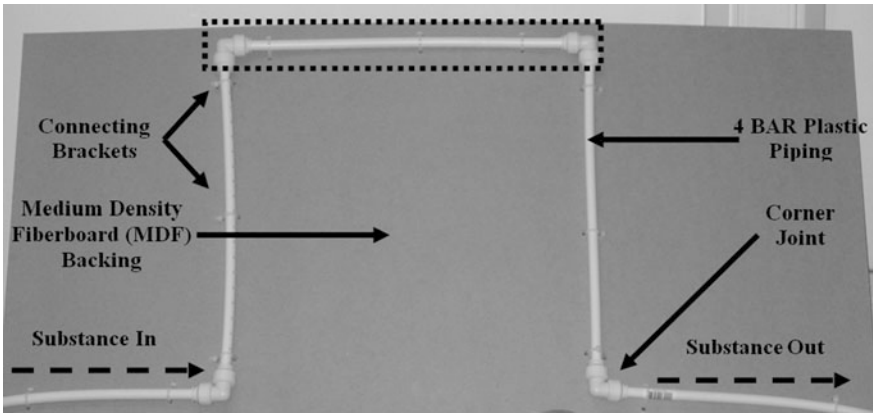

Fig. 19 Experimental setup used to produce the leaks and test data to be analyzed

images to present the current image in the scene change detector were taken once the flow had begun. An additional test using this data was be to compare two of the reference and two of the current images together, this is in order to provide proof that the system will not trigger whilst there is no leak and that the system can additionally detect a leak in progress.

8.2 Morphological Scene Change Detection with Feature Extraction for Leaks (MSCD-FEL)

This system was an augmented version of the morphological scene change detector (MSCD) discussed previously [1] and combined with an adapted version of the Charpy Stress–Strain analysis system [21]. The MSCD-FEL system could be considered similar to a combination of the acoustic and infrared radiometric testing systems mentioned previously. This is that the system would visually identify the leak in a similar manner to the way the acoustic system would detect sound and would additionally be analyzed via a grayscale and binary method for the triggering mechanism, again in a similar manner to the infrared radiometric testing via the search protocols or "fingerprint". The behavioral level is shown in Fig. 20; the inputs to the system are the system clock (clk), the global reset for the system and the current and reference images. Unlike the previous systems, the trigger value is not entered by the user and is built into the trigger block from the MSCD section; this will now output a numerical signal corresponding to the situation analysis result. The RTL schematic is shown in Fig. 21, the black dashed line represents were the two previously developed systems are connected together. To the left of the dashed line is the modified version of the charpy system from [21] whilst on the right is the MSCD system with the new triggering mechanism.

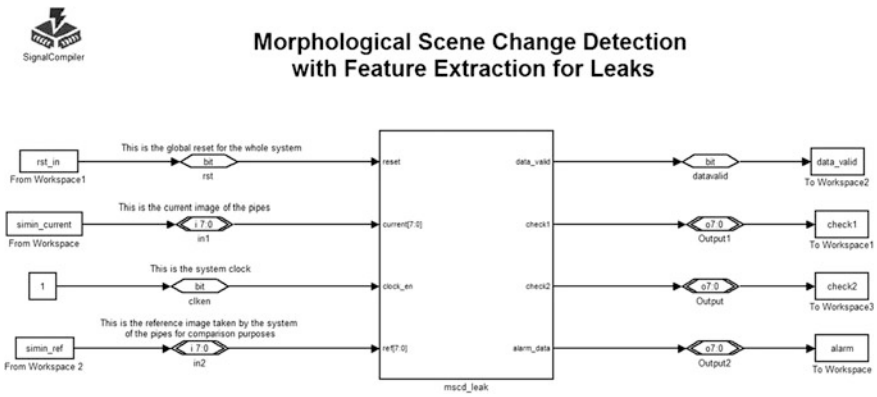

Fig. 20 The behavioral level schematic for the MSCD-FEL system

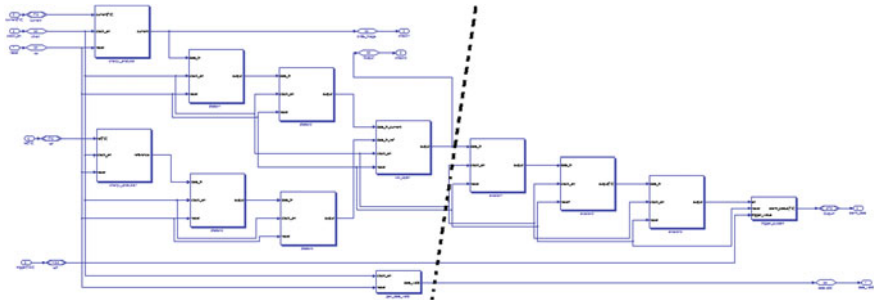

Fig. 21 The RTL schematic for the MSCD-FEL system

For the charpy feature extraction process, the filter mechanism will not let any eight-bit grayscale value under '180' into the system and then after the mean of each image segment has been calculated, anything within the range of '100' and '130' was output via an AND gate in order to produce a binary signal for the MSCD. The new trigger on the MSCD had a series of comparators to detect the count value and if the value falls within the boundaries discussed in the results section, then the corresponding numerical value for that situation was output as the alarm data. Any further information on how the two systems originally worked along with their gate level schematics can be found in their respective publications.

8.3 Resultant Images and Analysis

The three main cases considered in this publication are shown in Fig. 22; these show the leak from the damaged section of pipe for a liquid, a leaking corner joint for a liquid and steam from a corner joint. In each situation, the liquid or gas

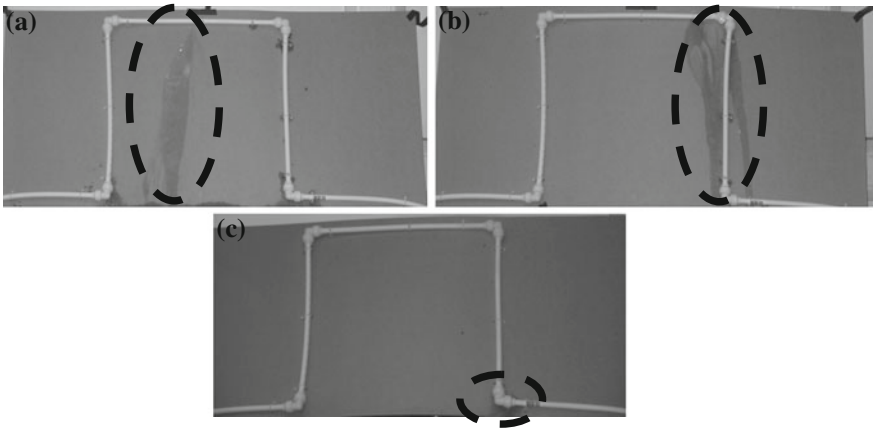

Fig. 22 The experimental situations that were investigated, **a** A leak in the centre of a pipe with a liquid content; **b** A leak at a corner connecting joint with a liquid content; **c** A leak at a corner connecting joint with a gas content

causes a discoloration in the environment; it is this that is searched for in the feature extraction situation. Additionally, the force of the escaping liquid in Fig. 22b causes the pipe to move which shows up in the MSCD section of the system. All the figures situations in Fig. 22 are the current image with a reference image being similar to that shown in Fig. 19 for the comparison during the XOR aspect of the MSCD. In these experiments, no compensation for lighting levels was discussed as in chemical plants etc., the work areas are fairly well illuminated and so this should not be a major contributing factor to the system and will not be discussed further. Figure 23 shows the results from the feature extraction process on the left side of Fig. 21, the jet of water escaping the pipe can be clearly seen as it matches the situation shown in Fig. 22a and that the majority of the leak has been successfully detected.

The reference scene in Fig. 23b does not show the escaping liquid and is thus makes the ideal image for the MSCD step, however, to improve the performance, these images are enhanced by mathematical morphology and the results are shown in Fig. 24a and b respectively for the current and reference images.

In Figure 24b, a clear outline of the original piping is visible and so this enhancement has clearly helped and is shown to be effectively removed in Fig. 24c due to the piping appearing in Fig. 24a, thus proving that the MSCD is performing its desired function effectively. Several other key features have been removed from the current image before the counting is made and this will improve the accuracy of the system. Obviously the liquid tests provide a clearer picture due to them occupying more pixels in the resultant images. The gas test is shown in Fig. 22(c) and causes visible condensation around the leaky joint and over time a haze is built up in front of the camera. This will in turn additionally add a minimal effect to the result but provides an additional parameter that can be searched for and allows

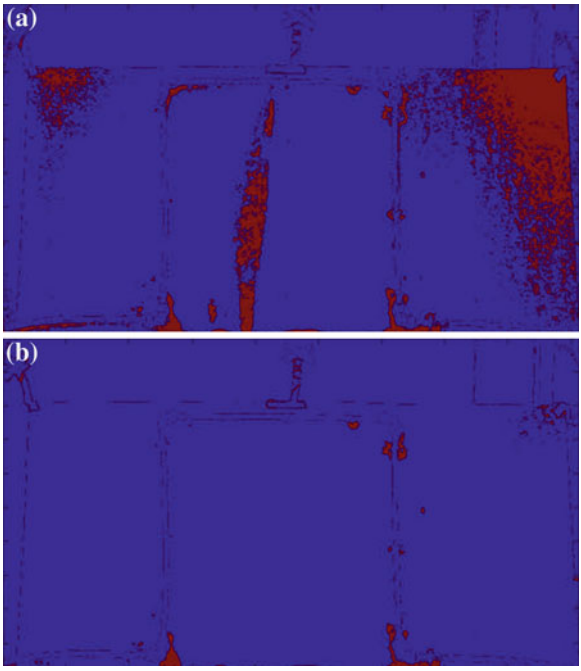

Fig. 23 Resultant images from the feature extraction classifier for a single case, **a** The classifier current image output; **b** The classifier reference image output

more pixels to be involved in the counting process to help separate the data from noise. The parameters for the trigger in the MSCD are now discussed along with their corresponding numerical output values and the percentages of the total image for easier interchanging of the image size:

- **Situation 1:** No or minimal change = Trigger output of '0'.
- **Situation 2:** Small pixel area detected (0.14–0.33 % of image pixels) meaning possible gaseous leak or leak already in progress = Trigger output of '1'.
- **Situation 3:** Large pixel area detected (11–25 % of image pixels) meaning a liquid leak has just happened = Trigger output of '2'.
- **Situation 4:** Extremely large pixel area detected (>25 % of image pixels) meaning massive leak or error in the system = Trigger output of '3'.

In situation 2, this was tested when two images of a leak that were already underway were taken and as the shadows and environmental changes cause by the leak had already taken effect in the environment, this meant that the only change was the movement of the liquid itself and so this was enough to cause the system to be triggered after the analysis. Many test situations and images were takes and so due to space restrictions not all of these can be shown in this paper, but enough evidence has been provided to show the system functions correctly.

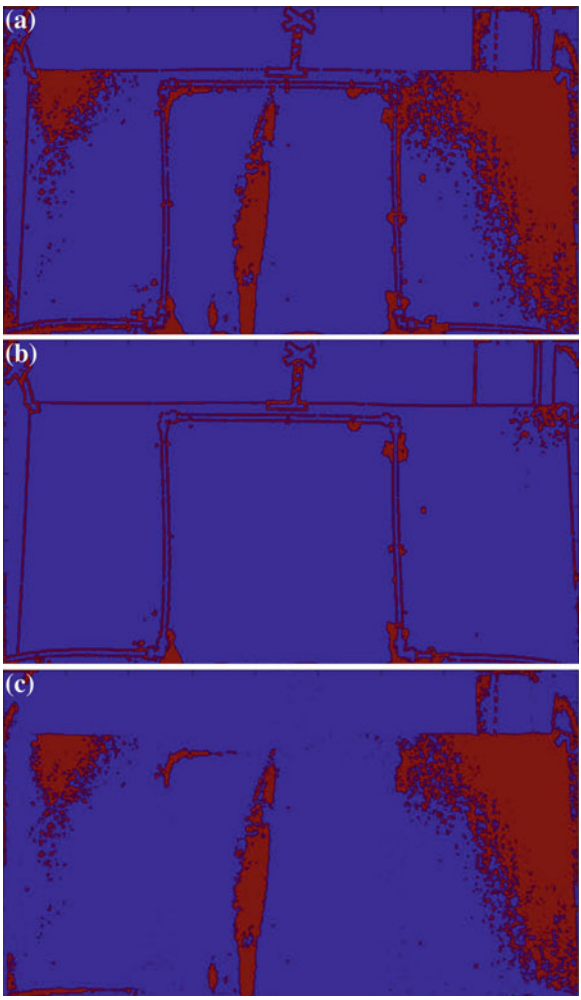

Fig. 24 Resultant images from the post processing stage for a single test case and the scene change detector, **a** The post processed current image; **b** The post processed reference image; **c** The final result from the scene change detector used for the counting trigger

9 Conclusions

This chapter has presented the details of how the actual scene change detection mechanism works and was created for use with Simulink/DSP Builder to make a system that can always detect changes in the two images. The research has also shown that it is possible to obtain good results without having to use soft morphological operations as some of the common literature says. There is the fact that because the XOR gate was used, some of the old background image does come through but the series of environmental tests helped to compensate for this. The tests were performed using different sets of images including indoors, outdoors, close-up, distance shots etc. and also included shadows, animal interference,

augmenting the system with 'low light' abilities and for intruder hiding to give the user a full set of conditions to assist them in calibrating and choosing their threshold level. How the system collects its reference image and possible implementation of the refresh circuitry were discussed along with how the overall system can be combined with an SOPC camera for future developments.

Methodologies for including digital watermarks was also discussed to allow for tamper proof images that have the greater potential as evidence and for in criminal investigations. The watermarks have been successfully embedded into the image using the DSP Builder design tool for use in embedded systems, bringing the possibility of a small portable security system closer to reality. It is a simple process to change the watermark by simply taking the binary version of a different image and sending it into the system, making it very robust. Finally, an adaptation of the architecture was developed that allowed for the detection of leaks, which provides a large amount of functionality for detecting if gases or liquids escaping from pipes. With a set of parameters for the extraction of features that can easily be changed by modifying the value tags in DSP Builder, the system can be used in differing situations and the user can input the optimum parameters after an analysis of the scene where the system is to be step up. Overall this is a very useful algorithm and can be adapted to many different circumstances as shown here.

Acknowledgments Andrew Tickle would also like to thank members of his family, Laura and Frank Tickle, and his friends and co-workers, James R. Buckle, Paul K. Harvey and Si "Ella" Li for their cooperation in the participation of the security field tests and to the EPSRC (Engineering and Physical Science Research Council) for funding the research work at the time. They would also like to thank Professors Jeremy Smith and Jim Lucas for their support, guidance and advice during the course of conducting this research and to Dr Alex Mason for the chance to contribute to this book.

References

1. A.J. Tickle, J.S. Smith, Q.H. Wu, Feasibility of a portable morphological scene change detection security system for field programmable gate arrays, vol 69780, in *Proceeding.of SPIE 6978*: *Visual Information Processing XVII*, Orlando, Florida, USA, March 2008, 10p
2. A J Tickle, P K Harvey and J S Smith "Applications of a Morphological Scene Change Detector (MSCD) for Visual Leak and Failure Identification in Process and Chemical Engineering" *Proc. SPIE 7833*: *Unmanned/Unattended Sensors and Sensor Networks*, Toulouse, France, September 2010 (8 pp)
3. A.J. Tickle, D. Kamfwa, Integration of a digital watermarking system into a Morphological Scene Change Detector (MSCD) for tamper prevention and detection, in *Proceeding SPIE 8540*: *Unmanned/Unattended Sensors and Sensor Networks*, Edinburgh, Scotland, Sept 2012, 8p
4. E. Stringa, *Morphological Scene Change Detection Notes* (Institute for Systems, Informatics, and Safety, 2005), pp. 1–12
5. C.S. Regazzoni, G. Fabri, G. Vernazza, *Advanced Video-based Surveillance Systems* (Kluwer Academic Publisher, Norwell, 1999), pp 1–100
6. E. Stringa, C.S Regazzoni, Real time video-shot detection for scene surveillance applications. IEEE Trans. Image Proces. **9**, 69–79 (2000)

7. J.D. Courtney, Automatic video indexing via object motion analysis. Pattern Recognit. **30**, 607–625 (1997)
8. M. Bogaert, N. Chleq, P. Cornez, C.S. Regazzoni, A. Teschioni, M Thonnat, The PASSWORD Project, in *Proceeding of the IEEE International Conference on Image Processing*, (1996), pp. 675–678
9. A.J. Tickle, J.S. Smith, Q.H. Wu, Development of morphological operators for field programmable gate arrays. J Conf Series **76**, 012028 (2007)
10. A.J. Tickle, J.S. Smith, Q.H. Wu, Feasibility of a multifunctional morphological system for use on field programmable gate arrays. J Conf Ser **76**, 012055 (2007)
11. A.K. Jain, *Fundamentals of Digital Image Processing* (Prentice-Hall, Englewood Cliffs, 1989)
12. K. Skifstadt, R Jain, Illumination independent change detection for real world sequences. Comput. Vis. Graph. Image Proces. **46,** 395–418 (1989)
13. A.J. Tickle, J. Sun, L. Gan, J.S. Smith, Feasibility of an encryption and decryption system for messages and images using a Field Programmable Gate Array (FPGA) as a portable steganography platform. Proc SPIE **7100**, 71002N (2008)
14. C.T. Hsu, J.L. Wu, Hidden digital watermarks in images. IEEE Trans Image Proces. **8**(1), 58–68 (1999)
15. D. Kundur, D. Hatzinakos, Digital watermarking for telltale tamper proofing and authentication. Proc. IEEE **87**(7), 1167–1180 (1999)
16. C.T. Li, *Digital Watermarking for Multimedia Security Management* (University of Warwick, Coventry, 2005), pp. 3–11
17. S.P. Mohanty, N. Ranganathan, R.K. Namballa, VLSI Implementation of Visible Watermarking for Secure Digital Still Camera Design. Proceedings of 17th IEEE International Conference on VLSI Design, 2004
18. A. Khan, A.M. Mirza, Genetic perceptual shaping utilising cover image and conceivable attack information during watermark embedding. Inf. Fus. **8**(4), 354–365 (2007)
19. T. Wada, F. Huang, Advances in Image and Video Technology. pp 340–341, 2009
20. A.J. Tickle, Y. Meng, J.S. Smith, Simulation of a dead reckoning embedded system security patrol robot for deployment inside structures and buildings. Proc. SPIE **7833**, 2010
21. A.J. Tickle, A.R. Camargo, J.S. Smith, Visual analysis of ductility/brittleness of welding fracture points on charpy test specimens using graphical blocks on field programmable gate arrays. Proc. SPIE **7100**, 71002M (2008)
22. J. Serra, *Image Analysis and Mathematical Morphology: Theoretical Advances* vol 2 (Academic Press, London, 1988)
23. B. Chanda, Application of Binary Mathematical Morphology to Separate Overlapped Objects. Pattern Recogn. Lett. **13**(9), 639–645 (1999)
24. F. Wu, Synthesised Processors Running on FPGA Architectures, University of Liverpool, EEE Ph.D. Thesis, 2008
25. Altera Corporation, Edge detection using SOPC Builder and DSP Builder tool flow. www.altera.com, pp. 1–43, 2005
26. Altera Corporation, "Using SOPC Builder and DSP Builder Tool Flow" www.altera.com, pp. 1–45, 2005

Chapter 16
Design of AC–DC Converter for Magnetic Energy Harvesting Device

K. Tashiro, H. Wakiwaka, Y. Uchiyama and G. Hattori

Abstract We propose the design of AC–DC converter for a magnetic energy harvesting device. When this device is used as an energy source for wireless sensor applications, the DC output voltage should be larger than 1.5 V. First of all, we investigate the efficiency of conventional circuit whose has power conditioning module varied input power. It is found that efficiency of this module is at most about thirty percent. In the next place, we investigate the basic properties of an AC–DC converter with a Cockcroft-Walton circuit. Experimental results reveal that the optimum conditions are related with the number of steps, input voltage, input resistance, and dummy load. From a magnetic field of 675 nT at 60 Hz, the new magnetic energy harvesting device used Cockcroft-Walton circuit can provide a DC output voltage of 1.5 V. Compared with the previous device installed conventional power conditioning module we developed, the required magnetic field is as low as 1/400 in amplitude. In contrast, the measured efficiency of the device is better than 80 % when the magnetic field is larger than 20 μT.

Keywords AC–DC converter · Magnetic · Energy harvesting

1 Introduction

Energy harvesting is a key technology to construct a wireless sensor network without a battery, which uses environmental energy as a power source [1]. After the miserable earthquake in 2011, the Japanese government requested the development of an energy harvesting device with high frequency electromagnetic field.

K. Tashiro (✉) · H. Wakiwaka · Y. Uchiyama · G. Hattori
Department of Electrical and Electronic Engineering, Shinshu University, Wakasato 4-17-1, Nagano, Japan
e-mail: tashiro@shinshu-u.ac.jp

A. Mason et al. (eds.), *Sensing Technology: Current Status and Future Trends I*, Smart Sensors, Measurement and Instrumentation 7, DOI: 10.1007/978-3-319-02318-2_16,

The required output voltage is 1.5 V and the capacity to harvest more than 100 μW of energy [2].

We have been proposed magnetic energy harvesting from our environmental magnetic field at power frequency [3]. Because power-lines are necessary for our modern life, we are required to coexist with undesirable magnetic power-line noise. ICNIRP2010 provides a guideline that an acceptable level for human health in a public space is 0.2 mT in the power-line frequency range of between 25 and 400 Hz [4].

In previous report [5], we considered an AC–DC module for a magnetic energy harvesting device. It consisted of a magnetic energy harvesting module, typical full-wave rectifier circuit and DC–DC converter. The magnetic energy harvesting module we developed can provide 100 mW from a magnetic field of 90 μT at 60 Hz. However, total efficiency of this device was less than 1 %. From the experiment, we pointed out the importance of impedance matching in the device.

The purpose of this study is to improve the efficiency of this device. In this paper, we adopt Cockcroft-Walton circuit (CW circuit) for the AC–DC converter. The building block of the CW circuit consists of two diodes and two capacitors, and can provide twice value of DC output voltage. In an ideal case, the number of building block can make the multiple the value of the DC output voltage. Although a CW circuit is considered to use for energy harvesting device with high frequency electromagnetic field [6], it is known that the optimum conditions depend on the numerous parameters in the device.

In this chapter, we focus on CW circuits for use in a magnetic energy harvesting device. First of all, we verified experimentally the efficiency of conventional power conditioning module, with each two kinds of generator. In the next place, we investigate the basic properties of this circuit as a parameter of the number of steps, as parameters of input voltage, input resistance and dummy load. Incorporating our magnetic energy harvesting module and CW circuit, we examined the magnetic field required to produce a DC output voltage of 1.5 V. Compared with previous device we developed, we also considered the total efficiency through experimental results.

2 Experimental Setup

2.1 Energy Harvesting Module

Figure 1 shows the equivalent circuit of the energy harvesting module. Here, L (H) is coil inductance, R (Ω) is coil resistance, C (F) is resonance capacitor and R_L (Ω) is dummy load. From Faraday's law of induction and Thevenin's theorem, the amplitude of the voltage source V_{in} (V) can be expressed by:

$$V_{in} = 2\pi^2 fna^2 \times B(\mathrm{V}) \tag{1}$$

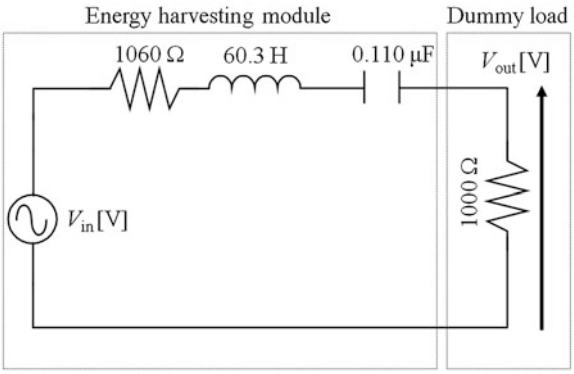

Fig. 1 Equivalent circuit of the energy harvesting module

where f (Hz) is the frequency of magnetic field, n (turn) is the number of coil windings, a (m) is mean radius of coil and B (T) is the mean flux density crossed with the mean cross section of the coil. From the maximum power transfer theorem, we chose a load R_L (Ω) to be the same as the coil resistance and used the voltage drop as the output voltage V_{out} (V) for calculating the harvesting energy W (W) with:

$$W = V_{out}^2/R_L = V_{in}^2/(4R)\,(\mathrm{W}) \tag{2}$$

Substituting (2) gives

$$W = \left(\pi^4 f^2 n^2 a^4/R\right) \times B^2(\mathrm{W}) \tag{3}$$

This means that the harvesting energy is proportional to the square of the magnetic flux density. Table 1 shows the specifications of the energy harvesting module. It should be noted that the estimation value with (3) was in good agreement with the measured value. For a magnetic field of 90 μT at 60 Hz, the estimated energy becomes 100 mW.

Since an ultra-low power wireless sensor node can be activated with 1 mW energy, it is possible to construct a wireless sensor network without a battery. In recent years, wireless energy transmitter kit has sold on the open market for energy

Table 1 Specifications of the energy harvesting module

Property	Symbol	Value
Mean radius (mm)	a	0.105
Number of turn	n	18395
Inductance of coil (H)	L	60.3
Resistance of coil (Ω)	R	1060
Resonant capacitor (μF)	C	0.110
Dummy load (Ω)	R_L	1000
Frequency (Hz)	f	60
Estimated voltage (V), from Eq.(1)	V_{in}	$B \times 2.40 \times 10^5$
Estimated energy (W), from Eq.(3)	W	$B^2 \times 1.31 \times 10^{-7}$

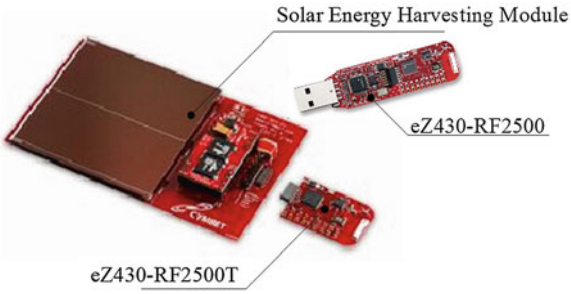

Fig. 2 The eZ430-RF2500 wireless application produced by texas instruments

harvesting technology. Therefore the authors demonstrated driving wireless transmission used wireless kit (eZ430-RF2500, Texas Instruments [as shown in Fig. 2]) [3]. This tool is constructed by Access Point and End Device. The condition of energy transmission is able to shown on PC moniter, shown in Fig. 3, and we can look see amount of energy. This result is confirmed the 3.3 V of voltage the ends of Access Point from 7 μT at 60 Hz.

2.2 Conventional Circuit

Figure 4 shows comparison previous with new energy harvesting module expressed by block diagram. In order to compare conventional circuit to Cockcroft-Walton circuit, we investigated efficiency from ratio of output power versus input power with eZ430-RF2500. eZ430-RF2500, shown in Fig. 2, is available only rectification circuit and has external input terminal for exclusive use. It is able to connect optional input source for this circuit. In order to explore basic specification, input source was used two kinds source.

2.2.1 Efficiency of Power Conditioning Module

Figure 5 shows the building block of a circuit combined conventional circuit and oscillator whose output resistance is 50 Ω. We also prepared several dummy loads

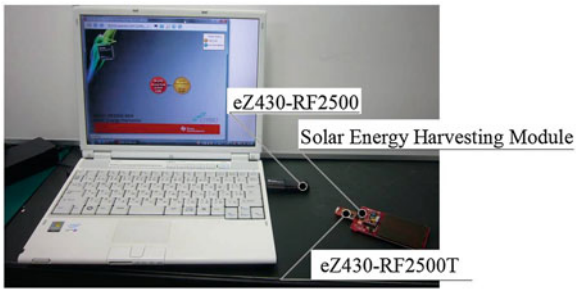

Fig. 3 Demonstration setup with wirelss power transmission and sensor moniter

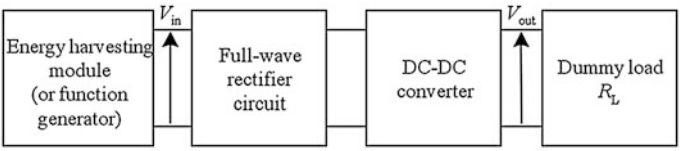

Fig. 4 Block diagram of energy harvesting device

whose resistance were from 100 Ω and 1 kΩ and installed a dummy load, resistance of 10 Ω, between the function generator and power conditioning module. We examine the dependency of the input resistance on the output voltage and efficiency. The efficiency of the device was calculated by (4).

$$\eta = \frac{W_{\text{out}}}{W_{\text{in}}} \times 100(\%) \tag{4}$$

where W_{in} and W_{out} represent the input and output energy, respectively. Both of them were calculated from the voltage drop in the dummy loads. In order to evaluate the efficiency, we used (3) to calculate the input energy. And in order to estimate efficiency as a parameter of W_{in}, the input power was from 1 to 10 mW at 60 Hz.

2.2.2 Efficiency of Energy Harvesting Module

Figure 6 shows the building block diagram of connecting energy harvesting module at input part. It consists of energy harvesting module which coil has 28 cm outer diameter and power conditioning module. Table 1 shows specific of energy harvesting module. Output terminal with power conditioning module installed 1 kΩ. Because the maximum power transfer theorem is considered, dummy load

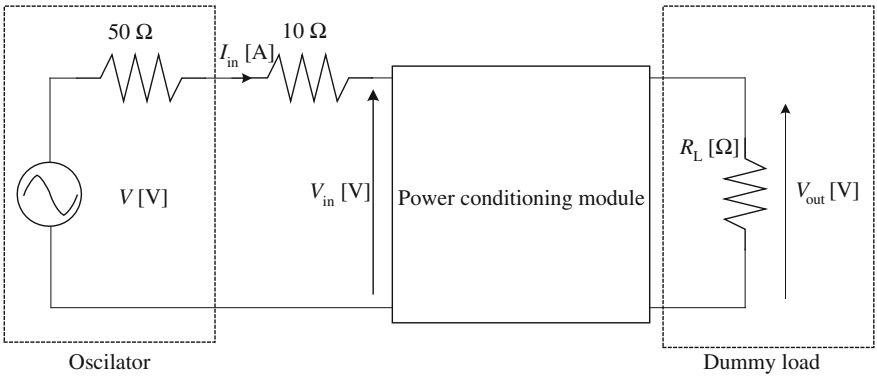

Fig. 5 Block diagram of connecting oscillator at input part

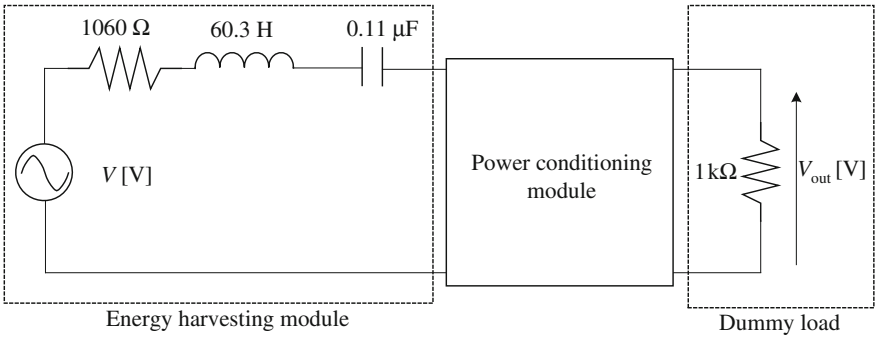

Fig. 6 Block diagram of connecting energy harvesting module at input part

that output terminal at power conditioning module is installed is near the resistance of energy harvesting module.

In order to evaluate the energy harvesting device, we used a Simple-Cubic-3 coil system (SC3) [7, 8] for generating a uniform magnetic field. SC3 was composed of three square coils connected in series, and the distance was the half side length of the coil. The side length was 2 m, and the number of windings was 24:12:24. In an area of radius of 50 cm from the center, SC3 can generate a uniform magnetic field within ± 1 % deviation [8].

Since the diameter of the modules was 28 cm, we used this area to simulate power line magnetic noise. Figure 7 shows the schematic design of the experimental setup. To evaluate amplitude dependence, the harvested energy was calculated from the measured output voltage. The frequency was 60 Hz, and the amplitude range was from 0.353 to 90.2 μT. The efficiency of the device was calculated using (4). In case of this calculation of efficiency, W_{out} is output energy from the voltage drop in the dummy loads. But W_{in} defines only the energy that the energy harvesting module could possibly harvest.

2.3 Cockcroft-Walton Circuit

Figure 8 shows the building block of a CW circuit we developed. It consists of low-voltage-driving Schottky diodes (1N5818, ST Microelectronics corp.) and capacitors. Based on the results of circuit simulation, we chose capacitors of 47 μF because of low ripple voltage and fast step time. In this paper, we defined the number of steps s, which corresponds to two times the number of connected building blocks in series and a new energy harvesting module. We prepared CW circuits whose numbers of steps are 2, 4, 6, 8, 10. Figure 9 shows the block diagram of the energy harvesting device.

First of all, we investigate the basic properties of these circuits with a function generator (WF1947, NF corp.) whose output resistance is 50 Ω. The input voltage

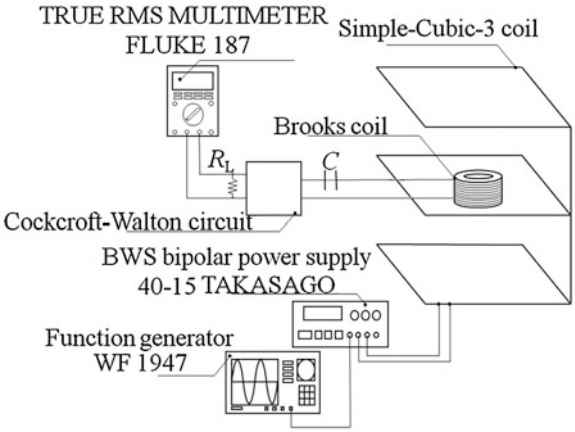

Fig. 7 Experimental set up

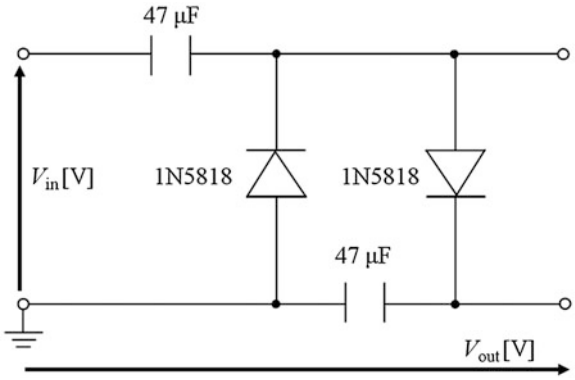

Fig. 8 Cockcroft-walton circuit. (s = 2)

of 60 Hz was provided from 10 $mV_{p\text{-}p}$ to 5 $V_{p\text{-}p}$. We also prepared several dummy loads whose resistances were from 100 Ω to 1 MΩ. Because the magnetic energy harvesting module we developed had the resistance of 1 kΩ, we also installed a dummy load between the function generator and the CW circuits to examine the dependency of the input resistance on the output voltage and efficiency. The efficiency of the device was calculated by the following (4) and measured output energy in the same way as Sect. 2.2.2.

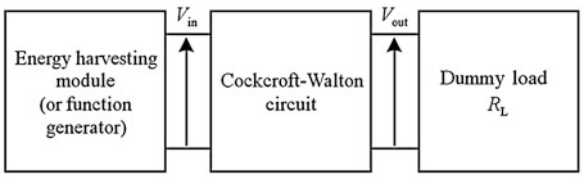

Fig. 9 Block diagram of a new energy harvesting module

3 Results

3.1 Conventional Circuit

3.1.1 Effecency of Power Conditioning Module

Figure 10 shows the efficiency of power conditioning module for input power. As shown in Fig. 10, maximum efficiency is 31.7 % when installed dummy load is 10 kΩ and input power is 3 mW. This indicates that output power of energy harvesting module is approximately three out of ten versus input power at a maximum. In comparison to each result, there is tend to closely equal to the maximum power transfer theorem when input power and dummy load are varied. Therefore it was found that efficiency of energy harvesting module with conventional circuit is dependency installed dummy load.

3.1.2 Efficiency of Energy Harvesting Module

Figure 11 shows the efficiency of energy harvesting module as a function of the magnetic flux density. In this experiment, we used a dummy load of 1 kΩ. In contrast previous circuit of using conventional circuit and function generator, we demonstrated as soon as possible virtual. According to Fig. 10, the best efficiency of 4.57 % was achieved into 60 μT at 60 Hz of uniform magnetic flux density. The range over 60 μT was not find out efficiency. It is found that induced voltage of the ends of dummy load don't generate over the 60 μT.

Figure 12 shows the voltage ratio V_{out}/V_{in} as a function of the number of steps, as a parameter of the input voltage and results of LTspice analysis. Figure 13 shows the model with a CW circuit for LTspice. The input resistance was 50 Ω, and no dummy load was connected to the output. It was found that the output

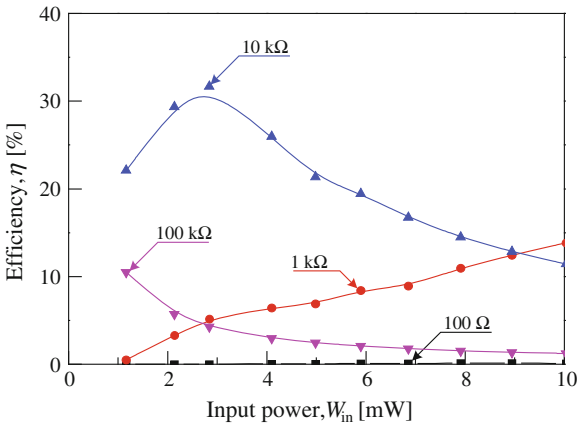

Fig. 10 Efficiency as a function of the input power

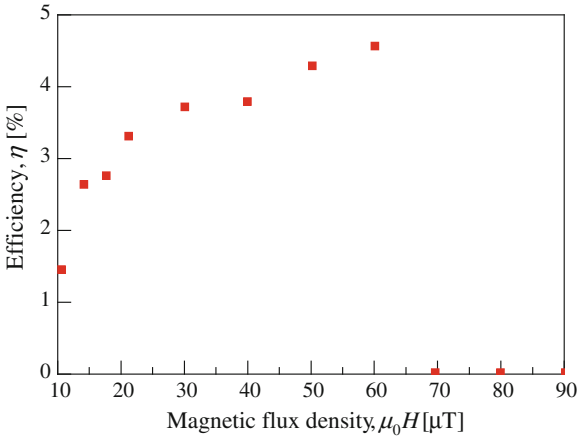

Fig. 11 Efficiency as a function of the Magnetic flux density. The input resistance was 1 kΩ

voltage was approaching to the theoretical value of V_{in} ($V_{p\text{-}p}$) × s, when the input voltage was larger than 1 $V_{p\text{-}p}$. We compared measured values with theoretical values, when the input voltage was 1 $V_{p\text{-}p}$. The measured output voltage for $s = 2$, 4, 6, 8, and 10 were 86.3, 85.8, 85.3 %.

Table 2 shows examples of suitable dummy loads, as parameters of input resistance and the number of steps. In this consideration, we defined the suitable dummy load where the efficiency was a maximum value at the input voltage of 1 $V_{p\text{-}p}$. When the input resistances were 50 Ω and 1 kΩ, the maximum output energy approached to 100 and 10 μW, respectively. If there were no losses in the CW circuits, from the maximum power transfer theorem, the achievable output energy is 5 mW for $R_{in} = 50$ Ω and 0.25 mW for $R_{in} = 1$ kΩ, respectively. From this experiment, the achieved energy was about 2 % for $R_{in} = 50$ Ω and 4 % for $R_{in} = 1$ kΩ, respectively. It should be noted that the efficiency will increase when

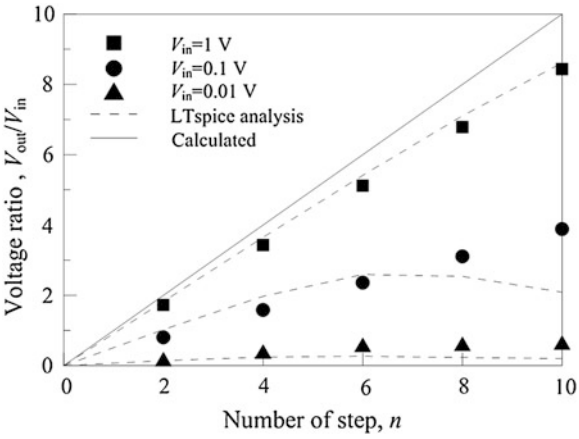

Fig. 12 Voltage ratio as a function of the number of step, as a parameter of the input voltage. The input resistance was 50 Ω, and no dummy load was connected to the output

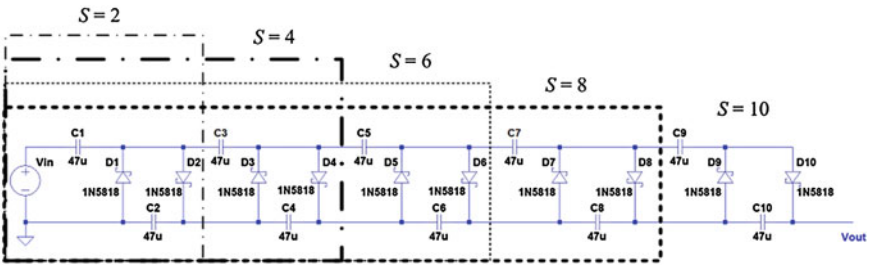

Fig. 13 LTspice model for CW circuit ($s = 10$ combined from $s = 2$ to $s = 8$)

Table 2 Suitable dummy load at the input voltage was $1V_{p\text{-}p}$

Number of step	Dummy load, R_L (kΩ)	
	($R_{in} = 50\ \Omega$)	($R_{in} = 1000\ \Omega$)
2	0.5	5
4	5	20
6	10	50
8	20	100
10	50	200

the input voltage is increased. It was also found that the suitable dummy load becomes large when the input resistance was large.

Figure 14 shows harvested power as a function of dummy load, as a parameter of the number of steps. In this experiment, we used dummy loads of 1, 10, 100 k and 1 MΩ. The magnetic field was 90.2 μT at 60 Hz. The estimated energy of the magnetic harvesting module was 106 mW from (3), and the corresponding measured energy was 104 mW. In this figure, the estimated efficiency was also plotted. From this experiment, suitable dummy loads were found for CW circuits having a different number of steps. If the number of steps was 2, the best efficiency of 87.3 % was achieved with the dummy load of 10 kΩ. When the dummy load was 100 kΩ, the maximum efficiency was 80.3 % when the number of steps was 6.

4 Discussion

It was found that the optimum conditions of CW circuits depend on the number of steps, the input voltage and the dummy load. According to the ICNIRP2010 guideline, the usable magnetic field is up to 200 μT. However, the value of the magnetic field depends on environmental conditions. Table 3 shows an example of suitable conditions for a usable magnetic field. These values correspond to the 1/50, 1/20, 1/10 and 1/5 of the values found in the ICNIRP2010 guideline. If the magnetic field is larger than 10 μT, we should select a dummy load of 10 kΩ with

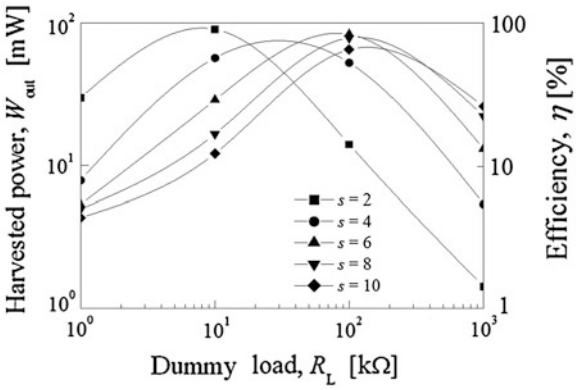

Fig. 14 The harvested power as a function of dummy load, as a parameter of the number of step. In this experiment, we used dummy load of 1, 10, 100 k and 1 MΩ. The magnetic field was 90.2 μT at 60 Hz

Table 3 An example of suitable conditions for usable magnetic field

Magnetic flux density, B (μT)	Dummy load, R_L (kΩ)	Output voltage, V_{out} (V)	Harvested power, W_{out} (mW)	Number of step, s
4	100	3.64	0.132	6
10	10	3.37	1.13	2
20	10	6.57	4.32	2
40	10	13.2	17.5	2

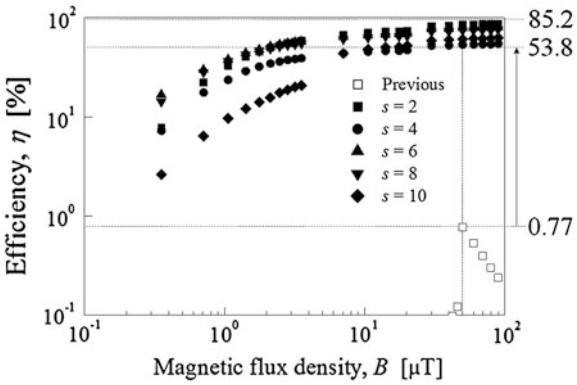

Fig. 15 Comparison of the efficiency as a function of magnetic field, as a parameter of the number of steps. The output load was 10 kΩ when the number of steps was 2 and 4. When the other conditions, that was 100 kΩ

one CW circuit ($s = 2$). Figure 15 shows a comparison of the efficiency as a function of magnetic field, as a parameter of the number of steps. We also plotted the results of previous device, and the optimum dummy load was selected for each conditions. With the previous device, maximum efficiency was achieved with a magnetic field of 50 μT. In contrast, with the same magnetic field, the new device can dramatically improve the efficiency between 53.8 and 85.2 %. It should be noted that the new device can achieve the efficiency of 10 % even if the magnetic field is as low as 353 nT.

5 Conclusion

In this chapter, we compared previous to new energy harvesting module installed AC–DC converter with CW circuits for a magnetic energy harvesting device. Using a magnetic field of 675 nT at 60 Hz, the new magnetic energy harvesting device can provide DC output voltage of 1.5 V. Compared with the previous device we developed, the required magnetic field is as low as 1/400 in amplitude. In contrast, the efficiency of the device was dramatically improved to larger than 10 % even if the magnetic field was less than 1 μT.

References

1. R.J.M. Vuller, R. Van Schaijk, I. Doms, C. Van Hoof, R. Merten, Micropower energy harvesting. Solid-State Electron. **53**, 684–693 (2009)
2. Ministry of Internal Affairs and Communications, Development of electromagnetic energy harvesting technology, vol. A247, p. 2, March 2012
3. K. Tashiro, H. Wakiwaka, S.-I. Inoue, Y. Uchiyama, Energy harvesting of magnetic power-line noise. IEEE Trans. Magn. **47**, 4441–4444 (2011)
4. ICNIRP, Guideline for limiting exposure to time-varying electric and magnetic fields (1 Hz to 100 kHz). Health Phys, **99**(6), 818–836 (2010)
5. K. Tashiro, H. Wakiwaka, Y. Uchiyama, Loss measurement in power conditioning module for power-line magnetic noise energy harvesting device. J. Jpn. Soc.Appl. Electromagn. Mech. **20**(2), 440–445 (2012)
6. A. Harb, Energy harvesting: state-of-the-art. Renewable Energy **36**, 2641–2654 (2011)
7. K. Tashiro, A. Matsuoka, H. Wakiwaka, Simple-Box-9 coil system: a novel approach to design of a square coil system for producing uniform magnetic fields. Mater. Sci. Forum **670**, 275–283 (2011)
8. A. Matsuoka, K. Matsumura, A. Kubota, K. Tashiro, H. Wakiwaka, Residual magnetization measurements of a motor to be used in satellites. Proc. of SPIE **7500,** 750012-1–750012-6 (2009)

Chapter 17
Modern Methods of Monitoring Radiological Contamination of Water Reservoirs

O. Korostynska, A. Mason, S. Ikezawa and A. I. Al-Shamma'a

Abstract Radiation contamination of water can occur due to natural or man-made sources and events. Although periodical monitoring of water quality takes place in most regulated water reservoirs, the tragic events like Chernobyl and Fukushima and the potential threat of intentional contamination of water justify the need for the development of novel real-time monitoring methods that would alert the authorities or public if the permissible level of radiation in water reservoir is exceeded. This book chapter focuses on the most common sources of radiological contamination of water; it reviews the current regulatory approach to the measurement of such contamination and critically discusses the advantages and limitations of traditional laboratory based methods of water samples analysis as compared to novel emerging technologies that could be potentially implemented into online monitoring system for continuous verification of water quality and safety.

Keywords Radiation contamination · Water quality monitoring · Real-time analysis · Gamma ray scintillation counters · Plasma-mass spectrometry · Environmental monitoring platform

1 Introduction

The implementation of The European Water Framework Directive has triggered the need for new methods and systems which enable the monitoring of chemical and biological pollutants in real time [1]. To ensure water is potable, its monitoring

O. Korostynska · A. Mason (✉) · A. I. Al-Shamma'a
Built Environment and Sustainable Technologies (BEST) Research Institute, Liverpool John Moores University, Byrom Street, Liverpool L3 3AF, UK
e-mail: A.Mason1@ljmu.ac.uk

S. Ikezawa
Graduate School of Information Production and Systems, Waseda University, Kitakyushu, Fukuoka, Japan

A. Mason et al. (eds.), *Sensing Technology: Current Status and Future Trends I*, Smart Sensors, Measurement and Instrumentation 7, DOI: 10.1007/978-3-319-02318-2_17,

for the presence of all type of contaminants should be carried out continuously from its source to the tap all over the planet, as all water sources are inadvertently connected and influenced by each other in a long run.

Radioactive pollution of water can also be due to discharges and/or by-products released to the external environment by activities using naturally occurring radioactive materials or artificial radionuclides [2]. Moreover, water distribution systems are vulnerable to intentional and inadvertent contamination, including the radiological contamination as a result of industrial or natural catastrophes [3]. The Fukushima accident dramatically recalled the need to rapidly check the radionuclide activity concentration in drinking water to ensure the radiological protection of the public. In this situation, the major constraint for a testing laboratory during an accidental situation is less the accuracy of the result than the rapidity of the data availability, as water is needed for many uses. The impact of human activities such as agriculture and industry, especially nuclear, on water resources has to be evaluated to account for the consequences on health and environment that contaminated water can potentially inflict.

Concern about total radionuclides content in water intended for human consumption is a matter of national policy and security. WHO guidelines for drinking water suggest performing an indirect evaluation of committed dose by measuring alpha and beta gross radioactivity and checking compliance to derived limit values. Testing laboratories that carry out radionuclide activity measurements required by national authorities must obtain specific accreditation for radioactivity measurement on food and/or drinking-water samples and use International Standards to do so. The international approach proposed by WHO to assess the safety of drinking-water with respect to its radionuclide content is to set up radionuclide screening levels and guidance levels, expressed as activity concentration, based on an annual dose derived from an annual risk of cancer.

There is an acute need in on-line monitors that are able to detect the excess of pollutants established by the official water quality regulations. Currently water quality assessments are based on the analysis of the physical, chemical and bacteriological parameters and require customised apparatus and trained staff. Reliable, comparable and ‘fit for purpose’ results are an essential requirement for any public health decision based on radioactivity measurements, therefore the international standards of tested and validated radionuclide test methods are an important tool for production of such measurements [4]. The International Standardisation Organization (ISO) provides the most comprehensive reference to the standards on radioactivity test methods [5].

Ionisation is the main phenomenon that makes radiation detection and measurement possible. Charged particles cause ionisation of the matter along its path until they stop. Any exposure to radiation involves some level of risk to health of the people or to the environment, as there is a recognised link between environmental radioactivity and public health. International Commission on Radiological Protection (ICRP) and WHO recommend a dose limit for the ingestion of drinking water with derived activity concentration limits for radionuclides that are referred to national regulations. This value of 0.1 mSv/year for 1 year’s consumption of

2 L/day of drinking water, regardless of the origin of the radionuclides, natural or man-made, is referred to as the individual dose criterion (IDC), also called the Total Indicative Dose (TID) in the EC Drinking Water Directive [6]. In the USA the Code of Federal Regulations stipulates that if two or more radionuclides are present in drinking water, the sum of their annual dose equivalent to the total body or to any organ shall not exceed 0.04 mSv/year [4].

Public health protection is a matter of national concern, therefore normally all radiological tests are performed by accredited laboratories using common standards. Thus, testing laboratories that carry out radionuclide activity measurements required by national authorities must obtain specific accreditation for radioactivity measurement on food and/or drinking-water samples and use International Standards to do so. Also, the monitoring of the radionuclides' concentration in mineral bottled water is attracting a lot of interest and is becoming more and more important, as it is extensively used for the preparation of powder milk for children in lactation period [7].

The WHO guidance levels for radionuclides in drinking water varies from 0.1 Bq/L for ^{210}Po to 10,000 Bq/L for ^{3}H. Countries with nuclear facilities (industrial, medical, research and military) can modify these values by national legislation, usually by lowering them, such as in the case of tritium for which the reference level is set up at 740 Bq/L in the USA or at 100 Bq/L by the EC. The range of the different permissible activity concentration places constraints on the selection of measurement procedures and equipment for testing laboratories in charge of the radioactivity monitoring of drinking water [4].

In most drinking water, since the usual activity concentrations of individual radionuclides are low and their determination is time consuming, detailed analysis is normally not justified for routine monitoring [4]. Therefore, no routine measurements of aqueous reservoirs' state include testing for radiological contamination on daily or continuous basis.

Sub-Committee 3 Radioactivity measurement of ISO TC147 has developed standards on test methods used for the monitoring of waters for regulatory purposes, research, etc. [8]. Its terms of reference cover laboratory test methods, in situ and on-line measurements, of any individual radionuclide of natural or artificial origin, as well as radionuclide non-specific parameters. Among others, the drinking water quality guidelines specify the methods for the determination of tritium activity concentration using a liquid scintillation counting method, the measurement of gross alpha activity (ISO 9696), gross beta activity (ISO 9697), and gamma-ray spectrometry. Also established are the methods for the calibration and use of germanium spectrometers for the measurement of gamma-ray energies and emission rates and the calculation of source activities from these measurements.

As modern use of nuclear technology expands, continuous real-time assessment technologies are especially vital in perceived cases of intentional radiological contamination of aqueous reservoirs and after natural or man-made accidents, such as Fukushima and Chernobyl [3]. Nuclides like ^{129}I and ^{237}Np contribute to liquid releases from nuclear power stations and nuclear fuel reprocessing sites. Therefore, new methods and equipment are being developed for the monitoring of

radiological contamination of water, and accordingly the official standards and regulations are periodically amended to comply with the industry and policy needs and to benefit from the technological achievements, which usually offer new, more accurate, faster and cheaper methods of water sample analysis than current off-line bulky laboratory based methods. For example, two alternative test methods to determine the gross alpha and gross beta activities were published with a new sample preparation stage by direct evaporation to dryness described in ISO 10704 in 2009 and with a different type of measuring equipment by liquid scintillation counting detailed in ISO 11704 in 2010 [9].

Although radioactivity measurements are performed regularly by testing laboratories on environmental samples and reported to national authorities for regulatory purposes and public information, very often these measurements are post-factum, i.e. when the radiological contamination already occurred and therefore its level has to be monitored. Increasing regulatory pressure on the monitoring of drinking water has already dramatically increased analytical needs of testing laboratories in terms of improved detection limit and quality program as national authorities seek to lower any expected risk to public health [4]. As mentioned above, no continuous assessment of radiological pollution of water is performed in most cases. This is not least due to the fact that such measurements are lab based, expensive and require specially trained and authorised personnel. Therefore, novel real-time monitoring techniques capable of providing information on the presence of radionuclides in water reservoirs in situ are necessary and they must detect the excess of radiological pollutants established by the official water quality regulations [10].

2 Sources of Radioactive Contamination of Water

The Radioactivity in drinking water may be either man-made, resulting from waste discharges and atomic bomb fallout, or produced naturally, from the dissolution of gases and rock minerals. Drinking water can contain significant concentration of radionuclides of natural origin, mainly U and Th and their decay products in high radioactive disequilibrium, as well as ^{40}K. This is generally due to the geological features of the reservoirs and the solubility of the chemical compounds in which radionuclides are bound. The maximum limit of uranium in drinking water recommended by World Health Organization (WHO) is 15 μg/L.

For example, Tritium, ^{3}H, is an unstable isotope of Helium that is produced during fusion reactions and to a lesser degree fission reactions (10^5 times less). Tritium decays via β^- emission to the stable isotope ^{3}He. Tritium has a $t_{1/2}$ of 12.3 years, and poses a particular biological threat in the form of tritiated water, HTO. Tritium can enter the body via ingestion, inhalation, or contact with the skin, either as HTO or in gaseous form (tritium oxide, but only 0.004 % of this is converted to HTO and retained as free water. Tritiated water generally follows the same kinetic process through the body as normal water, therefore it is so dangerous

when present in water at elevated levels. A particular concern when dealing with exposure to HTO is if tritium is transferred into the DNA of a cell; the subsequent β decay can destroy or rearrange the molecule. However, this effect is almost certainly over shadowed by the ionising damage the β particle will cause within the cell and its neighbours [11, 12].

Exposure to ^{131}I has been linked to various health risks, including tumour growth, thyroid cancer, hyperthyroidism, autoimmune disease of thyroid cells, malignant and benign nodules, and Graves disease [13, 14].

Notably, ^{210}Pb ($t_{1/2} = 22.26$ years) is one of the most difficult naturally occurring radionuclides to analyse directly via radiometric measurement due to its low-energy radioactive decay [15]. Because it originates from the successive decay of many short-lived intermediates starting with ^{222}Rn, ^{210}Pb is of interest in both environmental and health studies. The radiotoxicity of ^{210}Pb, mainly resulting from its relatively long radiological half-life in comparison to environmental processes, its chemical similarities with alkaline earth elements, and the high energy associated with the decay of its progeny, has pushed many governmental organisations to include in their legislation strict regulations for exposure to this radionuclide.

Consequently, on-line monitoring of water quality would prevent many millions of people from unsafe exposure and use of contaminated water. The next section critically reviews the existing approaches to water radioactivity monitoring, including traditional techniques, such as γ-spectrometry and α-spectrometry coupled to radiochemical treatment, and relatively novel procedures, like ultra-low level liquid scintillation counting (LSC), radiometric and inductively coupled plasma-mass spectrometry techniques and environmental network monitoring systems. It is believed that modern technological advancements would enable safer use of nuclear radiation through continuous monitoring of radioactivity in water reservoirs.

3 Current Methods of Water Radioactivity Monitoring

3.1 Traditional Water Radioactivity Measurement Techniques

Gamma ray spectrometry is a powerful tool for environmental radioactivity measurements with analytical capabilities which almost always afford Limits of Detection (LoDs) better than those generally required. On the other hand, in the case of water analysis, gamma spectrometry generally does not offer an adequate sensitivity if it is applied to untreated samples [2]. Radiochemical separation methods have to be employed for most radionuclides of interest especially if large quantities of samples (e.g., above 50 L) are required. Also practical problems arise in terms of sampling, not to mention the time-consuming concentration process.

Many radiometric methods have been proposed by standardisation organisations, such as the International Standardization Organization (ISO) and the American

Society for Testing and Materials (ASTM), or public institutions, e.g., the US Department of Energy (DOE) and the US Environmental Protection Agency (EPA). Notably, due to the lack of methods suitable for online monitoring regimes, much effort has been devoted to set up quick and easy procedures.

For example, gross α/β radiation in water is usually measured using thick source method [16], thin source method, or liquid scintillation. Alpha activity is mostly due to the uranium isotope (^{234}U, ^{235}U and ^{238}U) and to ^{226}Ra. Beta activity, to a large extent, is usually due to ^{40}K and short-lived daughters of ^{238}U (^{234}Th and ^{234m}Pa) [17]. Gross alpha and beta activity screening procedures determine if radionuclide specific analysis is required to further characterise the water. Gross alpha and beta activity is usually measured by counting the dry residue of a water sample. In ISO method 9696 and 9697 the residue is first sulphated by addition of sulphuric acid; a fixed amount of dry salts is then evenly dispersed on a steel planchet and counted by a proportional counter or other suitable counter (zinc sulfide scintillation counter for α emissions, plastic scintillation counter for β emissions).

The availability of low-background liquid scintillation counters equipped with alpha–beta discrimination device provides an alternative for gross alpha and beta determination. The LSC method offers several advantages over the traditional procedure: (1) simultaneous alpha and beta measurement through alpha–beta discrimination technique-reduced counting times; (2) high (close to 100 %) and rather constant detection efficiency for alpha emitters and for high energy beta emitters; (3) faster and more reproducible sample preparation; (4) spectral energy response through inspection of emission spectra.

Liquid scintillation analysis (LSA) is a useful tool in the analysis of environmental level radionuclide concentrations. Liquid scintillation counting is an analytical technique which is defined by the incorporation of the radiolabeled analyte into uniform distribution with a liquid chemical medium capable of converting the kinetic energy of nuclear emissions into light energy. Advanced LSA systems provide discrimination between alpha and beta radiations, and reliable passive and active background reduction systems [16, 18]. LSA variations are also currently used for U and Ra isotopes and ^{3}H measurements. Due to the optimal detection power of the LSC technique, overall performance is often satisfactory. On the other hand, the spectral resolution is usually poor and this is an obvious disadvantage if isotopic analysis is to be carried out [2].

Ultra-low level liquid scintillation counting coupled to extractive techniques and alpha/beta discrimination allows rapid and simple determination of all radiometric parameters relevant to dose evaluation, namely gross alpha and beta activity, uranium and radium isotopes content. For tritium and radon determination well established procedures, based on LSC, can also be used. Recommended gross alpha and beta activity screening methods generally employ gas proportional counting techniques.

Interestingly, ^{210}Pb decays into ^{210}Bi through the emission of a low energy β-particle (64 keV), which is rapidly reabsorbed by the sample matrix before reaching the detector. An alternative for the direct measurement of ^{210}Pb is through γ-spectrometry of the ray emitted with an energy of 47 keV; with an average only four times per 100 decays. However, the low energy and rate of

emission associated with this mode of decay make this type of measurement time-consuming, especially at low activities (up to several days of counting per sample). Other measurement alternatives, based on the achievement of secular equilibrium between ^{210}Pb and its progeny (^{210}Bi or ^{210}Po) are effective for the indirect determination of ^{210}Pb activity. Nevertheless, these approaches necessitate long storage periods (up to 2 months) and complex separation procedures [15]. Consequently, an alternative to radiometric measurements that would provide similar analytical performance would be beneficial.

Uranium can be measured using non-radiometric techniques (spectrophotometry, fluorimetry, atomic adsorption, atomic emission). However, these techniques, while allowing the determination of the total concentration of uranium, do not supply any information about its isotopic composition [17].

Inductively coupled plasma mass spectrometry can be used for the determination of many radioisotopes including ^{99}Tc, ^{226}Ra, ^{235,236,238}U, ^{232}Th, and ^{239,240}Pu, based on their masses instead of their radioactive properties. For radioactive isotopes with short half-lives, radiometric techniques generally offer better and faster analyses than ICP-MS since the number of disintegrations per mole of atoms is higher than for long-lived radionuclides. Nevertheless, for some of these short half-life radionuclides such as ^{210}Pb, determination by conventional radiometric techniques is tedious and time-consuming and consequently, the detection of this radionuclide by mass spectrometry might be a viable alternative [15].

^{226}Ra activity concentration can be determined by several radiometric methods [17]:

- Gamma spectrometry by using a germanium semiconductor detector: this method requires a strong sample preconcentration to detect very low concentration limits because of the rather modest counting sensitivity.
- Alpha spectrometry after electrodeposition or selective precipitation of radium as barium(radium)sulphate or adsorption of Ra on a MnO_2-coated disk: this technique has the advantage of being highly sensitive and specific, and all alpha emitting radium nuclides can be determined directly. The method requires, however, several separation steps to isolate radium from the matrix.
- By liquid scintillation counting: this method is based on a radon extraction with a scintillation cocktail immiscible with water followed by a measurement using a liquid scintillation counter (LSC) of the alpha and beta emission of radon and its decay products in radioactive equilibrium with the parent. Radon, being a noble gas, is easily and selectively extracted by an organic phase, whereas all the other radioisotopes, present in ionic form, are not extracted.

It is beyond the remit of this book chapter to list all the methods of detection of radionuclides in water which are approved and standardised as these can be found in respective documents as discussed in previous section. However, Table 1 below gives examples of the most common radiochemical methods for measuring radionuclides in water, which are approved in many countries and the exact procedures are defined by the international standards.

Table 1 Examples of common radiochemical methods for measuring radionuclides in water

Radionuclide or activity	Procedure	Counting device
Gross α/β	Thick source method Thin source method	Alpha and beta counters
	Liquid scintillation	LSC
Am-241	Separation by ion exchange plus electrodeposition	Semiconductor α spectrometer
Pb-210	Radiochemical separation of decay product Bi-210	Beta counter
Po-210	Autodeposition on metal planchets	Semiconductor α spectrometer
Pu isotopes (α emitters)	Separation by ion exchange plus electrodeposition	Semiconductor α spectrometer
Ra-226	Coprecipitation and emanometry, solvent extraction (Rn-222 decay products)	Lucas cells
	Coprecipitation and LSC	LSC
Ra-228	Radiochemical separation of Ra-228 and then of decay product Ac-228	Beta counter
Sr-90	Radiochemical separation of Sr-90 or decay product Y-90	Beta counter LSC (Cherenkov)
Th isotopes	α spectrometry	α spectrometer
U isotopes	Separation by ion exchange plus electrodeposition	Semiconductor α spectrometer
	Solvent extraction	LSC

All of these methodological approaches require a preliminary sample treatment or radiochemical separation, even if water does not need lengthy pre-treatment procedures as it is the case for the majority of environmental matrices [2]. Nevertheless, radiochemical separation techniques are often cumbersome. Pu, Th, and U isotopes are usually separated by ion exchange or extraction chromatography, electrodeposited on steel planchets, and measured by high resolution alpha spectrometry. ^{226}Radium can be selectively precipitated and measured in the same way or determined indirectly through the decay product ^{222}Rn by the emanometric technique [19]. The beta emitters ^{210}Pb and ^{90}Sr can be isolated by means of extraction chromatography [20] or selective precipitations and directly counted or measured by gross beta counting of the decay products ^{210}Bi and ^{90}Y, respectively. The next section focuses on the mass spectrometry assessment method for the determination of radioactivity in drinking water.

3.2 Assessment of Radioactivity in Drinking Water by Mass Spectrometry

Several non-radiometric techniques based on Mass Spectrometry (MS) are available for the quantitative determination of radionuclides. The various types of MS instruments depend primarily on the type of ion sources, the system for sample

introduction and the detection unit. The most successful approaches for ion generation resort to Inductively Coupled Plasma (ICP), Direct Current Plasma (DCP), Microwave Induced Plasma (MIP), Spark Source (SS), Thermal Ionization (TI), Glow Discharge, Laser Microprobe (LM), and Secondary Ion (SI) systems [2]. In particular, ICP-MS has been showing great potential to detect radionuclides in a vast array of environmental, clinical, and food matrices. ICP-MS is becoming a valid alternative to radiometric detection techniques.

In ICP-MS approach the determinations are based on a number of subsequent processes, i.e., atomisation, conversion of atoms into a stream of ions, separation of ions on the basis of their mass/charge ratio (m/z), and counting of the number of ions. The majority of the ions formed are singly charged. In this case, the m/z ratio is simply the mass of the ion. ICP-MS is nowadays a leading technique because of its stability, multi-elemental screening capabilities, excellent detection limits, relative freedom from sample matrix interferences, reduced sample preparation, large dynamic range (low ng/L to high mg/L), and fast analysis [2].

New avenues are opened by ICP-MS as regards the possibility to distinguish among specific isotopes and to measure isotope ratios. In addition to this, ICP-MS allows specific stable isotopes to be better used in medical tracer studies, thus avoiding the use of radioactive isotopes. The combination of all these features makes of the plasma an ideal source for MS. On the other hand, the major drawbacks of this technique are the high initial purchase cost of the instrumentation along with the daily costs of maintenance. ICP-MS instruments can be based on a Quadrupole (Q), a Sector Field (SF), or a Time-of-Flight (ToF) system with single or multiple ion collection. Q- and SF-spectrometers are by far more popular than ToF instruments [2]. Q-instruments have lower resolution power ($m/\Delta m$) than the SF-based ones, thus being less able to discriminate the analyte mass from the masses of other single or multiple ions. The main disadvantage of this method is that interferences generated by oxides and hydroxides of the analyte and of the elements present in the matrix can severely impact on analytical accuracy.

ICP-MS has in recent years greatly benefitted from the adoption of ancillary instrumentation such as the Dynamic Reaction Cell (DRC) or the Collision Cell (CC) [15, 21–25]. The DRC is basically a Q device acting as a band-pass mass filter which may be pressurised with a reactive gas thus promoting ion–molecule reactions and suppressing analytical isobaric interferences.

While mass spectrometric determination does not rival detection limits achievable by radiometric counting, radiometric determination of ^{90}Sr, a pure beta-emitter, is hindered by long analysis times (several weeks); the comparatively fast analysis achieved via ICP–MS enables same-day preparation and analysis of samples, making this an important technique for the environmental monitoring of areas contaminated by radioactivity [26].

The explosions of the Fukushima Daiichi Nuclear Power Plants, caused by hydrogen explosions destroying the external nuclear reactor buildings on March 2011, resulted in massive releases of various radionuclides (^{131}I, ^{137}Cs, ^{134}Cs, ^{136}Cs, and ^{132}Te) into the atmosphere. Notably, the ICP-DRC-MS was applied to screening test of strontium and plutonium in environmental samples at Fukushima [27].

3.3 ENMS Detection Stations

The Environmental Network Monitoring System (ENMS) concept is used for the remote surveillance of radioactivity (contamination and exposition) [28]. ENMS is based on two types of entities: the Detection Station (DS) and the Central Station (CS). The Central Station is the link between the operator and one or several Detection Stations through an appropriate telecommunication mode. There are no distance restrictions between CS and DS. The DS continuously monitors the radiation level and compares it to user defined alarm levels. The radiation levels are typically expressed in Bq/volume unit (i.e. for water/air contamination) or μSv/h (i.e. for exposition).

The ENMS concept is designed for native scaling-up to accommodate small scale and local as well as nationwide—or even worldwide—radiological monitoring networks. The National Institute for Radioelements has developed a number of DSs for water radiological monitoring in environmental or in industrial and medical applications, for example, ENMS-WGS D1b and ENMS-WGS D5b (displayed in Fig. 1a) [28]. These systems weight 8 and 25 kg respectively, are easy transportable for operation in water purification plants, desalination plants, in sea, lakes, rivers and can perform measurements in continuous immersion regime for 1 year. At the core of these systems is NaI detector probe, the components of which are depicted in Fig. 1b. Notably, the power supply to the system can be via battery or using the solar energy for remote long-term operation in suitable locations.

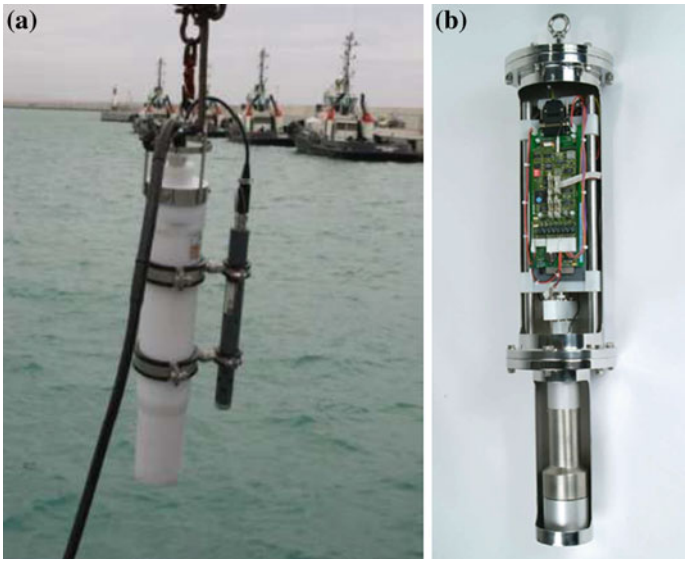

Fig. 1 Environmental network monitoring system ENMS-WGS D5b: **a** at field trial and **b** NaI detector probe that is at the core of the system [28]

3.4 A Move Towards Transparency of Information About Environmental Radiological Contamination for Public Use

The Chernobyl disaster almost 30 years ago claimed the lives and health of many people not only in Ukraine, but in countries such as Belarus, Russia and Europe [29, 30]. Air, water and soil were contamination with radiation and even now the 30-km exclusion zone around Chernobyl exists where no one lives. Contamination of drinking water (predominantly from ^{131}I) was a major issue for the first few weeks after that catastrophe, with the Kyiv reservoir being polluted in particular [3]. Activity fell rapidly in the reservoir due to dilution and absorption of radionuclides by soil. However the bed sediments act as a sink and will store contaminants for years to come. Radio caesium levels in fish (located in lakes as far away as Germany) increased rapidly following the accident, but soon declined to the current low levels (except for closed lakes which could poses significant activity for decades to come). Strontium-90 contamination of fish did not prove to be a major exposure pathway as it would have accumulated in the fish bones, but the consumption of fish was deemed to be dangerous. Current contamination levels of open surface water are low and are safe enough for irrigation purposes. Caesium-137 released from Chernobyl has been attributed to the high levels detected in reindeer meat in Finland, Norway, Russia, and Sweden. Sadly, at the time of the Chernobyl disaster, the true information on the radiation levels in air and water was hidden from the public, and people were unaware of the consequences they are about to face [31, 32].

True scale of the Fukushima accident was also not immediately revealed to the public, with information on the level of radiation in water being ten-fold reduced according to the official sources. Clearly, radioactive contamination negatively affects the abundance of living beings through the radiation and chemical toxic effects of radionuclides or the effects of mutation accumulation over time [33]. Radiation can have short-term direct radiotoxic effects or long-term indirect mutation effects on living organisms. The short-term radiotoxic effects include oxidative stress, increased damage to DNA, immuno-suppression and many others. Such physiological effects can result in reproductive failure and death. Reproductive failure associated with radiation occurs as a consequence of embryo mortality [34]. Mutation effects due to radioactive contamination are widespread, although more difficult to study due to their long-term nature that can extend across generations. Mutations arise from DNA damage that is not repaired thereby causing a reduction in fitness.

Thus, real-time radiation detectors have become an essential tool for emergency personnel who may have to respond to unknown accidents, incidents, or terrorist attacks, which could involve radioactive material [35]. More and more ordinary citizens are interested in personal radiation protection, as well. Reasons include lost radiation sources, transportation of nuclear waste, industrial accidents, radiological terrorism, and the possibility of nuclear weapons being used in a war.

Mapping radioactivity levels in air, water and the terrestrial environment may be used as a precursor to carrying out more detailed surveys that serve to validate, or extend, existing data and to identify areas of potential public harm [36].

It has been recognised that the water supply systems of small, remote communities may differ from those of urban centres, quite often based on economic and environmental factors. In many cases these communities rely on groundwater for their water supply. With this in mind, a survey of radioactivity in groundwater (110 sites) was conducted as a precursor to providing a baseline of radiation exposure in rural and remote communities in Queensland, Australia, that may be impacted upon by exposure pathways associated with the supply, treatment, use and wastewater treatment of the resource. Radionuclides in groundwater, including ^{238}U, ^{226}Ra, ^{222}Rn, ^{228}Ra, ^{224}Ra and ^{40}K were measured and found to contain activity concentration levels of up to 0.71, 0.96, 108, 2.8, 0.11 and 0.19 Bq/L respectively [36]. Activity concentration results were classified by aquifer lithology, showing correlation between increased radium isotope concentration and basic volcanic host rock.

An illustrative example of the change in public and government attitude towards releasing true information on radiological pollution of the environment is Japan, where now Tokyo Electric Power Company (TEPCO) performs daily analysis at a number of key sites near Fukushima station and this information is available to public on the website [37].

Also, due to the fact that information on radiation contamination in Japan following Fukushima tragedy has not been coming from places of authority in a free and timely fashion, an alternative, more open approach was needed. Kyoto University Research Reactor Institute (KURRI) was working with Fukushima Transportation Inc. to use a system to monitor radiation in Fukushima City that is in real time and is accessible by anyone over the internet [38]. This cooperation resulted in Kyoto Univ. RAdiation MApping System (KURAMA), which is a GPS-aided mobile radiation monitoring system. It was needed to quickly produce precise maps of air dose rates to facilitate a better understanding of issues such as the inhabitants' state of exposure and scale of environmental contamination. This sparked the development of a system that could carry out cross-sectional air dose rate measurements using data collected from vehicles roaming designated areas and providing a near real-time visualization of the measurements.

Figure 2 shows the configuration of KURAMA. A vehicle containing the in-vehicle device travels around the area and continuously measures radiation levels in arbitrary locations. Measurement times and locations are retrieved from the GPS, tagged to the corresponding measurements, and sent to servers through the Internet. A near real-time visualisation of the area's radiation dose distribution is plotted on top of map data with the results. A conventional passenger car was used as the measuring vehicle and a measurer operated the in-vehicle device. The external dimensions of the device are $34.5 \times 17.5 \times 19.5$ cm^3 (Fig. 3). Also, by installing the software program developed with LabVIEW into the CompactRIO, KURAMA-II is fully automated as long as it remains connected to a power source and it does not require special operation to function.

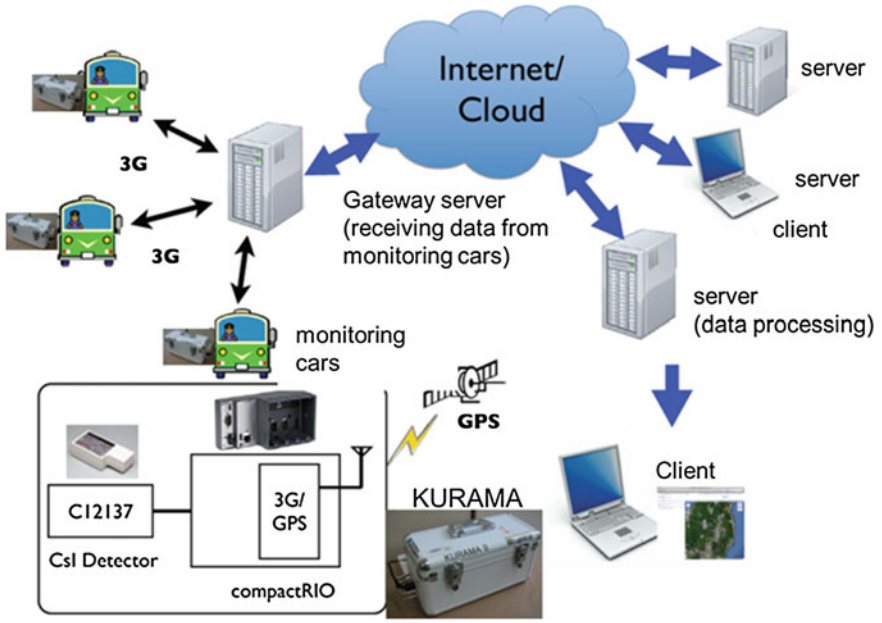

Fig. 2 KURAMA-II's system configuration [39]

Fig. 3 KURAMA-II's in-vehicle device [39]

The project has proven to be a huge success and now, few years in operation, over 20,000 users of mobile radiation dosimeters report daily the dose level in their respective areas and this information is immediately available online for public and regulatory use. Following KURAMA success, new portable systems to measure in real-time the radiological contamination of soil and water are being developed by the scientists all over the world.

4 Conclusion

Due to deleterious effects of excess levels of ionising radiation on human health and environment, there is a need in continuous real-time monitoring of radionuclides present in the water reservoirs. This became especially evident following such large-scale the nuclear disasters as Chernobyl and Fukushima. This book chapter briefly reviewed the current regulatory approach to the measurement of radioactive contamination of water.

The analytical techniques discussed in this chapter are in most cases capable of successfully quantifying radionuclides in drinking water. Drinking, recreational, irrigation and livestock waters are periodically screened for the presence of radionuclides using gross alpha and beta activity screening techniques in many countries worldwide. The combination of radiochemical methods and gamma spectrometry for water samples allow the requirements of international regulations to be met for the vast majority of radionuclides. In some cases rapid methods, based on LSC, can be successfully employed. Nevertheless, for some radioelements, the measurements by radiometric techniques are still lengthy and cumbersome despite the improvement in analytical techniques. Plasma-mass spectrometric techniques, either based on Q systems or on high resolution SF systems, are gaining wide popularity as regards their applicability to the determination of long-lived radionuclides.

Although most of the methods employed are still lab based, require bulky and expensive specialised equipment and trained staff, there is a change in public attitude towards the information on the level of radiation in air, soil and water. As a consequence, there is an emerging trend of portable, real-time radiation dosimeters that continuously conduct radiological assessment of the environment and these data are instantly available online for public use. These novel technologies can be potentially implemented into online monitoring system for continuous verification of water quality and safety.

Acknowledgments We would like to acknowledge the support of DAIWA Anglo-Japanese Foundation for providing a grant to visit Japan Ref. 9050/9942 to assess the current methods of monitoring the radiological contamination of water sources. This work is also in part financially supported by the European Community's Seventh Framework Programme through the FP7-PEOPLE-2010-IEF Marie-Curie Action project 275201, Water-Spotcheck.

References

1. European Council, Directive 2000/60/EC of the European Parliament and of the Council of 23 October 2000 establishing a framework for Community action in the field of water policy, OJ L, vol. 327, pp. 1–73, Dec. 2000
2. S. Caroli, M. Forte, C. Nuccetelli, R. Rusconi, S. Risica, A short review on radioactivity in drinking water as assessed by radiometric and inductively coupled plasma-mass spectrometry techniques. Microchem. J. **107**, 95–100 (2013)
3. K. Arshak, O. Korostynska, Advanced Materials and Techniques for Radiation Dosimetry (Artech House, London, 2006)

4. D. Calmet, R. Ameon, A. Bombard, M. Forte, M. Fournier, M. Herranz, S. Jerome, P. Kwakman, M. Llaurado, S. Tokonami, ISO standards on test methods for water radioactivity monitoring. Appl. Radiat. Isot.
5. ISO. ISO Standards catalogue. 13.280: Radiation protection. Available: http://www.iso.org/iso/products/standards/catalogue_ics_browse.htm?ICS1=13&ICS2=280&
6. European Commission, Laying Down Requirements for the Protection of the Health of the General Public With Regard to Radioactive Substances in Water Intended for Human Consumptional, in COM147 vol. 201200074NLE, ed. Brussels, Belgium, 2012
7. D. Desideri, M.A. Meli, L. Feduzi, C. Roselli, A. Rongoni, D. Saetta, 238U, 234U, 226Ra, 210Po concentrations of bottled mineral waters in Italy and their dose contribution. J. Environ. Radioact. **94**, 86–97 (2007)
8. ISO, ISO/TC 147/SC 3 Radioactivity measurements, ed (2005)
9. ISO, 11704:2010 Water quality-measurement of gross alpha and beta activity concentration in non-saline water-liquid scintillation counting method, ed (2010)
10. O. Korostynska, K. Arshak, V. Velusamy, A. Arshak, A. Vaseashta, *Recent Advances in Point-of-Access Water Quality Monitoring: Technological Innovations in Sensing and Detection of Chemical, Biological, Radiological, Nuclear Threats and Ecological Terrorism*, edited by A. Vaseashta, E. Braman, P. Susmann (Springer, Netherlands, 2012), pp. 261–268
11. J. Cadet, T. Douki, D. Gasparutto, J.-L. Ravanat, Radiation-induced damage to cellular DNA: measurement and biological role. Radiat. Phys. Chem. **72**, 293–299 (2005)
12. P. Swiderek, Fundamental processes in radiation damage of DNA. Angewandte Chemie - International Edition **45**, 4056–4059 (2006)
13. C. Matthiesen, J.S. Thompson, D. Thompson, B. Farris, B. Wilkes, S. Ahmad, T. Herman, C. Bogardus Jr, The efficacy of radiation therapy in the treatment of graves' orbitopathy. Int. J. Radiat. Oncol. Biol. Phys. **82**, 117–123 (2012)
14. S. Merrill, J. Horowitz, A.C. Traino, S.R. Chipkin, C.V. Hollot, Y. Chait, Accuracy and optimal timing of activity measurements in estimating the absorbed dose of radioiodine in the treatment of Graves' disease. Phys. Med. Biol. **56**, 557–571 (2011)
15. D. Lariviere, K.M. Reiber, R.D. Evans, R.J. Cornett, Determination of 210Pb at ultra-trace levels in water by ICP-MS. Anal. Chim. Acta **549**, 188–196 (2005)
16. R. I. Kleinschmidt, Gross alpha and beta activity analysis in water—a routine laboratory method using liquid scintillation analysis, in *Low Level Radionuclide Measurement Techniques*, October 13, 2003–October 17, 2003, Vienna, Austria, 2004, pp. 333–338
17. D. Desideri, C. Roselli, L. Feduzi, M.A. Meli, Radiological characterization of drinking waters in Central Italy. Microchem. J. **87**, 13–19 (2007)
18. J.M. Pates, N.J. Mullinger, Determination of 222Rn in fresh water: development of a robust method of analysis by/separation liquid scintillation spectrometry. Appl. Radiat. Isot. **65**, 92–103 (2007)
19. B.K. Bhaumik, M. Soundararajan, Statistical evaluation of an optimum radon emanometric technique. Int. J. Radiat. Appl. Instrum. Part D. Nucl. Tracks Radiat. Meas. **17**, 503–506 (1990)
20. A. Heckel, K. Vogl, Rapid method for determination of the activity concentrations of 89Sr and 90Sr. Appl. Radiat. Isot. **67**, 794–796 (2009)
21. C.F. Brown, K.N. Geiszler, M.J. Lindberg, Analysis of 129I in groundwater samples: direct and quantitative results below the drinking water standard. Appl. Geochem. **22**, 648–655 (2007)
22. Y.L. Chang, S.J. Jiang, Determination of chromium species in water samples by liquid chromatography-inductively coupled plasma-dynamic reaction cell-mass spectrometry. J. Anal. Atom. Spectrom. **16**, 858–862 (2001)
23. K. Jitmanee, N. Teshima, T. Sakai, K. Grudpan, DRC ICP-MS coupled with automated flow injection system with anion exchange minicolumns for determination of selenium compounds in water samples. Talanta **73**, 352–357 (2007)
24. H. Liu, S.-J. Jiang, Determination of vanadium in water samples by reaction cell inductively coupled plasma quadrupole mass spectrometry. J. Anal. Atom. Spectrom. **17**, 556–559 (2002)

25. H.L. Ma, P.A. Tanner, Speciated isotope dilution analysis of Cr(III) and Cr(VI) in water by ICP-DRC-MS. Talanta **77**, 189–194 (2008)
26. V.F. Taylor, R.D. Evans, R.J. Cornett, Determination of 90Sr in contaminated environmental samples by tuneable bandpass dynamic reaction cell ICP-MS. Anal. Bioanal. Chem. **387**, 343–350 (2007)
27. M. Sakama, Y. Nagano, T. Saze, S. Higaki, T. Kitade, N. Izawa, O. Shikino, S. Nakayama, Application of ICP-DRC-MS to screening test of strontium and plutonium in environmental samples at Fukushima, Appl. Radiat. Isot. Appl Radiat Isot. **81**, 201–7 (2013)
28. IRE ELiT (2013). National Institute for Radioelements: Environmental Network Monitoring System (ENMS). Available: http://www.ire.eu/documents/fiche_services_2_wat.pdf
29. D.A. Belyj, A.N. Kovalenko, V.G. Bebeshko, Pathological states of some organs and systems in persons survived after acute radiation sickness: 15 years dynamics after the Chernobyl accident. Meditsinskaya Radiologiya I Radiatsionnaya Bezopasnost **49**, 24–36 (2004)
30. R.J. Berry, Early radiation casualties—what Chernobyl has taught us. J. Soc. Radiol. Protect. **7**, 55–59 (1987)
31. N.M. Nadezhina, I.A. Galstyan, L.A. Suvorova, V.N. Pokrovskaya, G.P. Gruzdev, V.G. Lelyuk, A.B. Kutuzova, Z.N. Rtishcheva, I.V. Uvacheva, Health status of Chernobyl acute radiation syndrome patients. Radiatsionnaya Biologiya. Radioekologiya **37**, 780–786 (1997)
32. N. Parmentier, J.C. Nenot, Radiation damage aspects of the Chernobyl accident. Atmos. Environ. **23**, 771–775 (1989)
33. A.P. Mller, I. Nishiumi, H. Suzuki, K. Ueda, T.A. Mousseau, Differences in effects of radiation on abundance of animals in Fukushima and Chernobyl. Ecol. Ind. **24**, 75–81 (2013)
34. A. Bonisoli-Alquati, T.A. Mousseau, A.P. Møller, M. Caprioli, N. Saino, Increased oxidative stress in barn swallows from the Chernobyl region. Comp. Biochem. Physiol. A Mol. Integr. Physiol. **155**, 205–210 (2010)
35. K. Arshak, O. Korostynska, Thin- and thick-film real-time gamma radiation detectors. Sens. J. IEEE **5**, 574–580 (2005)
36. R. Kleinschmidt, J. Black, R. Akber, Mapping radioactivity in groundwater to identify elevated exposure in remote and rural communities. J. Environ. Radioact. **102**, 235–243 (2011)
37. Result of Radioactive Nuclide Analysis around Fukushima Daiichi Nuclear Power Station, http://www.tepco.co.jp/en/nu/fukushima-np/f1/smp/index-e.html
38. Project KURAMA, Buses in Fukushima to Shed Light on Radiation in the Area, RocketNews24 (2011)
39. M. Tanigaki, National Instruments. Post-Fukushima: Using LabVIEW and CompactRIO to Monitor Radiation. NI Case Study (2012)

About the Editors

Dr. Alex Mason graduated from the University of Liverpool, UK, with a first class honors degree in Computer and Multimedia Systems, after which he went on to complete a Ph.D. in Wireless Sensor Networks and their Industrial Applications at Liverpool John Moores University (LJMU), UK. Upon completing his Ph.D. in 2008, he concentrated for 2 years solely on research, working on aspects of non-invasive and non-destructive sensing for the healthcare, automotive and defense sectors.

Dr. Mason currently holds the position of Reader in Smart Technologies within the School of Built Environment at LJMU, after holding a Senior Lecture post prior to this since 2010. He has continued research in healthcare and defense, in addition to new areas such as water quality monitoring. Since becoming more involved in Built Environment issues, he has also developed an interest in Structural Health Monitoring and is currently working closely with the UK Defense Science and Technology Laboratories in this field.

Dr. Mason is responsible for supervising a number of Ph.D. students in the areas of sensing and renewable energy technologies, has coauthored over 100 publications (including 4 patents), has helped to organize national and international conferences, and gave a number of invited talks on his work. He is also an active member of the IET in the UK, and has achieved Chartered Engineer status with them.

A. Mason et al. (eds.), *Sensing Technology: Current Status and Future Trends I*,
Smart Sensors, Measurement and Instrumentation 7, DOI: 10.1007/978-3-319-02318-2,

Dr. Subhas Chandra Mukhopadhyay graduated from the Department of Electrical Engineering, Jadavpur University, Calcutta, India in 1987 with a Gold medal and received the Master of Electrical Engineering degree from Indian Institute of Science, Bangalore, India in 1989. He obtained the Ph.D. (Eng.) degree from Jadavpur University, India in 1994 and Doctor of Engineering degree from Kanazawa University, Japan in 2000.Currently, he is working as a Professor of Sensing Technology with the School of Engineering and Advanced Technology, Massey University, Palmerston North, New Zealand. His fields of interest include Smart Sensors and Sensing Technology, Wireless Sensors Network, Electromagnetics, control, electrical machines and numerical field calculation etc.

He has authored/co-authored over 300 papers in different international journals and conferences, edited eleven conference proceedings. He has also edited ten special issues of international journals and fifteen books with Springer-Verlag as guest editor. He is currently the Series editor for the Smart Sensing, Measurements and Instrumentation of Springer-Verlag.

He is a Fellow of IEEE, a Fellow of IET (UK), a Topical editor of IEEE Sensors journal. He is also an Associate Editor for IEEE Transactions on Instrumentation and Measurements and a Technical Editor of IEEE Transactions on Mechatronics. He is a Distinguished Lecturer of IEEE Sensors council. He is Chair of the Technical Committee 18, Environmental Measurements of the IEEE Instrumentation and Measurements Society. He is in the editorial board of many international journals. He has organized many international conferences either as a General Chair or Technical programme chair.

Dr. Krishanthi Padmarani Jayasundera graduated from University of Peradeniya, Sri Lanka with honors degree in Chemistry. She obtained her both Master and Ph.D. in Organic Chemistry from Kanazawa University, Japan. After completing Ph.D. she worked as researcher nearly 12 years in New Zealand involving various projects related to organic synthesis. Currently, she is working as a Post-doctoral researcher with the Institute of Fundamental Sciences, Massey University, New Zealand. She has published over 30 papers in different international journals and conference proceedings.

Dr. Nabarun Bhattacharyya is Associate Director in Centre for Development of Advanced Computing (C-DAC), Kolkata, India, which is a premier R&D Institute under Department of Information Technology, Government of India. He is a Ph.D. from Jadavpur University, Kolkata, India. He has authored more than 100 papers in peer-reviewed journals and conferences and two book chapters on the topics electronic nose, electronic vision and electronic tongue. His research areas focus on machine olfaction, soft computing, pattern recognition embedded systems for agricultural and environmental applications. He is a member of IEEE.